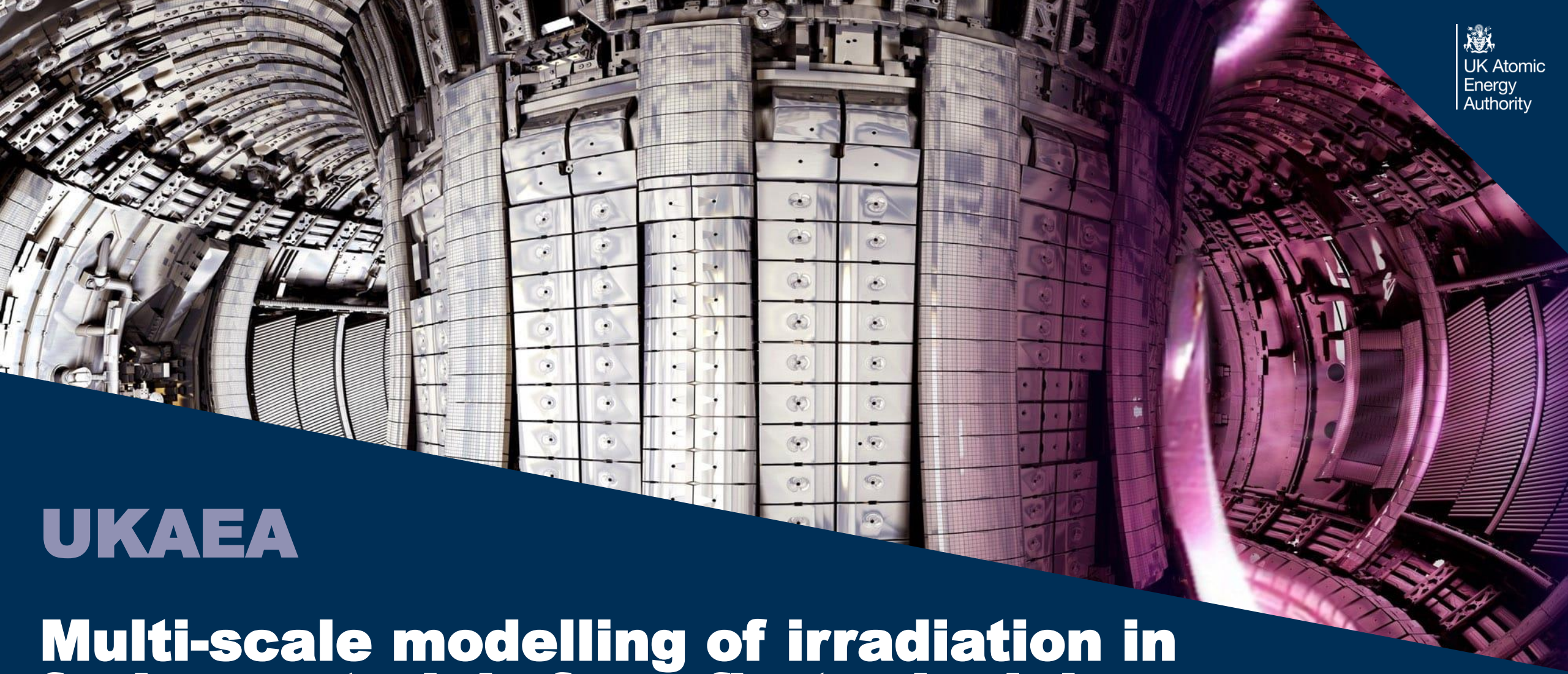

UK Atomic Energy Authority

UKAEA

Multi-scale modelling of irradiation in fusion materials from first principles

Duc Nguyen-Manh, Senior Research Scientist, Materials Division, UKAEA and Materials Department, University of Oxford, UK

Joint ICTP-IAEA-MAMBA School on Materials Irradiation: from Basics to Applications, Trieste, February 10-21, 2025

UKAEA host the Joint European Torus (JET) and MAST/STEP fusion devices

UK Atomic Energy Authority

UKAEA Mission

"To lead the delivery of sustainable fusion energy and maximise the scientific and economic benefit."

UKAEA Goals

The four interconnected strategic goals to deliver on this mission are:

1. Be a world leader in fusion research and development.

2. Enable the delivery of sustainable fusion power plants.

3. Drive economic growth and high-tech jobs in the UK.

4. Create places that accelerate innovation and develop skilled people for industry to thrive.

Outline

UK Atomic Energy Authority

Part I: Basics understanding of radiation damage in materials

- Materials challenges in nuclear fusion power plants
- MMM: bridging gaps from DFT
- Fundamental understanding of radiation damage from FP

Part II: Microstructure evolution of materials under irradiation

- Modelling of transmutation-induced precipitation
- Designing new outstanding radiation resistance materials
- First-principles phase-field modelling for HI transport at interface

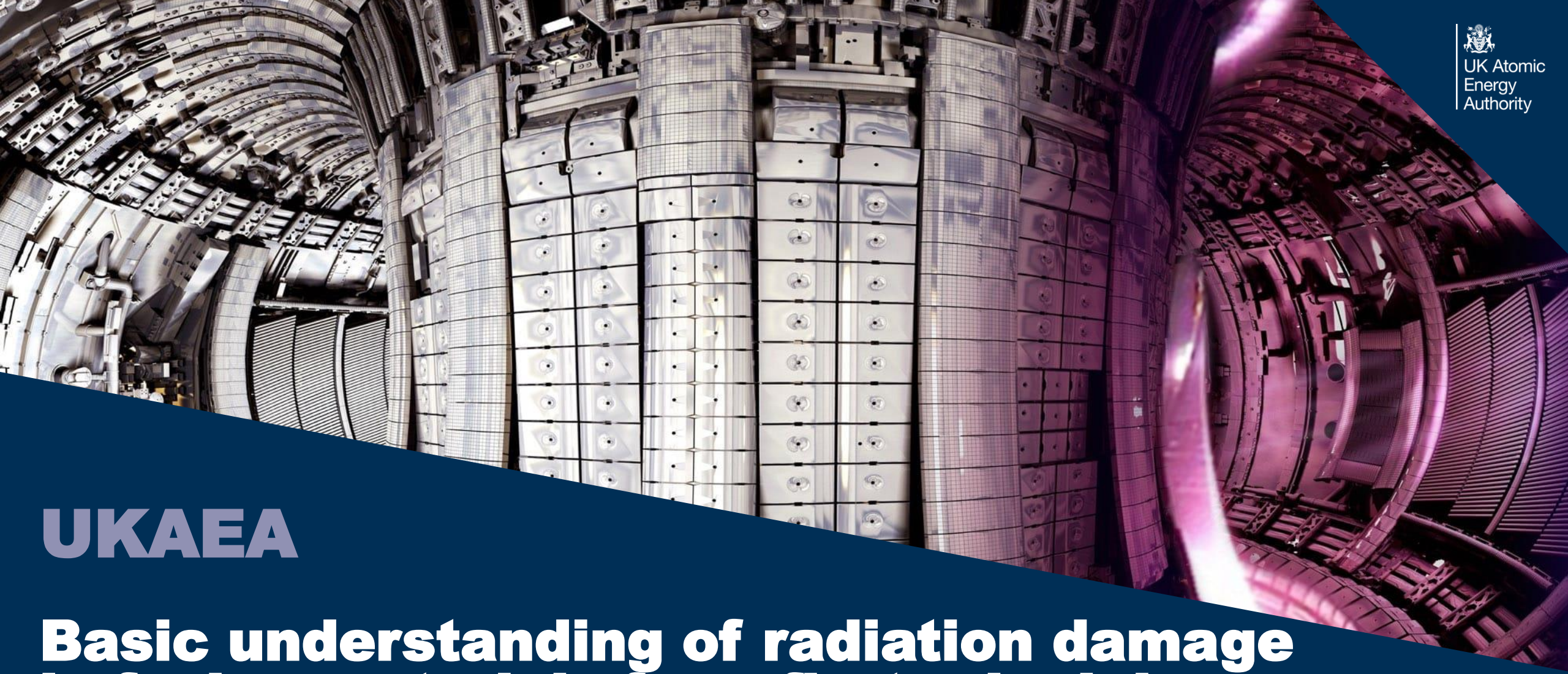

UK Atomic Energy Authority

UKAEA

Basic understanding of radiation damage in fusion materials from first principles

Duc Nguyen-Manh, Senior Research Scientist, Materials Division, UKAEA and Materials Department, University of Oxford, UK

Joint ICTP-IAEA-MAMBA School on Materials Irradiation: from Basics to Applications, Trieste, February 10-21, 2025

Fusion energy: from basics to applications

UK Atomic Energy Authority

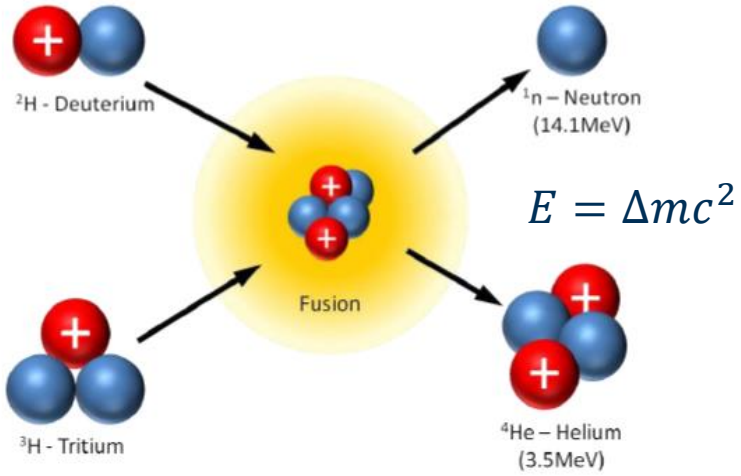

$$E = \Delta mc^2$$

Interplay of two opposing forces: the nuclear force, which combines together protons and neutrons, and the Coulomb force, which causes protons to repel each other.

Pierre-Gilles de Gennes once said of nuclear fusion: "*We say that we will put the sun into a box. The idea is pretty. The problem is,* ***we don't know how to make the box***".

- No carbon emissions
- Abundant fuels
- Reliable power
- Energy efficiency
- Less radioactive
- No chain reaction

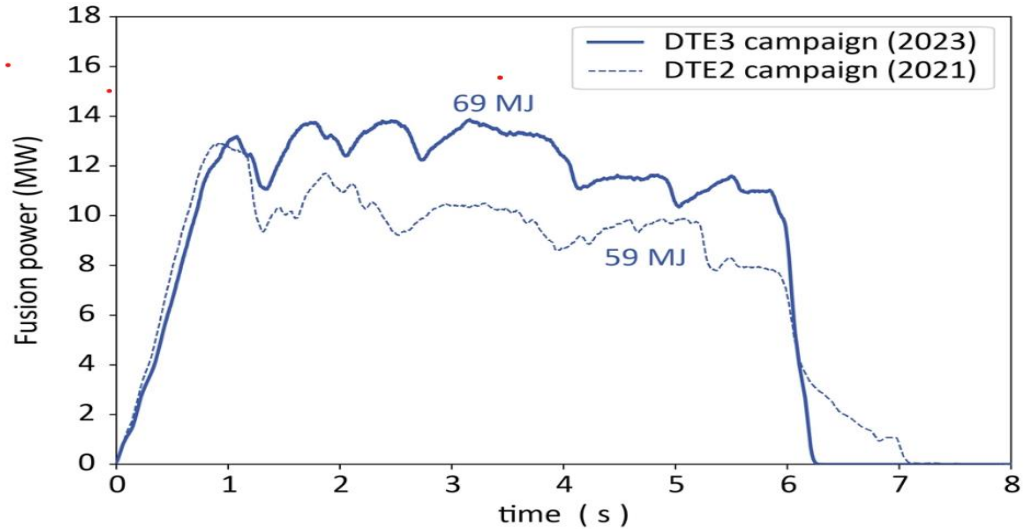

Fusion needs integrated solutions

UK Atomic Energy Authority

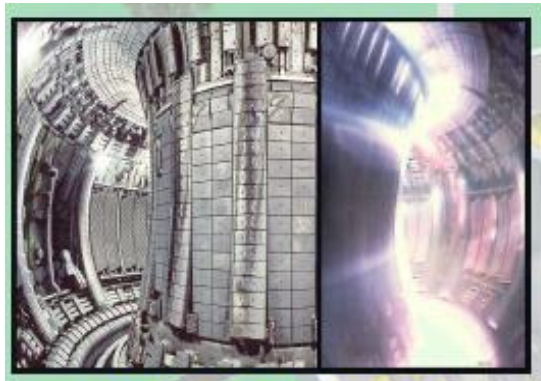

High performance plasmas in JET

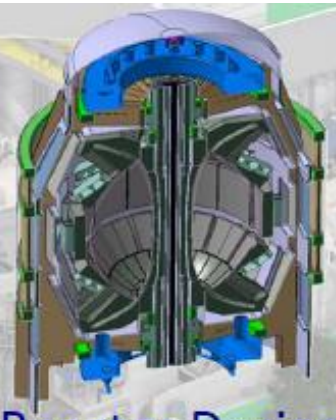

Reactor Design STEP and DEMO

Advanced computing and digital design

Heat exhaust in MAST Upgrade

Develop materials in Materials Research Facility (MRF)

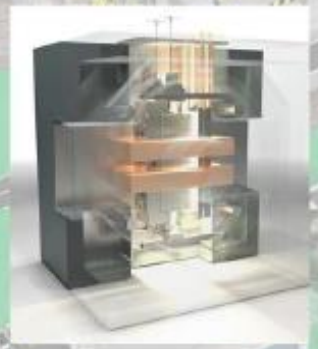

Test components in Fusion Technology Test Facilities (FTF)

Tritium handling in Hydrogen-3 Advanced Technology (H3AT)

Robotic handling in RACE

3 4 December 2020

Materials challenges for plasma facing materials for fusion engineering applications

UK Atomic Energy Authority

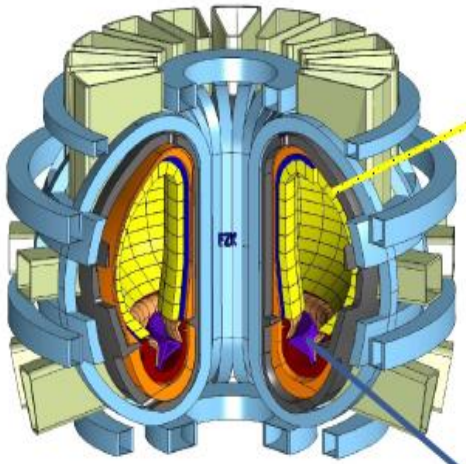

Power plant 0

An exceedingly challenging materials science and engineering problem.

United Kingdom Atomic Energy Authority

M. Rieth, 2011

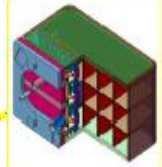

Blanket: ≤150 dpa/5 years, 2.5 MW/m²

Reduced activation ferritic-martensitic steels, assuming

→ EUROFER (9Cr-WVTa) 350-550 °C
→ ODS-EUROFER 350-650 °C

He cooled structure, liquid lithium or lithium-ceramics for tritium breeding; ~85 % power

Divertor: ~30 dpa/2 years, ≥10MW/m²

Materials, cooling method: undecided
Operating temperature 350-1300 °C ?

Cooled tungsten shield to sustain direct impact of He and other particles from plasma, absorbing ~15% of total fusion power

CCFE is the fusion research arm of the United Kingdom Atomic Energy Authority

CULHAM CENTRE FOR FUSION ENERGY

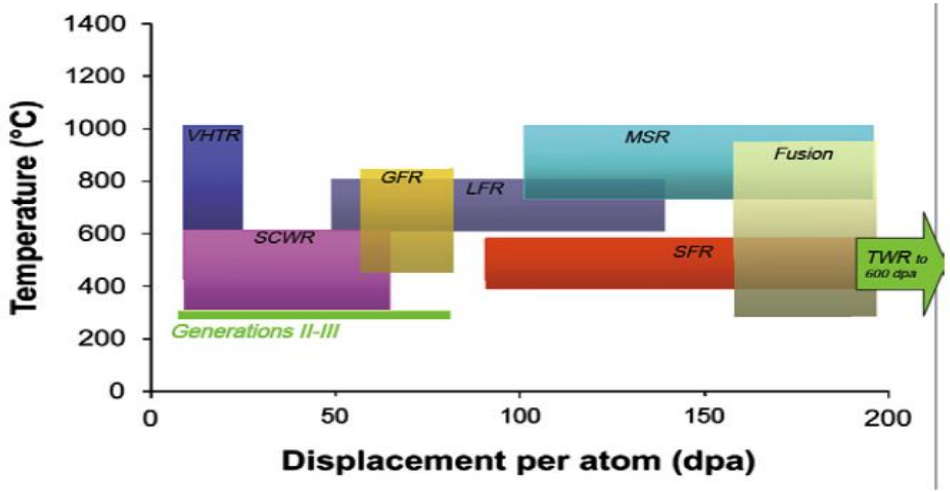

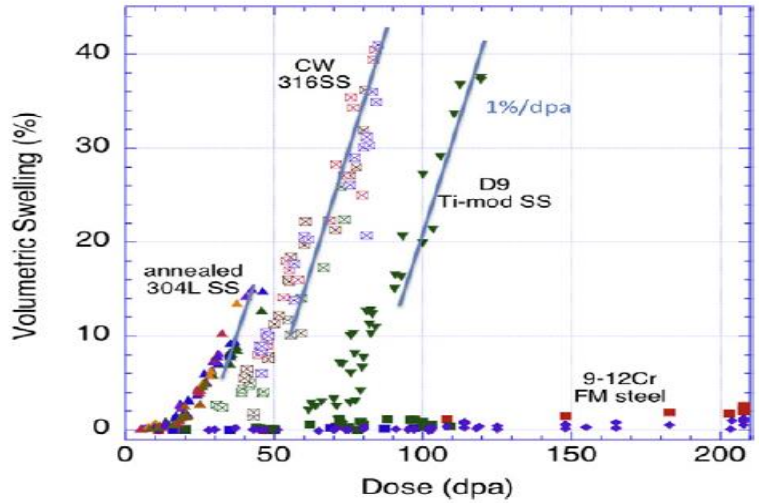

UKAEA's Materials Research Facility

UK Atomic Energy Authority

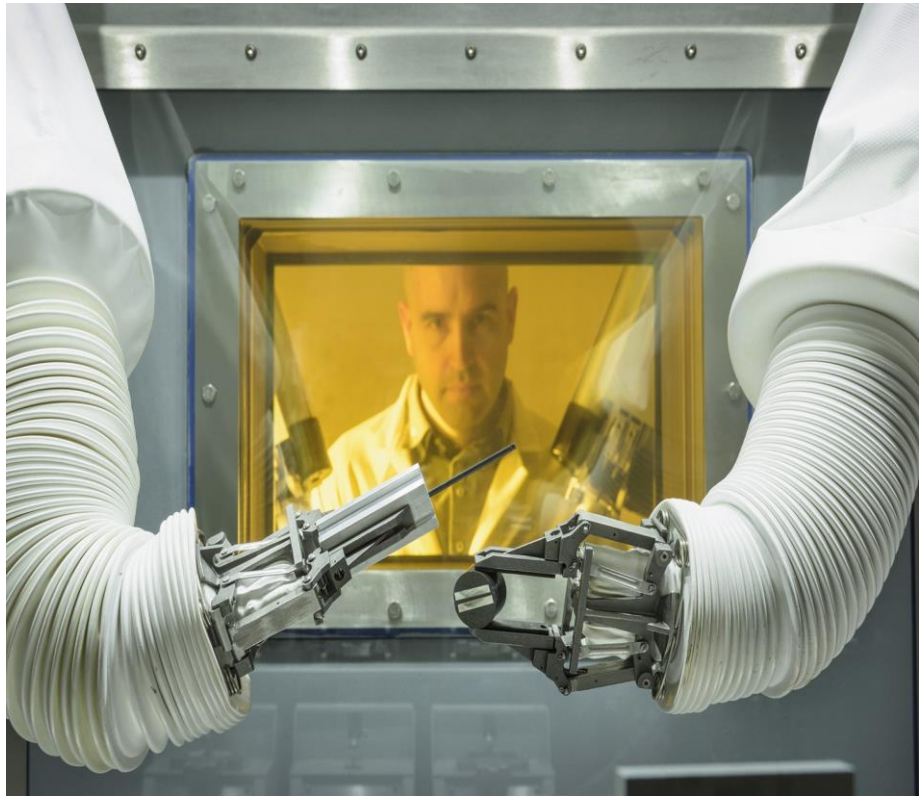

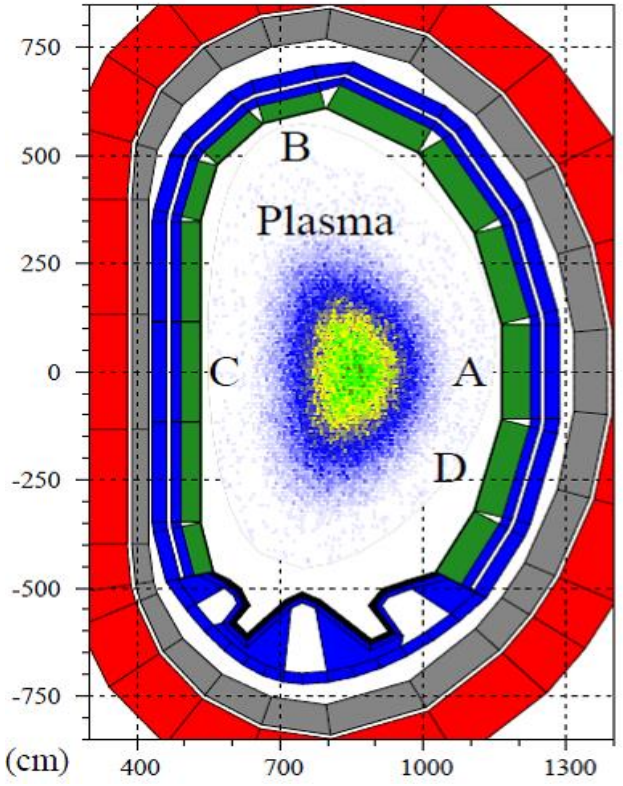

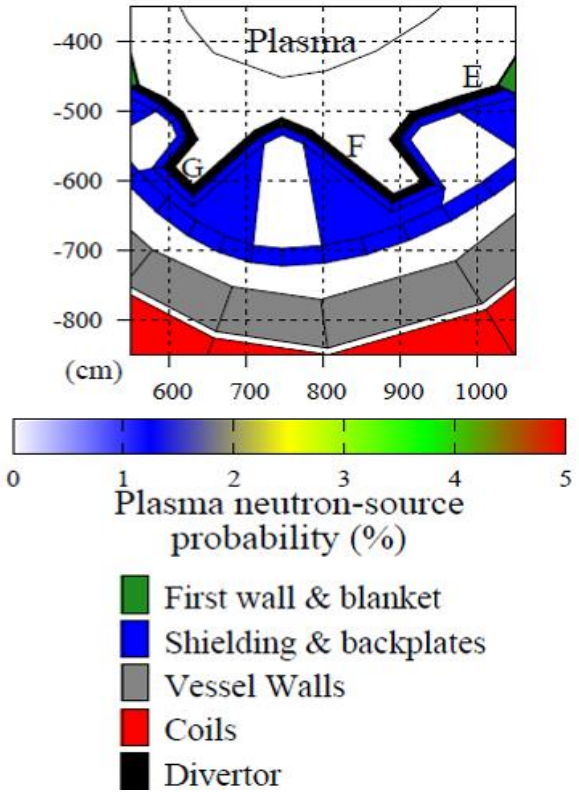

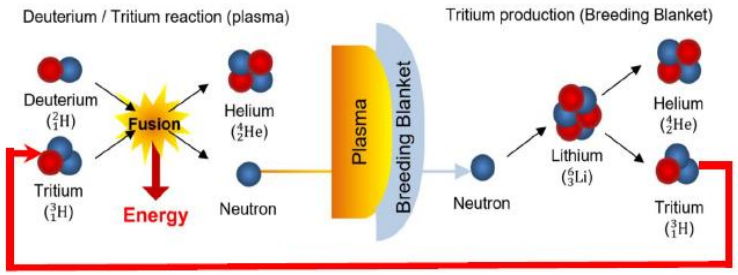

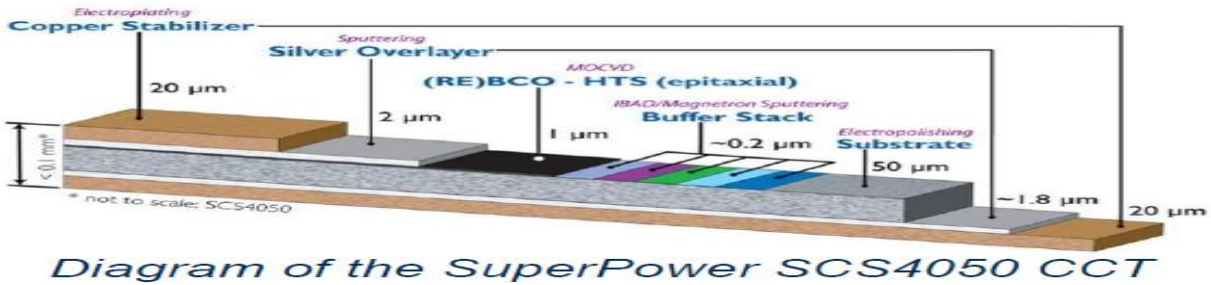

Diagram of the SuperPower SCS4050 CCT

Effect of 14 MeV neutrons: Nuclear burn up and transmutation reactions

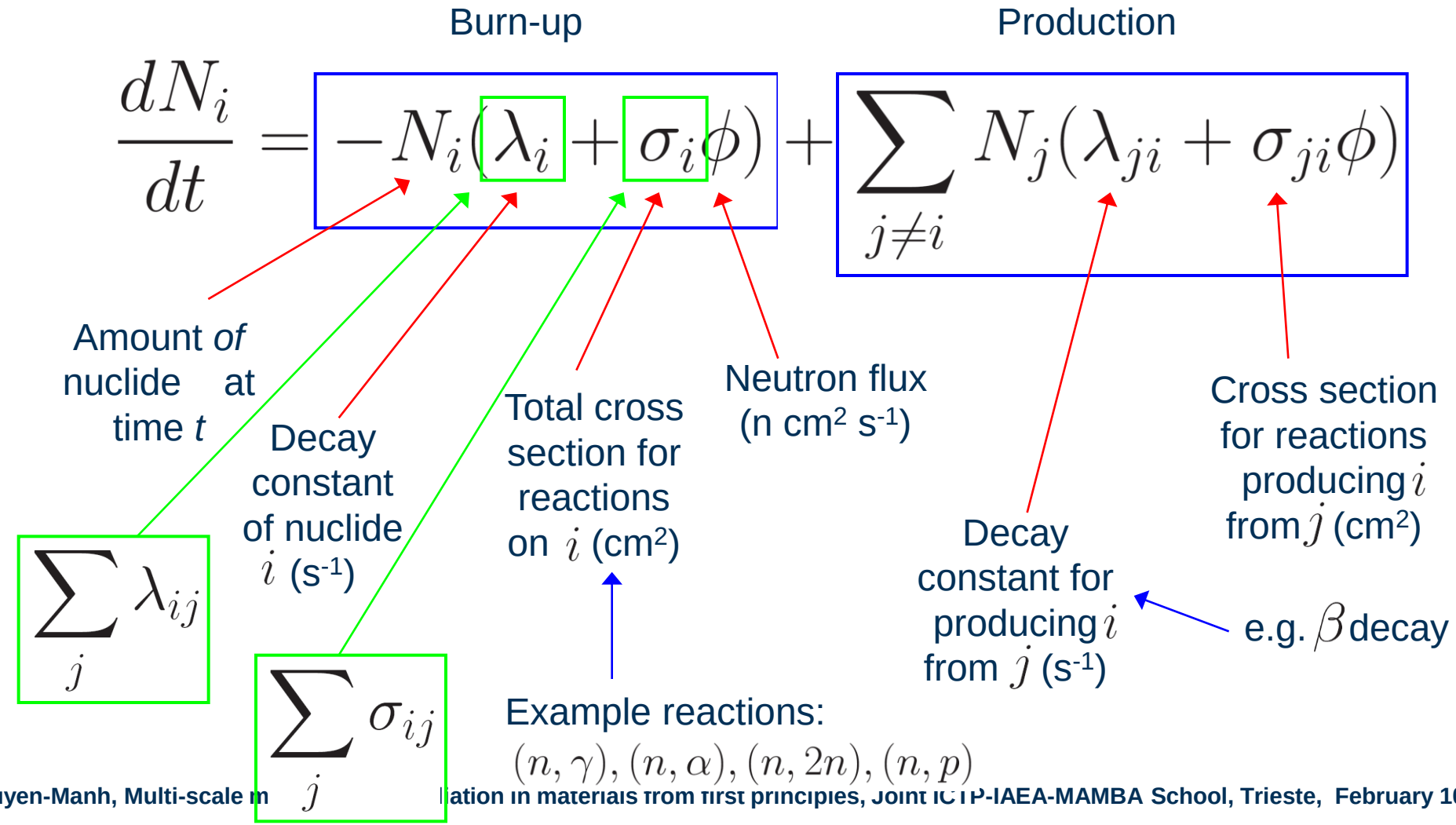

Transmutation in Tungsten

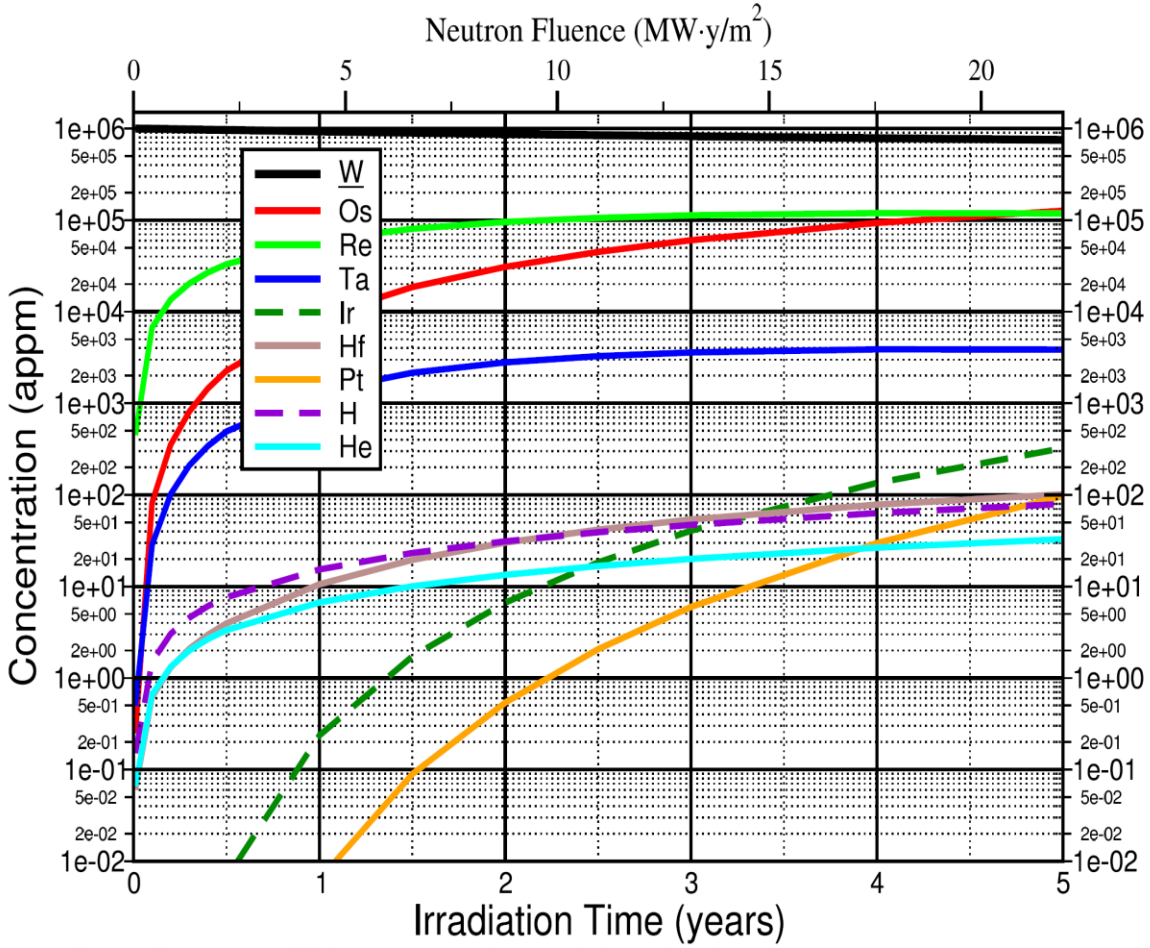

Figure 2: Transmutation of W during a 5-year irradiation under first wall conditions

	appm	%
W	7.5 x 10^5	75.1
Os	1.3 x 10^5	12.6
Re	1.2 x 10^5	11.8
Ta	3.9 x 10^3	0.4
Ir	323	>0.1
Hf	101	>0.1
Pt	97	>0.1
H	79	>0.1
He	33	>0.1

Transmutation in Fe

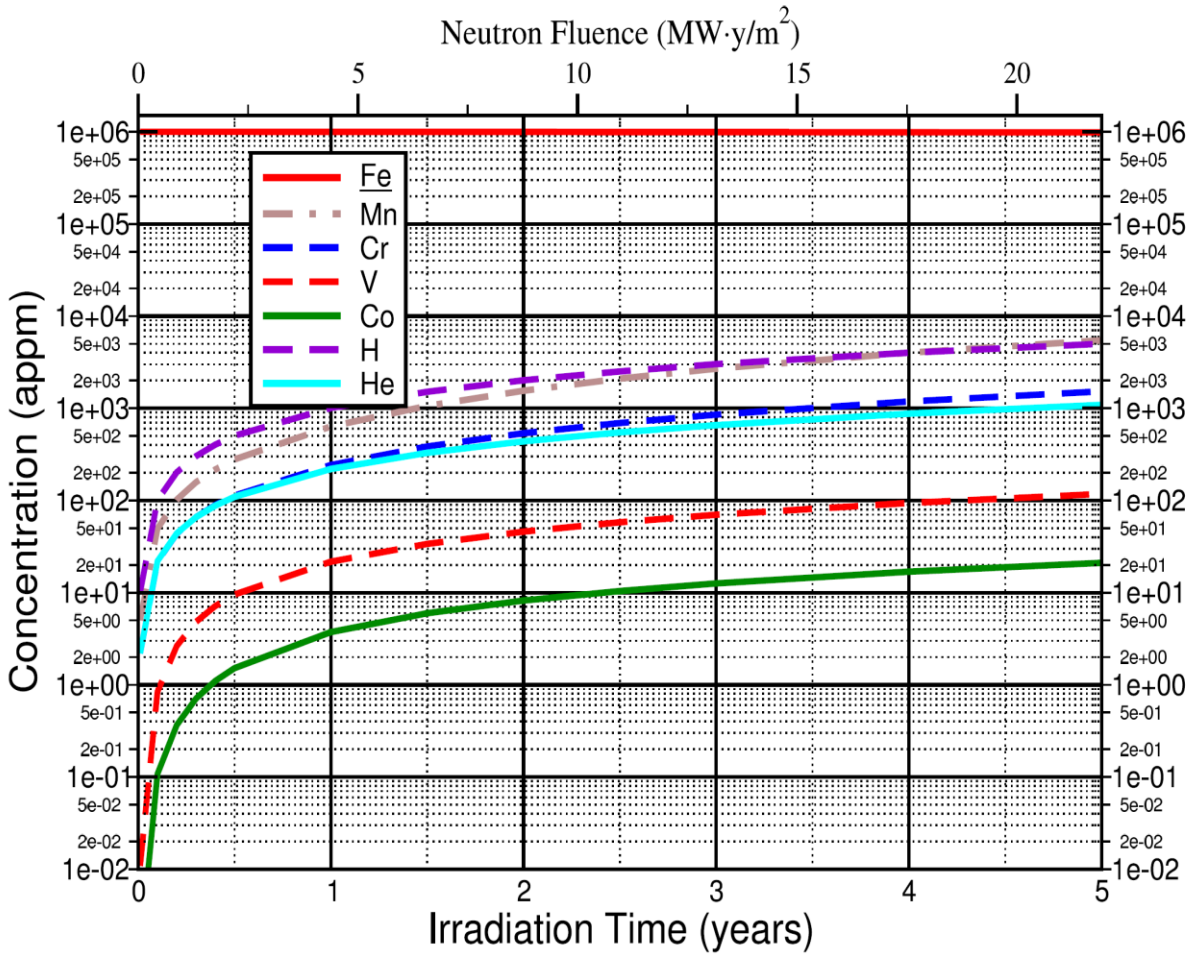

Figure 12: Transmutation of Fe during a 5-year irradiation under first wall conditions

	appm	%
Fe	9.9 x 10^5	98.6
Mn	5.5 x 10^3	0.6
Cr	1.5 x 10^3	0.2
V	118	>0.1
Co	21	>0.1
H	5.0 x 10^3	0.5
He	1.1 x 10^3	0.1

In-vessel material components of STEP devices and operating temperature windows

UK Atomic Energy Authority

Inboard First Wall
Heat flux estimate*: 1.3 MW/m^2
Coolant: D_2O
Heat sink type: Integrated Tile-on-heat sink
Structural Material: CuCrZr
Armour: Solid tungsten

Outboard First Wall
Heat flux estimate*: 1.4 MW/m^2
Coolant: Helium
Heat sink type: Tile-on-heat sink
Structural material: Vanadium
Armour: Solid tungsten

Outboard Limiters
Steady state heat flux*: 1 MW/m^2
Transient long duration heat flux*: 5.0 MW/m^2
Mitigated disruption heat flux*: 2.2 GW/m^2 (0.75 ms)
Coolant: Helium
Heat sink type: Pipe-in-pipe jet impingement
Structural Material: Tungsten alloy
Armour: Solid tungsten

Divertor medium heat flux targets
Flat top heat flux estimate*: <10 MW/m^2
Ramp-up heat flux estimate*: <10 MW/m^2
Coolant: D_2O
Heat sink type: Integrated Tile-on-heat sink
Structural Material: CuCrZr
Armour: Solid tungsten

Divertor high heat flux targets
Flat top heat flux estimate*: <10 MW/m^2
Ramp-up heat flux estimate*: <20 MW/m^2
Coolant: D_2O
Heat sink type: Monoblock
Structural Material: CuCrZr pipe, tungsten block
Armour: Solid tungsten

Divertor strike point targets
Flat top heat flux estimate*: <10 MW/m^2
Ramp-up heat flux estimate*: <10 MW/m^2
ELM heat flux estimate: 0.1-1 MJ/m^2
Coolant: D_2O
Heat sink type: Dual channel drilled block
Structural Material: CuCrZr pipe, tungsten block
Armour: Capillary Porous Structure tin Liquid Metal Armour

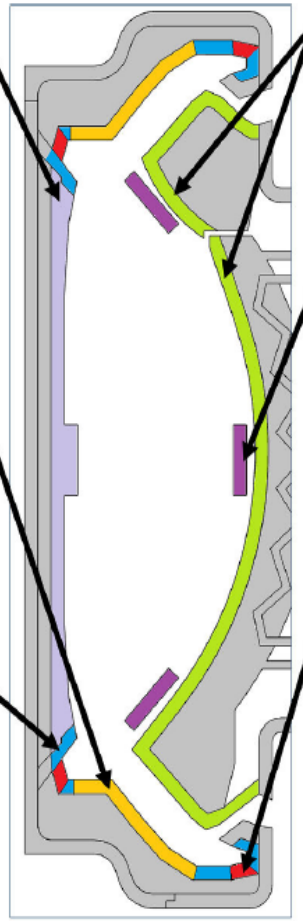

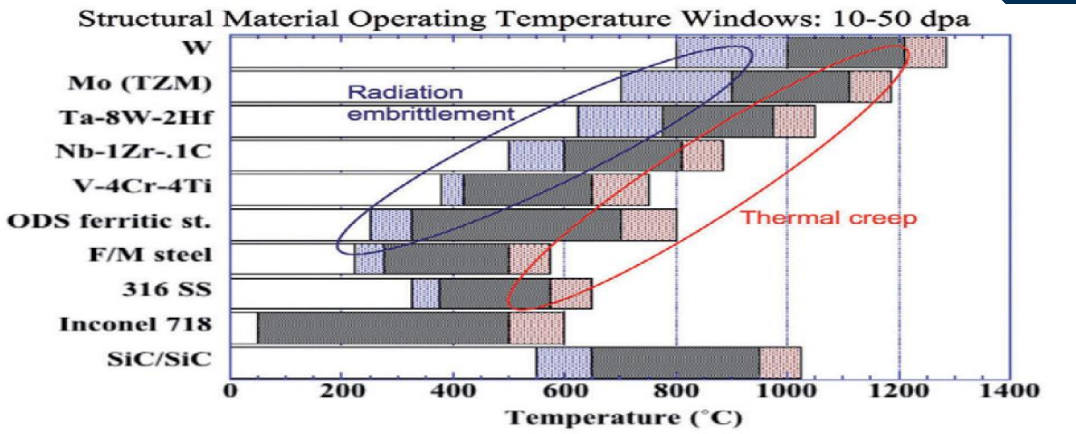

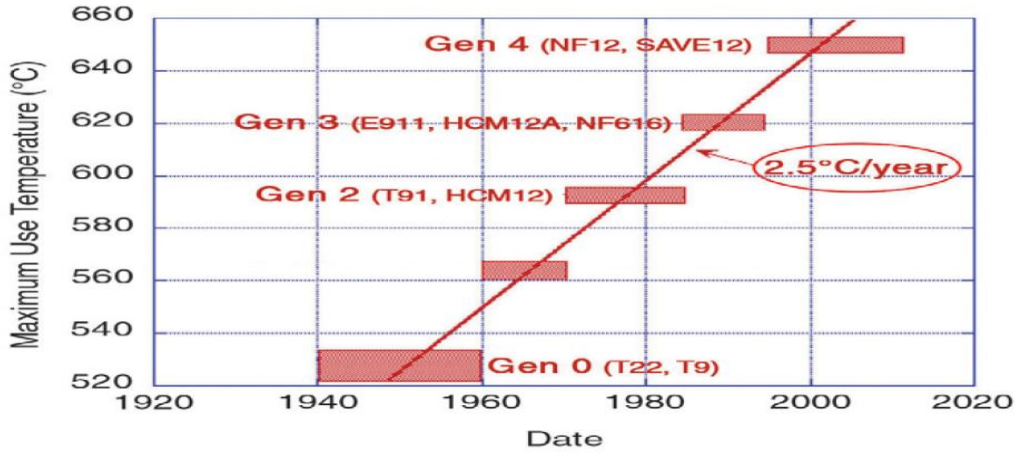

Historical rate of improvement in maximum operating temperature of structural steels
S. Zinkle et al., Materials Today. 12 (2009) 12

J. Cane et al., Phil. Trans. R. Soc. A, 382 (2024) 20230408

ARAFM alloy design strategy and TMT optimisation

Composition	Cr	W	Mn	Si	V	Ta	C	N	Ti
WP1.1 (Target)	9.000	2.000	0.400	Trace	0.300	0.070	0.070	0.025	0.000
WP1.1 (Actual)	9.170	2.000	0.430	0.039	0.380	0.110	0.080	0.029	0.010
WP1.2 (Target)	9.000	2.000	0.400	Trace	0.000	0.070	0.070	0.000	0.070
WP1.2 (Actual)	9.380	1.950	0.450	0.027	0.020	0.120	0.090	0.010	0.030
WP1.3 (Target)	9.000	2.000	0.050	Trace	0.000	0.070	0.070	0.000	0.070
WP1.3 (Actual)	9.560	2.060	0.080	0.029	0.020	0.120	0.090	0.009	0.030
WP2.1 (Target)	8.000	2.000	0.100	0.100	0.200	0.100	0.100	0.001	0.000
WP2.1 (Actual)	7.920	2.010	0.130	0.170	0.240	0.150	0.120	0.006	0.000
WP2.2 (Target)	8.000	2.000	0.100	0.100	0.200	0.100	0.100	0.009	0.000
WP2.2 (Actual)	8.070	2.000	0.120	0.160	0.260	0.140	0.120	0.012	0.000
WP2.3 (Target)	8.000	2.000	0.050	0.050	0.200	0.100	0.100	0.009	0.000
WP2.3 (Actual)	8.040	2.030	0.080	0.050	0.270	0.140	0.120	0.016	0.000

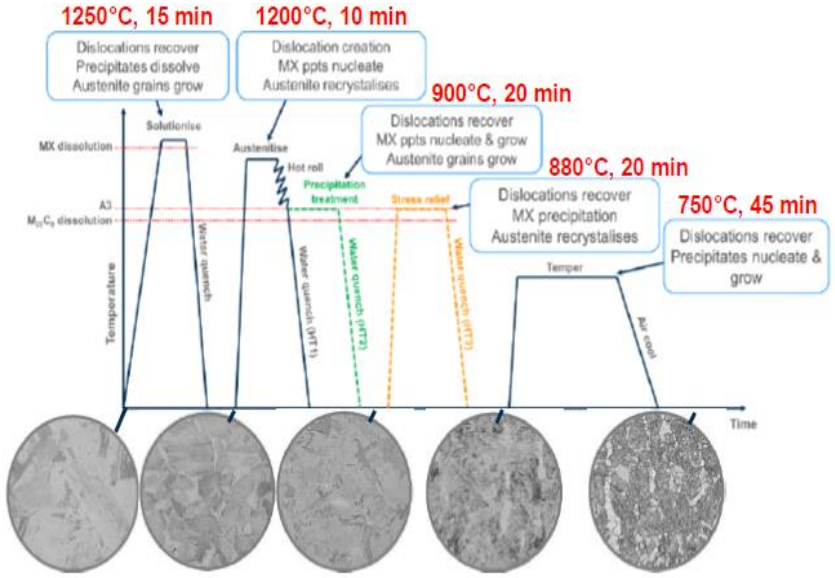

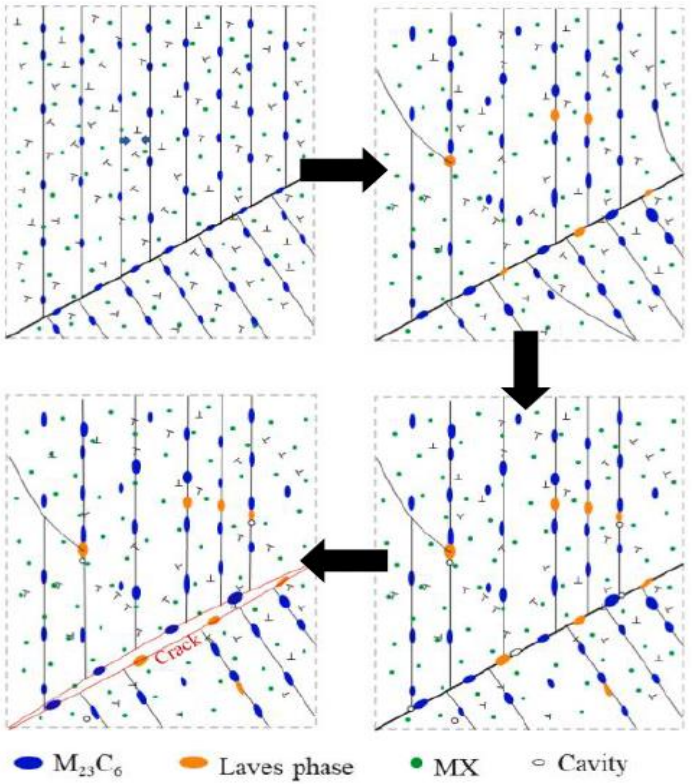

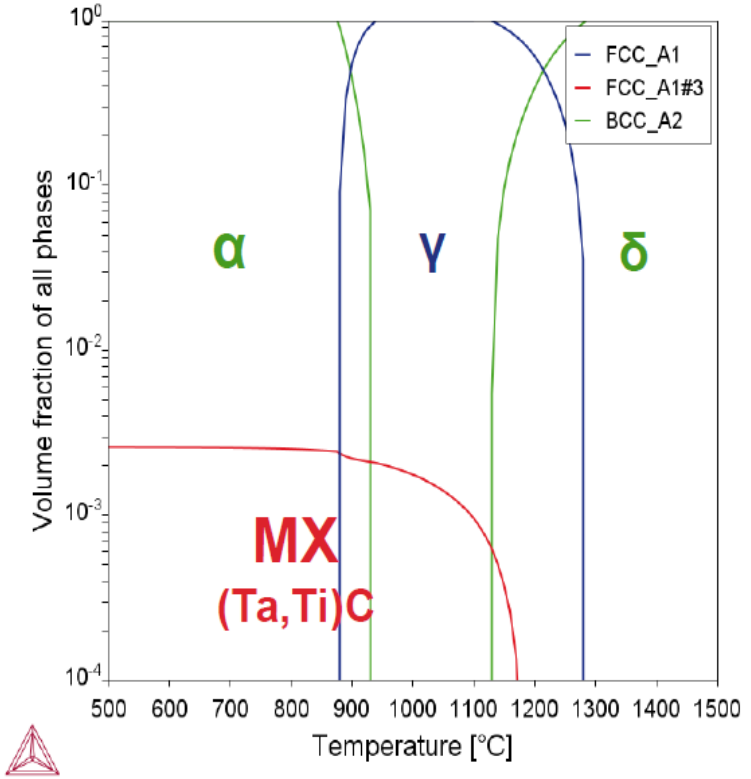

- Phase predicted at equilibrium in steels using CALPHAD method
- **Crack initiation at M23C6 primary cause of creep failure**: reducing Cr and C reduces driving forces of M23C6 precipitates
- **Changing the alloy composition** can be made – no M23C6
- Strategy for ARAFM with **TiC or VN induced-precipitated steels**

NEURONE (NEUtron iRradiatiOn of advaNces stEels) programme (2024-2028)

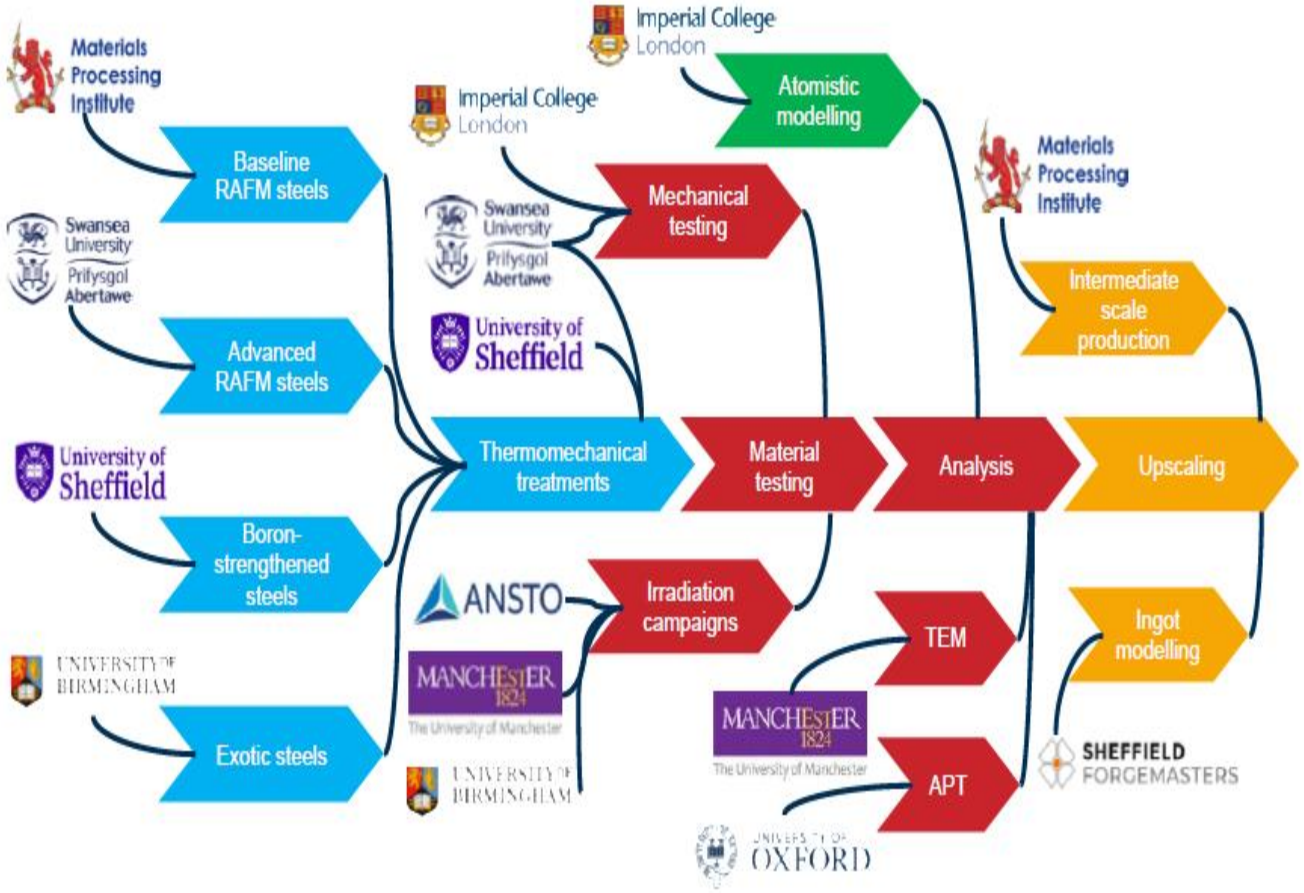

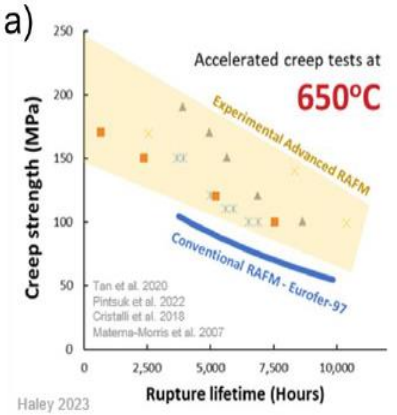

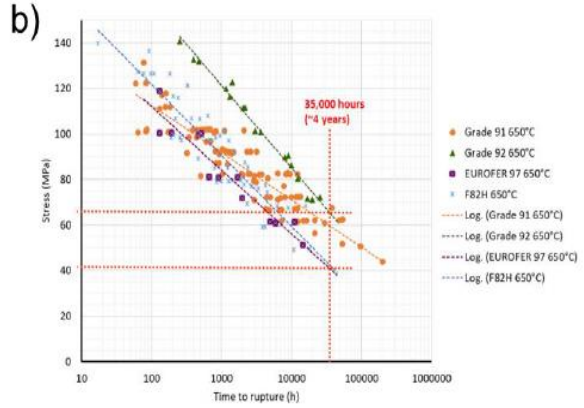

- NEURONE studies largely driven by STEP
- Produce advanced steels for use in the LIBRTI
- Ideal target temperature of 650C for ARAFM steels with **thermodynamic and irradiation stability**
- Understand and manipulate defect sinks through **controlled precipitate evolution, second phase interface optimisation, novel microstructure design**
- Governing factors of steel performance through **interaction of thermal creep and irradiation damage**

D. Bowden, Review and report of FY 2023/2024 progress, 22 October 2024

International workshops on MoD-PMI from 2014

UK Atomic Energy Authority

CECAM Flagship Workshop on Challenges a
Perspectives on Computational Modelling for
Fusion Reactors, Lausanne, October 28-29 , 2024
Organized by Nicola Marzari et al.

Multi-scale modelling of microstructure evolution for materials in fusion environment

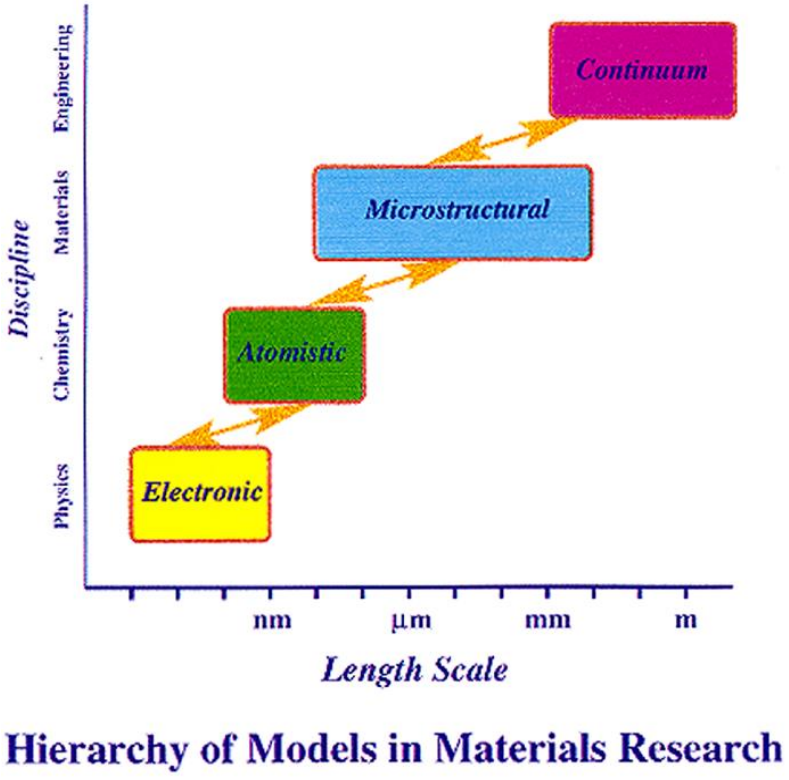

Hierarchy of Models in Materials Research

DNM et al., Phil. Trans. Royal Soc. London, 315, 529 (1995)

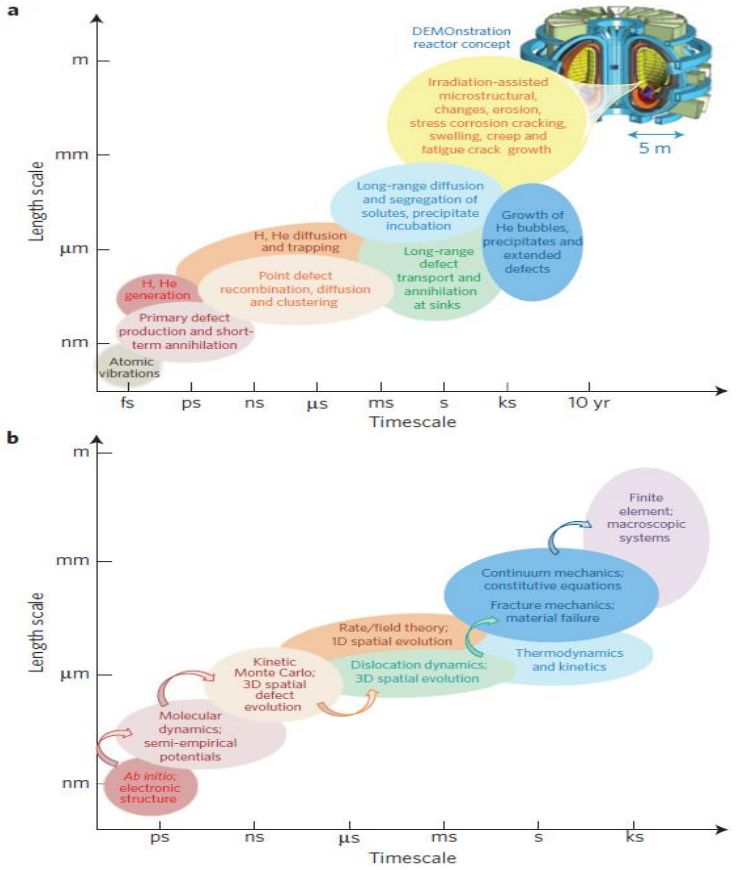

J. Knaster et al. Nature Phys. 12, 424 (2016)

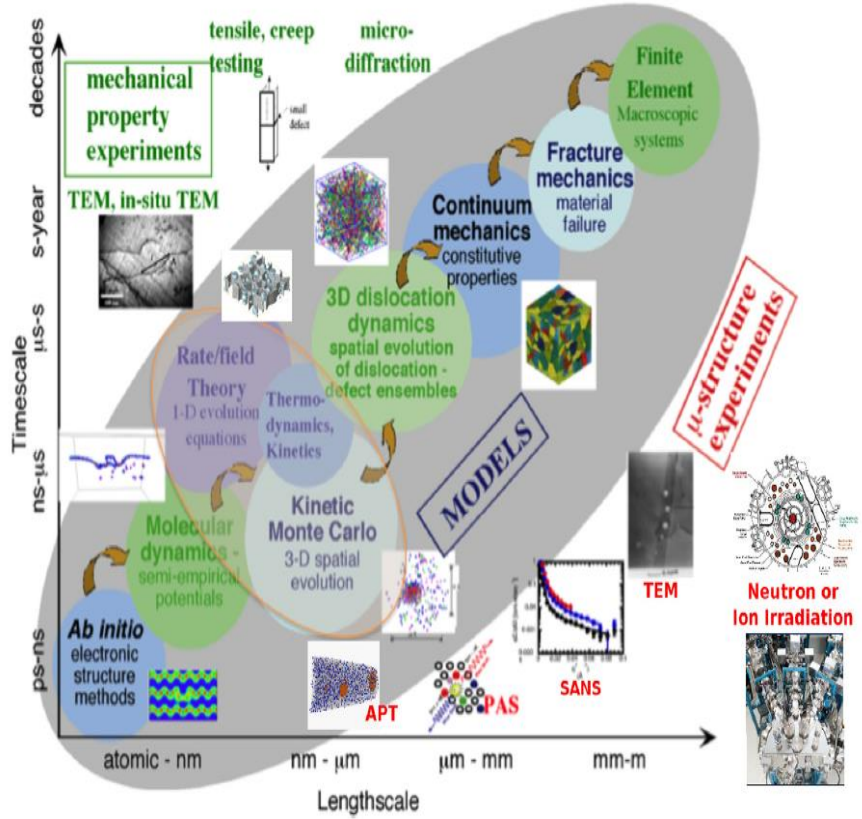

M.R. Gilbert et al., J. Nucl. Mater. 554, 153113 (2021)

First-principles modelling of atoms, molecules, solids and materials from Density Functional Theory (DFT)

UK Atomic Energy Authority

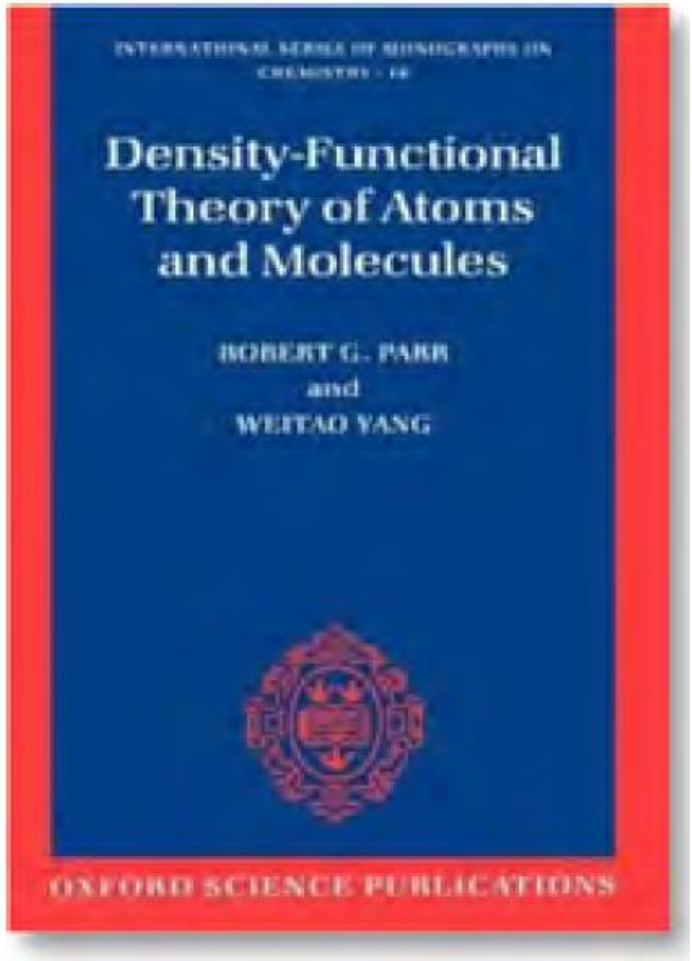

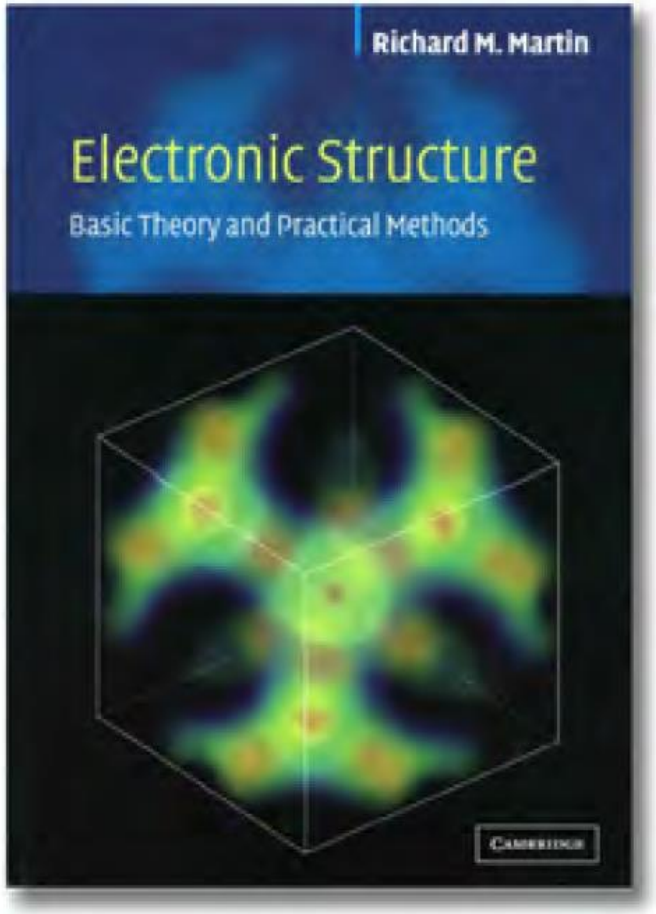

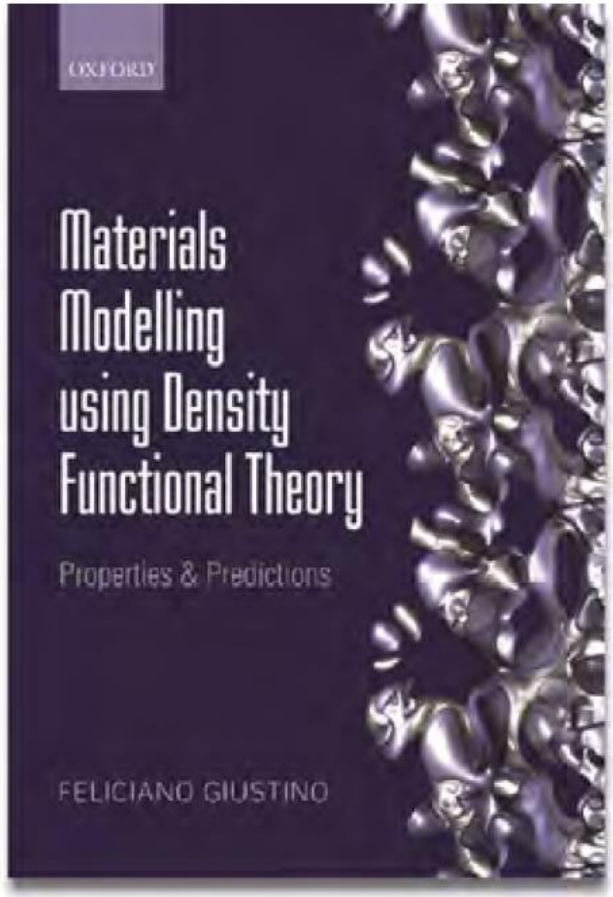

Why is DFT popular for predicting materials properties

- **Transferability**
  We can use the same codes/methods for very different materials

- **Simplicity**
  The Kohn-Sham equations are conceptually very similar to the Schrödinger equation for a single electron in an external potential

- **Reliability**
  Often we can predict materials properties with high accuracy, sometimes even before experiments

- **Software sharing**
  The development of DFT has become a global enterprise, e.g. open source and collaborative software development

- **Robust platform**
  Often the shortcomings of DFT can be cured by using more sophisticated approaches, which still use DFT as their starting point

Reproducibility of different DFT codes

UK Atomic Energy Authority

$$\Delta_i(a,b) = \sqrt{\frac{\int_{0.94V_{0,i}}^{1.06V_{0,i}} \left(E_{b,i}(V) - E_{a,i}(V)\right)^2 dV}{0.12V_{0,i}}}$$

- AE (All Electron) codes: WIEN2K, FLEUR…
- PAW (Projector Augmented Wave): VASP…
- USPP (Ultra-Soft Pseudo Potentials): CASTEP, QE..
- NCPP (Norm-Conserving Pseudo Potentials): OpenMX…

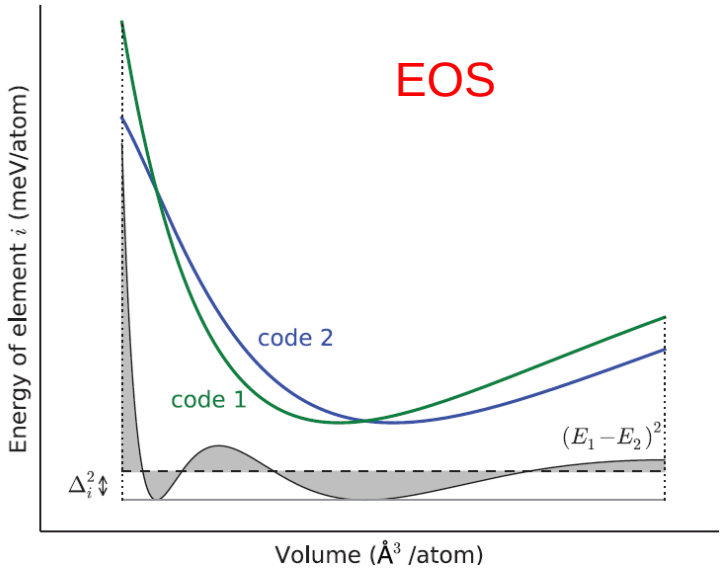

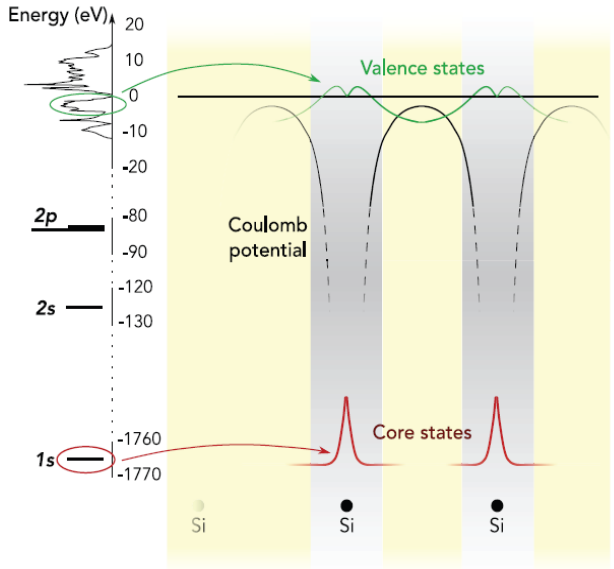

		average <Δ>	AE: Elk	AE: exciting	AE: FHI-aims/tier2	AE: FLEUR	AE: FPLO/T+F+s	AE: RSPt	AE: WIEN2k/acc
AE	Elk	0.6		0.3	0.3	0.6	1.0	0.9	0.3
	exciting	0.5	0.3		0.1	0.5	0.9	0.8	0.2
	FHI-aims/tier2	0.5	0.3	0.1		0.5	0.9	0.8	0.2
	FLEUR	0.6	0.6	0.5	0.5		0.8	0.6	0.4
	FPLO/T+F+s	0.9	1.0	0.9	0.9	0.8		0.9	0.9
	RSPt	0.8	0.9	0.8	0.8	0.6	0.9		0.8
	WIEN2k/acc	0.5	0.3	0.2	0.2	0.4	0.9	0.8	
PAW	GBRV12/ABINIT	0.9	0.9	0.8	0.8	0.9	1.3	1.1	0.8
	GPAW09/ABINIT	1.4	1.3	1.3	1.3	1.3	1.7	1.5	1.3
	GPAW09/GPAW	1.6	1.5	1.5	1.5	1.5	1.8	1.7	1.5
	JTH02/ABINIT	0.6	0.6	0.6	0.6	0.6	0.9	0.7	0.5
	PSlib100/QE	0.9	0.9	0.8	0.8	0.8	1.3	1.1	0.8
	VASPGW2015/VASP	0.6	0.4	0.4	0.4	0.6	1.0	0.8	0.3
USPP	GBRV14/CASTEP	1.1	1.1	1.1	1.0	1.0	1.4	1.3	1.0
	GBRV14/QE	1.1	1.0	1.0	0.9	1.0	1.4	1.3	1.0
	OTFG9/CASTEP	0.7	0.4	0.5	0.5	0.7	1.0	1.0	0.5
	SSSP/QE	0.5	0.4	0.3	0.3	0.5	0.9	0.8	0.3
	Vdb2/DACAPO	6.3	6.3	6.3	6.3	6.3	6.4	6.5	6.2
NCPP	FHI98pp/ABINIT	13.3	13.5	13.4	13.4	13.2	13.0	13.2	13.4
	HGH/ABINIT	2.2	2.2	2.2	2.2	2.0	2.3	2.2	2.1
	HGH-NLCC/BigDFT	1.1	1.1	1.1	1.1	1.0	1.2	1.1	1.0
	MBK2013/OpenMX	2.0	2.1	2.1	2.1	1.9	1.8	1.8	2.0
	ONCVPSP(PD0.1)/ABINIT	0.7	0.7	0.7	0.7	0.6	1.0	0.8	0.6
	ONCVPSP(SG15)1/QE	1.4	1.4	1.3	1.3	1.3	1.6	1.5	1.3
	ONCVPSP(SG15)2/CASTEP	1.4	1.4	1.4	1.4	1.3	1.6	1.5	1.4

K. Lejaeghere et al., Science vol. 351 (2016) 6280

Microstructural evolution of irradiated materials

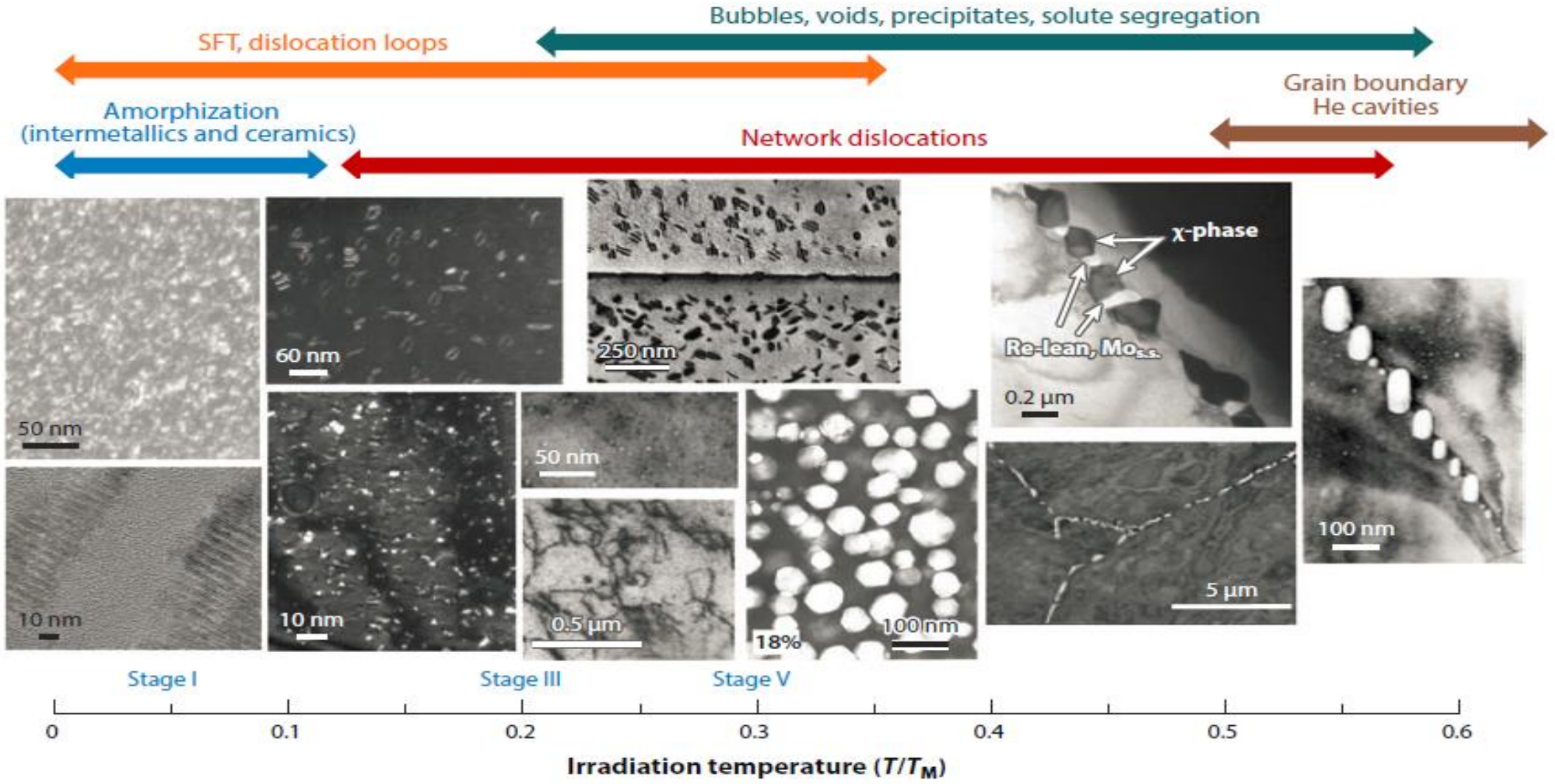

DFT calculations of irradiation induced defects in bcc-TM: A systematic trend

UK Atomic Energy Authority

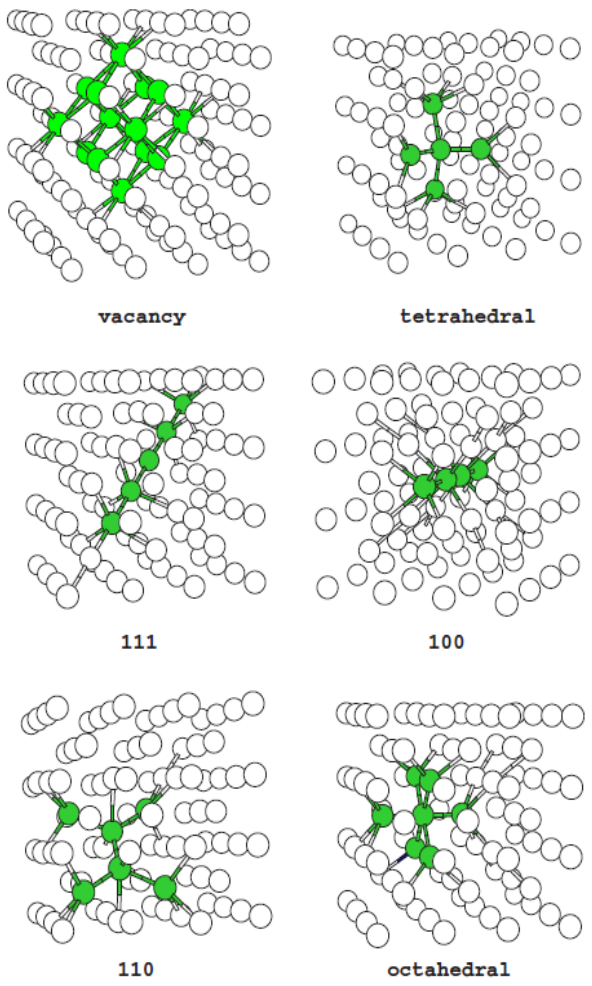

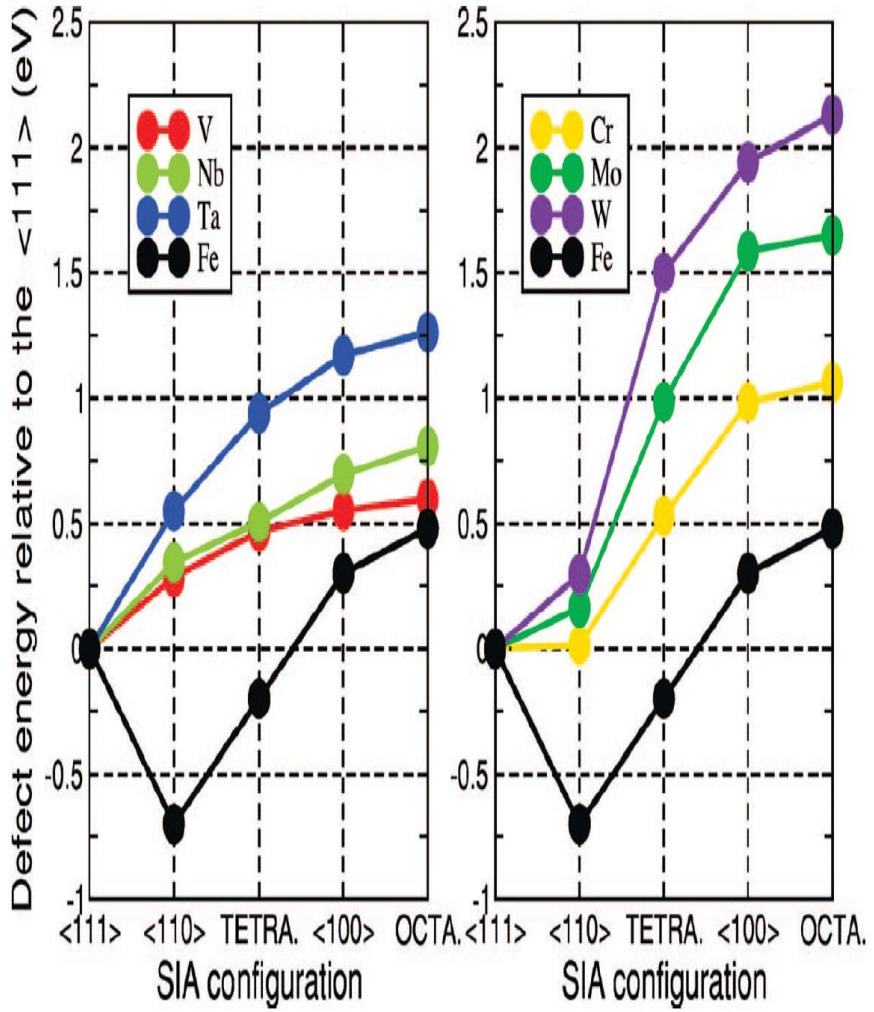

TABLE I. The first four rows of this table give basic parameters of all the bcc transition metals of groups 5B and 6B, and those for Fe (group 8) evaluated using DFT, and compare them with the experimentally measured values taken from Refs. 56 and 20. The remaining rows of the table give defect formation (f), migration (m), and binding (b) energies (in eV units). Values referring to the interstitial configurations (⟨111⟩ dumbbell, etc.) give the formation energies of the corresponding defect structures.

	V	Nb	Ta	Cr	Mo	W	Fe
a (Å)	3.04[a]	3.32[a]	3.31[a]	2.85[a]	3.17[a]	3.18[a]	2.84[b]
	3.03[c]	3.30[c]	3.30[c]	2.88[c]	3.15[c]	3.16[c]	2.87[c]
B (Mbar)	1.71[a]	[a]1.73	1.99[a]	1.92[a]	2.68[a]	3.05[a]	1.82[b]
	1.62[c]	1.70[c]	2.00[c]	1.90[c]	2.72[c]	3.23[c]	1.68[c]
H_f^v	2.51[a]	2.99[a]	3.14[a]	2.64[a]	2.96[a]	3.56[a]	2.15[a]
	2.1–2.2[d]	2.6–3.1[d]	2.8–3.1[d]	2.0–2.4[d]	2.6–3.2[d]	3.5–4.1[d]	1.6–2.2[d]
H_m^v	0.62[a]	0.91[a]	1.48[a]	0.91[a]	1.28[a]	1.78[a]	0.64[b], 0.67[e]
	0.5–1.2[d]	0.6–1.0[d]	0.7–1.9[d]	0.95[d]	1.3–1.6[d]	1.7–2.0[d]	0.55[d]
$H_f^{2v}(1NN)$	4.94[f]	5.62[f]	6.01[f]	5.01[f]	5.60[f]	6.71[f]	4.08[b]
	3.90–3.99[g]	5.11[g]	5.47[g]	3.34[g]	5.75[g]	7.32[g]	3.31[g], 3.85[h]
$H_f^{2v}(2NN)$	4.80[f]	5.57[f]	5.89[f]	5.16[f]	5.78[f]	6.93[f]	4.01[b]
	3.90–4.21[g]	5.11[g]	5.50[g]	3.35[g]	5.77[g]	7.36[g]	3.34[g], 3.83[h]
$H_b^{2v}(1NN)$	0.08[f]	0.36[f]	0.27[f]	0.27[f]	0.32[f]	0.41[f]	0.22[b]
	0.30–0.45[g]	0.39[g]	0.43[g]	0.26[g]	0.45[g], 0.39[j]	0.58[g], 0.45[i]	0.27[g], 0.22,[i] 0.19[h]
$H_b^{2v}(2NN)$	0.22[f]	0.41[f]	0.39[f]	0.12[f]	0.14[f]	0.19[f]	0.29
	0.30–0.23[g]	0.39[g]	0.41[g]	0.25[g]	0.43[g], 0.25[i]	0.54[g], 0.29[j]	0.24[g], 0.15[i], 0.30[e], 0.21[h]
⟨111⟩ dumbbell	3.367[a]	5.253[a]	5.832[a]	5.685[a]	7.417[a]	9.548[a]	4.61[b]
	3.14[j]	4.795[k]	7.157[l], 5.858[i]	5.68[m]	7.34[j]	8.919[k]	4.72,[m] 4.34[e]
⟨111⟩ crowdion	3.371[a]	5.254[a]	5.836[a]	5.660[a]	7.419[a]	9.551[a]	4.64[b]
	3.15[h]	4.857[k]	7.158[k], 5.859[l]		7.34[j]	8.893[k]	
⟨110⟩ dumbbell	3.652[a]	5.597[a]	6.382[a]	5.674[b]	7.581[a]	9.844[a]	3.93[b]
	3.48[j]	4.482[k]	6.847[k], 6.557[l]	5.66[m]	7.51[j]	9.641[k]	4.03[m], 3.64[e]
Tetrahedral	3.835[a]	5.758[a]	6.771[a]	6.189[a]	8.401[a]	11.05[a]	4.32[b]
	3.69[j]		6.845[l]		8.20[j]		4.43,[m] 4.26[e]
⟨100⟩ dumbbell	3.918[a]	5.949[a]	7.003[a]	6.643[a]	9.004[a]	11.49[a]	5.05[b]
	3.57[j]	4.821[k]	8.068[k], 6.987[l]	6.78[m]	8.77[j]	9.815[k]	5.18[m], 4.64[e]
Octahedral	3.964[a]	6.060[a]	7.095[a]	6.723[a]	9.067[a]	11.68[a]	5.21[b]
	3.62[j]		7.020[l]		8.86[j]		5.34[m], 4.94[e]

Understanding of crowdion defects in group VI (Cr, Mo, W) from electronic structure calculations

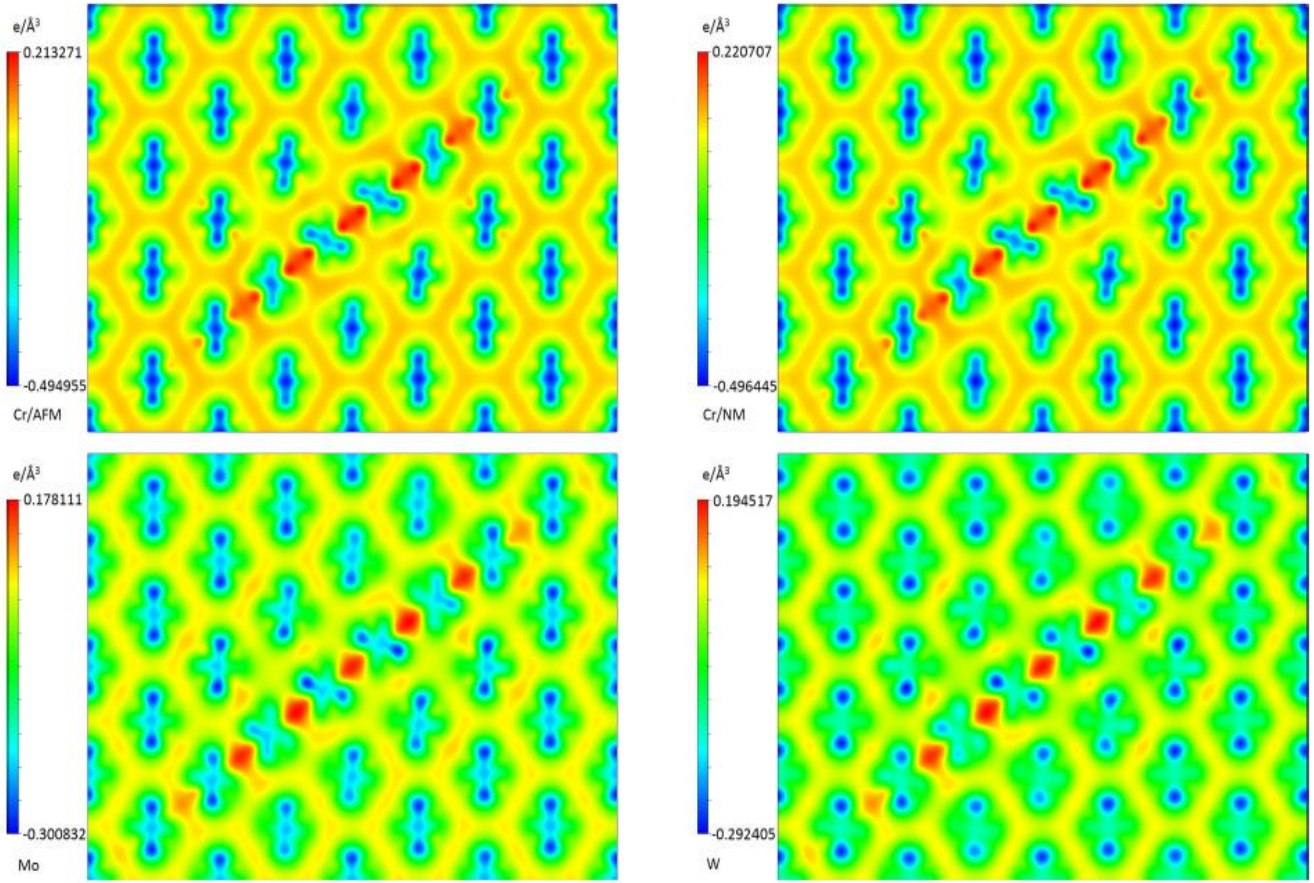

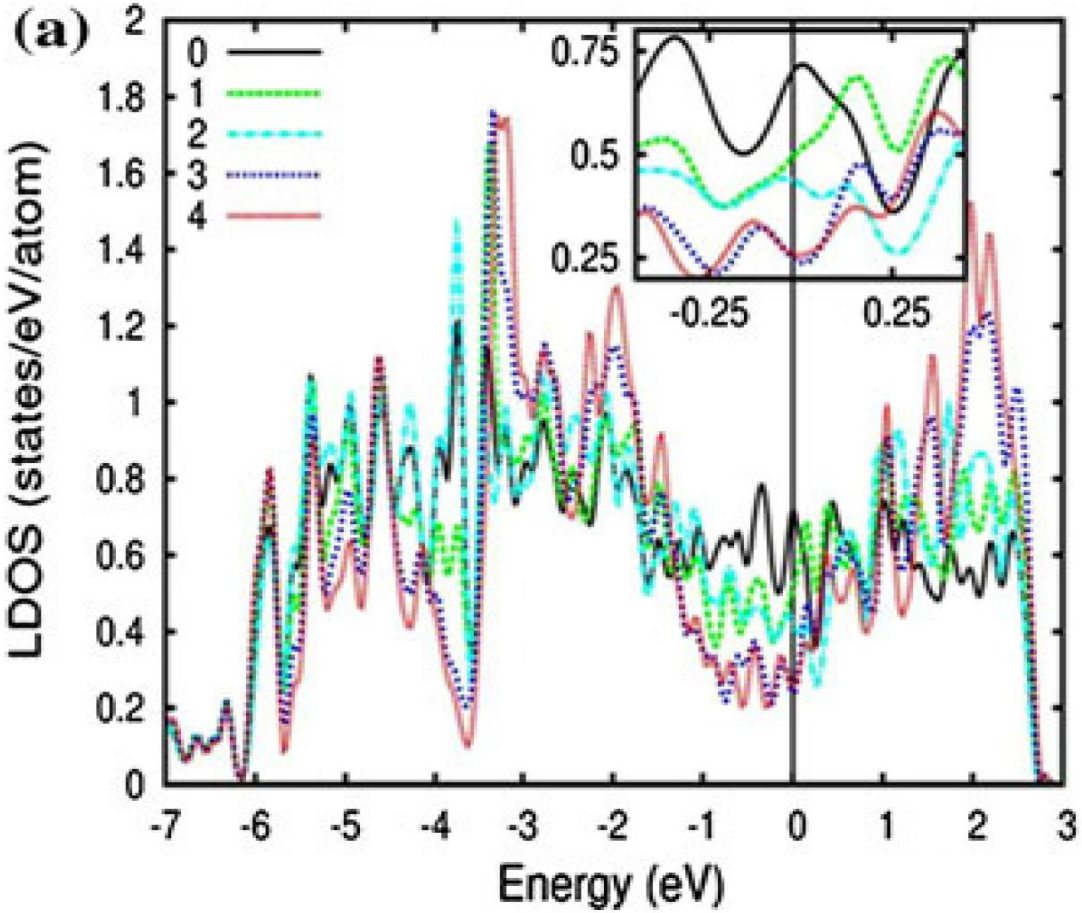

Resistivity recovery in bcc transition metals at low-temperature stage

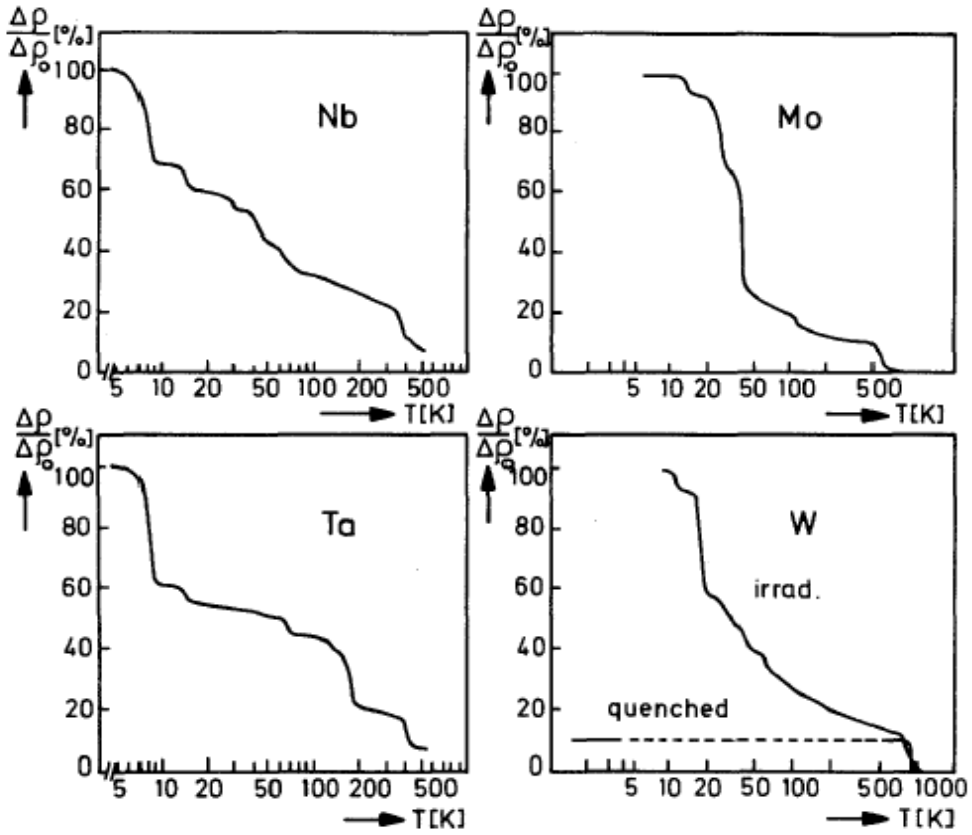

Fig. 4. Recovery curves for several bcc metals. The ratio residual resistivity $\Delta\rho$, observed at low temperature during an isochronal annealing procedure with a step-by-step increased annealing temperature, over the residual resistivity $\Delta\rho_0$ before annealing, is plotted versus the temperature T of the last step. This figure is taken from ref. [1].

T of recovery stage I: onset of mobility for self-interstitials

V: T<6K

Nb: T<6K

Ta: T<6K

Cr: T=40K

Mo: T=35K

W: T=27K

Fe: T=120K

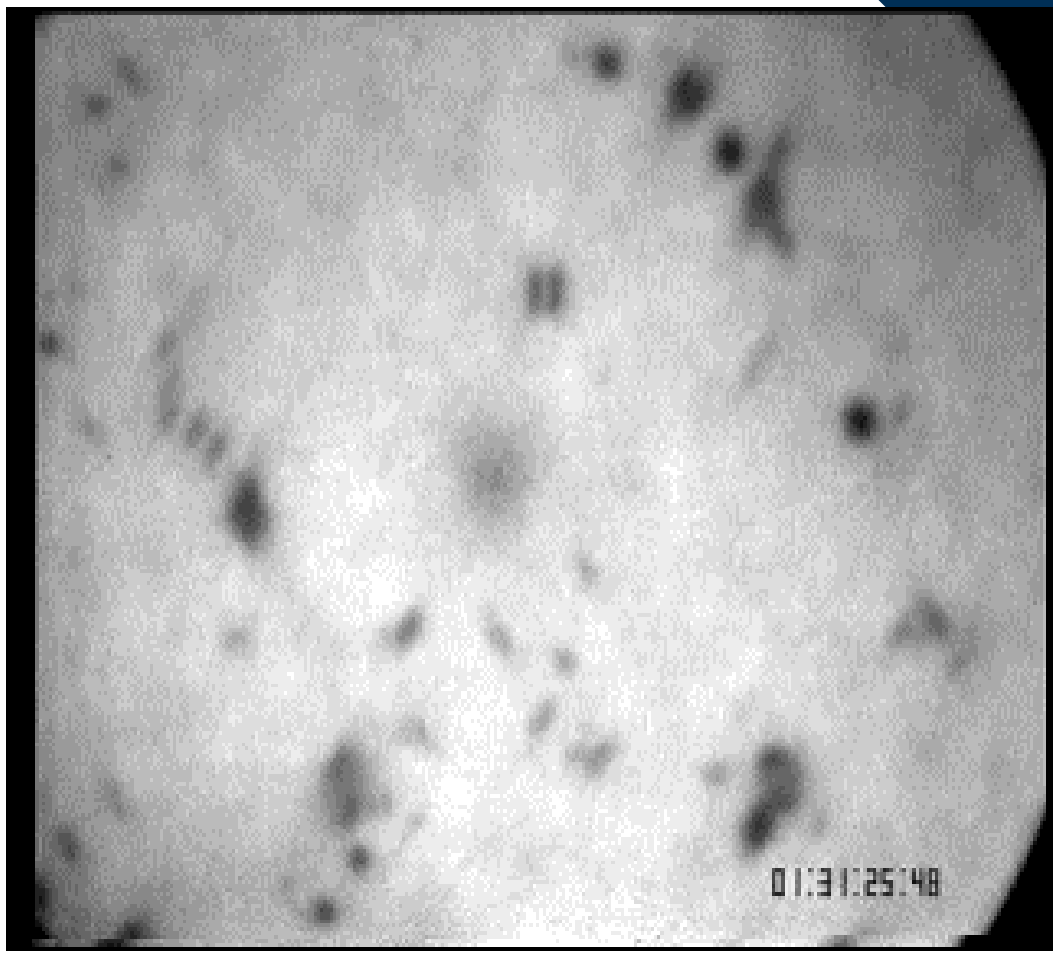

Experimental validation in 2020: Quantum diffusion of SIA defects in tungsten

nature materials
LETTERS
https://doi.org/10.1038/s41563-019-0584-0

Quantum de-trapping and transport of heavy defects in tungsten

Kazuto Arakawa[1*], Mihai-Cosmin Marinica[2], Steven Fitzgerald[3], Laurent Proville[2], Duc Nguyen-Manh[4], Sergei L. Dudarev[4], Pui-Wai Ma[4], Thomas D. Swinburne[5], Alexandra M. Goryaeva[2], Tetsuya Yamada[6], Takafumi Amino[7], Shigeo Arai[8], Yuta Yamamoto[8], Kimitaka Higuchi[8], Nobuo Tanaka[8], Hidehiro Yasuda[9], Tetsuya Yasuda[9] and Hirotaro Mori[9]

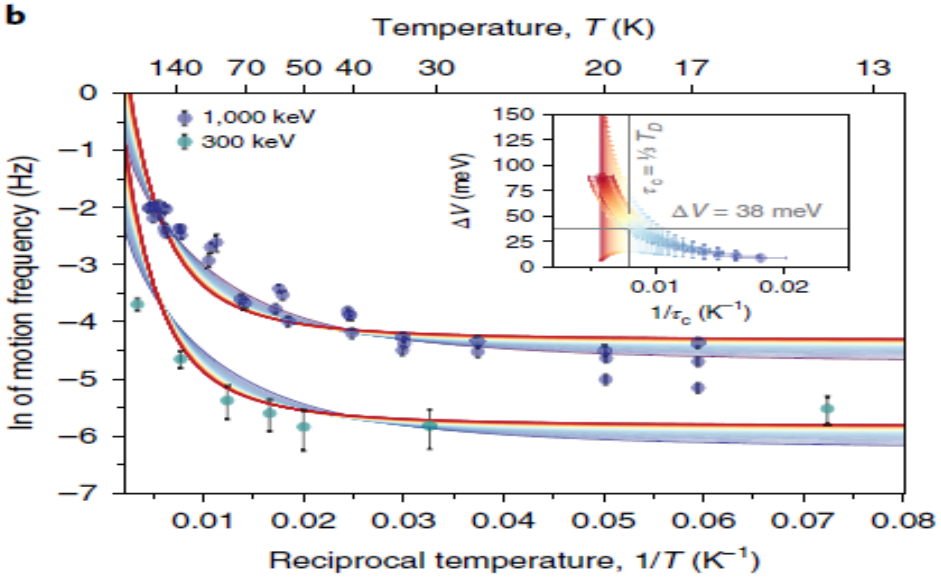

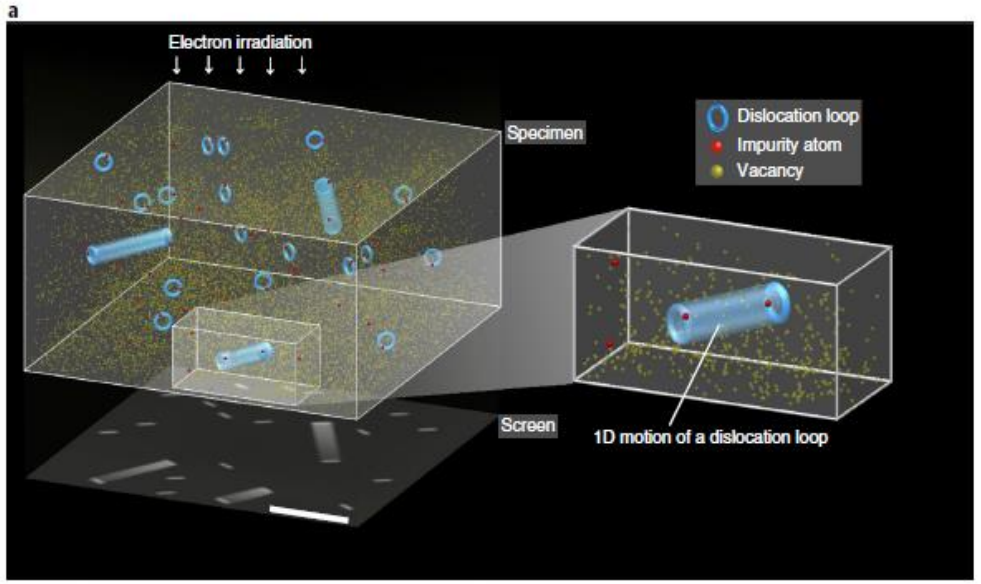

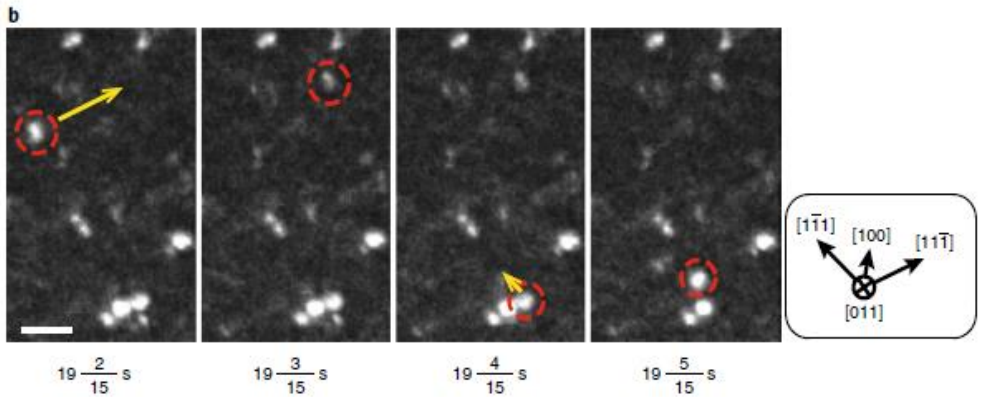

Analytic solution for crowdion diffusion using 1D potential predicted from DFT

$$\mathcal{L} = \sum_{n=-\infty}^{\infty} \left(\frac{m\dot{u}_n^2}{2} - \frac{\beta}{2}(u_{n+1} - u_n)^2 - V(u_n) \right)$$

"Spring constant" (along string)

Displacement of *n*th atom from position *na*

Periodic potential, period *a*

- Simple sine potential not good for bcc transition metals
- Double-sine captures double-hump
- Previous analysis carries through with some complications

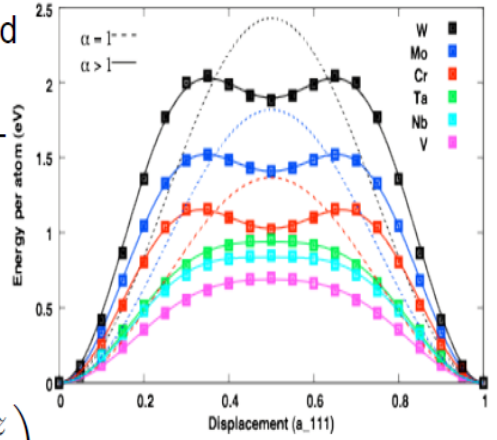

$$V_0 \left(\sin^2 \frac{\pi z}{a} + \frac{\alpha^2 - 1}{4} \sin^2 \frac{2\pi z}{a} \right)$$

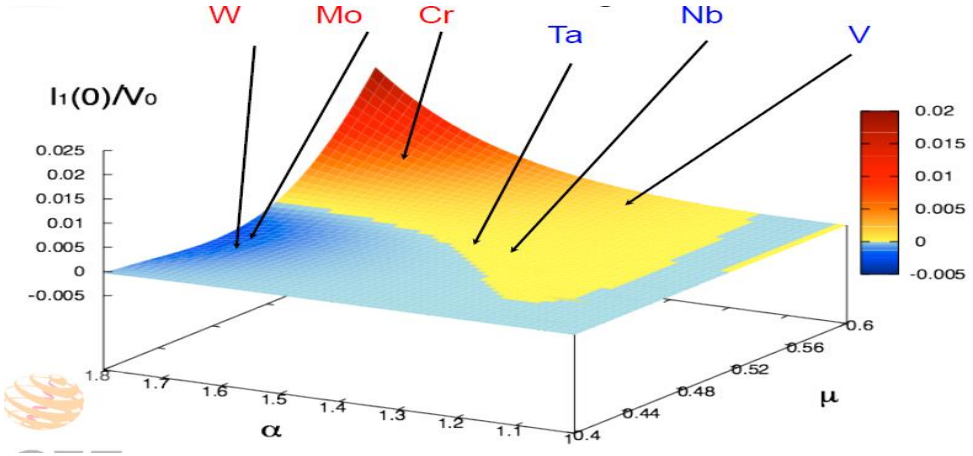

Predicted migration barrier for bcc-W is 2.6 meV

S.P. Fitzgerald and D. Nguyen-Manh, Phys. Rev. Lett. 101 (2008) 115504

Development magnetic potentials for modelling of radiation damage in Fe

PRL 106, 246402 (2011) PHYSICAL REVIEW LETTERS 1

Magnetic Bond-Order Potential for Iron

M. Mrovec,[1,2,*] D. Nguyen-Manh,[3] C. Elsässer,[1,2] and P. Gumbsch[1,2]
[1]IAM, Karlsruhe Institute of Technology, Kaiserstrasse 12, 76131 Karlsruhe, Germany
[2]Fraunhofer Institute for Mechanics of Materials IWM, Wöhlerstrasse 11, 79108 Freiburg, Germany
[3]EURATOM/CCFE Fusion Association, Culham Science Centre, Abingdon, OX14 3DB, United Kingdom
(Received 26 January 2011; published 14 June 2011)

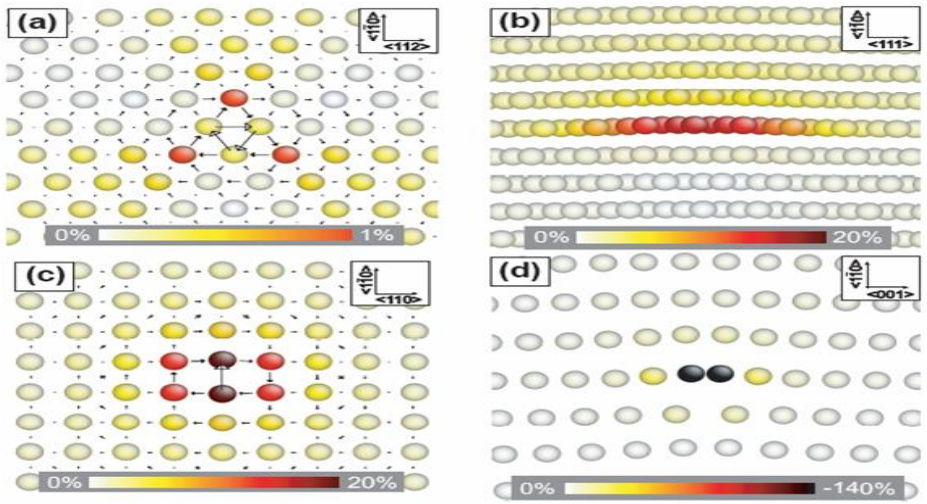

FIG. 2. (Color) Dislocation core structures of the 1/2[111] screw (a) and edge (b) and the [100] screw (c) and edge(d) dislocations. The coloring of the atoms shows the decrease of atomic magnetic moments.

Constrained non-collinear magnetism in disordered Fe and Fe–Cr alloys

D. Nguyen-Manh *, Pui-Wai Ma, M.Yu. Lavrentiev, S.L. Dudarev
CCFE, Culham Science Centre, Abingdon, Oxon OX14 3BD, United Kingdom

ARTICLE INFO
Article history:
Received 18 April 2014
Accepted 31 October 2014
Keywords:
First-principles modelling
Non-collinear magnetism
Disordered Fe-based alloys
Spin-lattice dynamics
Magnetic excitations

ABSTRACT
The development of quantitative models for radiation damage effects in iron, iron alloys and steels, particularly for the high temperature properties of the alloys, requires treating magnetic interactions, which control the phase stability of ferritic–martensitic, ferritic, and austenitic steels. Here, disordered magnetic configurations of pure iron and Fe–Cr alloys are investigated using Density Functional Theory (DFT) formalism, in the form of a constrained non-collinear magnetic model, with the objective of creating a database of atomic magnetic moments and forces acting between the atoms. From a given disordered atomic configuration of either pure Fe or Fe–Cr alloy, a penalty contribution additional to the usual spin-polarized DFT total energy is evaluated by constraining the magnitude and direction of magnetic moments. An extensive database of non-collinear magnetic moment and force components for various atomic configurations has been generated and used for interpolating the spatially-dependent magnetic interaction parameters, for applications in large-scale spin–lattice dynamics and magnetic Monte-Carlo simulations.

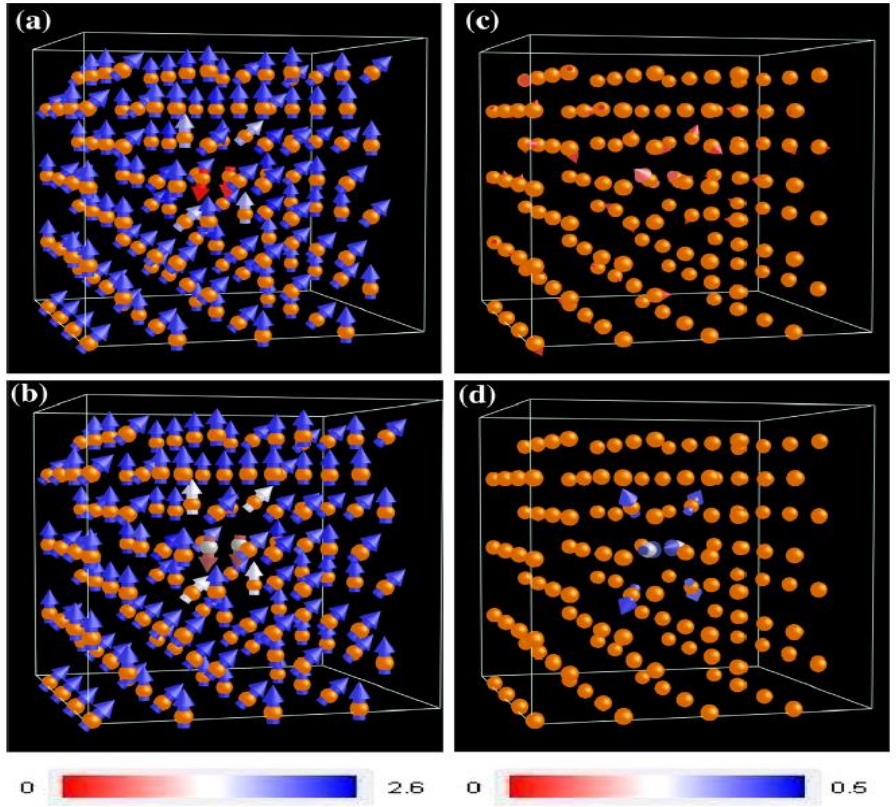

Object Kinetic Monte Carlo method using first principles data

UK Atomic Energy Authority

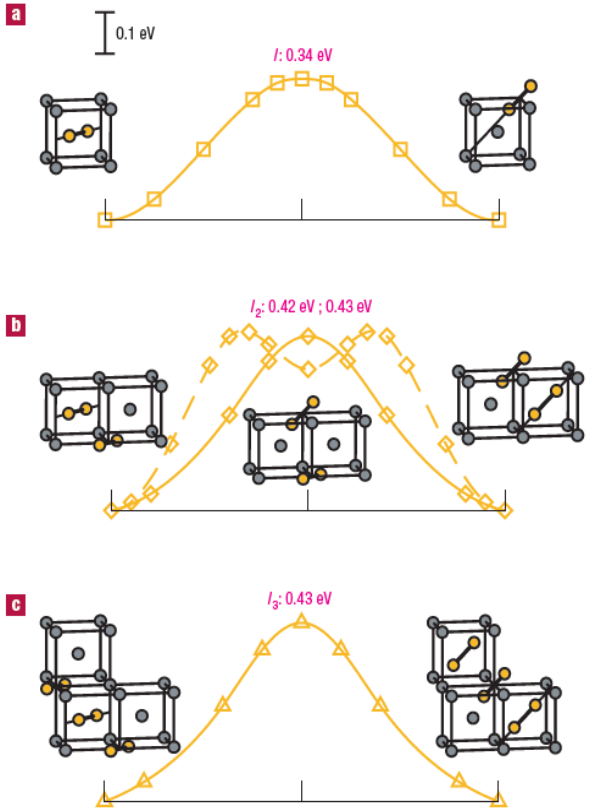

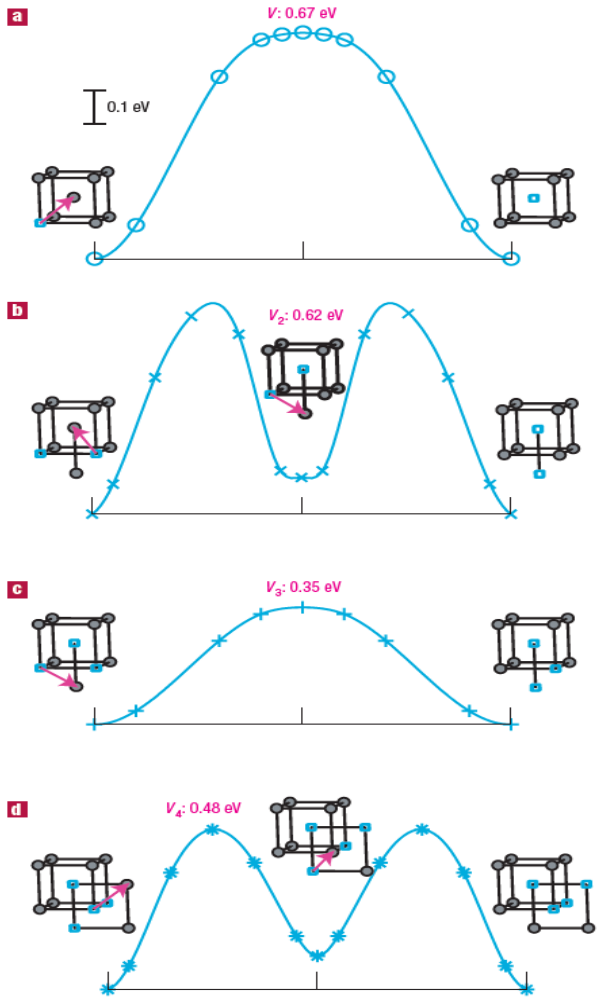

Figure 2 Migration of interstitial-type defects. Energy variation along the most favourable migration pathways for I, I_2 and I_3, determined by *ab initio* calculations. The corresponding migration energies and schematic representations of the migration mechanisms starting from the defect ground-states are shown: the orange and grey spheres indicate self-interstitial and lattice atoms respectively. The energy scale is the same for all graphs.

Multiscale modelling of defect kinetics in irradiated iron

CHU-CHUN FU, JACQUES DALLA TORRE, FRANÇOIS WILLAIME*, JEAN-LOUIS BOCQUET AND ALAIN BARBU

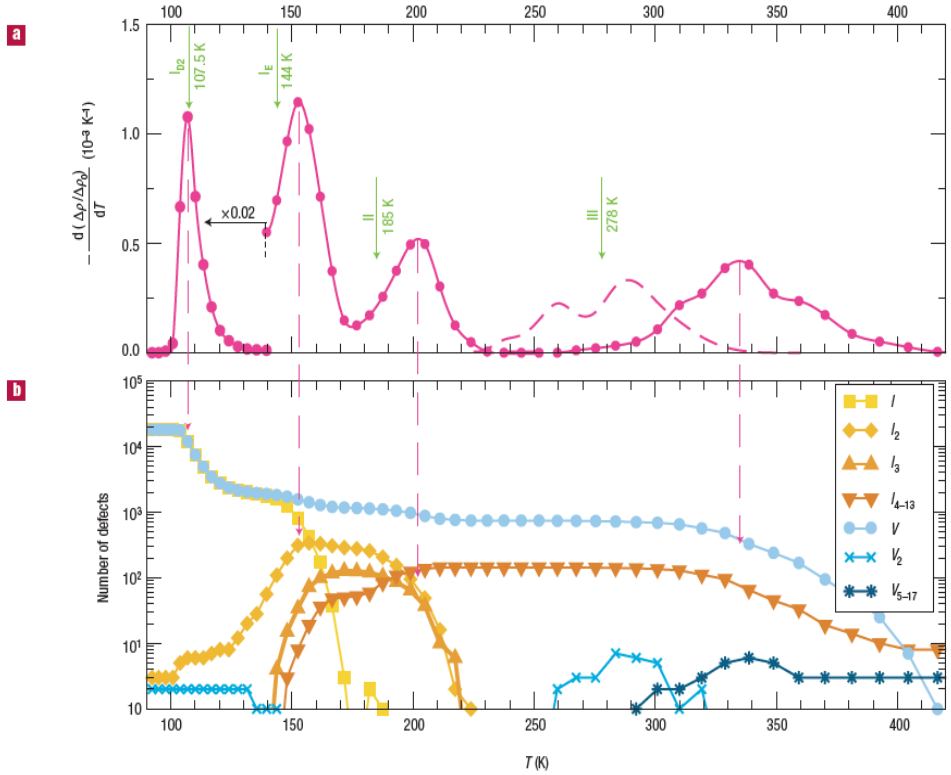

Self-interstitial atom (SIA) clusters in magnetic bcc-Fe: Formation of C15 structure

UK Atomic Energy Authority

PRL 108, 025501 (2012) PHYSICAL REVIEW LETTERS week ending 13 JANUARY 2012

Irradiation-Induced Formation of Nanocrystallites with *C*15 Laves Phase Structure in bcc Iron

M.-C. Marinica, F. Willaime,* and J.-P. Crocombette
CEA, DEN, Service de Recherches de Métallurgie Physique, F-91191 Gif-sur-Yvette, France
(Received 28 September 2011; revised manuscript received 22 November 2011; published 11 January 2012)

A three-dimensional periodic structure is proposed for self-interstitial clusters in body-centered-cubic metals, as opposed to the conventional two-dimensional loop morphology. The underlying crystal structure corresponds to the *C*15 Laves phase. Using density functional theory and interatomic potential calculations, we demonstrate that in α-iron these *C*15 aggregates are highly stable and immobile and that they exhibit large antiferromagnetic moments. They form directly in displacement cascades, and they can grow by capturing self-interstitials. They thus constitute an important new element to account for when predicting the microstructural evolution of iron base materials under irradiation.

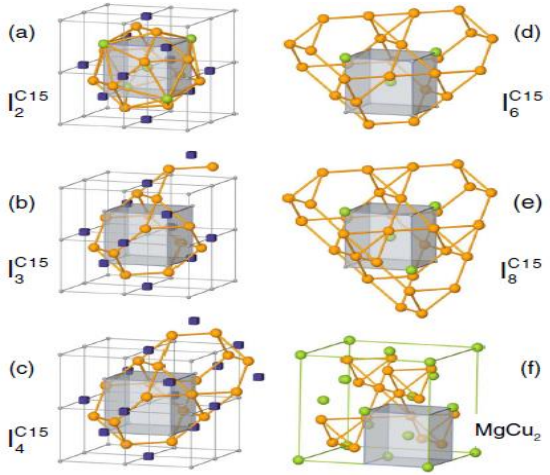

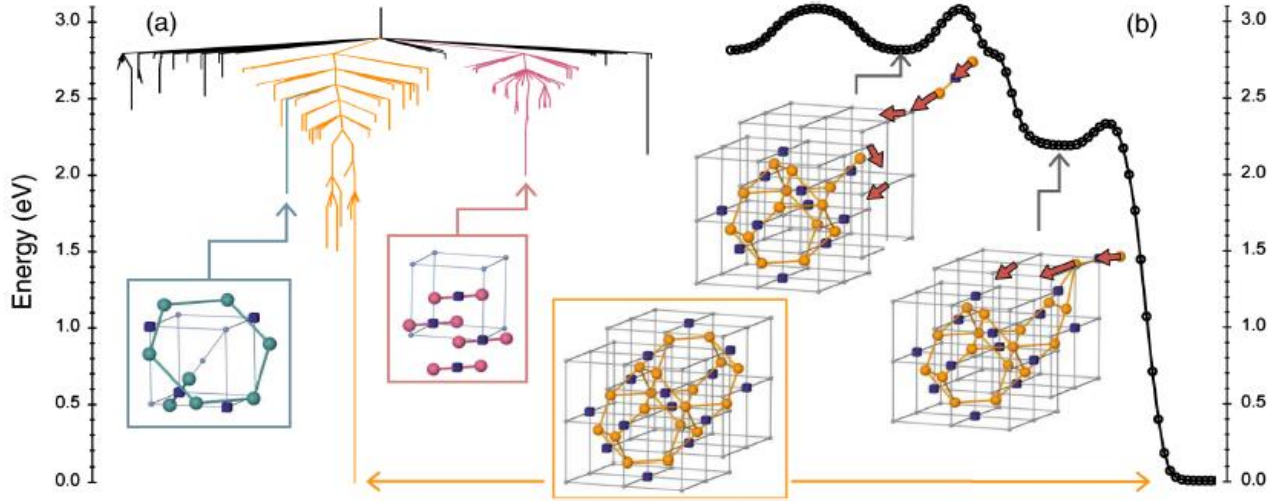

Molecular dynamic simulations of <111> crowdion in W and <110> dumbbell in Fe

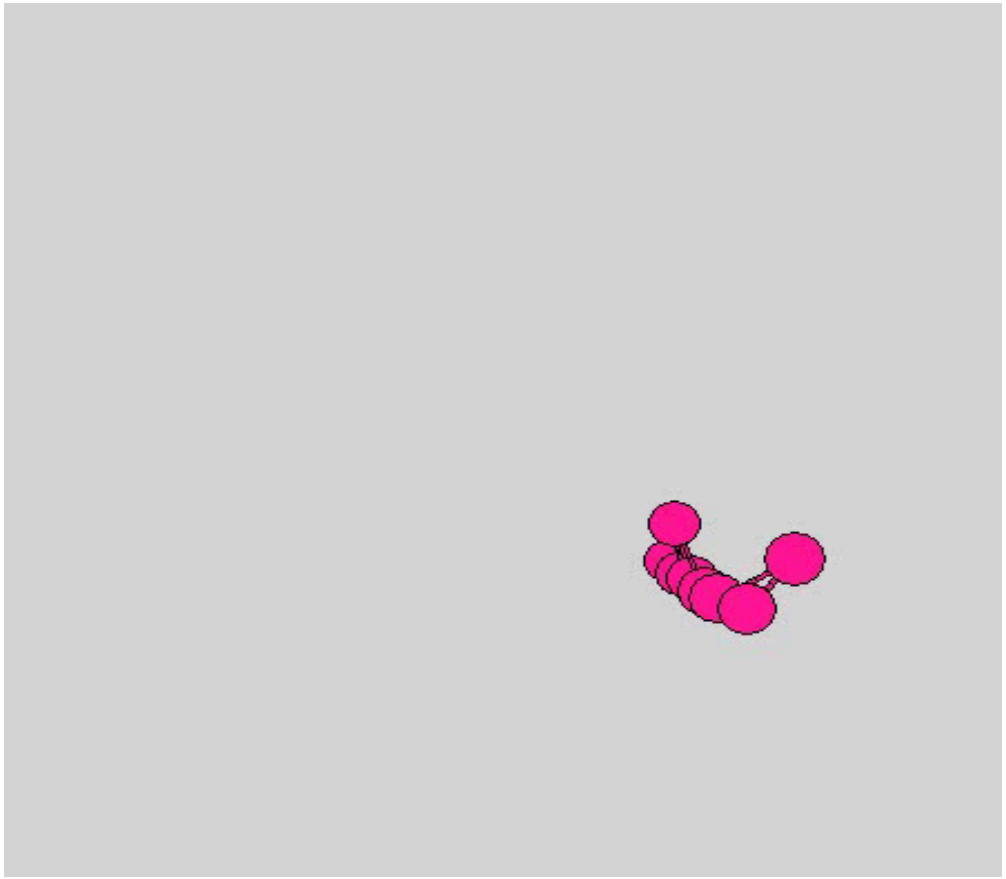

1D-motion of <111> crowdion

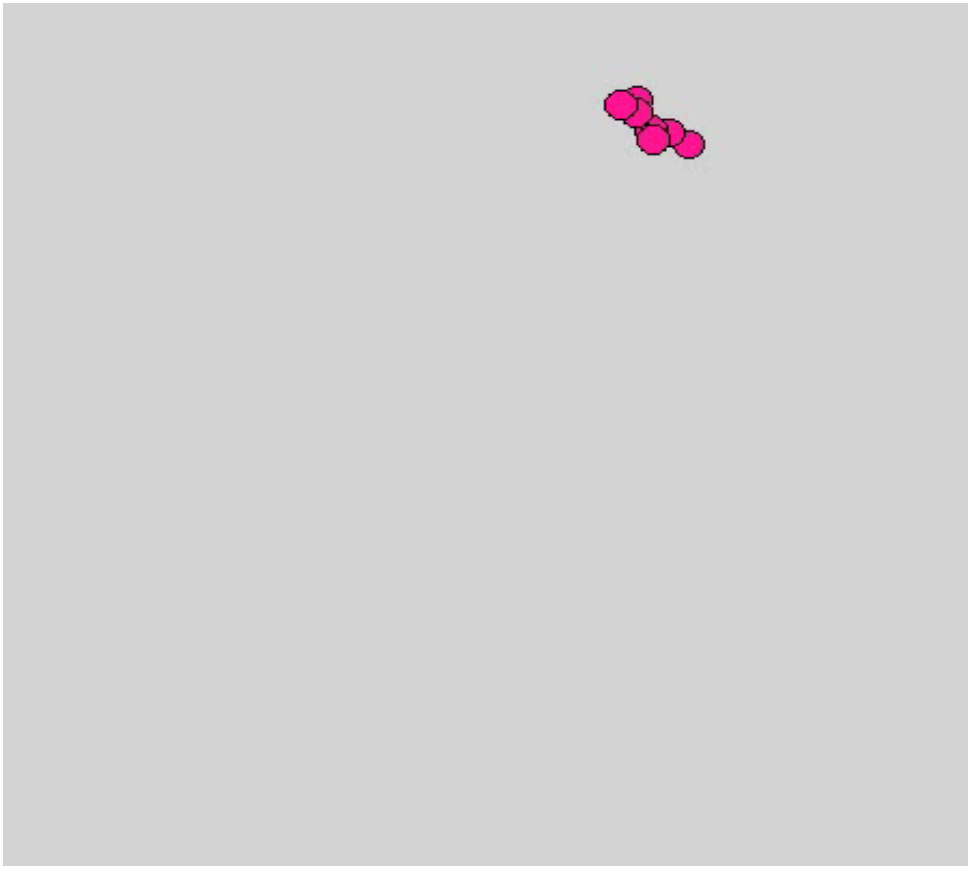

3D-motion of <110> dumbbell

Trapping of He&noble gases in W and comparison with thermal desorption

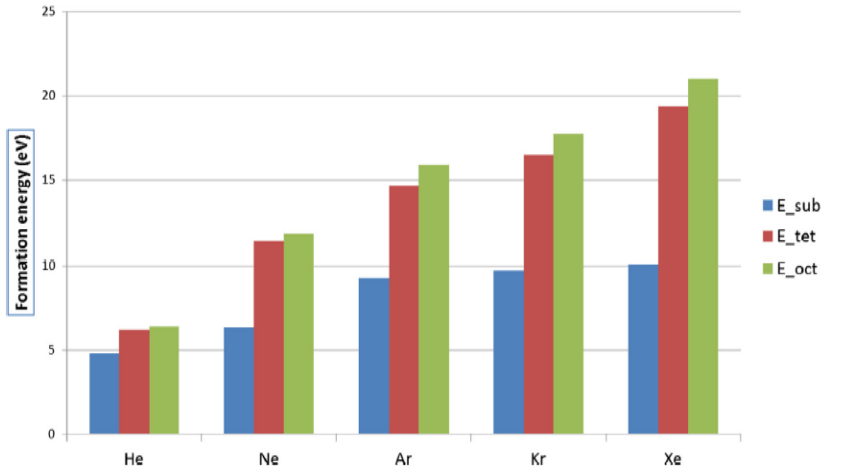

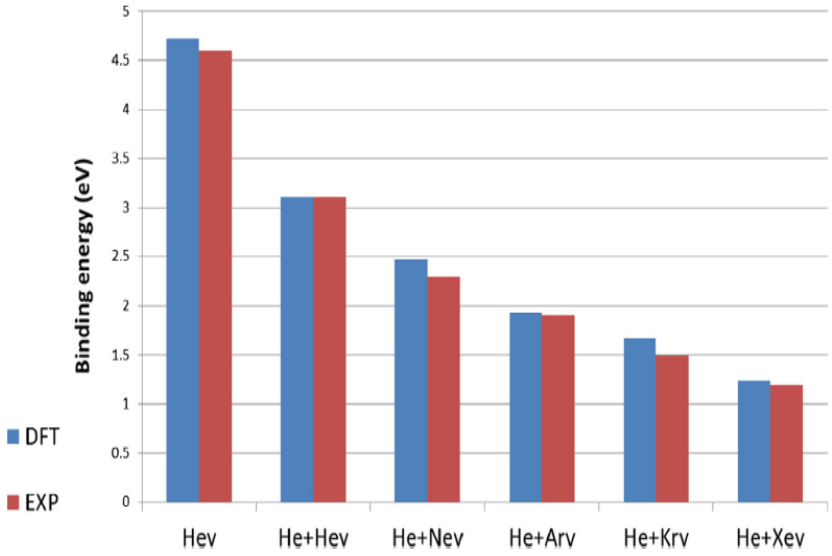

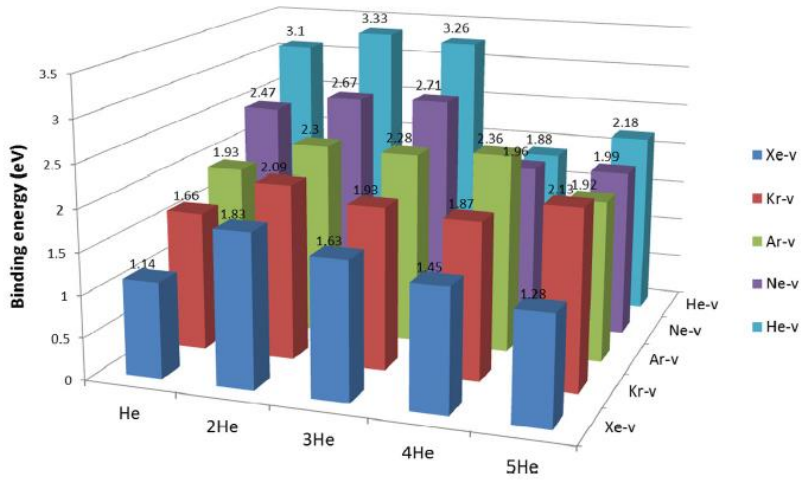

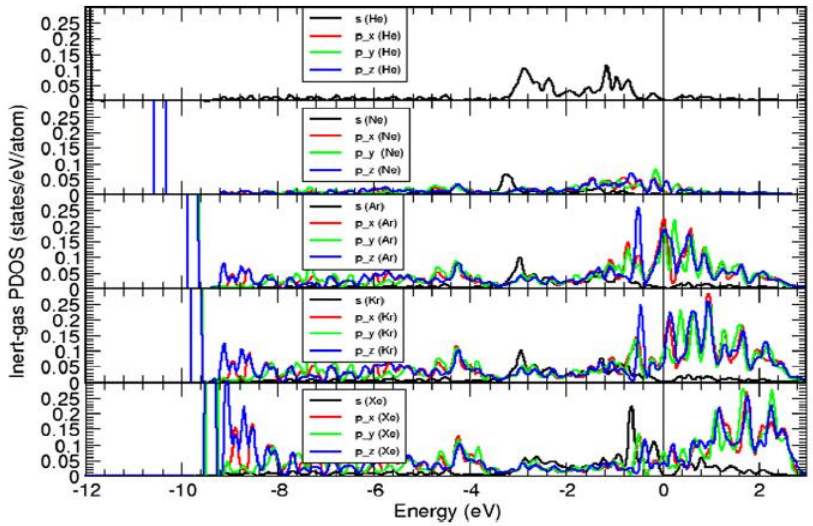

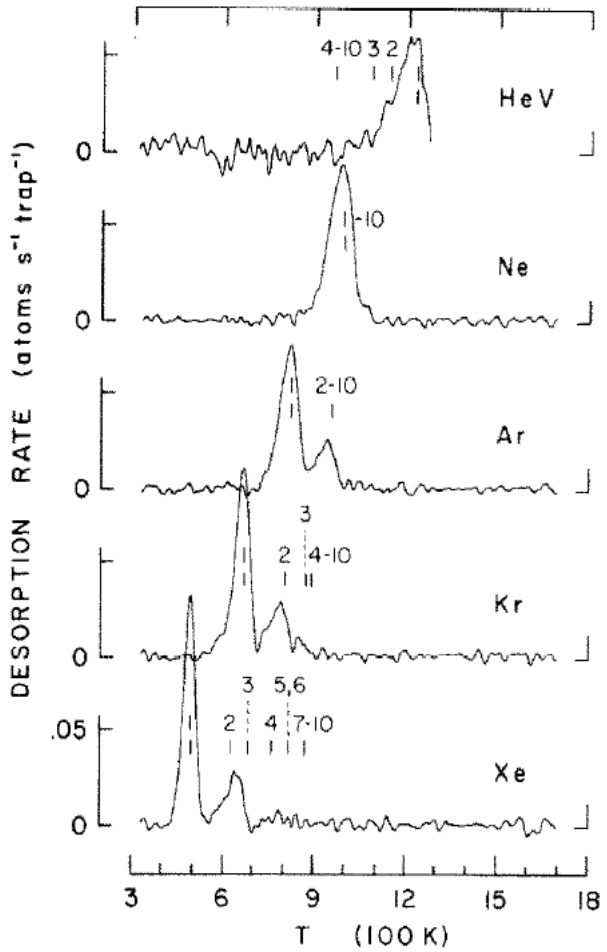

Volume relaxation and swelling under irradiation

UK Atomic Energy Authority

Available online at www.sciencedirect.com
ScienceDirect
Acta Materialia 89 (2015) 352–363
Acta MATERIALIA
www.elsevier.com/locate/actamat

Lattice swelling and modulus change in a helium-implanted tungsten alloy: X-ray micro-diffraction, surface acoustic wave measurements, and multiscale modelling

F. Hofmann,[a,*] D. Nguyen-Manh,[b,c] M.R. Gilbert,[b,c] C.E. Beck,[c] J.K. Eliason,[d] A.A. Maznev,[d] W. Liu,[e] D.E.J. Armstrong,[c] K.A. Nelson[d] and S.L. Dudarev[b,c]

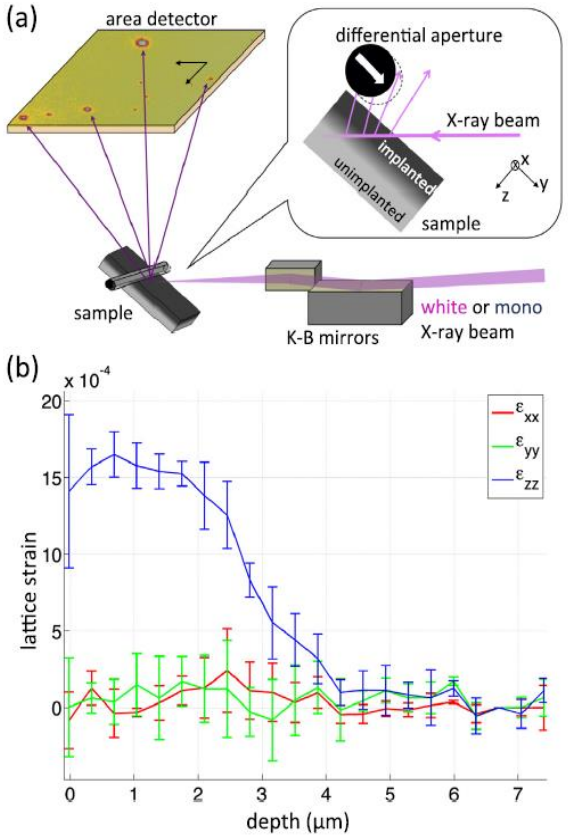

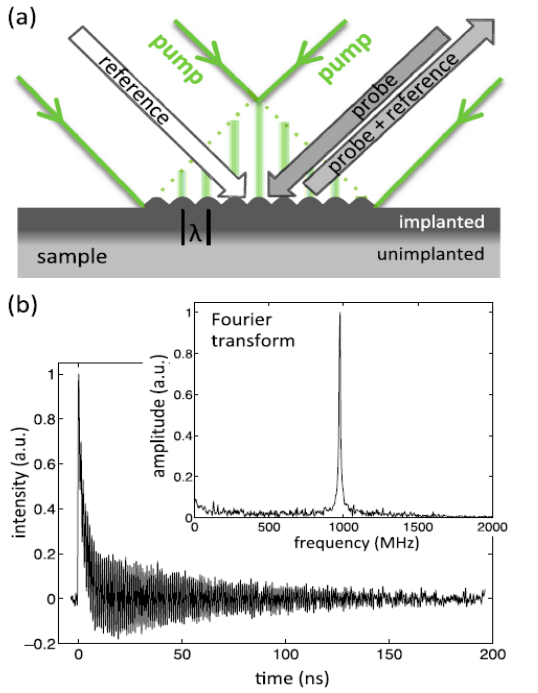

Fig. 3. Transient grating surface acoustic wave measurements: (a) Schematic of the experimental setup. (b) Measured intensity signal plotted as a function of delay time relative to the pump pulse for the unimplanted W-1% Re sample. Fourier transform of the signal showing a peak at the surface acoustic wave frequency (inset).

Density Functional Theory Modelling:

- Central defect in 4 x 4 x 4 tungsten BCC supercell => 128 atoms.
- Periodic boundaries, free to expand.

.attice swelling - Relaxation volume calculations:

- Estimate relaxation volume: $\Omega_r(\text{defect}) = \Omega(\text{defect}) - \Omega(\text{perfect})$
- Estimate lattice swelling: $\varepsilon_v = \sum_A n_A \Omega_r^{(A)}$ and $\varepsilon_{zz} = \frac{1(1+\nu)}{3(1-\nu)} \sum_A n_A \Omega_r^{(A)}$
- If we assume 1 He per V: predict ε_{zz} (HeV) = 2654 x 10^{-6} => ~ twice experimental ε_{zz}.
- Consider clustering [11]: 1555 appm He_2V complexes & 1555 appm SIAs: predict ε_{zz} (He_2V) = 1493 x 10^{-6} => **very good agreement with experimental ε_{zz} strain.**

elaxation volumes for vacancies and self-interstitial

V	V_2 (1NN)	V_2 (2NN)	V_2(3NN)	V_3(1NN(2) +2NN)	<111> SIA	Frenkel
-0.37 -0.34 [a] -0.38 [b]	-0.72 -0.65 [a]	-0.79 -0.74 [a]	-0.76 -0.69 [a]	-1.08	1.68	1.31

elaxation volumes for interstitial helium clusters

He (tetra)	He (octa)	He_2 (tetra)	He_3 (tetra)	He_4 (tetra)	He_5 (tetra)
0.36 0.33 [c]	0.37 0.34 [c]	0.80	1.16	1.65	2.03

elaxation volumes for helium - vacancy clusters

HeV (tetra)	HeV (octa)	He_2V (tetra)	He_3V (tetra)	He_4V (tetra)	He_5V (tetra)	He_6V (tetra)
-0.24	-0.23	-0.06	0.14	0.38	0.71	1.09

Kato D, Iwakiri H, Morishita K. Journal of Nuclear Materials 2011;417:1115.
Heinola K, Ahlgren T, Nordlund K, Keinonen J. Physical Review B 2010;82:094102.
Zhou HB, Jin S, Shu XL, Zhang Y, Lu GH, Liu F. EPL (Europhysics Letters) 2011;96:66001.

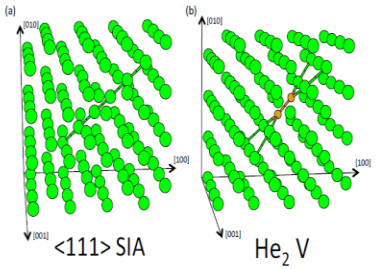

Calculation details:
Perdew-Burke-Ernzerhof electron exchange-correlation functional within generalized gradient approximation. Projector augmented wave (PAW) pseudopotentials implemented in the Vienna Ab-initio Simulation Package (VASP). 400 eV plane wave cutoff energy and 4 x 4 x 4 k-point mesh with 0.15 Å^{-1} spacing. Periodic boundary conditions with expansion in all directions allowed.

Modulus change calculations:

- Calculate elastic constants for different defects.
- Estimate SAW velocity change due to He-implantation: predicted (-1.8%) experimental (-2.2%)

=> excellent agreement; no free parameters.

		C_{11} (GPa)	C_{12} (GPa)	C_{44} (GPa)	A
Pure W experimental at 298 K [12-14]		522.8	203.5	160.7	1.01
Pure W	from DFT	537.4	188.2	153.7	0.88
	rescaled	522.8	203.5	160.7	1.01
W + SIA	from DFT	512.5	212.5	141.4	0.94
	rescaled	498.6	229.8	147.8	1.10
W + He_2V	from DFT	518.9	188.1	141.2	0.85
	rescaled	504.8	203.4	147.6	0.98

$$C_{ij}^{implanted} = (1 - 128(n_{SIA} + n_{He_2V}))C_{ij}^{W} + 128 n_{SIA} C_{ij}^{SIA} + 128 n_{He_2V} C_{ij}^{He_2V}$$

	A	K (GPa)	G (GPa)	E (GPa)	nu
Pure W	1.01	309.9	160.3	410.1	0.279
W + 1555 appm He_2V + 1555 appm SIAs	1.02	310.6	154.5	397.5	0.287

Predicted SAW velocities

in m/s	rescaled		direct from DFT		experiments
	Voigt	Reuss	Voigt	Reuss	
Perfect W	2667	2667	2680	2675	2679
W + He_2V + SIAs	2622	2618	2636	2628	2621
Change	-1.7%	-1.9%	-1.7%	-1.8%	-2.2%

Elastic corrections to defect energies

UK Atomic Energy Authority

An elastic correction energy accounting the for the elastic interaction between images in periodic boundary conditions can be calculated using the dipole tensor of the defect and the anisotropic elastic Green functions:

$$E_{\mathrm{el}}^{\mathrm{corr}} = E_{DD} + E_{\mathrm{strain}}^{\mathrm{corr}}$$

$$E_{DD} = \frac{1}{2}\sum_{n\neq 0} P_{ij}P_{kl}\frac{\partial}{\partial x_j}\frac{\partial}{\partial x_l}G_{ik}(\mathbf{R_n}) - \frac{1}{2V_{\mathrm{cell}}} \times \sum_{n\neq 0}\int_{V_{\mathrm{cell}}} P_{ij}P_{kl}\frac{\partial}{\partial x_j}\frac{\partial}{\partial x_l}G_{ik}(\mathbf{R_n}-\mathbf{r})d^3r.$$

$$E_{\mathrm{strain}}^{\mathrm{corr}} = -\frac{1}{V_{\mathrm{cell}}}\int_{V_{\mathrm{cell}}} P_{ij}P_{kl}\frac{\partial}{\partial x_j}\frac{\partial}{\partial x_l}G_{ik}(\mathbf{r})d^3r.$$

The self-strain correction part corrects the linear elastic part of the strain field

$$P_{ij} = V_{\mathrm{cell}}\left(C_{ijkl}\epsilon_{kl}^{\mathrm{app}} - \bar{\sigma}_{ij}\right).$$

Macroscopic stress of the simulation box

$$\bar{\sigma}_{ij} = \frac{1}{V_{\mathrm{cell}}}\int \sigma_{ij}dV,$$

$$\Omega_{ij} = S_{ijkl}P_{kl}$$

> For irradiated materials swell and creep, we can describe this using a tensorial eigenstrain that depends on the irradiation parameters (T, stress, PKA, dose and dose rate)

Relaxation volumes and swelling prediction with new interatomic potentials development

UK Atomic Energy Authority

TABLE XX. Elements of the dipole tensor P_{ij} (in eV units), the relaxation volume tensor Ω_{ij} (in Å^3 units), eigenvalues of the relaxation volume tensor $\Omega^{(i)}$ (in Å^3 units), and the relaxation volume of the defect Ω_{rel} (in atomic volume units Ω_0) computed for W.

W	P_{11}	P_{22}	P_{33}	P_{12}	P_{23}	P_{31}	Ω_{11}	Ω_{22}	Ω_{33}	Ω_{12}	Ω_{23}	Ω_{31}	$\Omega^{(1)}$	$\Omega^{(2)}$	$\Omega^{(3)}$	Ω_{rel}
⟨111⟩d	52.754	52.754	52.754	13.128	13.128	13.128	9.209	9.209	9.209	7.402	7.402	7.402	1.808	1.808	24.012	1.712
⟨111⟩c	52.745	52.745	52.745	13.151	13.151	13.151	9.207	9.207	9.207	7.414	7.414	7.414	1.793	1.793	24.036	1.711
⟨110⟩d	56.960	52.557	52.557	0.000	11.277	0.000	10.908	8.693	8.693	0.000	6.358	0.000	10.908	2.335	15.050	1.753
Tetra	47.359	59.114	59.114	0.000	0.000	0.000	5.693	11.606	11.606	0.000	0.000	0.000	5.693	11.606	11.606	1.791
⟨100⟩d	65.920	53.379	53.379	0.000	0.000	0.000	14.254	7.945	7.945	0.000	0.000	0.000	14.254	7.945	7.945	1.868
Octa	52.741	52.741	67.209	0.000	0.000	0.000	7.623	7.623	14.901	0.000	0.000	0.000	7.623	7.623	14.901	1.868
Vac	−9.984	−9.984	−9.984	0.000	0.000	0.000	−1.743	−1.743	−1.743	0.000	0.000	0.000	−1.743	−1.743	−1.743	−0.324

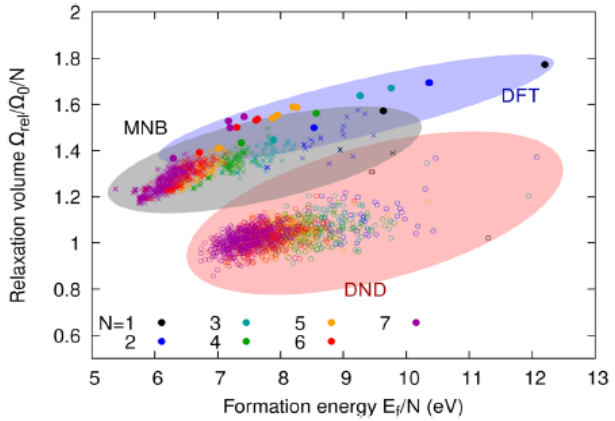

FIG. 3. Relaxation volumes of randomly generated interstitial defect clusters for different numbers of interstitial atoms in the defect, *N*. DFT values for energies and relaxation volumes from Ref. 13 are shown with filled circles. Crosses: the values computed with MNB potential; open circles are the values computed using the DND potential. Shaded ellipses are drawn to guide the eye to the regions covered by data generated using the relevant potentials. Note that the DND potential tends to predict a higher formation energy and lower relaxation volume of a defect cluster than the MNB potential.

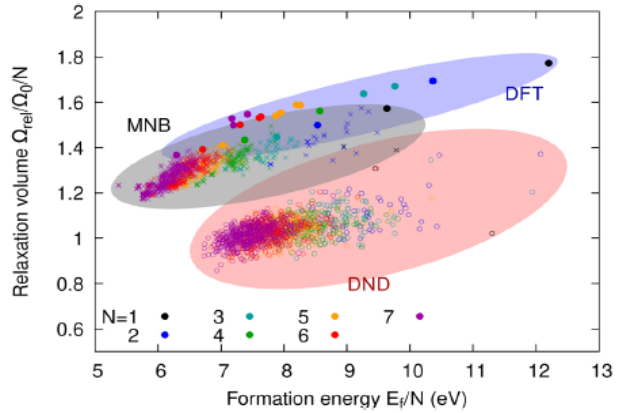

FIG. 3. Relaxation volumes of randomly generated interstitial defect clusters for different numbers of interstitial atoms in the defect, *N*. DFT values for energies and relaxation volumes from Ref. 13 are shown with filled circles. Crosses: the values computed with MNB potential; open circles are the values computed using the DND potential. Shaded ellipses are drawn to guide the eye to the regions covered by data generated using the relevant potentials. Note that the DND potential tends to predict a higher formation energy and lower relaxation volume of a defect cluster than the MNB potential.

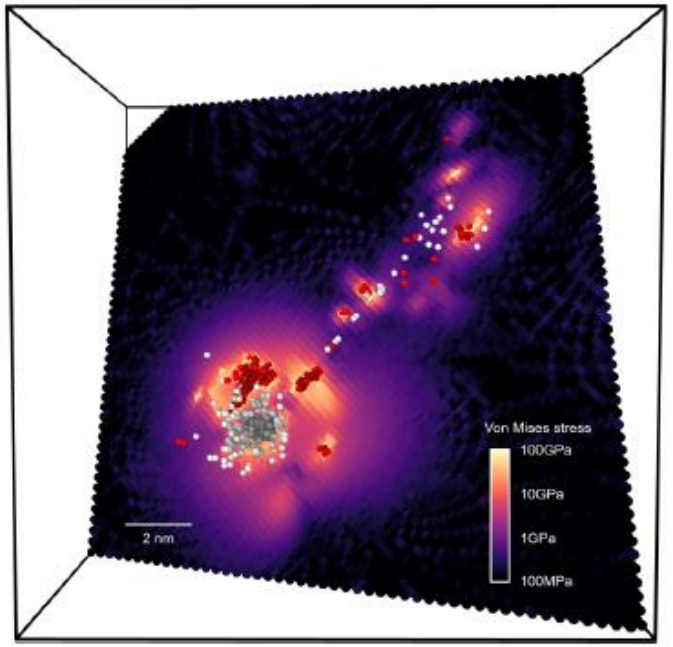

FIG. 1. A typical configuration of defects produced by a collision cascade event in tungsten, initiated by a 150 keV primary knock-on atom (PKA) and simulated using the method described in Sec. II D. Vacancies (white spheres), and interstitials (red), were identified using a Wigner-Seitz defect analysis.[37] The von Mises stress in a [211] plane intersecting the cascade is also shown. Note that close to the defects, the stresses can be as high as 100 GPa, comparable to the shear modulus ($\mu = 160$ GPa). In the study below, we analyze the complex stress fields of individual defects and clusters of defects formed in cascades, similar to those shown in this figure.

D. Mason, DNM et al., JAP, 126 (2019) 075112

Algorithms for high irradiation exposure (W)

Creation relaxation algorithm (CRA)

Create Frenkel pairs by moving atoms at random

Relax with appropriate boundary conditions

Repeat

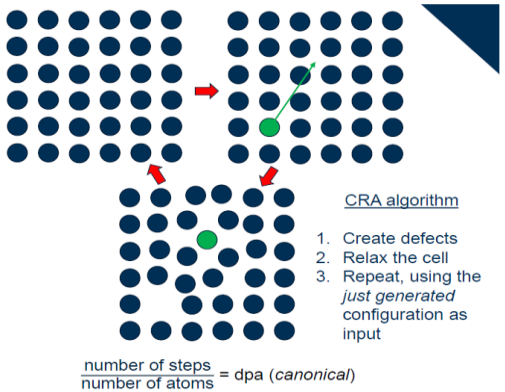

$\bar{g} = [011]$

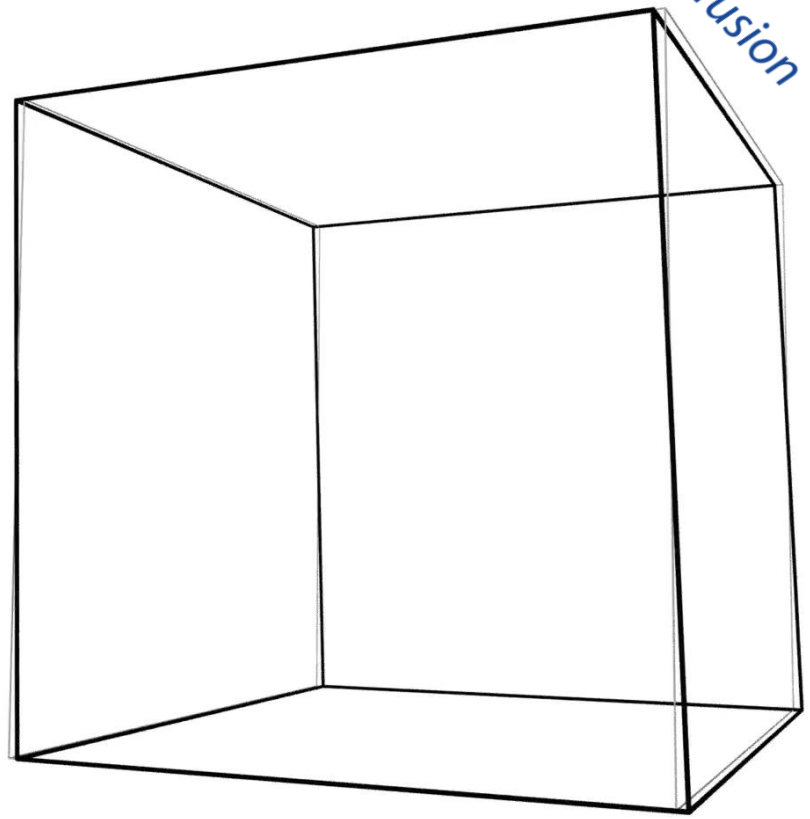

- vacancy
- self-interstitial

Modelling of electronic stopping power from TDDFT by H and He in W

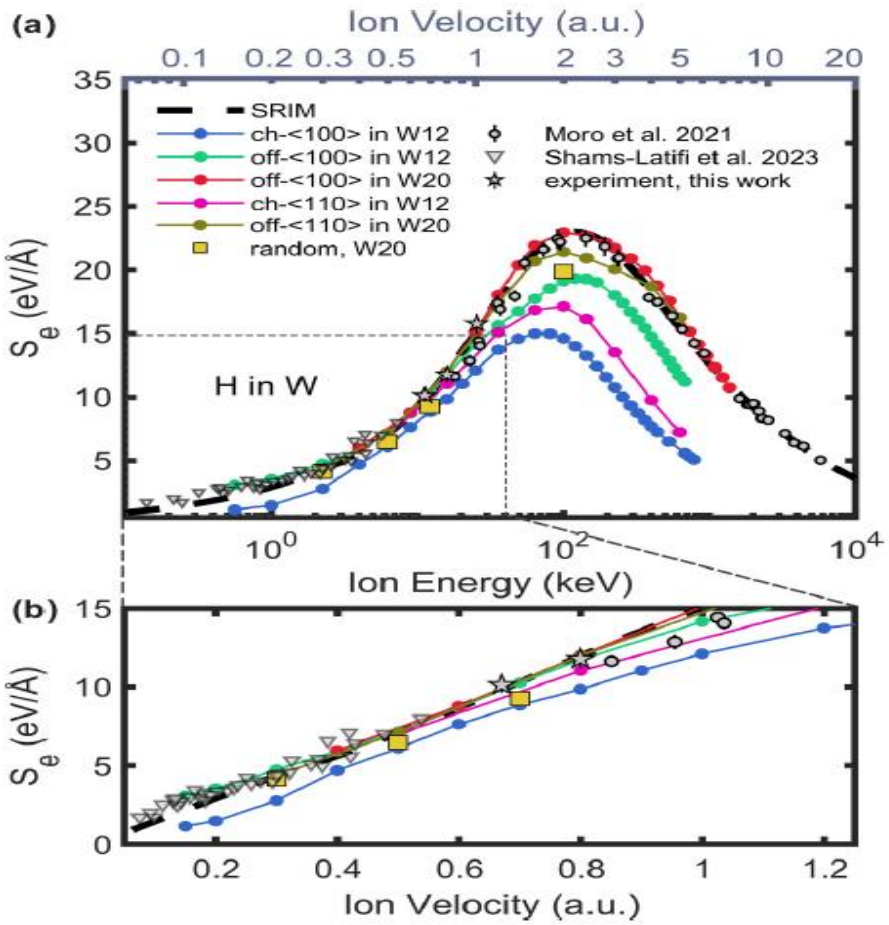

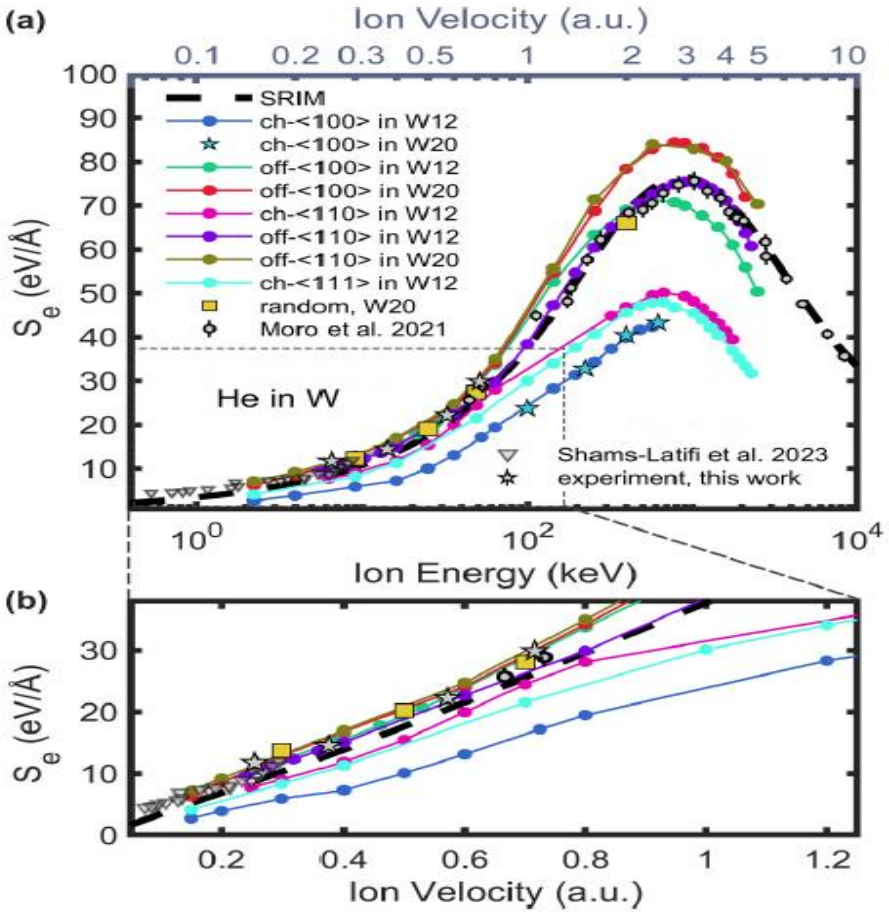

Magnetic cluster expansion for Fe-Cr

UK Atomic Energy Authority

PHYSICAL REVIEW B **81**, 184202 (2010)

Magnetic cluster expansion model for bcc-fcc transitions in Fe and Fe-Cr alloys

M. Yu. Lavrentiev, D. Nguyen-Manh, and S. L. Dudarev

$$E(\{\sigma_i\},\{\mathbf{M}_i\}) = NI^{(0)} + I^{(1)}\sum_i \sigma_i + \sum_{ij} I_{ij}^{(2)}\sigma_i\sigma_j$$

$$+ \sum_i \left(A^{(0)} + A^{(1)}\sigma_i + \sigma_i \sum_j A_{ij}^{(2)}\sigma_j \right) \mathbf{M}_i^2$$

$$+ \sum_i \left(B^{(0)} + B^{(1)}\sigma_i + \sigma_i \sum_j B_{ij}^{(2)}\sigma_j \right) \mathbf{M}_i^4$$

$$+ \sum_{ij} \left(J_{ij}^{(0)} + J_{ij}^{(1)}(\sigma_i + \sigma_j) + J_{ij}^{(2)}\sigma_i\sigma_j \right) \mathbf{M}_i \cdot \mathbf{M}_j .$$

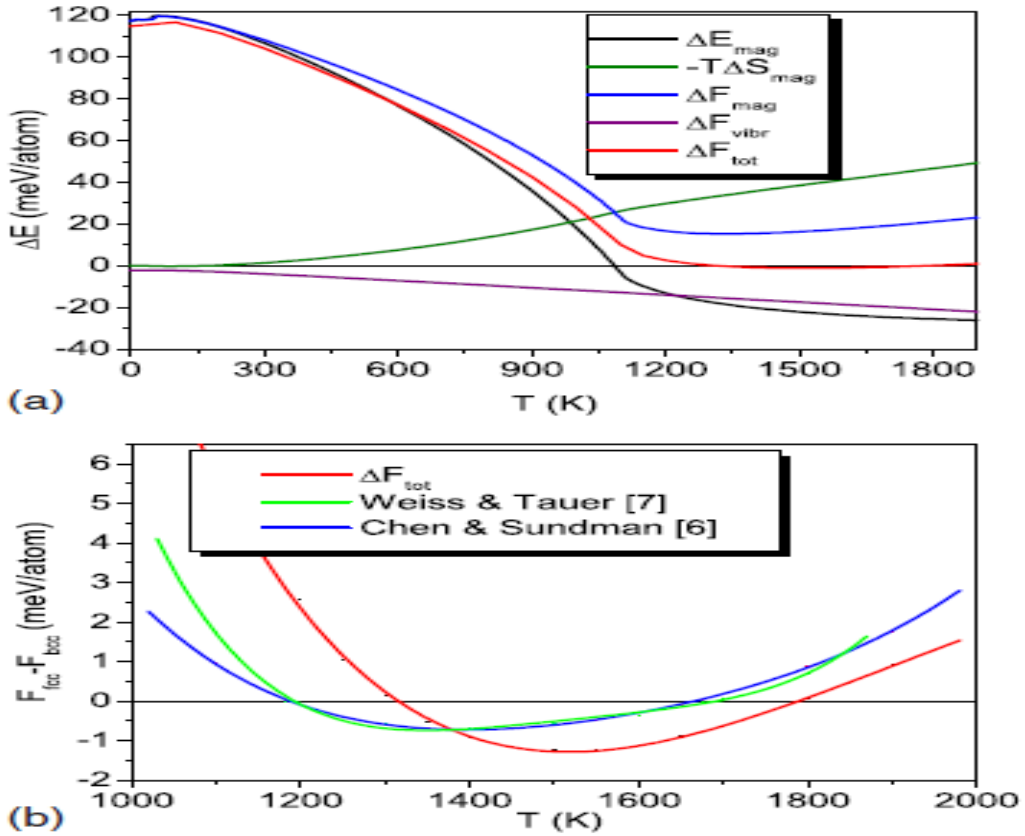

Magnetic machine learning potential: spin fluctuation effects at finite temperature

UK Atomic Energy Authority

scientific reports

OPEN

A machine-learned spin-lattice potential for dynamic simulations of defective magnetic iron

Jacob B. J. Chapman & Pui-Wai Ma

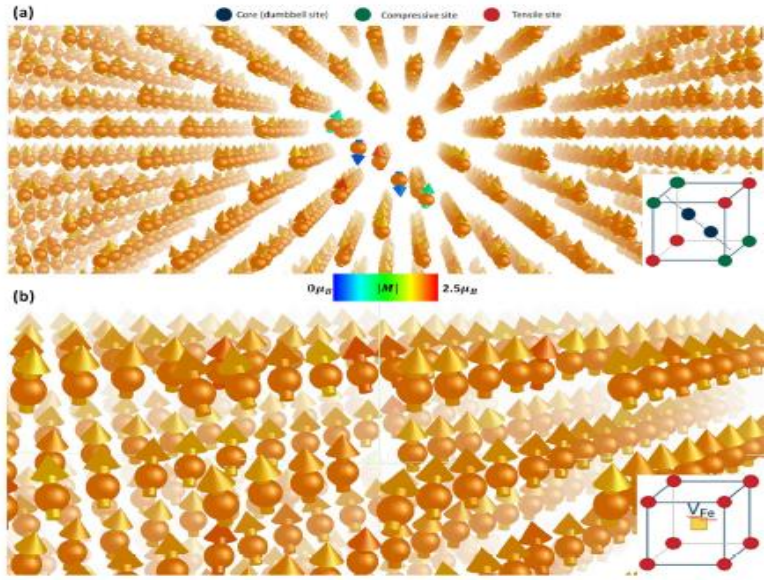

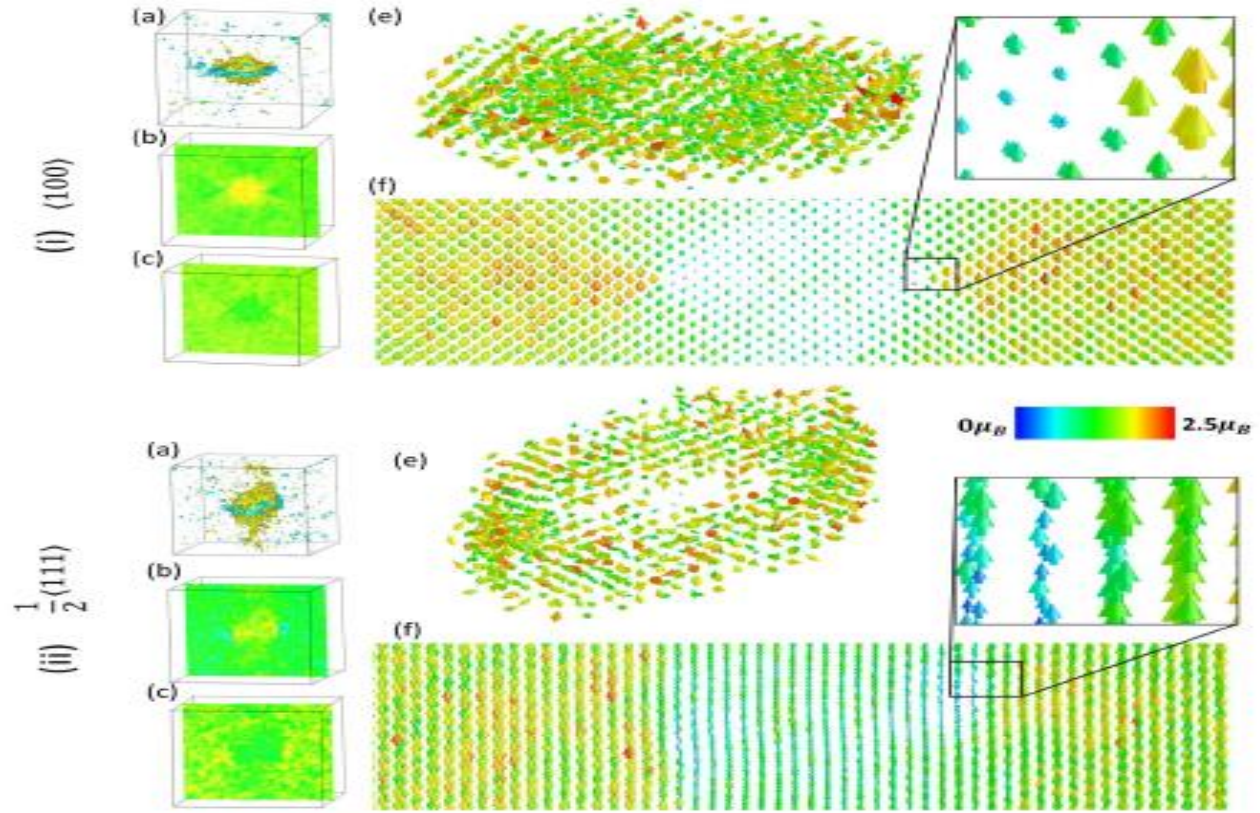

Figure 4. Spin-lattice dynamics simulations performed at 800 K for the (i) ⟨100⟩ and (ii) $\frac{1}{2}$⟨111⟩ interstitial dislocation loops. (**a**) The compressive and tensile stresses caused by the dislocations are shown via the isosurface of $\mathrm{Tr}(\langle\sigma_{ij}^{k}(t)\rangle)$, where $\langle\sigma_{ij}^{k}(t)\rangle$ is the time averaged Virial stress tensor of atom k. (**b**) 2D contour plot of $\mathrm{Tr}(\langle\sigma_{ij}^{k}(t)\rangle)$ through the (010) or (121) plane bisecting the centre of loop. (**c**) 2D contour plot of the magnetic moment magnitudes on the same plane as (**b**). (**d**) Sample of the instantaneous magnetic moments during dynamics of atoms in and near the dislocation loop. (**e**) Vector field representing the averaged magnetic moments near the loop.

First principles MD models of predicting threshold displacement energies in REBCO

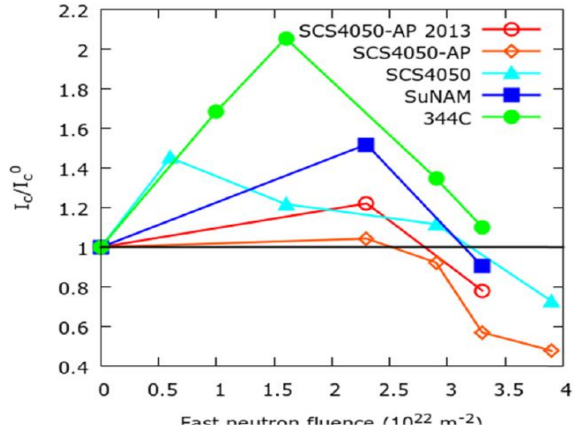

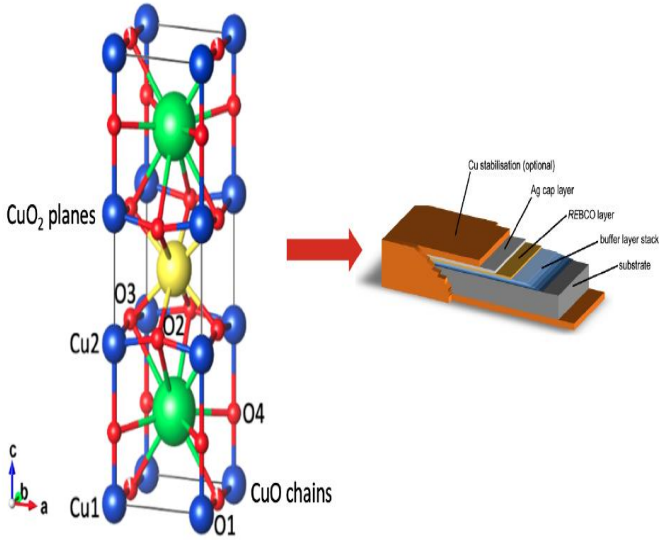

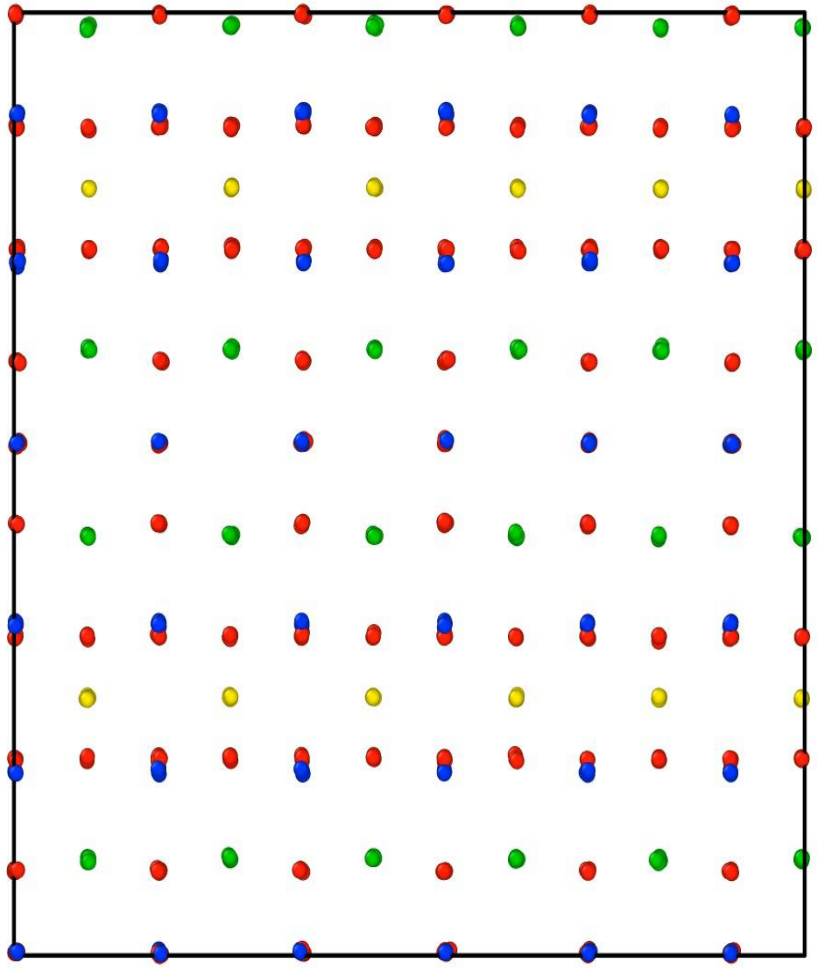

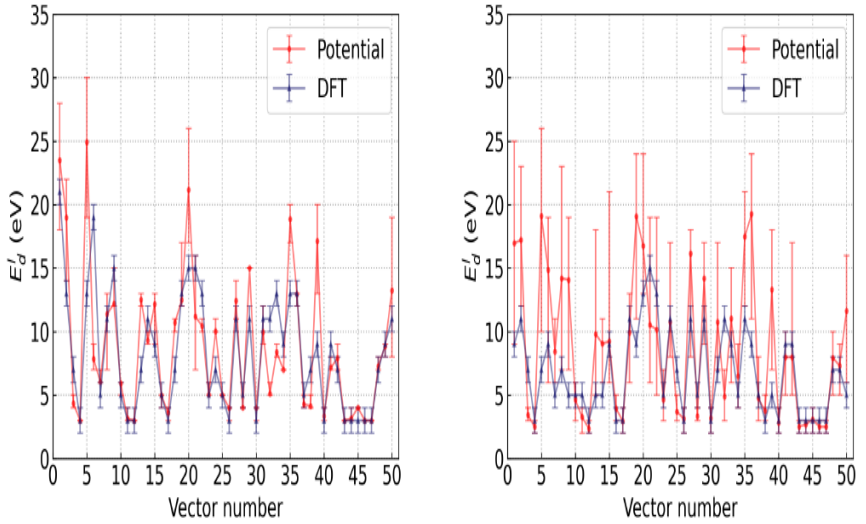

Comparison of TDE ($E_d^I(\phi,\theta)$) values from EP and DFT simulations at 25 K (left) and 360 K (right). Vector numbers correspond to one vector in a list of 50 random vectors. The error bars for the DFT results represent the PKA discretisation error, and the error bars for the potential represent the range of values obtained due to thermalisation.

- Directionally averaged TDE for the potential is 9.24 eV and 7.98 eV for 25 K and 360 K, respectively.
- Directionally averaged TDE for our DFT study is 7.88 eV and 7.25 eV for 25 K and 360 K, respectively.

Modelling of dissolution of precipitates in advanced RAFM steels using Universal MLIPs

UK Atomic Energy Authority

The Materials Project

Harnessing the power of supercomputing and state-of-the-art methods, the Materials Project provides open web-based access to computed information on known and predicted materials as well as powerful analysis tools to inspire and design novel materials.

The Materials Project by the numbers

MATERIALS	REGISTERED USERS
169,385	560,000+
INTERCALATION ELECTRODES	**CITATIONS**
4,678	42,000+
MOLECULES	**CPU HOURS/YEAR**
577,813	100 million

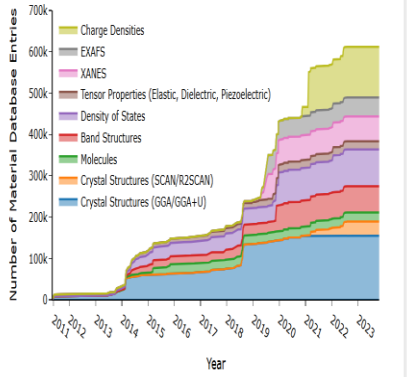

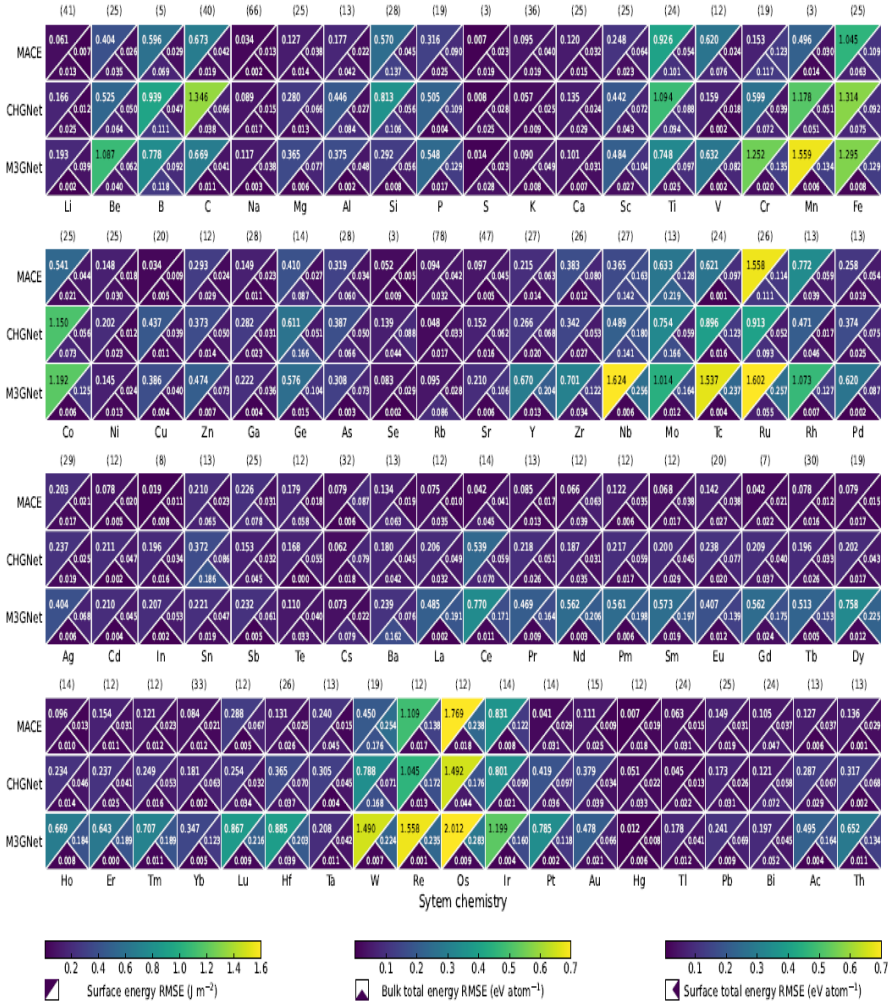

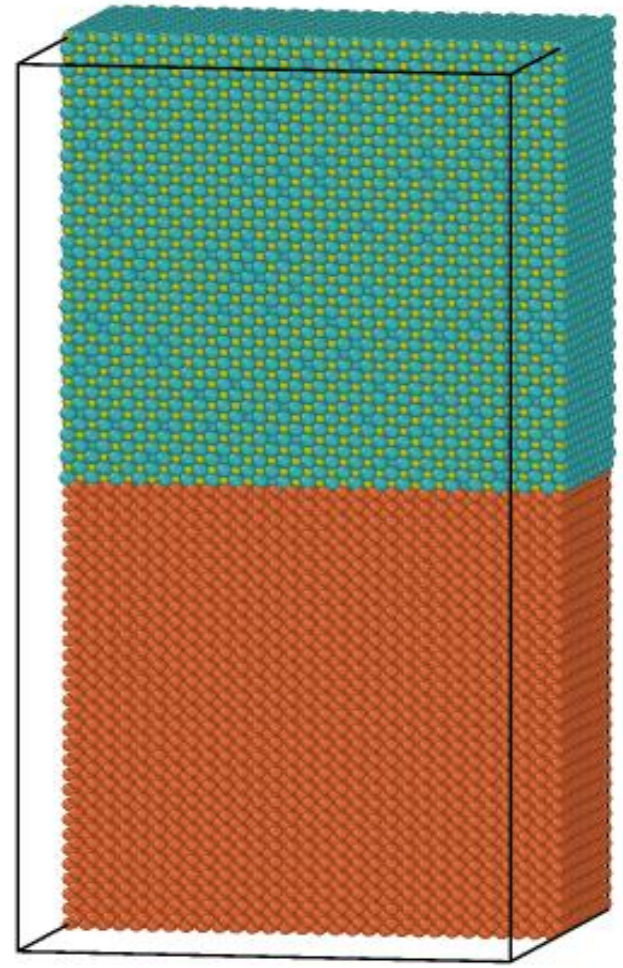

UK Atomic Energy Authority

Do you have any questions?

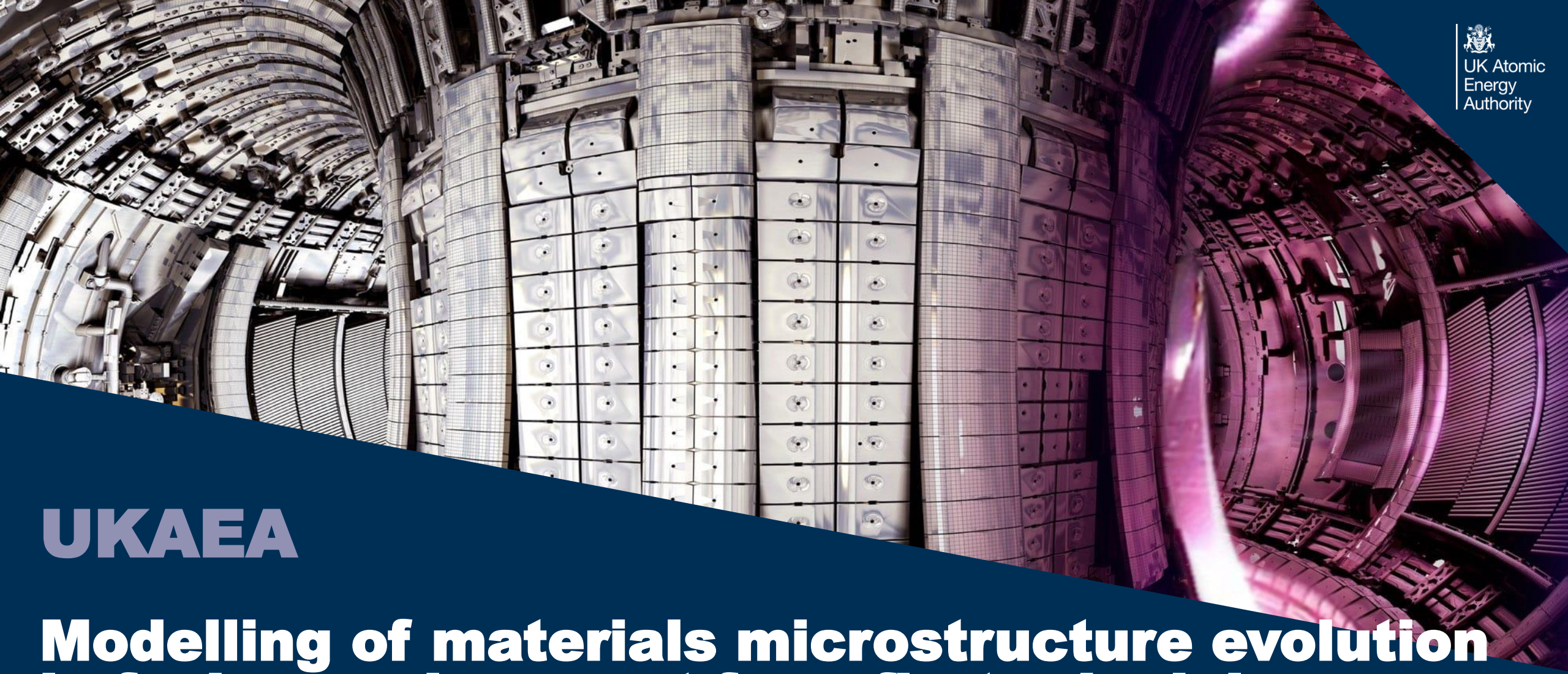

UK Atomic Energy Authority

UKAEA

Modelling of materials microstructure evolution in fusion environment from first principles

Duc Nguyen-Manh, Senior Research Scientist, Materials Division, UKAEA and Materials Department, University of Oxford, UK

Joint ICTP-IAEA-MAMBA School on Materials Irradiation: from Basics to Applications, Trieste, February 10-21, 2025

Composition stability of multi-component materials under irradiation

UK Atomic Energy Authority

Two conventional approaches to microstructure evolution modelling under irradiation

- **Conventional (deterministic) kinetic models**: The equilibrium phases are known a priori and will finally appear after long-time simulations involving nucleation, growth accelerated by irradiation diffusion
- **More general (statistical physics) models:** Predicting free-energy of various phases in presence of radiation induced defects (saturated vacancies and interstitials). The “final” steady-state configurations (microstructures) would be determined by minimisation of total free energy

To avoid uncertainties due complex microstructure in multi-component systems, the second approach using first-principles models

Evolutionary approach for determining first-principles Hamiltonian model of an alloy system: A genetic algorithm for construction of effective cluster interactions (ECIs). **Link to new development of MLPs descriptor: Atomic Cluster Expansion (ACE)**

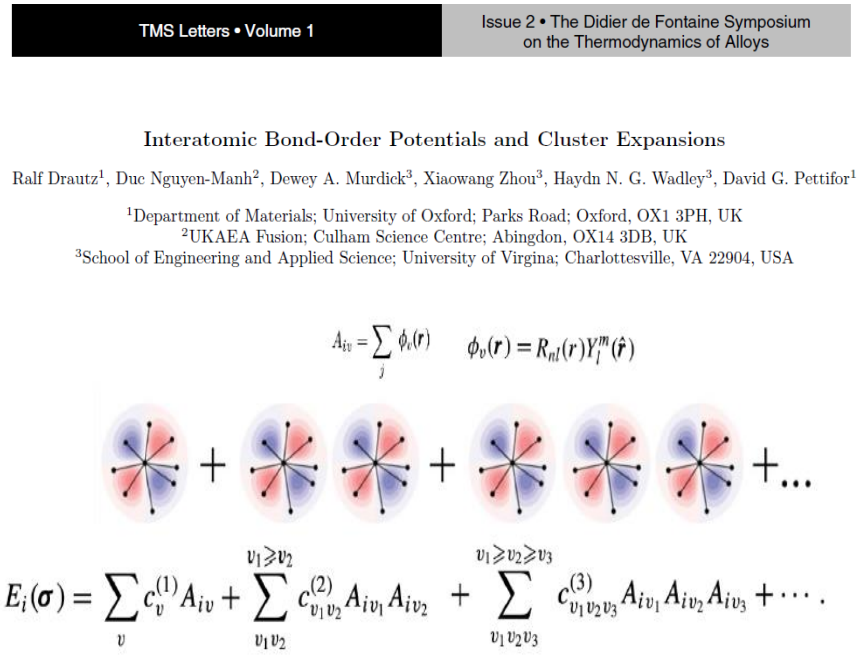
TMS Letters • Volume 1
Issue 2 • The Didier de Fontaine Symposium on the Thermodynamics of Alloys

Interatomic Bond-Order Potentials and Cluster Expansions

Ralf Drautz[1], Duc Nguyen-Manh[2], Dewey A. Murdick[3], Xiaowang Zhou[3], Haydn N. G. Wadley[3], David G. Pettifor[1]

[1]Department of Materials; University of Oxford; Parks Road; Oxford, OX1 3PH, UK
[2]UKAEA Fusion; Culham Science Centre; Abingdon, OX14 3DB, UK
[3]School of Engineering and Applied Science; University of Virgina; Charlottesville, VA 22904, USA

$$A_{iv} = \sum_j \phi_v(\mathbf{r}) \qquad \phi_v(\mathbf{r}) = R_{nl}(r) Y_l^m(\hat{\mathbf{r}})$$

$$E_i(\sigma) = \sum_v c_v^{(1)} A_{iv} + \sum_{v_1 \gtrless v_2}^{v_1 v_2} c_{v_1 v_2}^{(2)} A_{iv_1} A_{iv_2} + \sum_{v_1 \gtrless v_2 \gtrless v_3}^{v_1 v_2 v_3} c_{v_1 v_2 v_3}^{(3)} A_{iv_1} A_{iv_2} A_{iv_3} + \cdots .$$

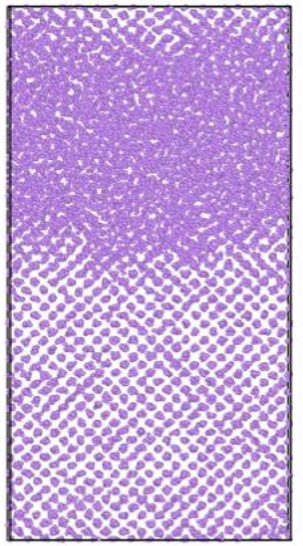

Prediction of melting temperature

Cluster expansion Hamiltonians for multi-component systems from matrix formulation

UK Atomic Energy Authority

Article

Configurational Entropy in Multicomponent Alloys: Matrix Formulation from Ab Initio Based Hamiltonian and Application to the FCC Cr-Fe-Mn-Ni System

Antonio Fernández-Caballero [1,2], Mark Fedorov [3], Jan S. Wróbel [3], Paul M. Mummery [1] and Duc Nguyen-Manh [2,*]

- Matrix formulation within orthro-normal basic sets of point functions
- Average over cluster configurations are obtained from symmetry independent correlation function
- General expression of configuration entropy

$$\Delta H^{CEH}_{mix}(\vec{\sigma}) = \sum_{\omega,n,s} J^{(s)}_{\omega,n} m^{(s)}_{\omega,n} \langle \Gamma^{(s')}_{\omega',n'}(\vec{\sigma}) \rangle_{\omega,n,s},$$

$$\langle \Gamma^{(s')}_{\omega',n'}[\vec{\sigma}] \rangle_{\omega,n,(s)} = \langle \gamma_{j_1,K}[\sigma_1]\gamma_{j_2,K}[\sigma_2]\cdots\gamma_{j_\omega,K}[\sigma_\omega] \rangle$$

$$= \frac{1}{\Omega[\omega,n]} \sum_{u=1}^{\Omega[\omega,n]} \gamma_{j_1,K}[\sigma_{\overrightarrow{(\omega,n)}_{u_1}}]\gamma_{j_2,K}[\sigma_{\overrightarrow{(\omega,n)}_{u_2}}]\cdots\gamma_{j_\omega,K}[\sigma_{\overrightarrow{(\omega,n)}_{u_\omega}}],$$

$$\gamma_{j,K}[\sigma_i] = \begin{cases} 1, & \text{if } j = 0, \\ -\cos\left(2\pi\lceil\frac{j}{2}\rceil\frac{\sigma_i}{K}\right), & \text{if } j > 0 \text{ and odd}, \\ -\sin\left(2\pi\lceil\frac{j}{2}\rceil\frac{\sigma_i}{K}\right), & \text{if } j > 0 \text{ and even}, \end{cases} \qquad (\tau_K^{-1})_{ij} = \begin{cases} \frac{1}{K}, & \text{if } j = 0, \\ -\frac{2}{K}\cos\left(2\pi\lceil\frac{j}{2}\rceil\frac{\sigma_i}{K}\right), & \text{if } j > 0 \text{ and } j-1 < K \text{ and j odd}, \\ -\frac{2}{K}\sin\left(2\pi\lceil\frac{j}{2}\rceil\frac{\sigma_i}{K}\right), & \text{if } j > 0 \text{ and j even}, \\ -\frac{1}{K}\cos\left(2\pi\lceil\frac{j}{2}\rceil\frac{\sigma_i}{K}\right), & \text{if } j-1 = K \text{ and j odd}. \end{cases}$$

$$S_{\omega,n}[\vec{\sigma}] \equiv \sum_{i=1}^{s[\omega,n]} \eta_{\omega_i,n_i} \tilde{S}_{\omega_i,n_i}[\vec{\sigma}] = \sum_{i=1}^{s[\omega,n]} \eta_{\omega_i,n_i} \sum_{\forall[(pq\cdots)_{\omega_i,n_i}]}^{K^{\omega_i}} k_B y^{(pq\cdots)_{\omega_i,n_i}}_{\omega_i,n_i}[\vec{\sigma}] ln\left(y^{(pq\cdots)_{\omega_i,n_i}}_{\omega_i,n_i}[\vec{\sigma}]\right),$$

Phase stability in compositionally complex and multi-component system: Short-range order (SRO) concept

UK Atomic Energy Authority

J. Phase Equilib. Diffus. (2017) 38:391–403
DOI 10.1007/s11669-017-0582-3

Short-Range Order in High Entropy Alloys: Theoretical Formulation and Application to Mo-Nb-Ta-V-W System

A. Fernández-Caballero[1,2] · J. S. Wróbel[3] · P. M. Mummery[2] · D. Nguyen-Manh[1]

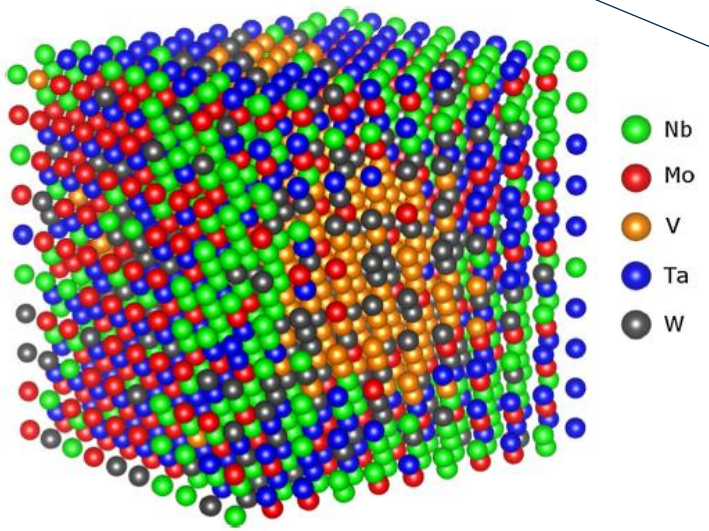

Fig. 2 Atomistic configuration for equimolar Mo-Nb-V-Ta-W HEAs obtained from the present MC simulations at 400 K (Color figure online)

Revisited configuration entropy from Cluster Expansion Method

PHYSICAL REVIEW MATERIALS **5**, 065401 (2021)

First-principles model for voids decorated by transmutation solutes: Short-range order effects and application to neutron irradiated tungsten

Duc Nguyen-Manh[1,2,*] Jan S. Wróbel[3] Michael Klimenkov[4] Matthew J. Lloyd[2] Luca Messina[5] and Sergei L. Dudarev[1,2]

$$y_{\omega,n}^{(AB\cdots)} = \overbrace{(\bar{\bar{\tau}}_K^{-1} \otimes \cdots \otimes \bar{\bar{\tau}}_K^{-1})}^{\omega}{}_{AB\cdots,ij\cdots} \langle \Gamma_{\omega,n}^{(ij\cdots)} \rangle$$

Cluster probabilities and correlation functions

$$\alpha_{2,n}^{AB} = 1 - \frac{\sum_s (\bar{\bar{\tau}}_K^{-1} \otimes \bar{\bar{\tau}}_K^{-1})_{A,B,(s)} \langle \Gamma_{2,n}^{(s)} \rangle}{\left(\sum_s (\bar{\bar{\tau}}_K^{-1})_{A,(s)} \langle \Gamma_{1,1}^{(s)} \rangle\right)\left(\sum_s (\bar{\bar{\tau}}_K^{-1})_{B,(s)} \langle \Gamma_{1,1}^{(s)} \rangle\right)}.$$

$$S_{conf}[T] = \int_0^T \frac{C_{conf}(T')}{T'} dT' = \int_0^T \frac{\langle [\Delta H_{mix}^{CEH}(T')]^2 \rangle - \langle [\Delta H_{mix}^{CEH}(T')] \rangle^2}{T'^3} dT',$$

Issues with tungsten as the plasma facing and structural materials for fusion decices

UK Atomic Energy Authority

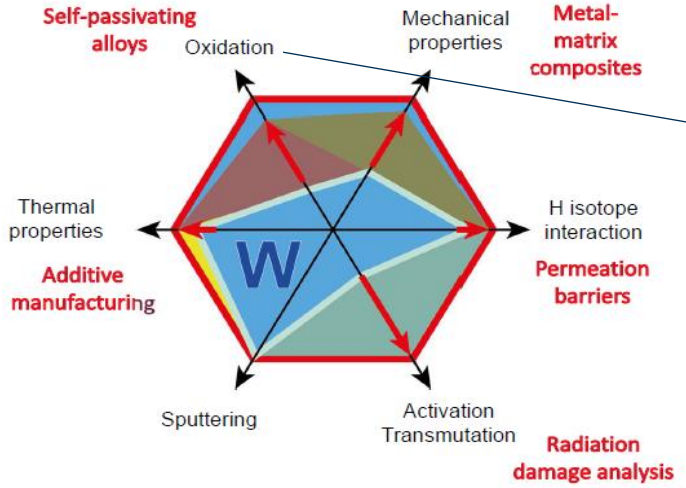

UKAEA is particularly interested in

- First-principles modelling of SMART composition stability: W-Cr-Y-Zr-O
- In-situ environmental STEM oxidation study of SMART
- H/D/T permeation, retention) in SMART materials
- Correlation APT/TEM/EELS
- Neutronics, safety of the plant

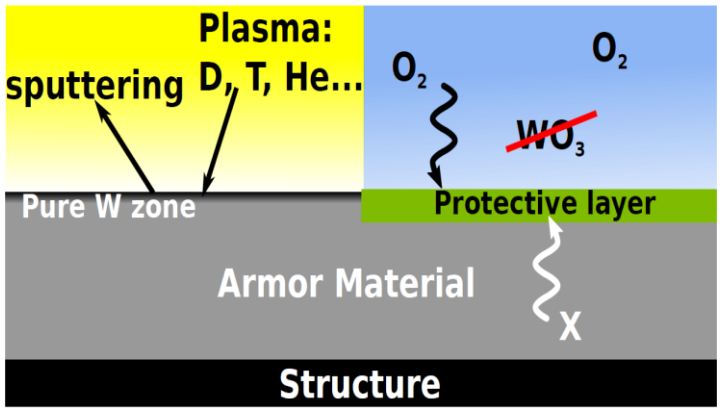

J. Coenen, AEM, 22 (2020) 1901326

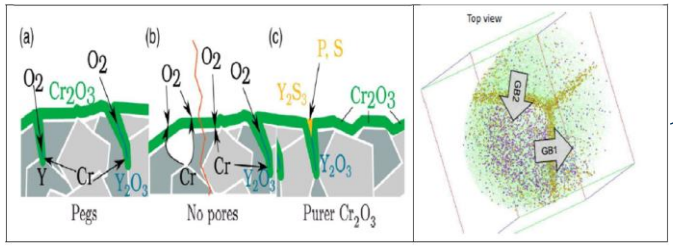

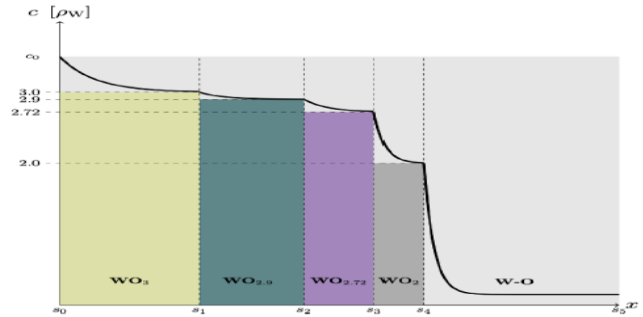

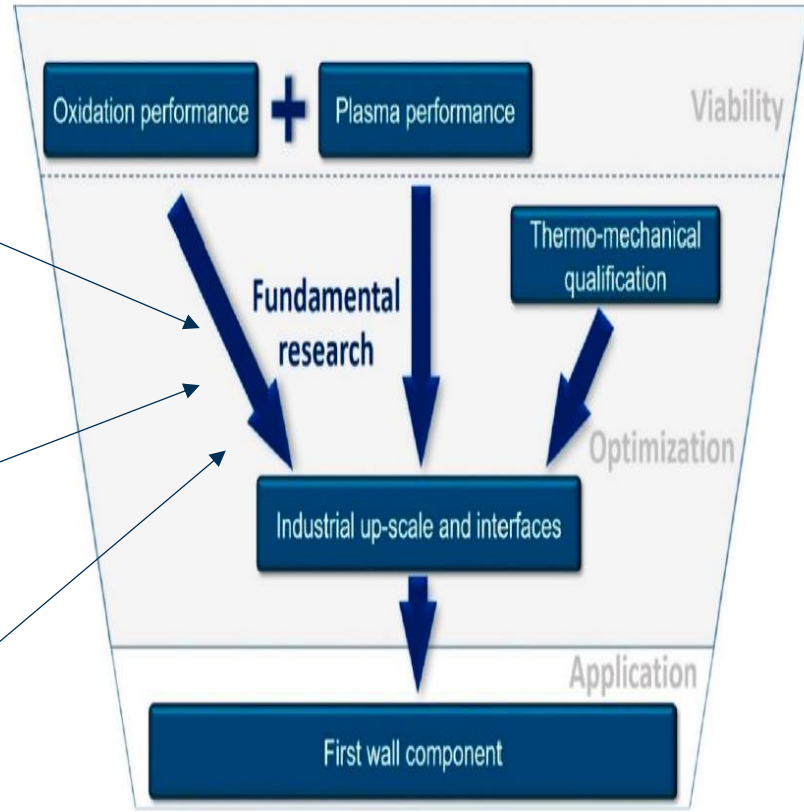

Figure 1. A structure of the research and development program on SMART materials.

A. Litnovsky et al. , Metals, 5 (2020) 1255

Exchange Monte Carlo method of co-segregation in W-Cr-Y-Zr alloys

UK Atomic Energy Authority

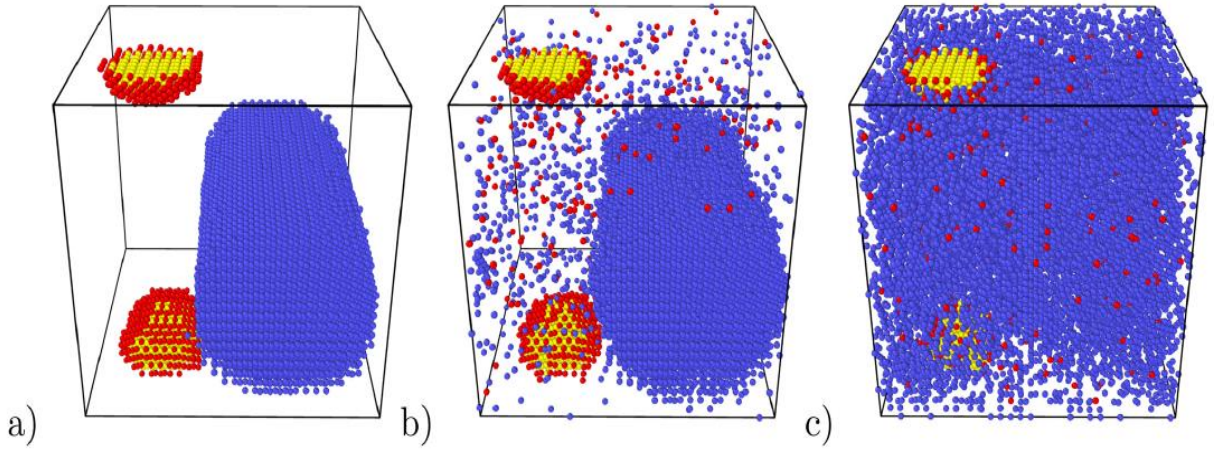

Fig. 9. Structure images for $W_{70}Cr_{28}Y_1Zr_1$ alloy at a) 300 K, b) 1000 K and c) 1800 K. W atoms were removed from the image for better visualization of the cluster of Cr (blue), Y (yellow) and Zr (red) atoms.

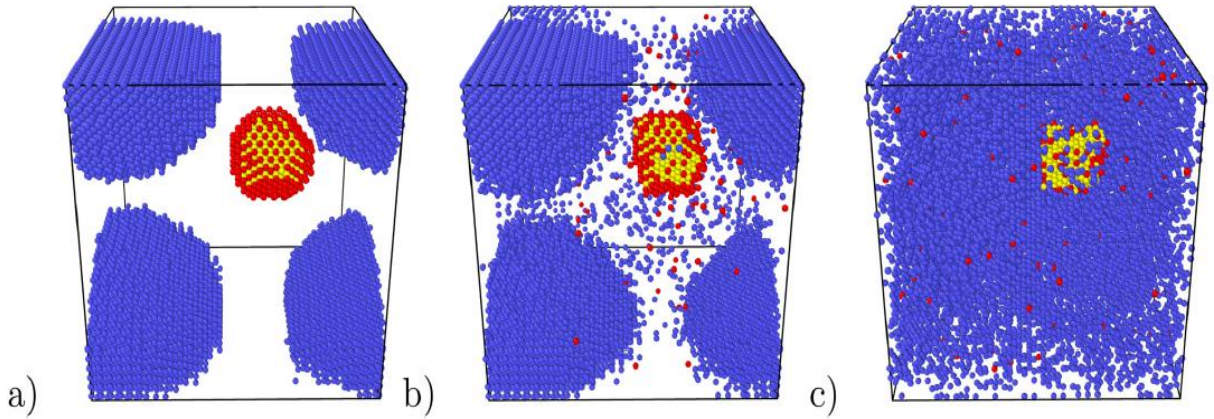

Fig. 10. Structure images for $W_{70}Cr_{29}Y_{0.5}Zr_{0.5}$ alloy at a) 400 K, b) 1000 K and c) 1800 K. W atoms were removed from the image for better visualization of the cluster of Cr (blue), Y (yellow) and Zr (red) atoms.

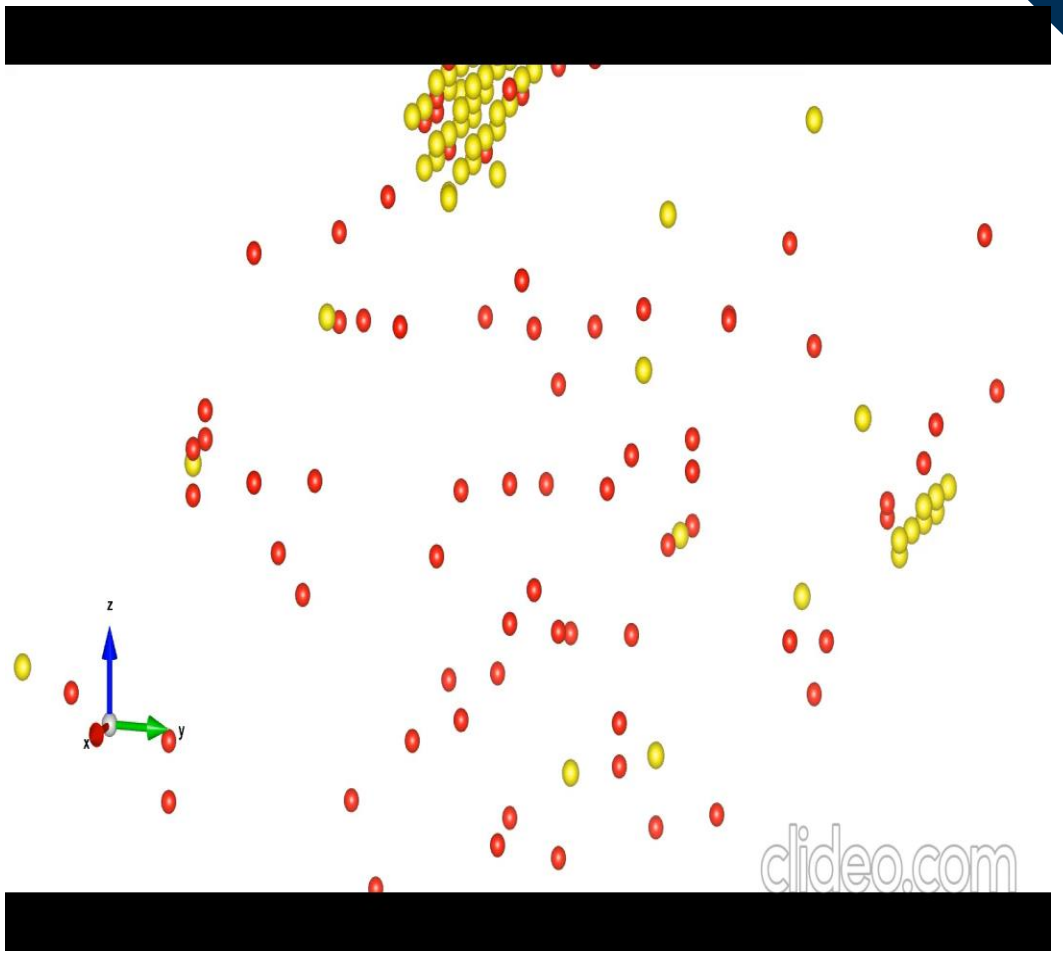

Spinodal decomposition (SD) vs. Standard microstructures in SMART W-Cr-Y-Zr materials

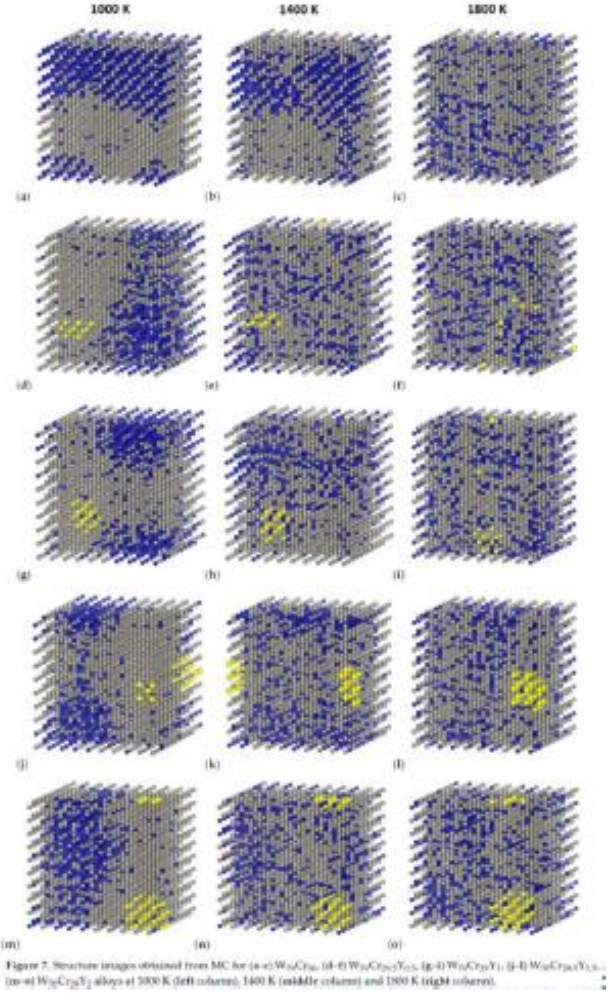

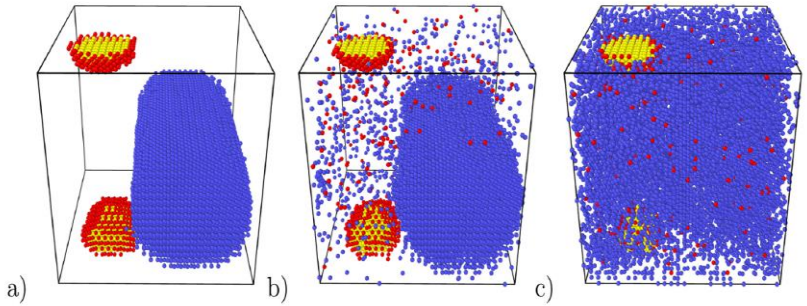

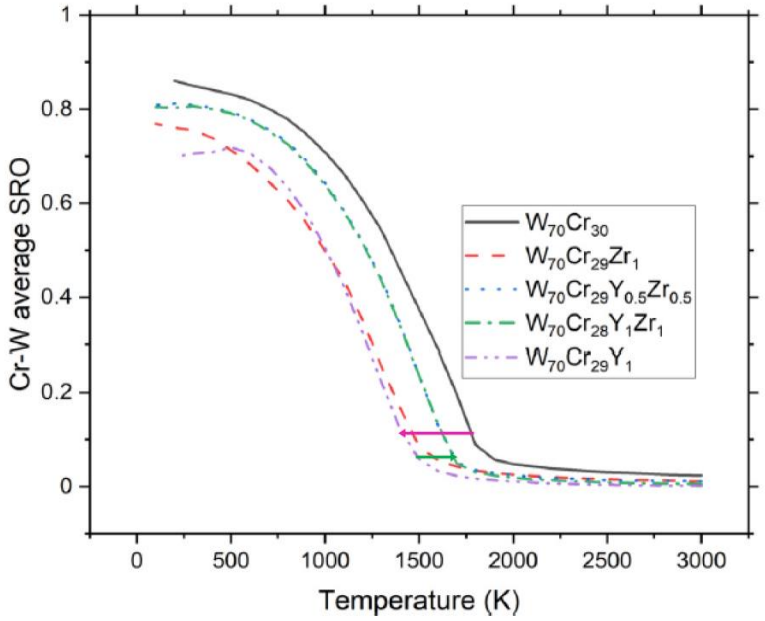

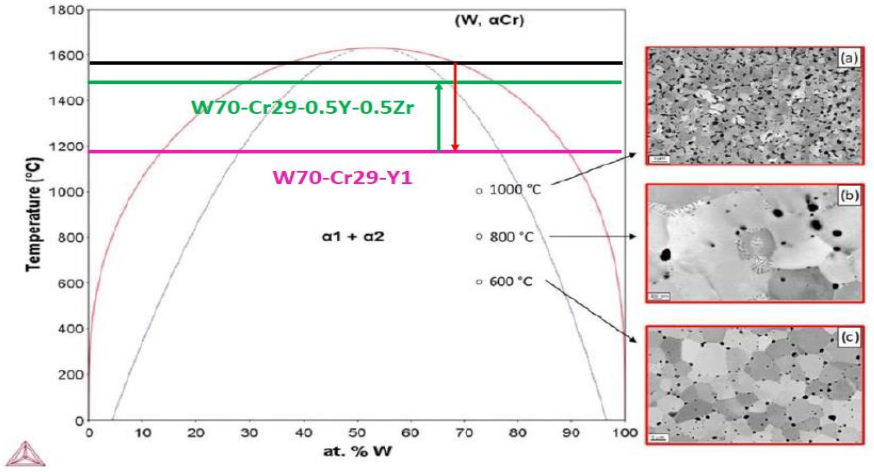

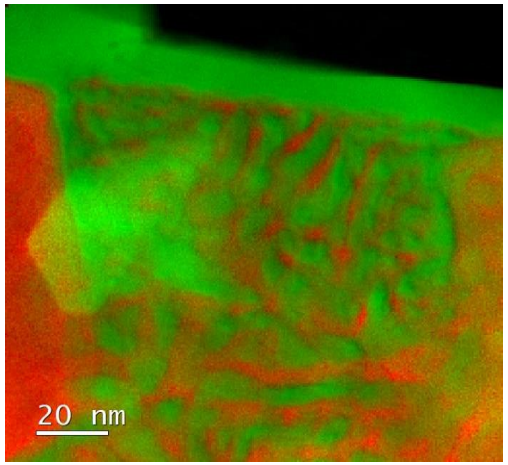

Cr
W

Cr-W phase separation observed during annealing

DNM, 2023 EUROfusion report, D. Sobieraj et al., JAMS, 2 (2023) 100011

Microstructures of SMART (Self-passivating Metallic Alloys with Reduced Thermo-oxidation) materials

UK Atomic Energy Authority

Before 2023

New microstructural optimisation after 2023 (WPMAT/HHFM. EUROfusion)

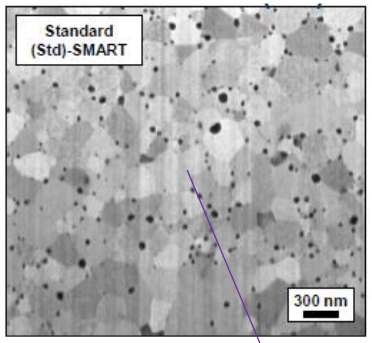

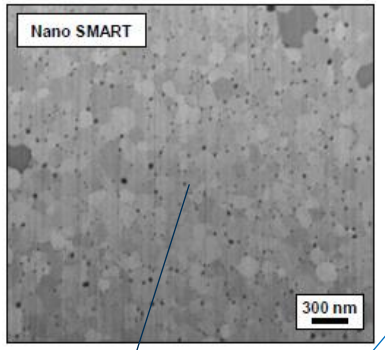

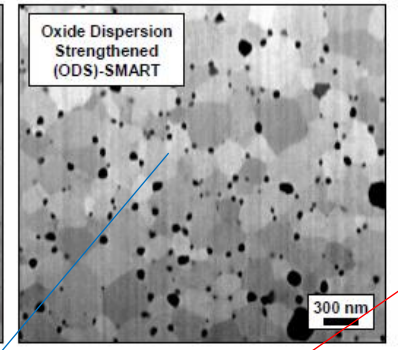

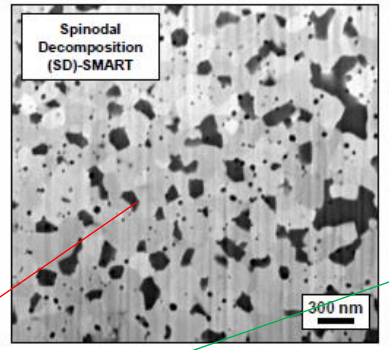

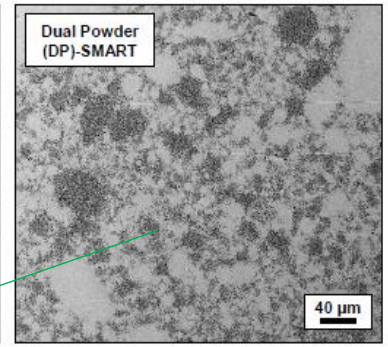

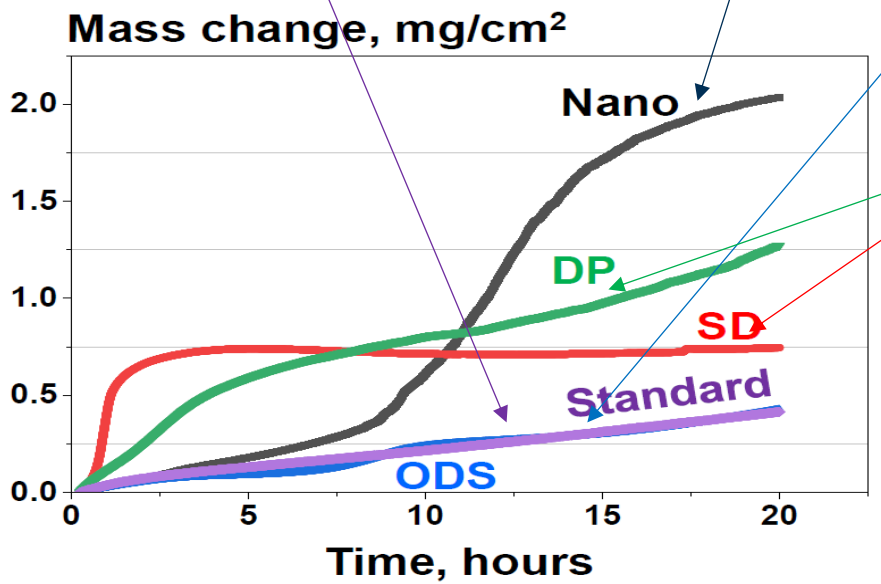

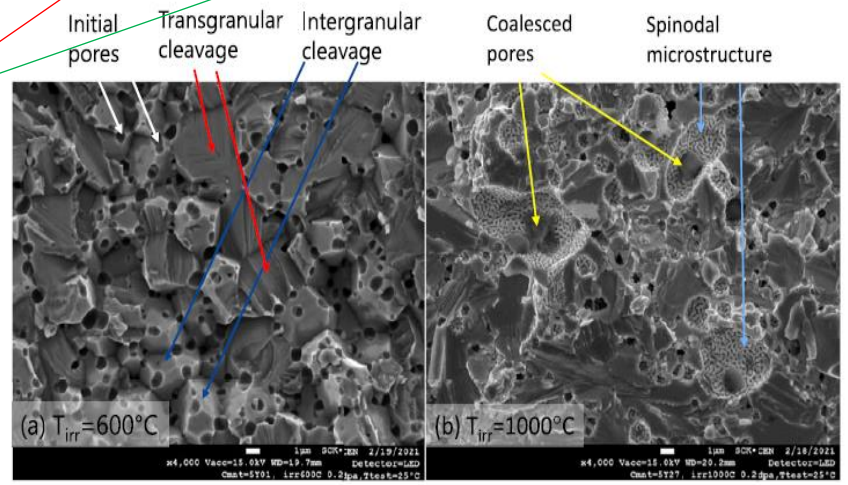

Microstructure of SMART W-Cr-Y under oxidation conditions, J. Chen et al., NME, 41 (2024) 101762; Metals, 14 (2024) 1092

Radiation damage in W: Loops, voids & transmutation induced precipitation under neutron irradiation

UK Atomic Energy Authority

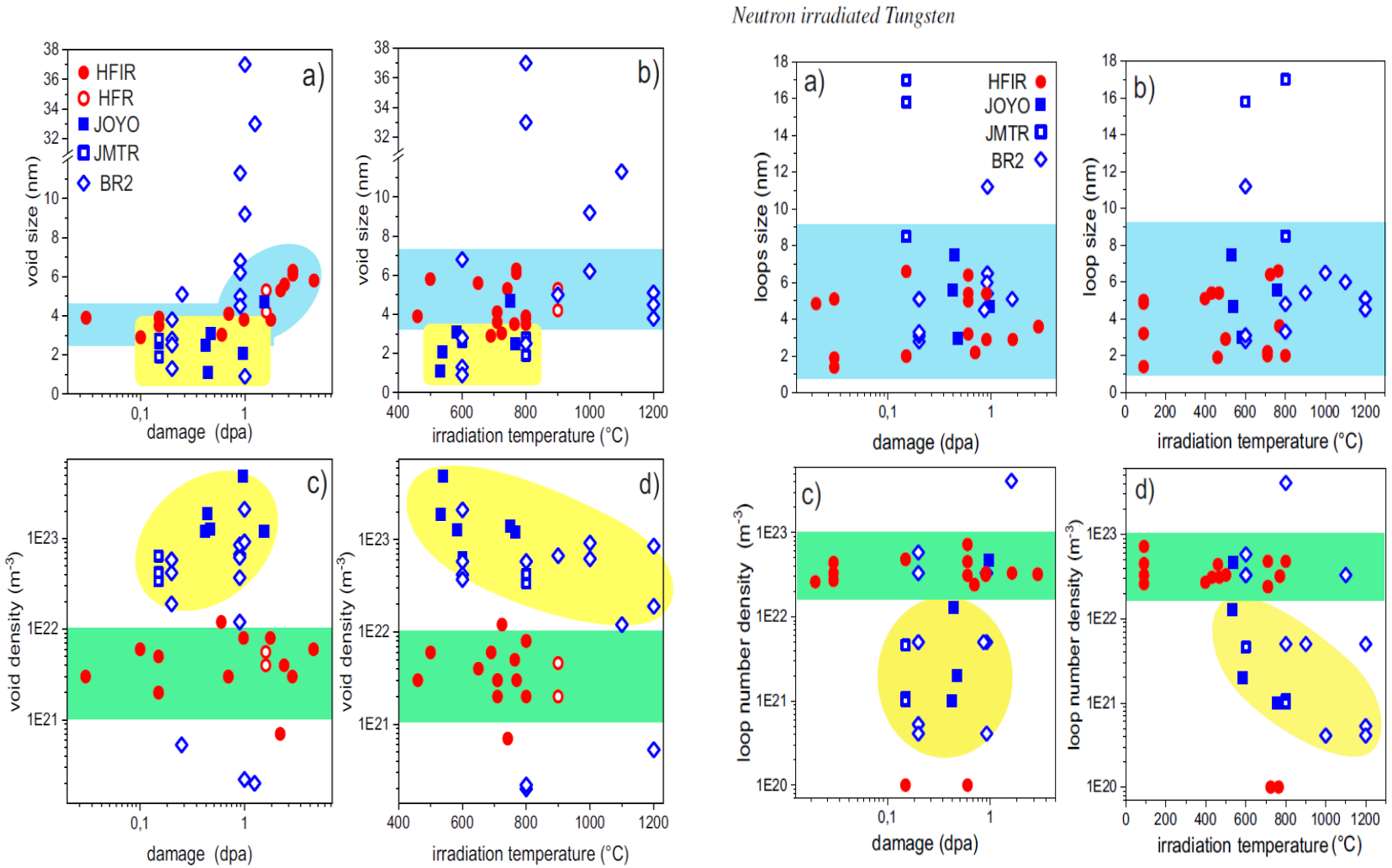

DNM, M. Klimenkov et al. , in preparation (2024)

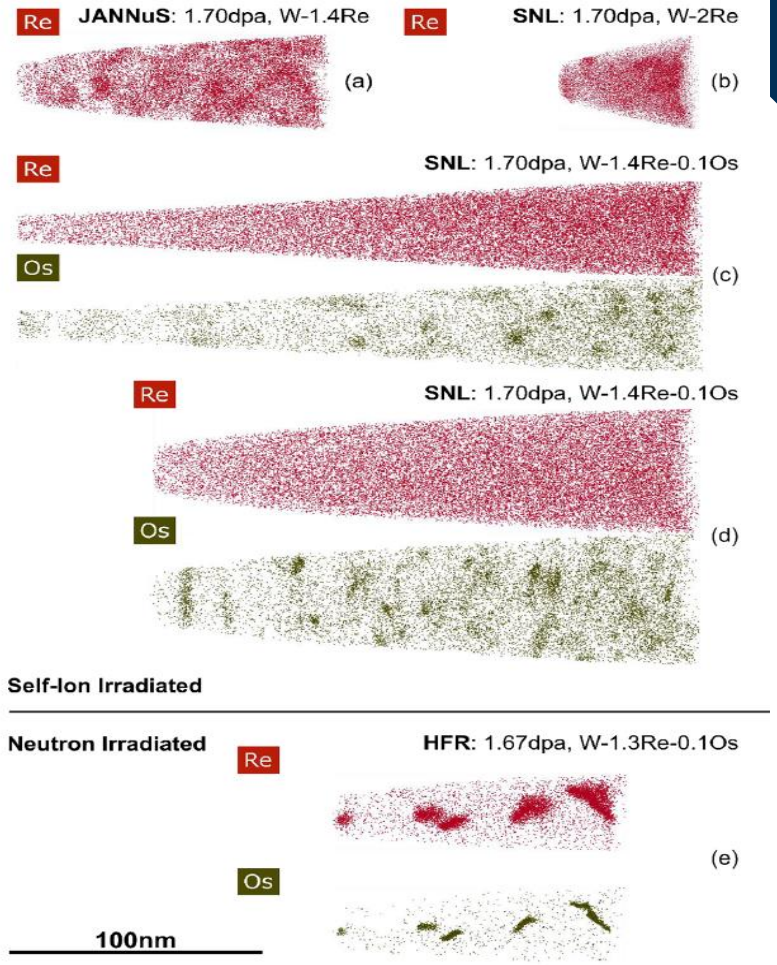

M.J. Lloyd et al.., Materialia (2024)

Modelling validation by APT and TEM experimental observations

Sample	Re (at.%)	Os (at.%)	Ta (at.%)
Single Crystal	1.26 ± 0.15	0.08 ± 0.02	0.01 ± 0.01
Polycrystalline	1.09 ± 0.07	0.08 ± 0.02	0.01 ± 0.01
FISPACT-II	1.4	0.1	0.02
EDX [9]	1.2	0.1	Undetectable

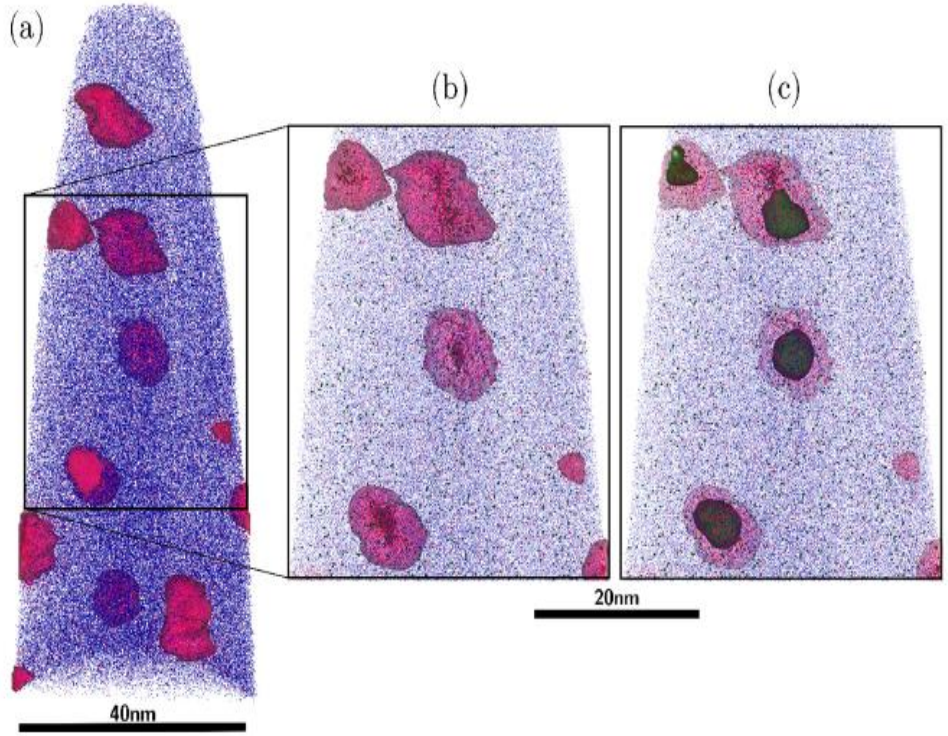

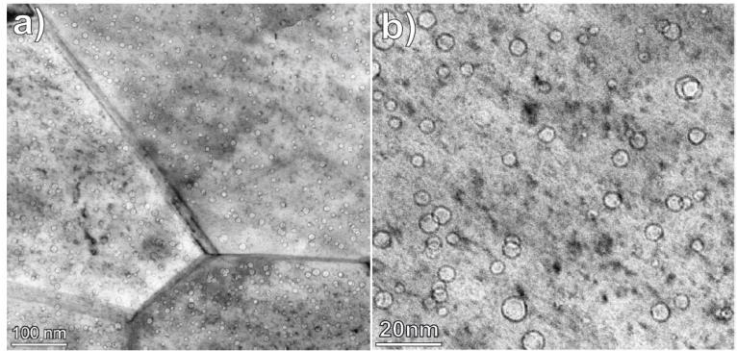

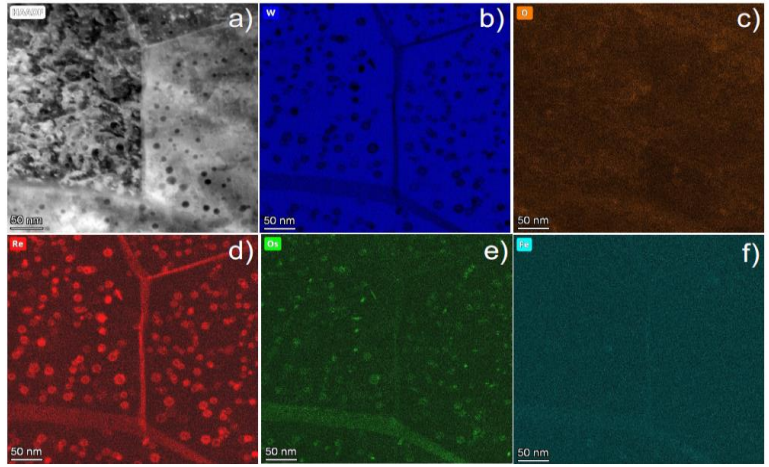

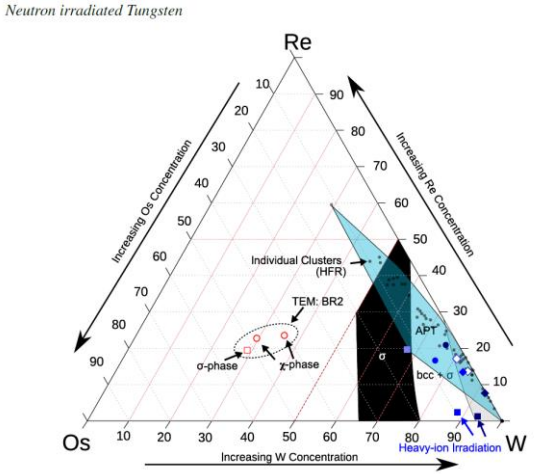

◇ **HFR:** Neutron Irradiated Pure-W, 1.67dpa, T_i = 1173K, W-1.2Re-0.1Os (Single Cystal)
◇ **HFR:** Neutron Irradiated Pure-W, 1.67dpa, T_i = 1173K, W-1.2Re-0.1Os
▮ **Surrey:** Ion Irradiated, 18dpa, Ti = 773K, W-1Re-1Os
◆ **Joyo:** Neutron Irradiated Pure-W, 0.96dpa, Ti = 811K, W-0.5Re
● **Joyo:** Neutron Irradiated W-10Re, 0.96dpa, Ti = 811K, W-9.3Re-0.5Os
◆ **HFIR:** Neutron Irradiated Pure-W, 0.90dpa, Ti = 773K, W-4.0Re-0.8Os
● **HFIR:** Neutron Irradiated W-10Re, 0.90dpa, Ti =773K, W-9.6Re-2.1Os
▮ **SNL:** Ion Irradiated, 1.70dpa, Ti = 1173K, W-1.4Re-0.1Os
▮ **HFIR:** Neutron Irradiated Pure-W, 1.80dpa, Ti = 1043K, W-6.38Re-3.23Os
○ **BR2:** Neutron Irradiated Pure-W, 1.25dpa, T_i = 1073K, W-2Re-0.2Os, χ-phase
□ **BR2:** Neutron Irradiated Pure-W, 1.25dpa, T_i = 1073K, W-2Re-0.2Os, σ-phase

DNM et al. Phys. Rev. Mater., 5 (2021) 065401; M. Klimenkov, Sci. Reports (2022), M. Lloyd Materialia (2023, 2024)

Effective Cluster Interactions in W-Re-Os-Vacancy system

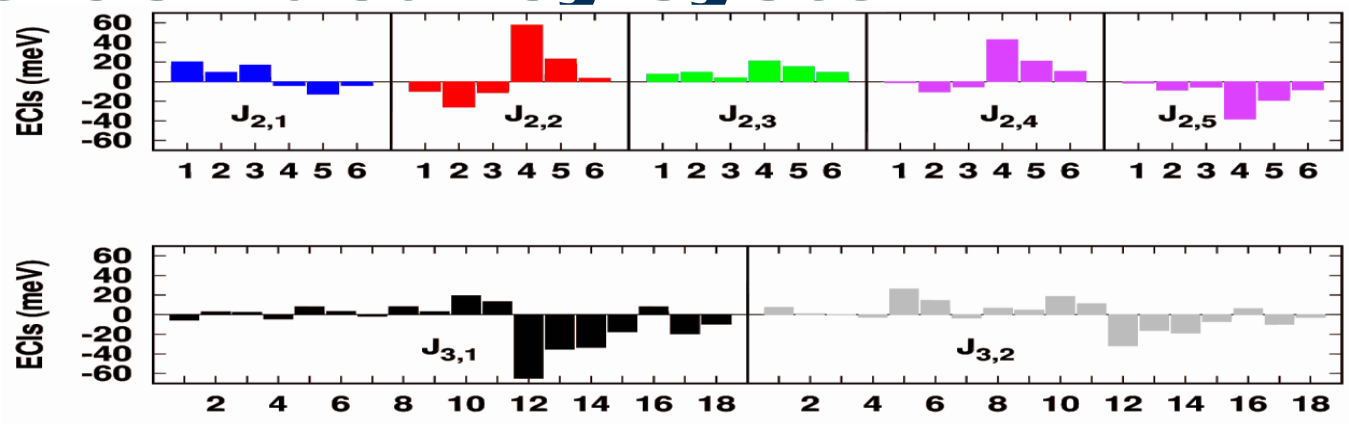

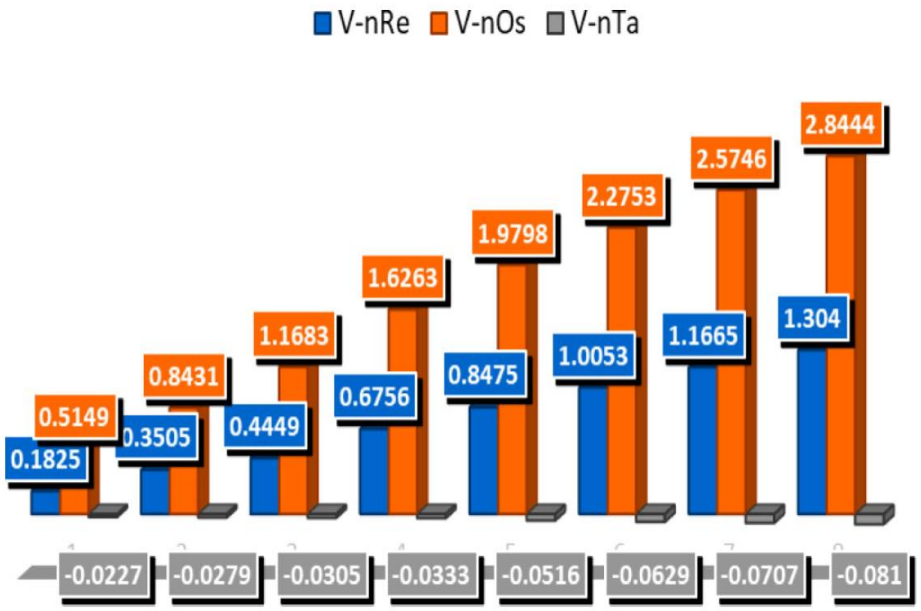

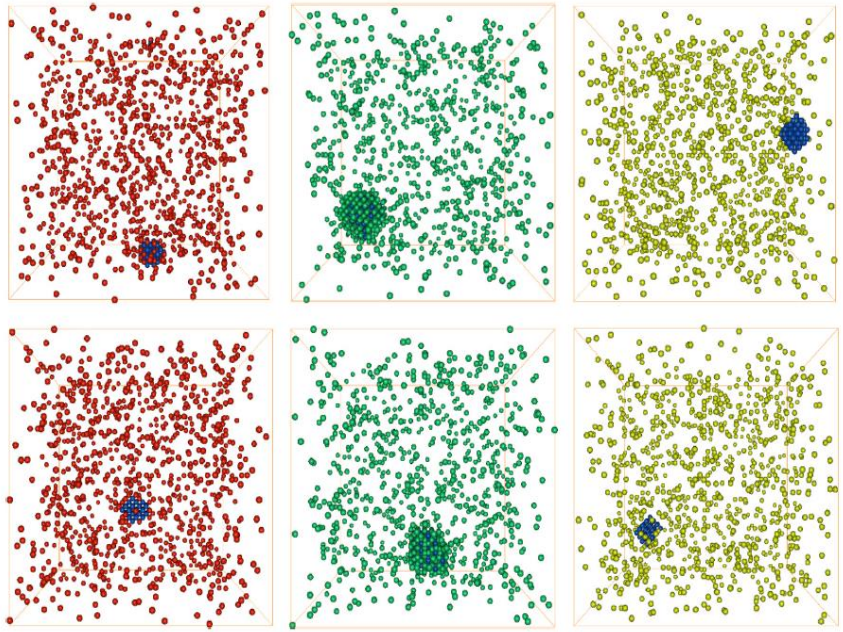

DFT data base of vacancy-solutes clusters

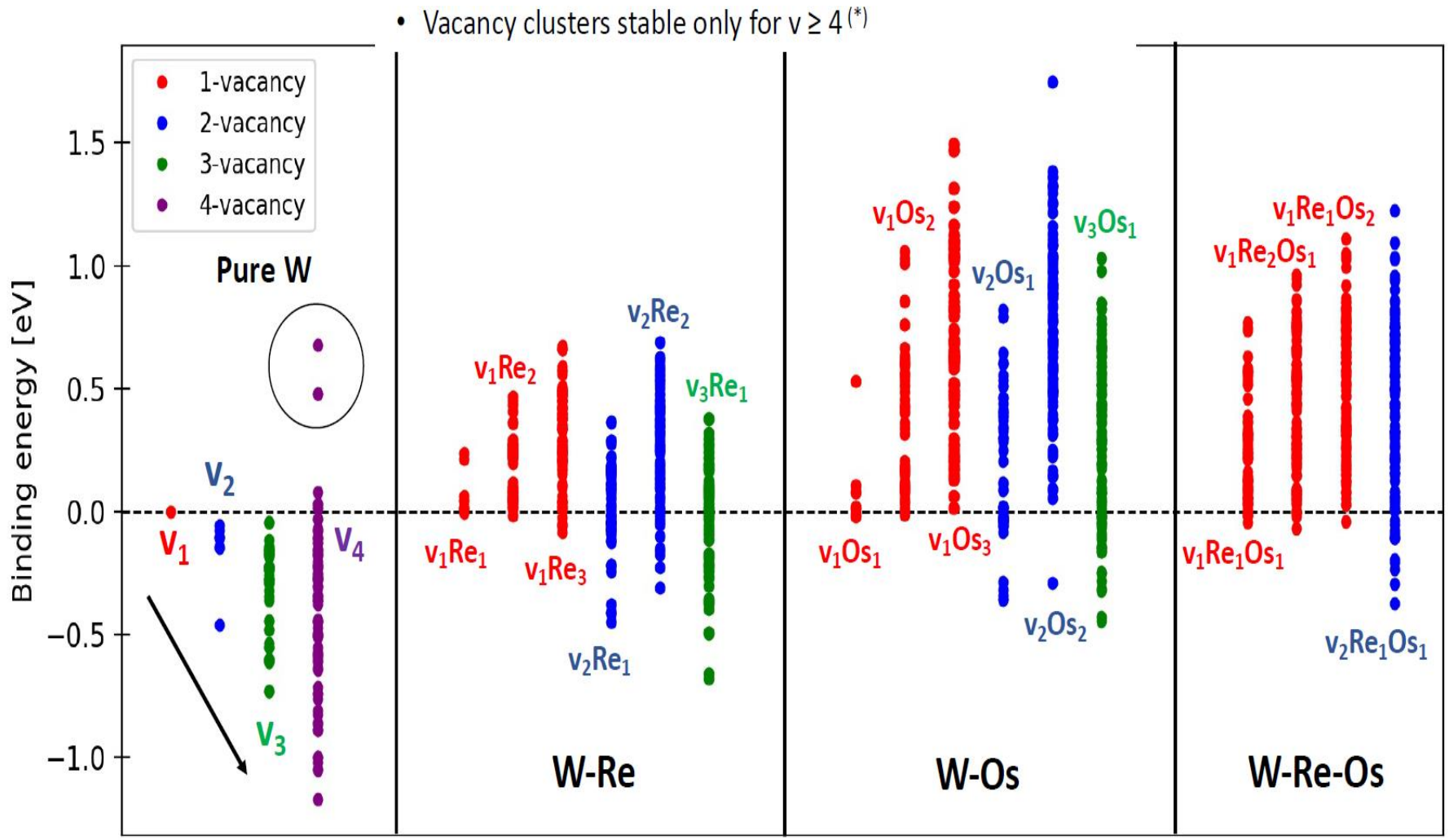

Predicted of facetted voids oriented along the (110) directions in neutron irradiated W

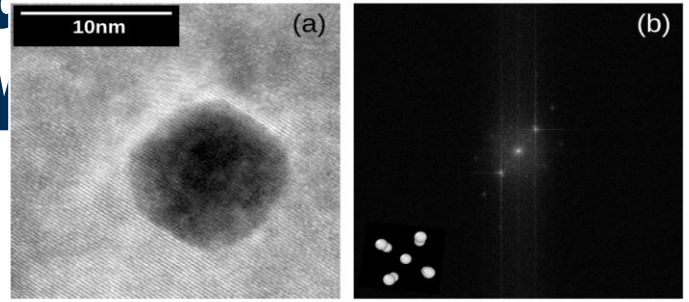

Figure 3.24: (a) High magnification HAADF image of a void in the single crystal neutron irradiated sample with (b) corresponding Fast-Fourier Transform (FFT) image showing the orientation of the void facets, which are aligned along the (110) directions.

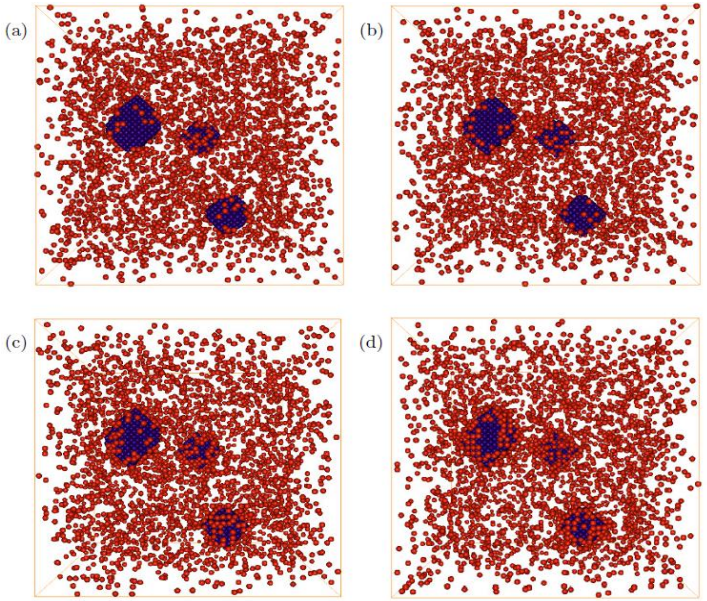

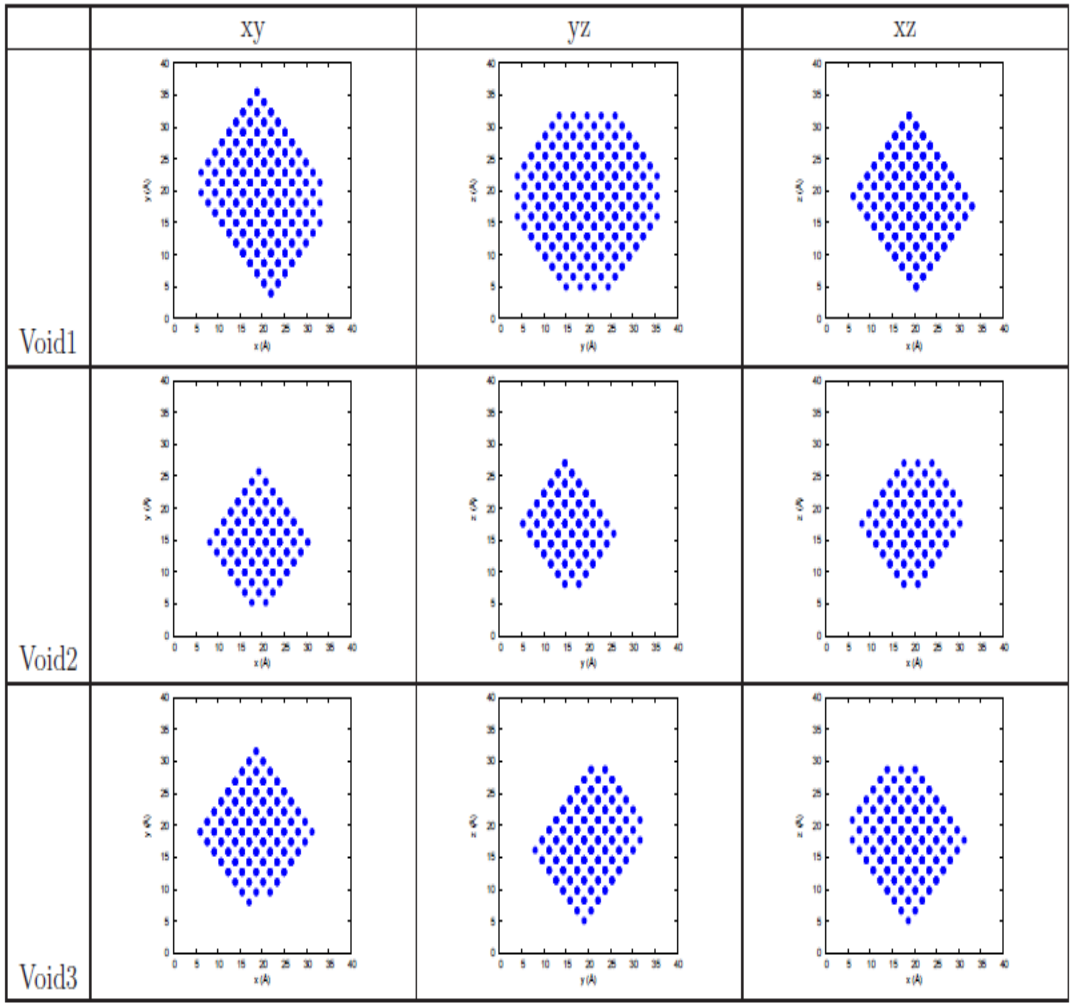

Application: Transmutation-induced void decorated by Re-Os SRO in neutron irradiated W

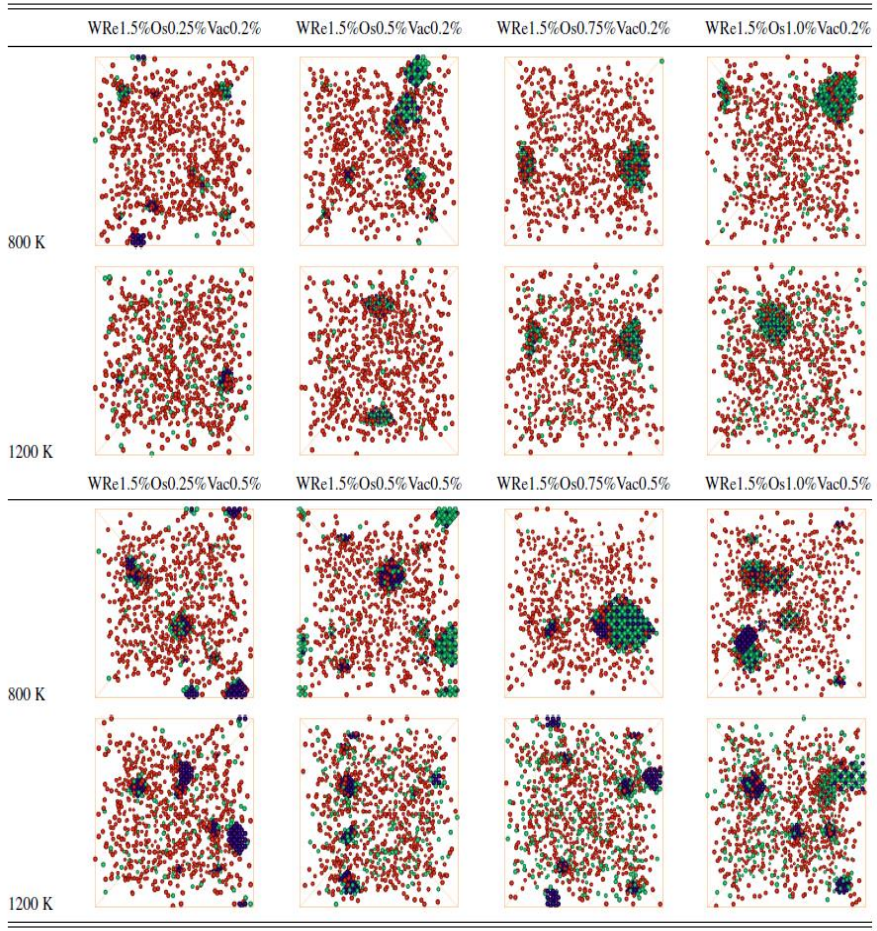

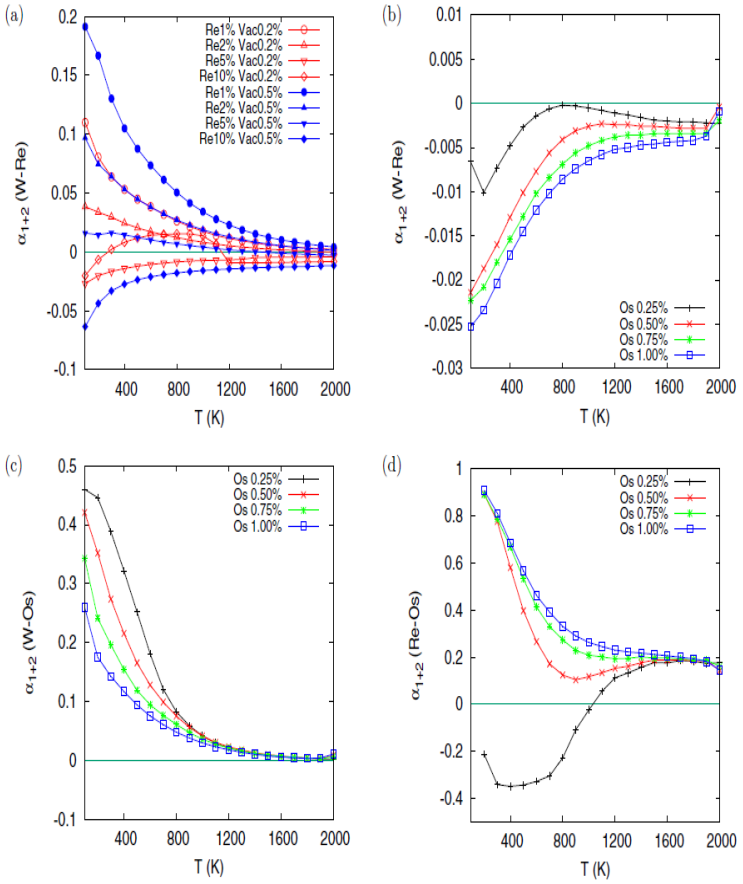

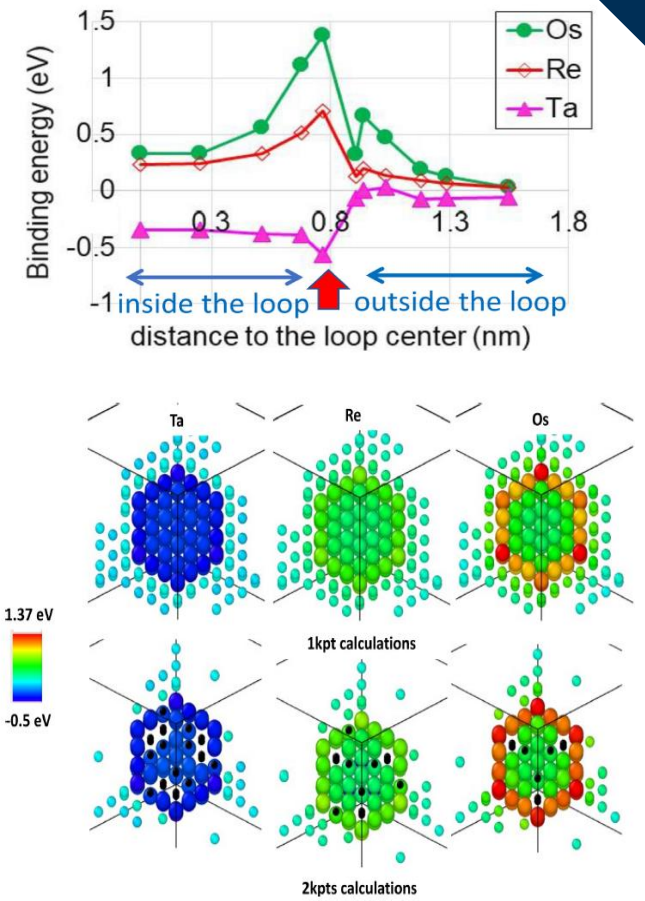

DNM et al. Phys. Rev. Mater., 5 (2021) 065401; M. Lloyd et al. , Materialia (2023, 2024)

Kinetic Monte-Carlo method using migration energies from first principles

UK Atomic Energy Authority

Table 1. Possible events within the KMC and SGMC models. Lattice sites are designated as follows: V = Vacancy, A,B = Atoms, AA = SIA, AB = Mixed Interstitial, S = Sink Site.

	Vacancies	Interstitals	Instantaneous	Deposition
KMC	V+A → A+V V+B → B+V	AA+A → A+AA AB+A → A+AB AB+B → B+AB AA⟨111⟩ → AA⟨111⟩ AB⟨111⟩ → AB⟨111⟩	AA+V → A+A AB+V → A+B AA+B → AB+A AA+S → A+S V+S → A+S AB+S → B+S	A → AA+V B → AB+V
SGMC	V+A → A+V V+B → B+V	AA+A → A+AA AB+A → A+AB AB+B → B+AB		A → B B → A

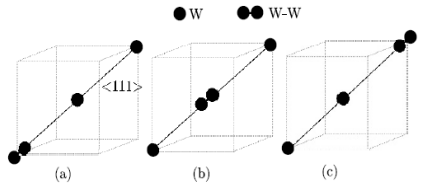

Fig. 1. Schematic diagram of the migration pathway for a se interstitial dumbbell in W, oriented along the [111] directio Reproduced from [20].

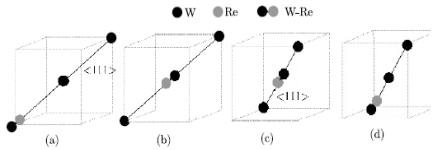

Fig. 2. Schematic diagram showing the migration pathway f the W-Re mixed interstitial dumbbell in W. In the case of tl mixed dumbbell, migration occurs through a series of rotatic and translation events, which from (a) to (d) effectively resul in a migration along the [100] direction. Reproduced from [2

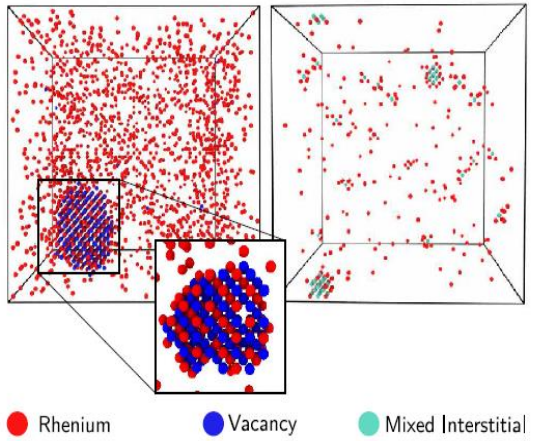

Fig. 4. Equilibriated configurations of W-Re-Vacancy and W-Re-Interstitial for a fixed starting defect concentration and change in chemical potential, $\Delta\mu$.

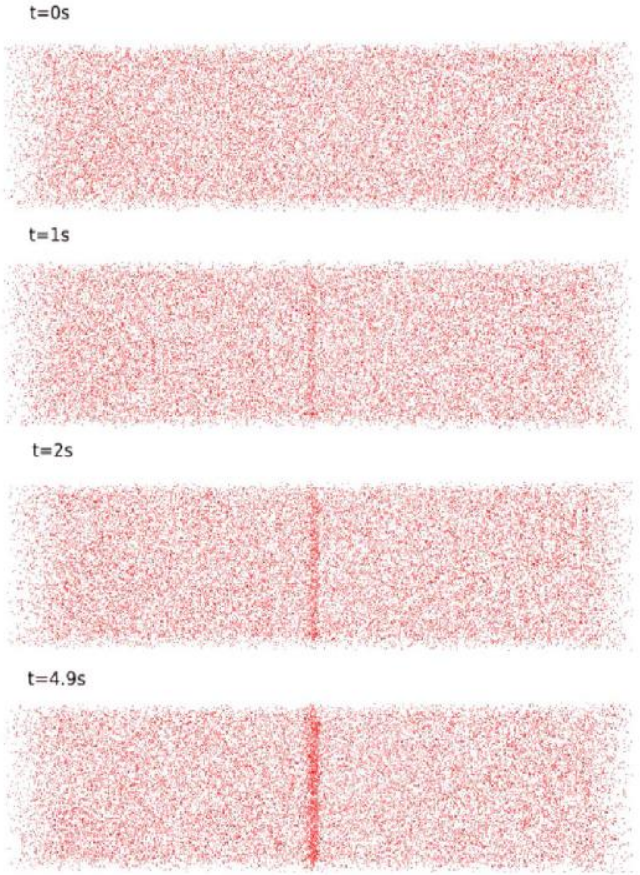

Fig. 10. Segregation of Re in a 1.4 at.%Re allot to a planar ideal sink at 1800 K after a total dose of 5.96×10^{-3} dpa with a dose rate of 1.19×10^{-3} dpa/s.

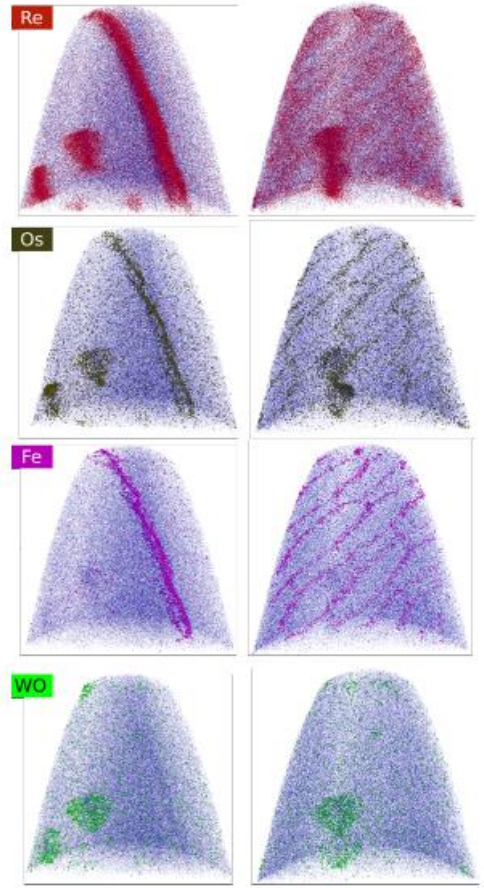

Radiation induced rich-Cr clustering in Fe-3Cr alloys due to SRO effect with C & N

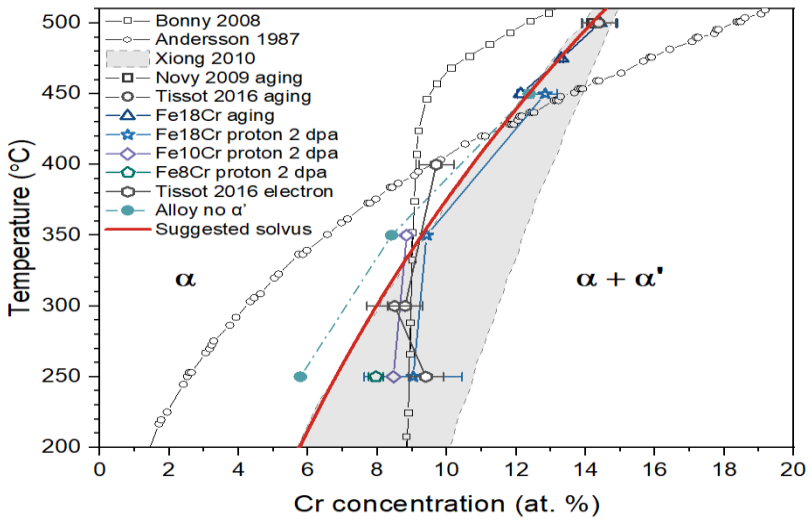

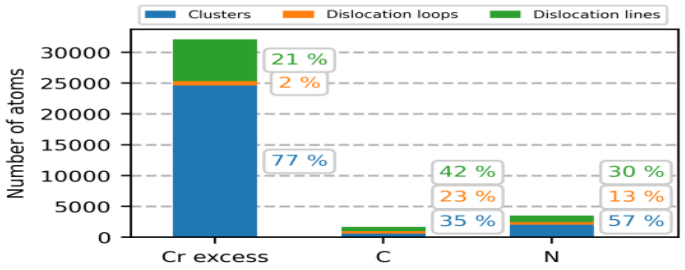

Excess Cr atoms are found predominantly in the clusters

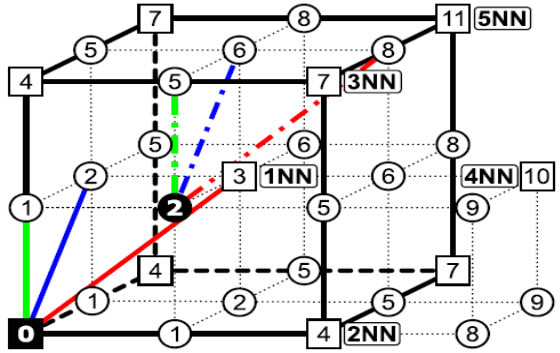

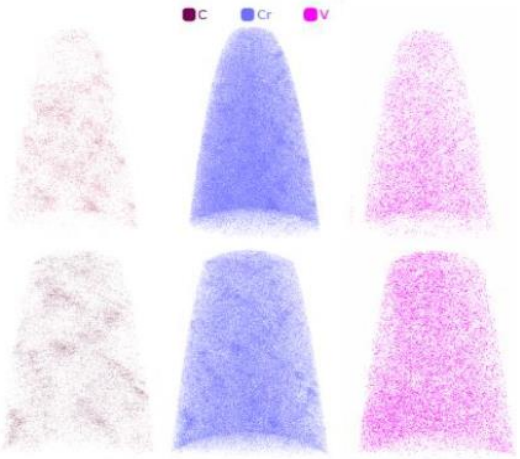

Cr-C clustering in irradiated RAMF alloys, J. Haley (2024)

Fe-3.28% Cr
0.007 at.% C
0.028 at.% N

650 K

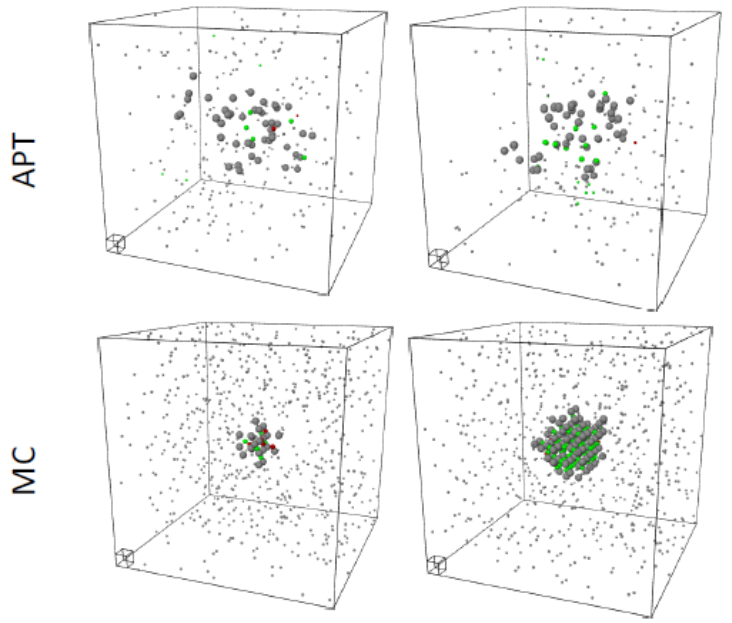

Visual comparison of example clusters found in APT measurements and MC simulations

M. Fedorov et al., J. Nucl. Mater., vol. 587 (2023) 154715

Emerging alloys for nuclear fusion applications

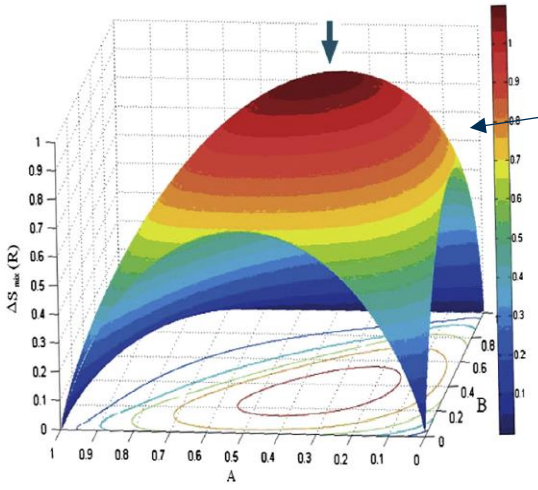

Random alloy configurations

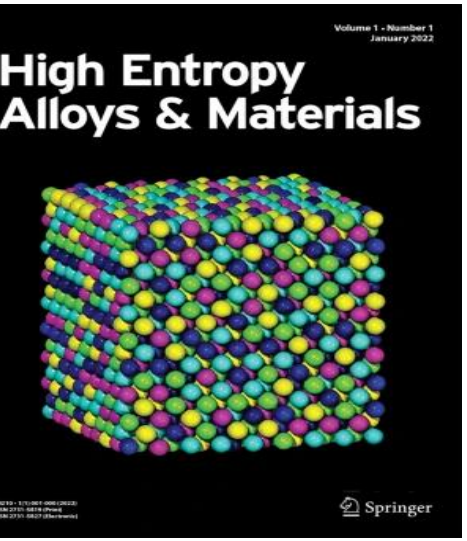

Editors: B. Cantor et al.

Journal of Nuclear Materials 581 (2023) 154422

Contents lists available at ScienceDirect

Journal of Nuclear Materials

journal homepage: www.elsevier.com/locate/jnucmat

Ab initio study of tungsten-based alloys under fusion power-plant conditions

Yichen Qian[a], Mark R. Gilbert[b], Lucile Dezerald[c], Duc Nguyen-Manh[b], David Cereceda[a,*]

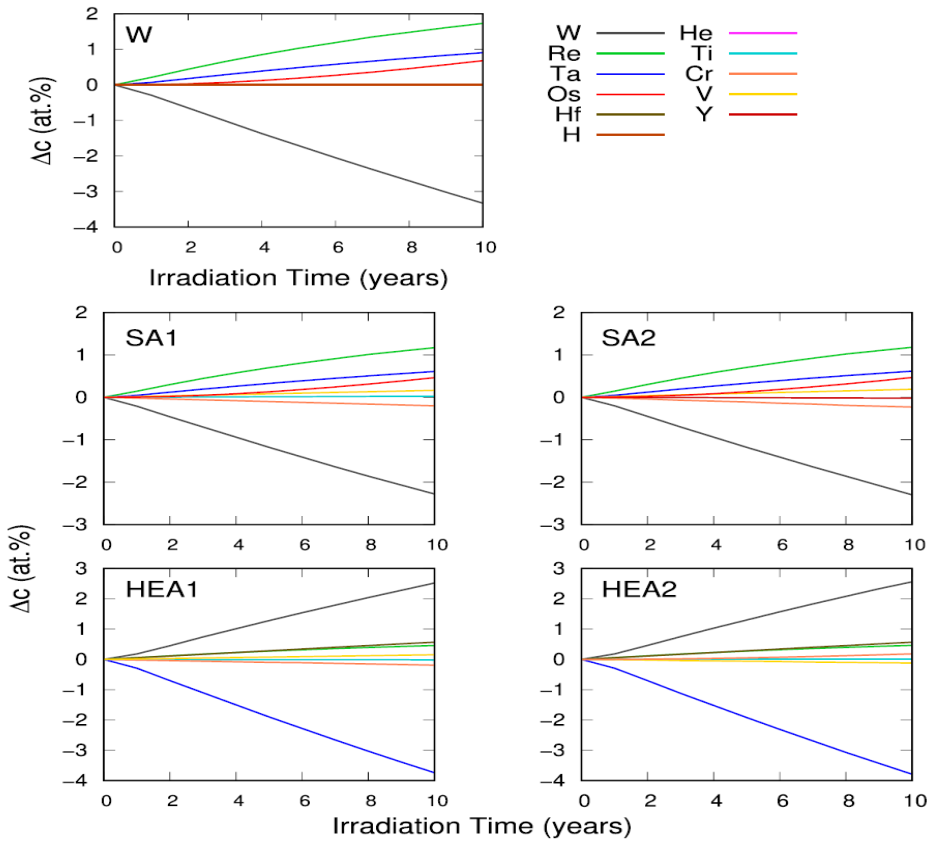

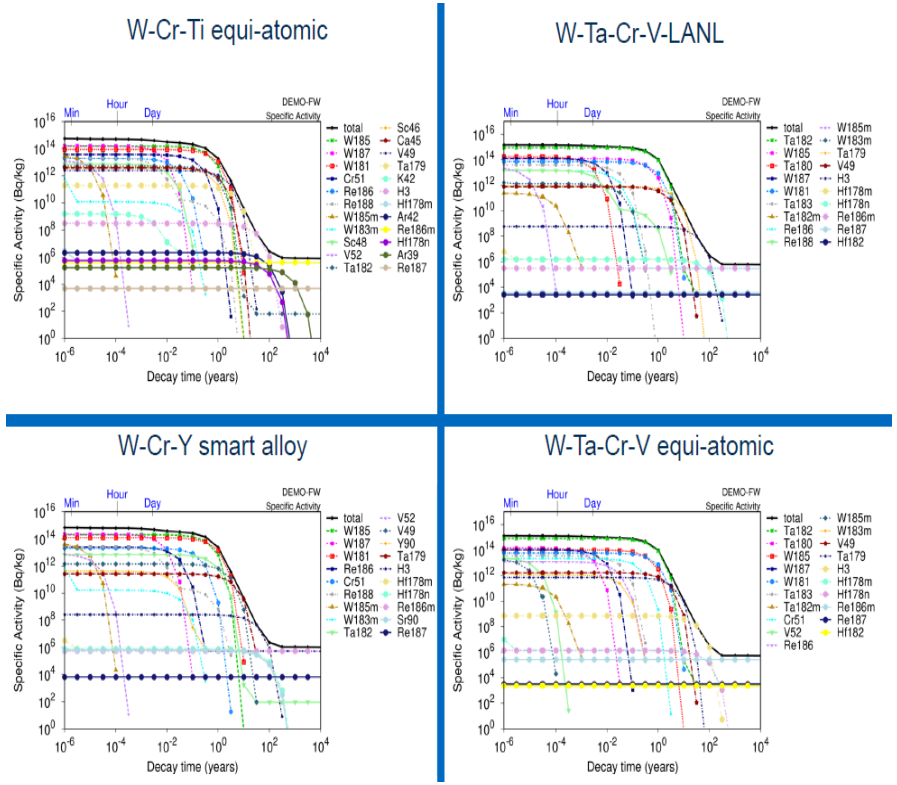

SA and HEA are low activation alloys

Microstructure evolution under irradiation in advanced fusion materials

UK Atomic Energy Authority

In-situ TEM/irradiation: Precipitation versus no-loop formation in W-Ta-Cr-V,
O. El Atwani et al., Science Advances, 5 (2019) 2022

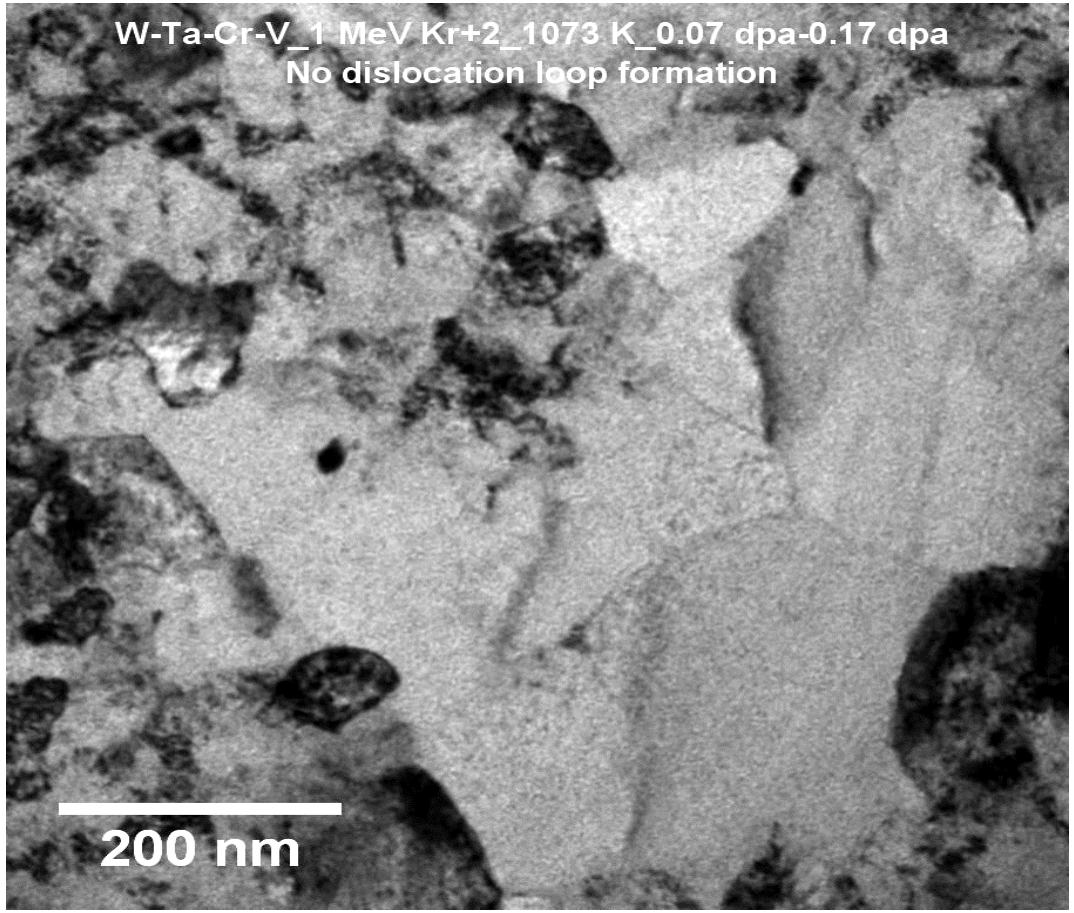

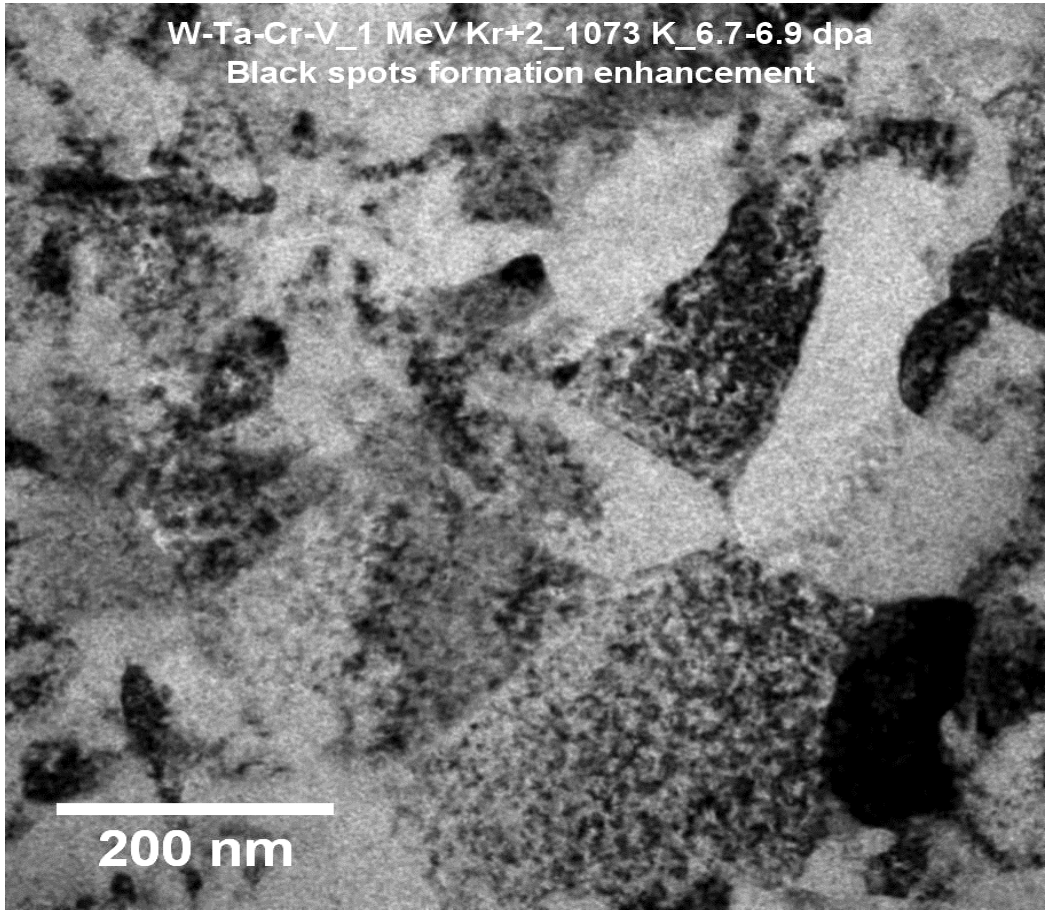

APT analysis of microstructure Cr/V-rich segregation before and after irradiation

UK Atomic Energy Authority

O. El Atwani et al., Science Advances, 5 (2019) 2022

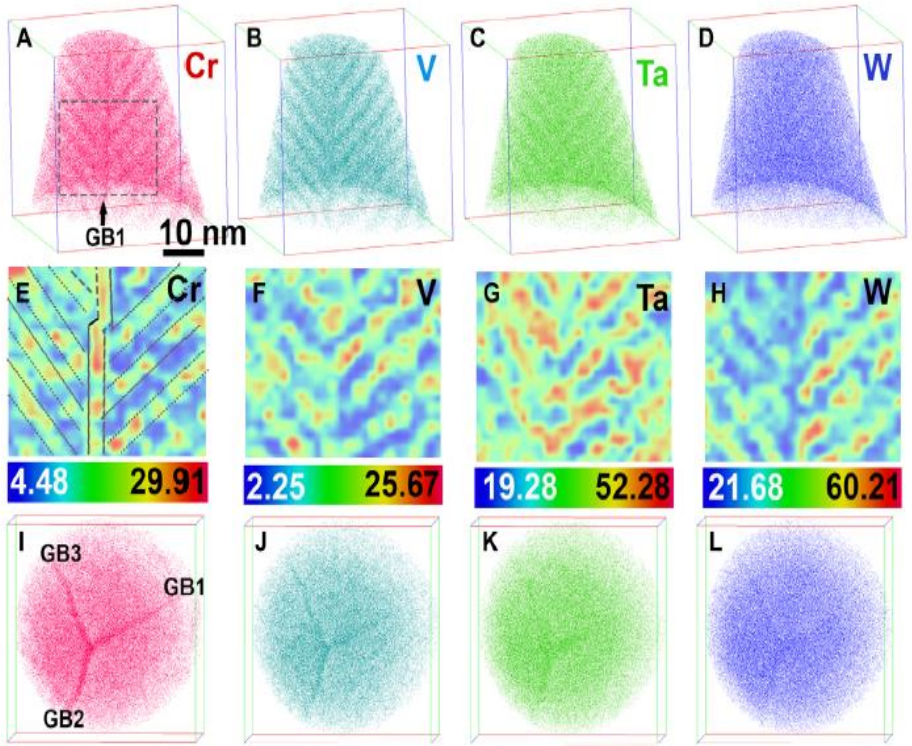

Fig. 2. APT analysis of the as-received HEA. (A) to (D) 3D distribution of Cr, V, Ta, and W. (E) to (H) 2D compositional maps with the color bars denote the concentration range for each element. (I) to (L) top-down view of three different GBs.

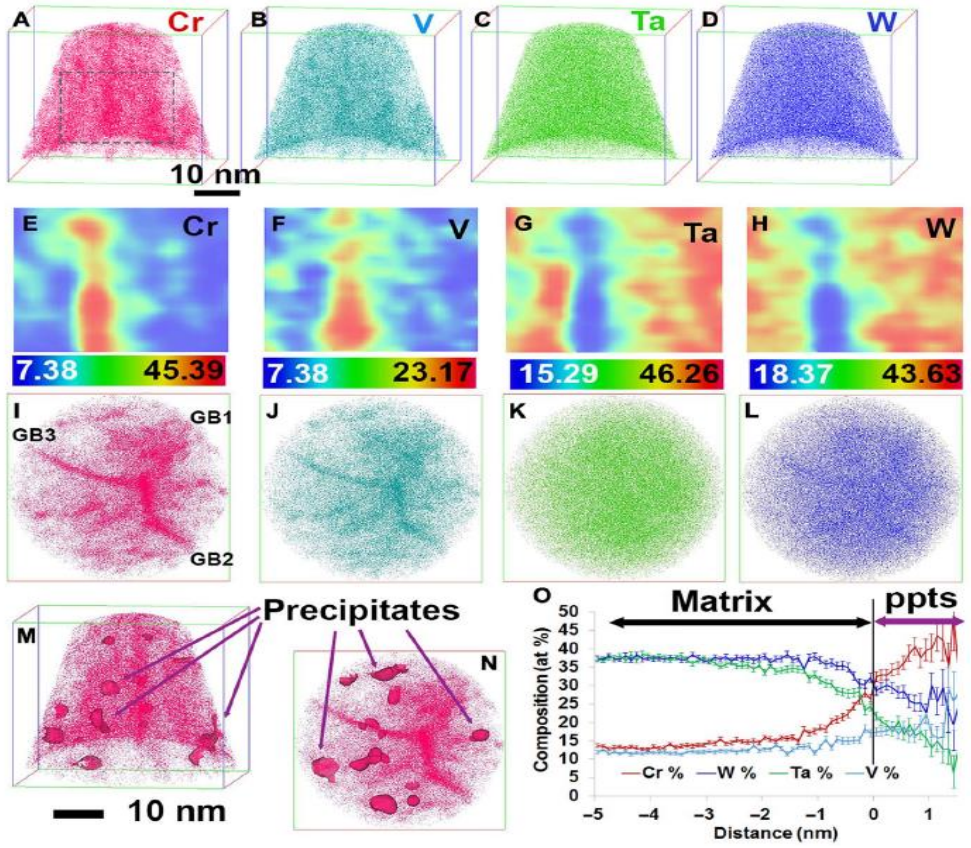

Lamellar-like structures generated at GBs

Radiation-induced precipitation of Cr/V clusters

Predicting composition and temperature dependence of single fcc HEAs Fe-Cr-Ni-Mn

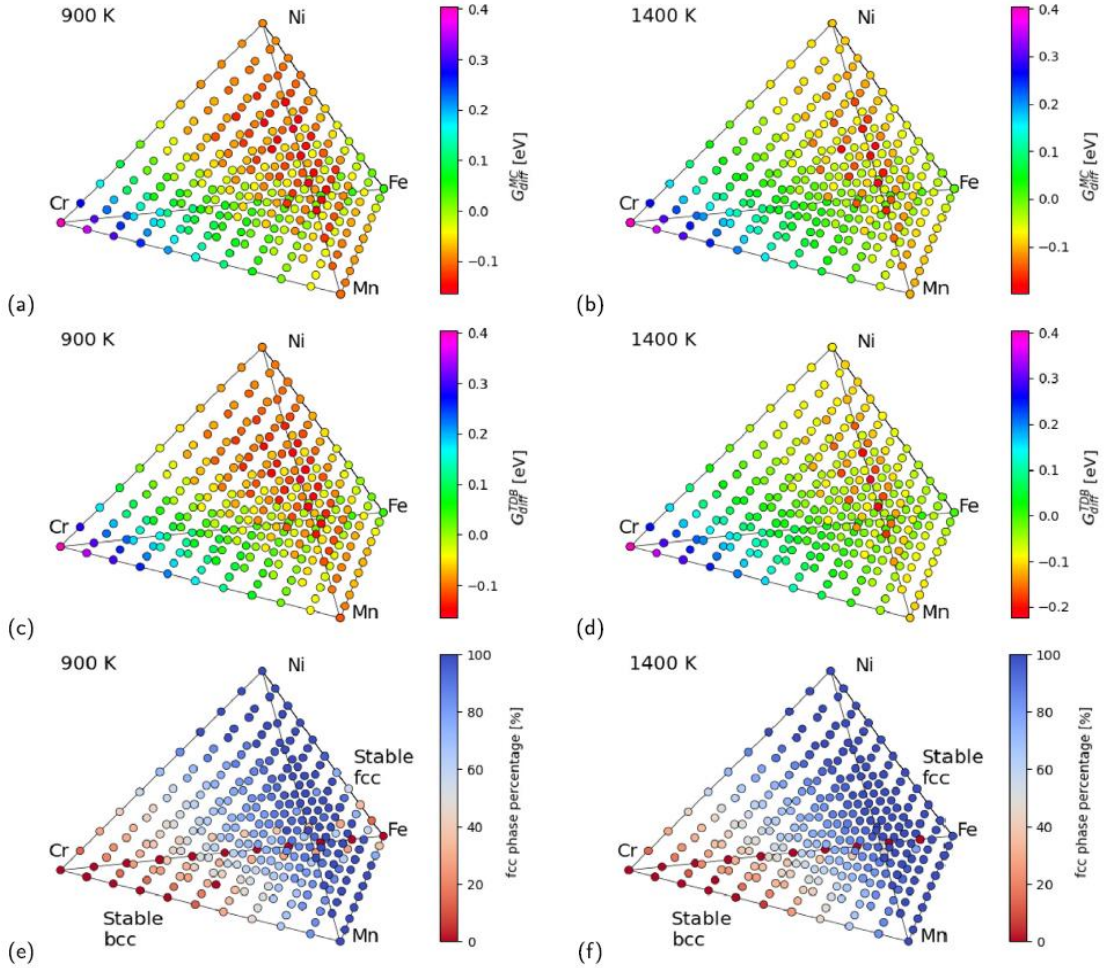

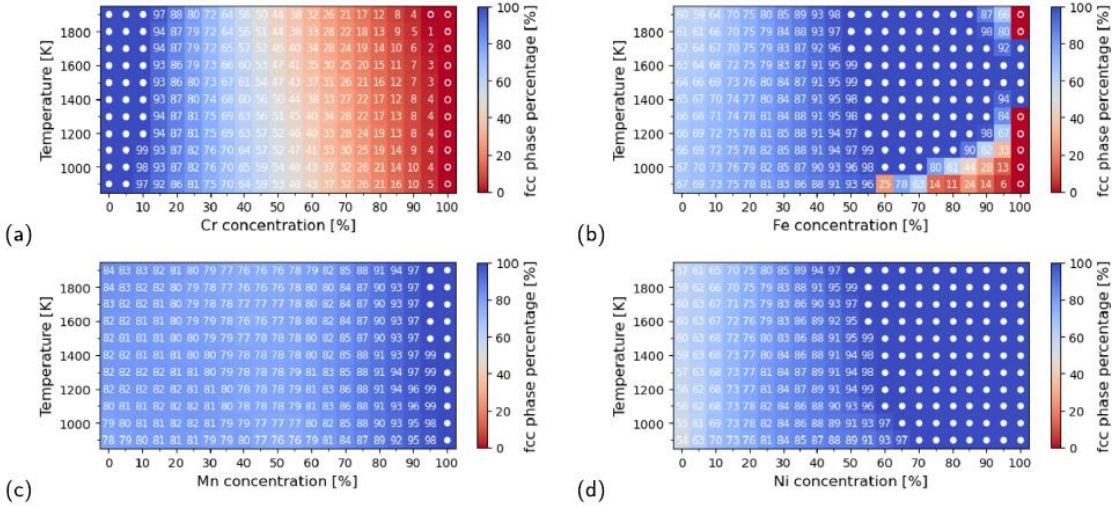

Target composition	Experiment		MC+TDB
	Composition	Phase %	Phase %
As-cast (MC @ 1000–1400 K)			
$[CrFeMn]_{80}Ni_{20}$	$Cr_{20.8}Fe_{23.8}Mn_{31.3}Ni_{24.7}$	77.5 fcc	77–78 fcc
	$Cr_{33.6}Fe_{28.6}Mn_{23.5}Ni_{14.3}$	21.8 bcc	22–23 bcc
$[CrFeMn]_{75}Ni_{25}$	$Cr_{23.1}Fe_{26.7}Mn_{24.2}Ni_{24.1}$	100 fcc	80–82 fcc
			18–20 bcc
$[CrFeMn]_{65}Ni_{35}$	$Cr_{21.2}Fe_{20.4}Mn_{22.6}Ni_{35.8}$	100 fcc	86–87 fcc
			13–14 bcc
Annealed (Expt. @ 1273 K, MC @ 1300 K)			
$[CrFeMn]_{80}Ni_{20}$	$Cr_{20.1}Fe_{27.1}Mn_{28.6}Ni_{24.1}$	75 fcc	77 fcc
	$Cr_{40.9}Fe_{27.2}Mn_{21.5}Ni_{10.5}$	23.8 σ	23 bcc
$[CrFeMn]_{75}Ni_{25}$	$Cr_{21.3}Fe_{25.9}Mn_{26.1}Ni_{26.7}$	87.5 fcc	81 fcc
	$Cr_{43.4}Fe_{26.0}Mn_{18.9}Ni_{11.8}$	10.4 σ	19 bcc
	$Cr_{79.9}Fe_{7.0}Mn_{9.6}Ni_{3.6}$	1.53 bcc	
$[CrFeMn]_{65}Ni_{35}$	$Cr_{21.3}Fe_{21.9}Mn_{22.0}Ni_{34.8}$	99.6 fcc	87 fcc
			13 bcc

M. Fedorov et al., Phys. Rev. B, 101 (2020) 174416; Acta Mat. 255 (2023) 119047

Radiation-induced segregation of Cr-V rich precipitates (black spots formation)

UK Atomic Energy Authority

SCIENCE ADVANCES | RESEARCH ARTICLE

MATERIALS SCIENCE

Outstanding radiation resistance of tungsten-based high-entropy alloys

O. El-Atwani[1]*, N. Li[2], M. Li[3], A. Devaraj[4], J. K. S. Baldwin[2], M. M. Schneider[1], D. Sobieraj[5], J. S. Wróbel[5], D. Nguyen-Manh[6], S. A. Maloy[1], E. Martinez[7]*

- TEM & APT analysis correlated back spots with second-phases rich in Cr-V
- No signs of irradiation-created loops even after 8 dpa
- Nano-mechanical testing shows nearly negligible hardening
- Supported also by recent collision cascade simulations in W38Ta36Cr15V11 (Y. Chen et al. JNM 585 (2023) 154646

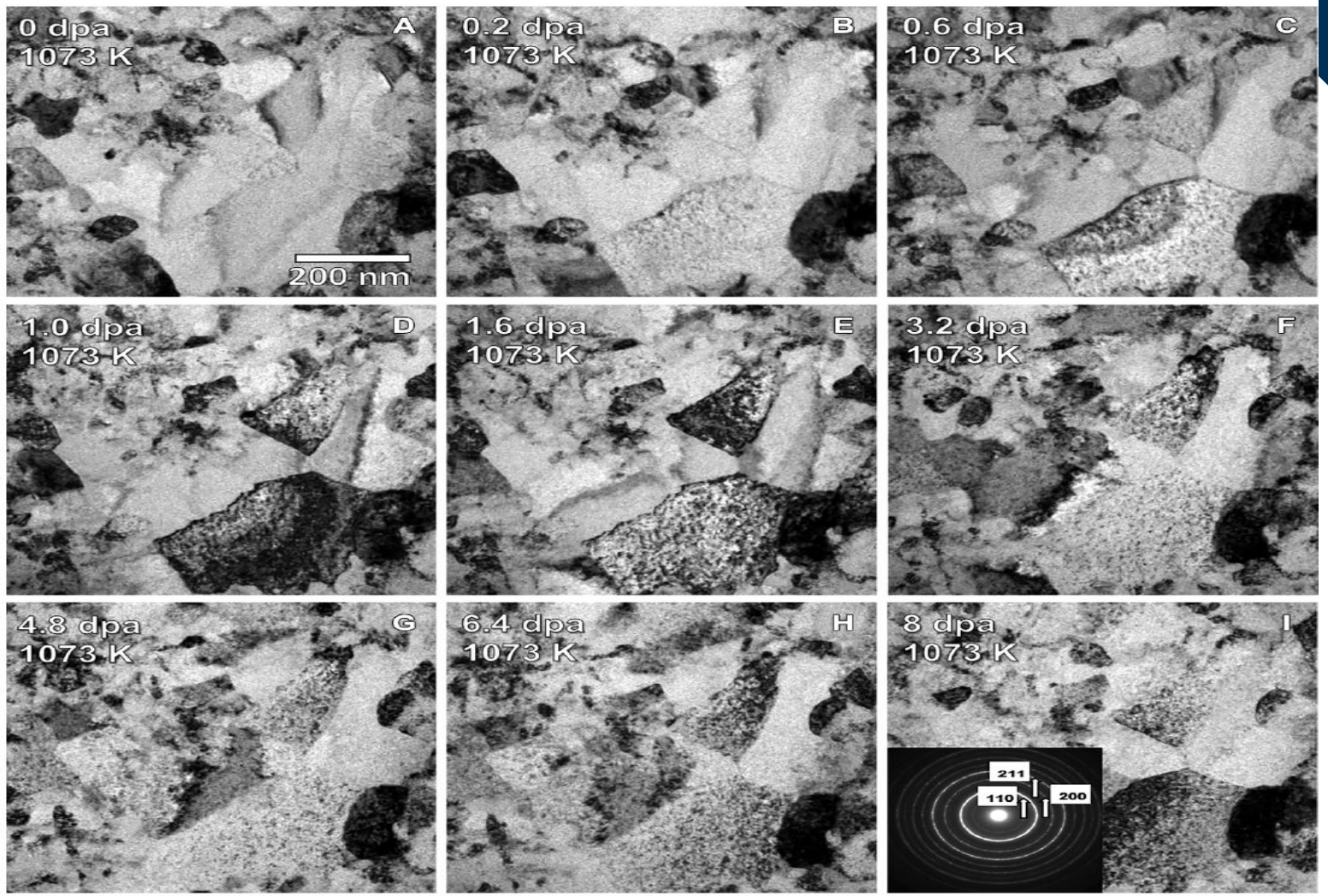

Radiation-induced microstructure of Cr-V rich bcc-phase precipitates with no dislocation loops

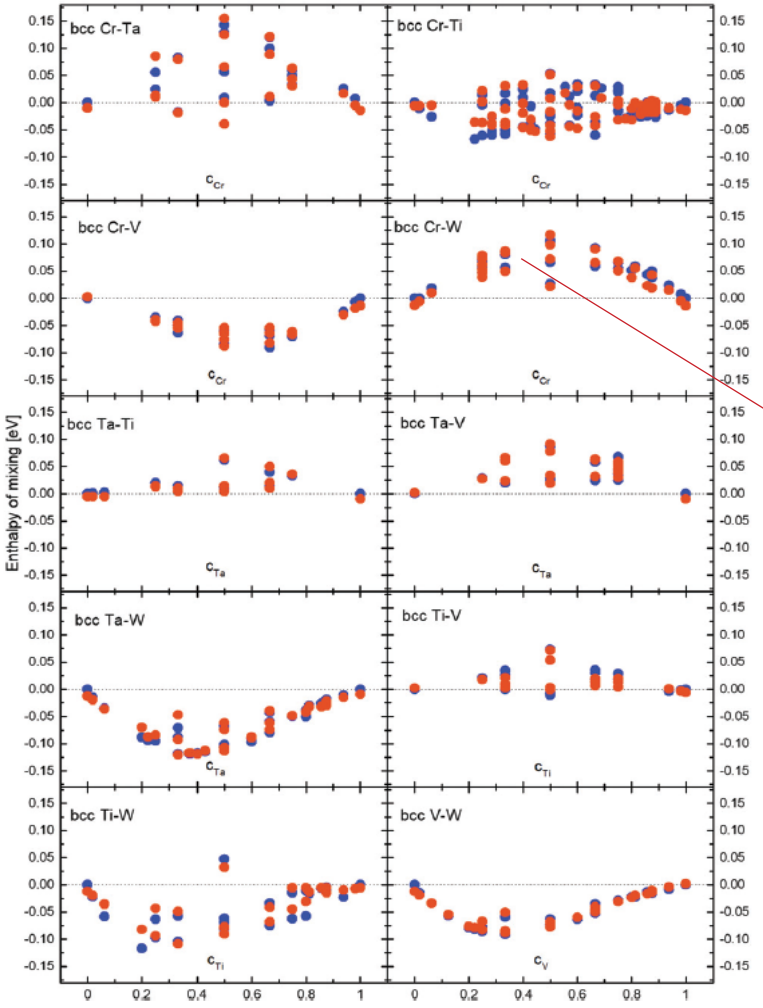

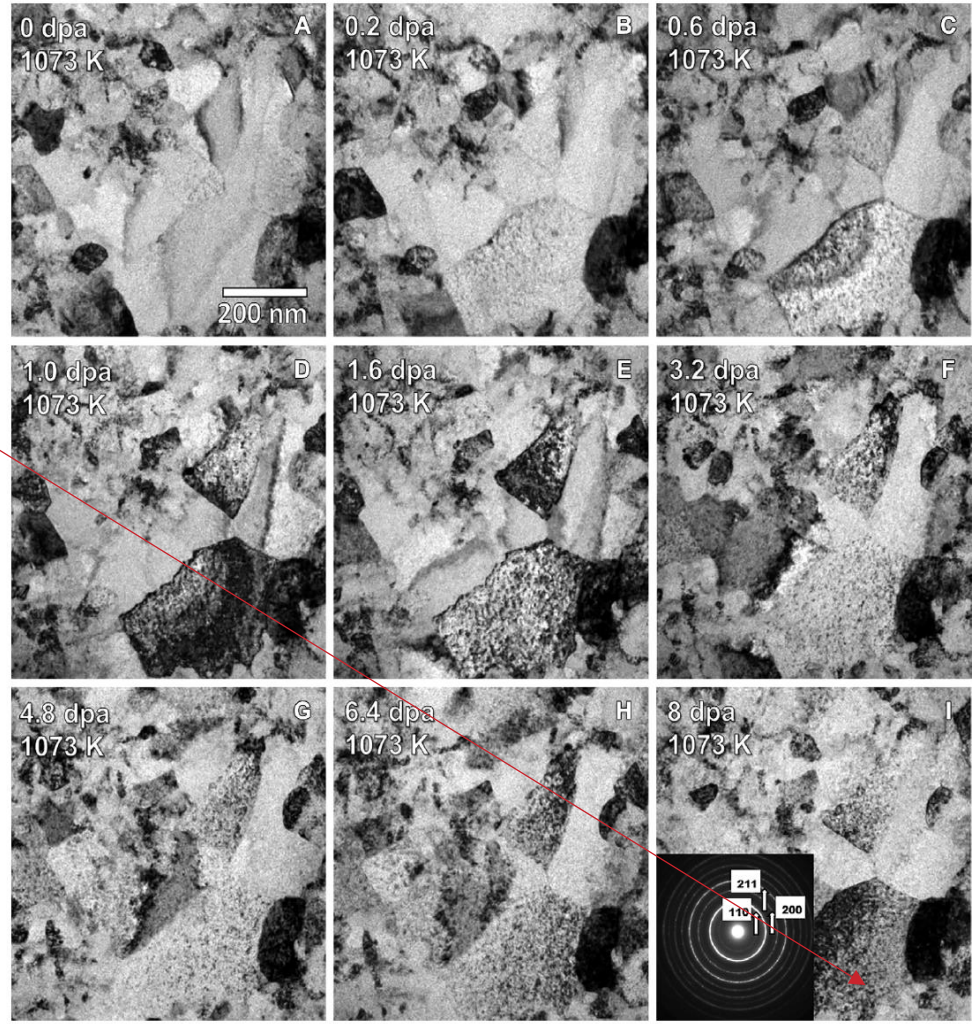

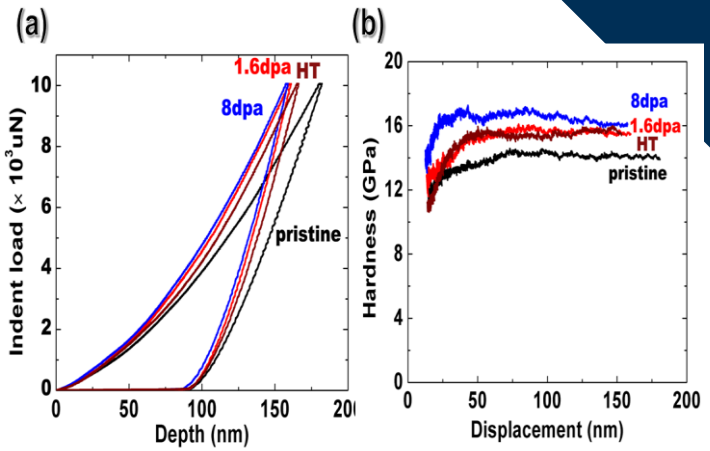

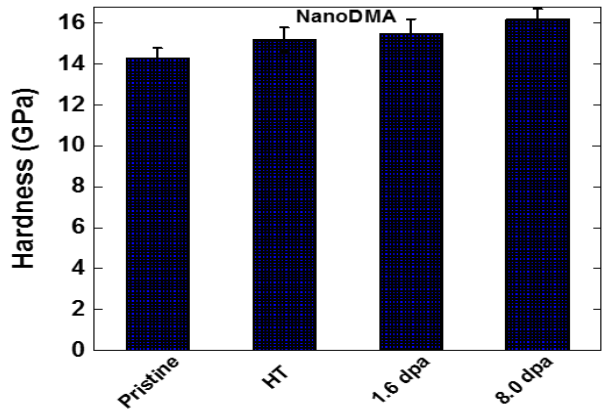

Small irradiation hardening

Predictive composition stability of outstanding radiation resistance in W38Ta36Cr15V11 multi-component materials

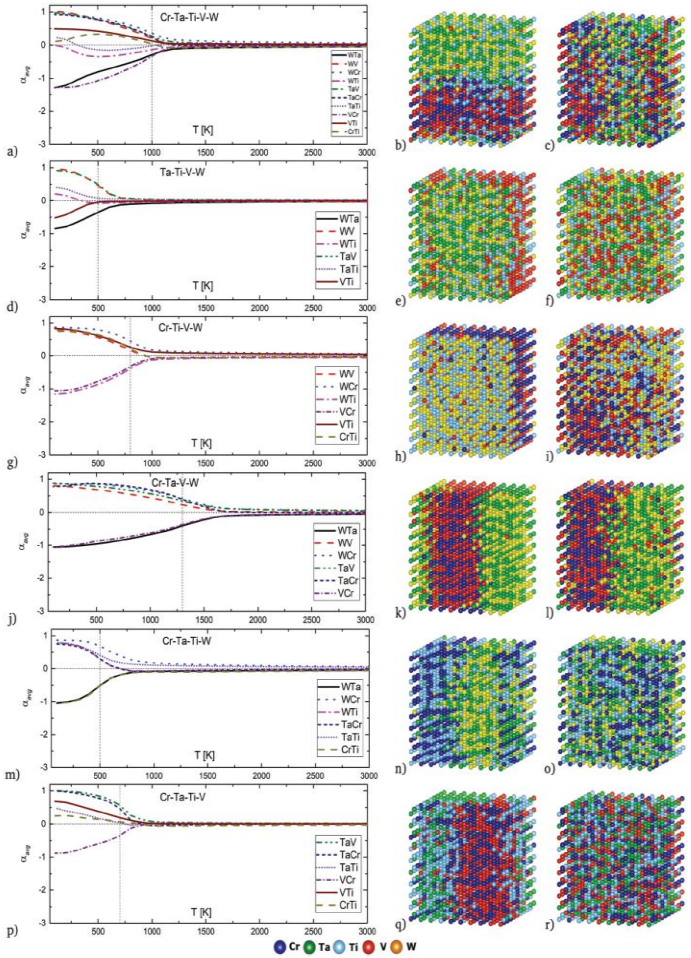

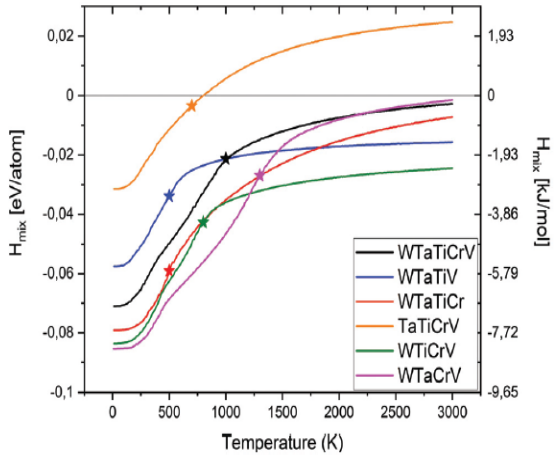

Fig. 4 Enthalpy of mixing for quinary and quaternary equiatomic alloys with their order–disorder transition temperatures marked with a star.

Table 2 Order–disorder transition temperatures and average melting points for equiatomic alloys

Alloy	ODTT [K]	T_m^{avg} [K]
Cr-Ta-Ti-V-W	1000	2362
Cr-Ta-Ti-W	500	2478
Ta-Ti-V-W	500	2488
Cr-Ta-V-W	1300	2535
Cr-Ti-V-W	800	2208
Cr-Ta-Ti-V	700	2103

SCIENCE ADVANCES | RESEARCH ARTICLE

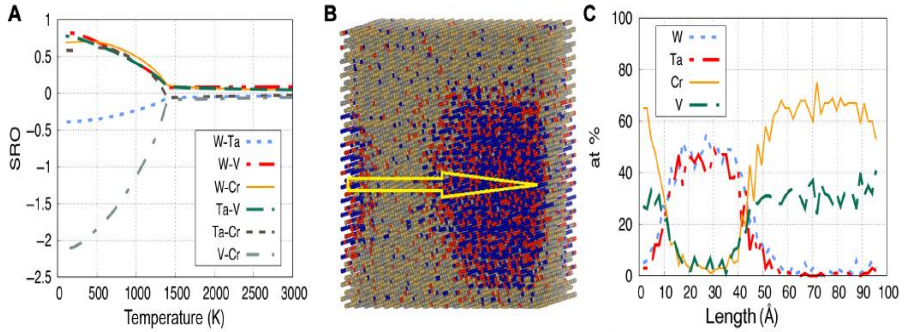

Fig. 6. Theoretical predictions of the atomic configurations. (**A**) Average SRO parameters in the $W_{38}Ta_{36}Cr_{15}V_{11}$ alloy as a function of temperature. (**B**) Atomic configuration in the $W_{38}Ta_{36}Cr_{15}V_{11}$ alloy at T = 1000 K after CMC simulations. (**C**) Average concentration profile of each element along the [001] direction across the Cr-V cluster.

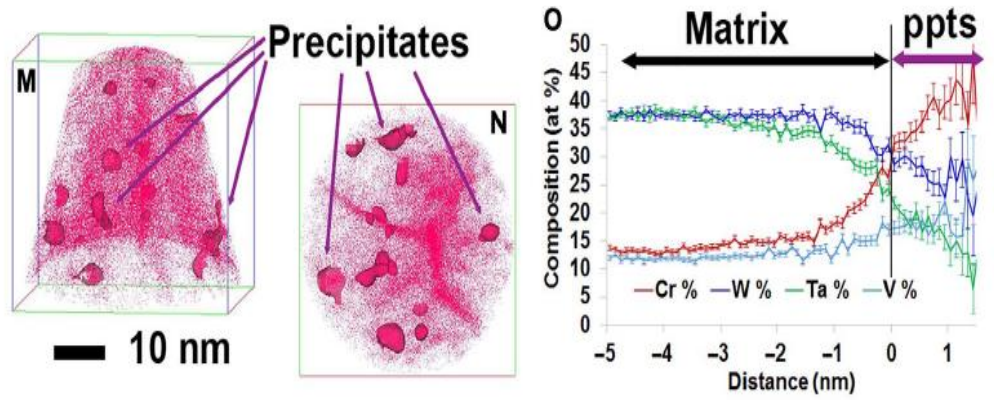

O. El Atwani et al., Science Advances, 5 (2019) 2022; D. Sobieraj et al., PCCP, 22 (2020), 23929

Segregation, ordering and precipitation in W-Ta-Cr-V alloys using MLPs

UK Atomic Energy Authority

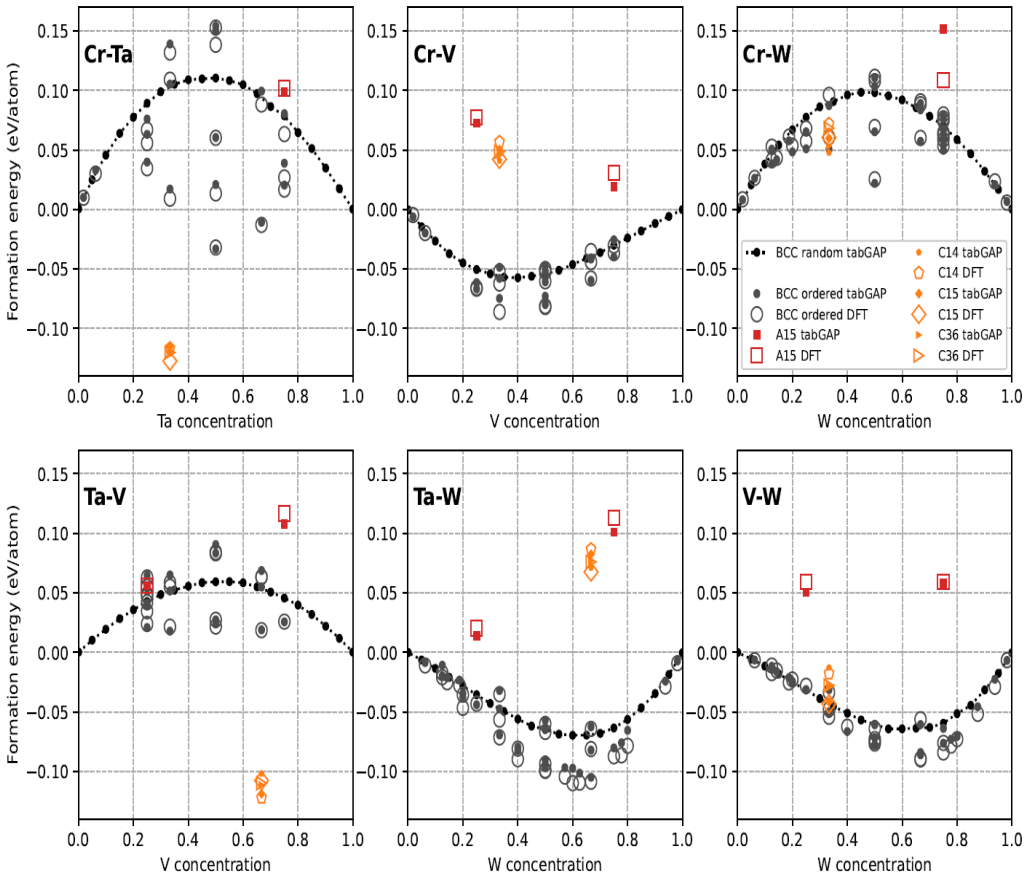

FIG. 1: Formation energies of relaxed binary alloys from DFT compared with the W–Ta–Cr–V tabGAP.

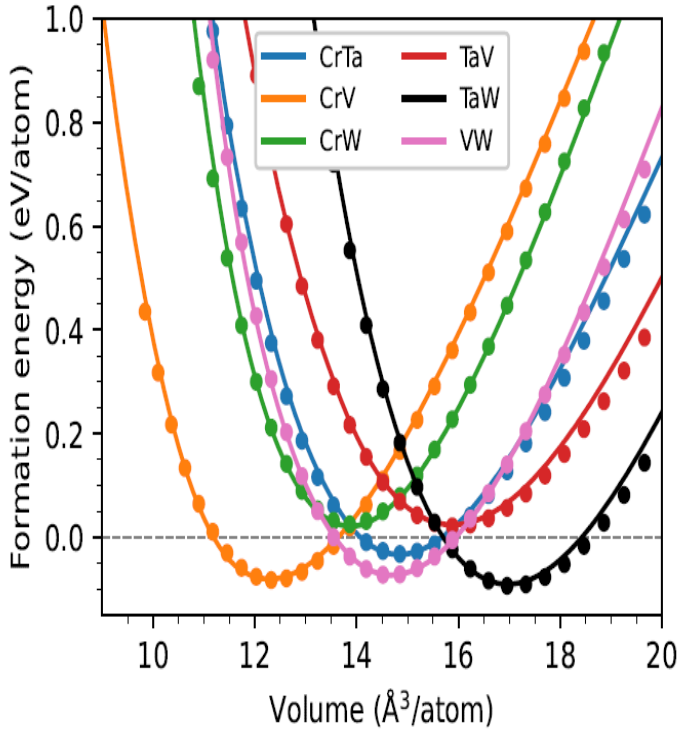

FIG. 2: Energy as a function of atomic volume for binary B2-ordered alloys. Lines are tabGAP predictions and points are DFT.

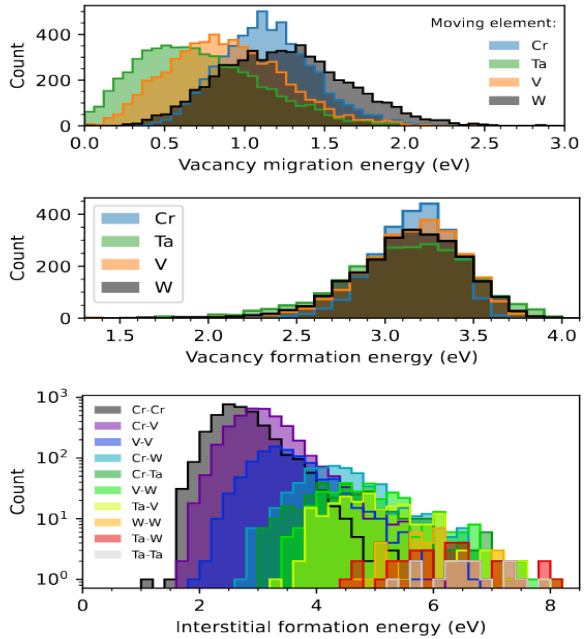

FIG. 4: Distributions of single-vacancy migration and formation energies and stable self-interstitial dumbbell formation energies in equiatomic WTaCrV calculated with the tabGAP. The distributions are plotted separately for each element, which for migration is the element that exchanges position with the vacancy, for vacancy formation the element that is removed, and for self-interstitials the two elements of the dumbbell configuration. The legend for interstitial dumbbells is given in order of the average formation energy (Cr–Cr lowest, Ta–Ta highest). Note the logarithmic scale for interstitials, since the vast majority of stable dumbbells are Cr– or V–containing pairs.

J. Byggmaster, D. Sobieraj, J. Wrobel, O. Et-Atwani,, E. Martinez, DNM, (2024)

Semi-coherent interfaces between WTa/CrV with presence of misfit dislocation grids

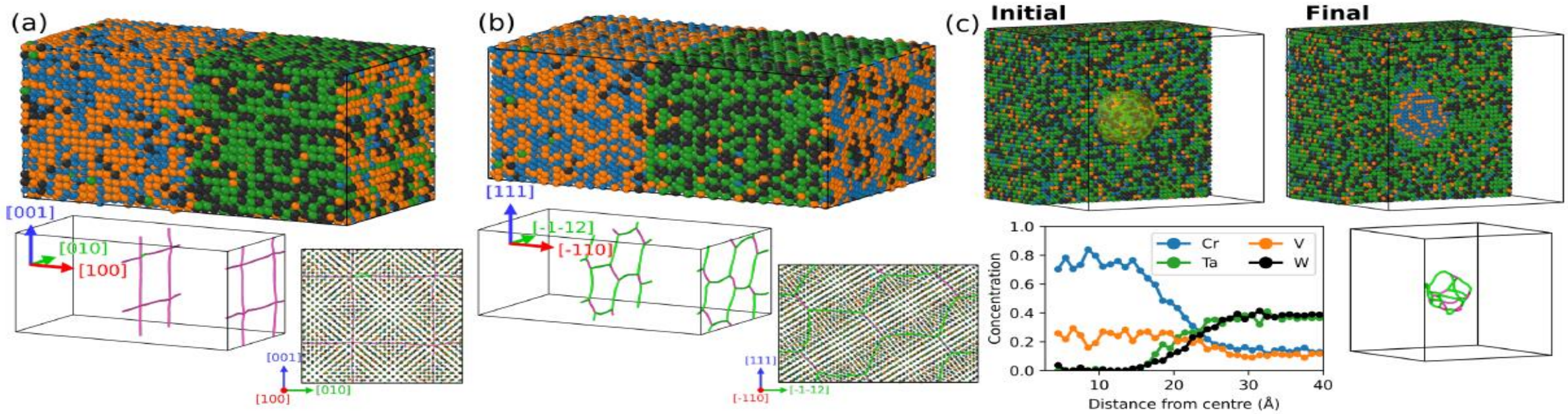

FIG. 13: Semicoherent interfaces between CrV and WTa after MC/MD relaxation, (a): (1 0 0)/(1 0 0) and (b): (1 1 0)/(1 1 0). The smaller snapshots show side views and cross sections of the misfit dislocation grids with pink lines representing ⟨1 0 0⟩ Burgers vectors and green lines 1/2⟨1 1 1⟩. The spacing between misfit dislocation lines in the interface plane is about 3 nm. (c) Semicoherent precipitate in WTaCrV before and after MC/MD relaxation, shown as half-box slices and the misfit dislocation network after relaxation. The plot shows the radial concentration profile starting from the centre of the relaxed precipitate.

J. Byggmaster, D. Sobieraj, J. Wrobel, O. Et-Atwani,, E. Martinez, DNM, Acta Mat. (2025)

Radiation-induced grain refinement with Hf addition into W-Ta-Cr-V-Hf alloys

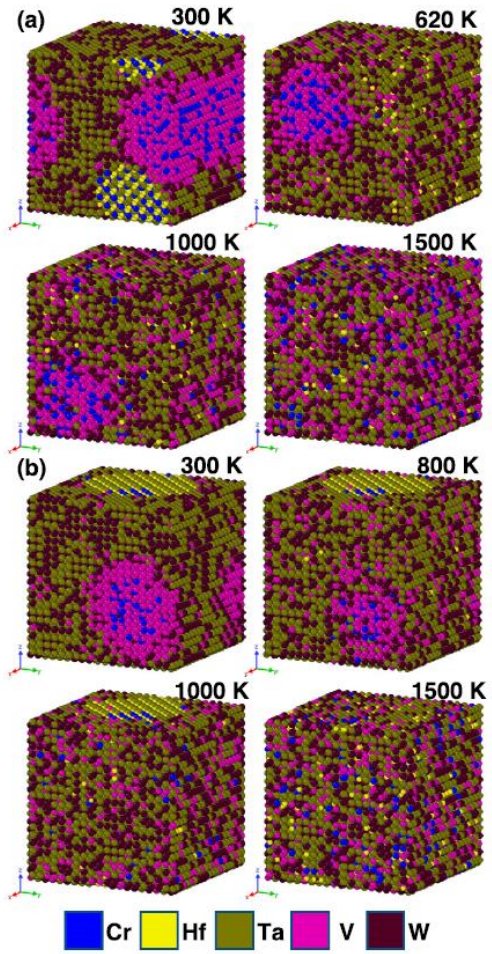

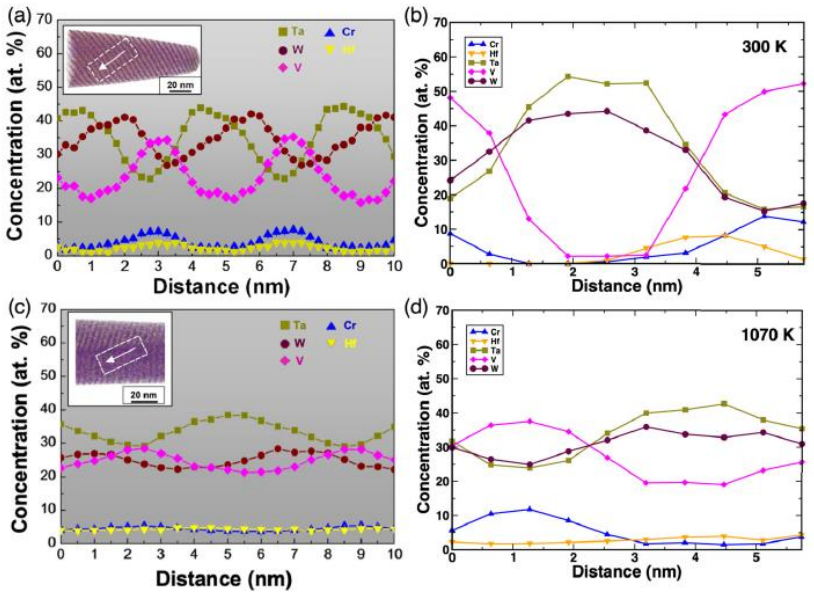

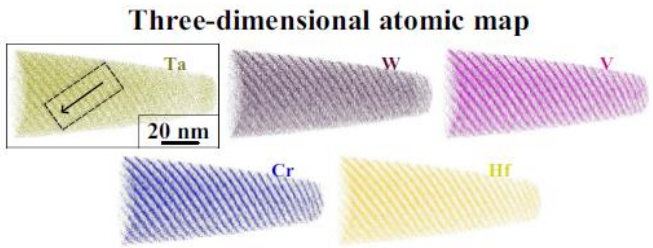

Evidence of grain refinement under irradiation

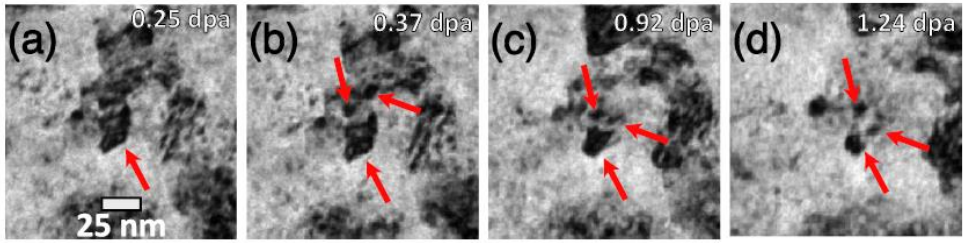

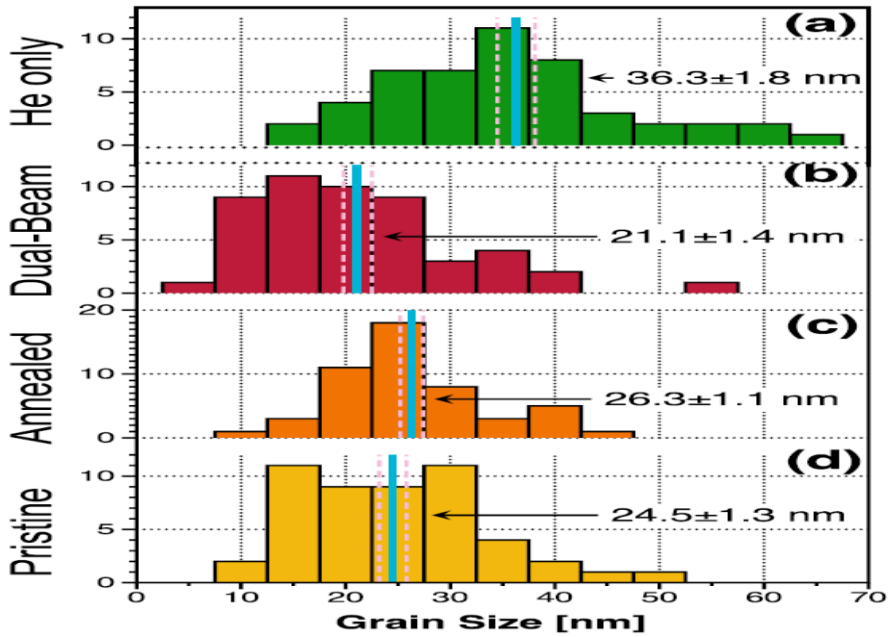

A. Alvarado et al., Scripta Mat., 233 (2023) 115506; O. El Atwani et al., Nature Comm.,14 (2023) 2516

Enhancement radiation resistance in binary W-Ta alloys through small V addition: Reduction of voids

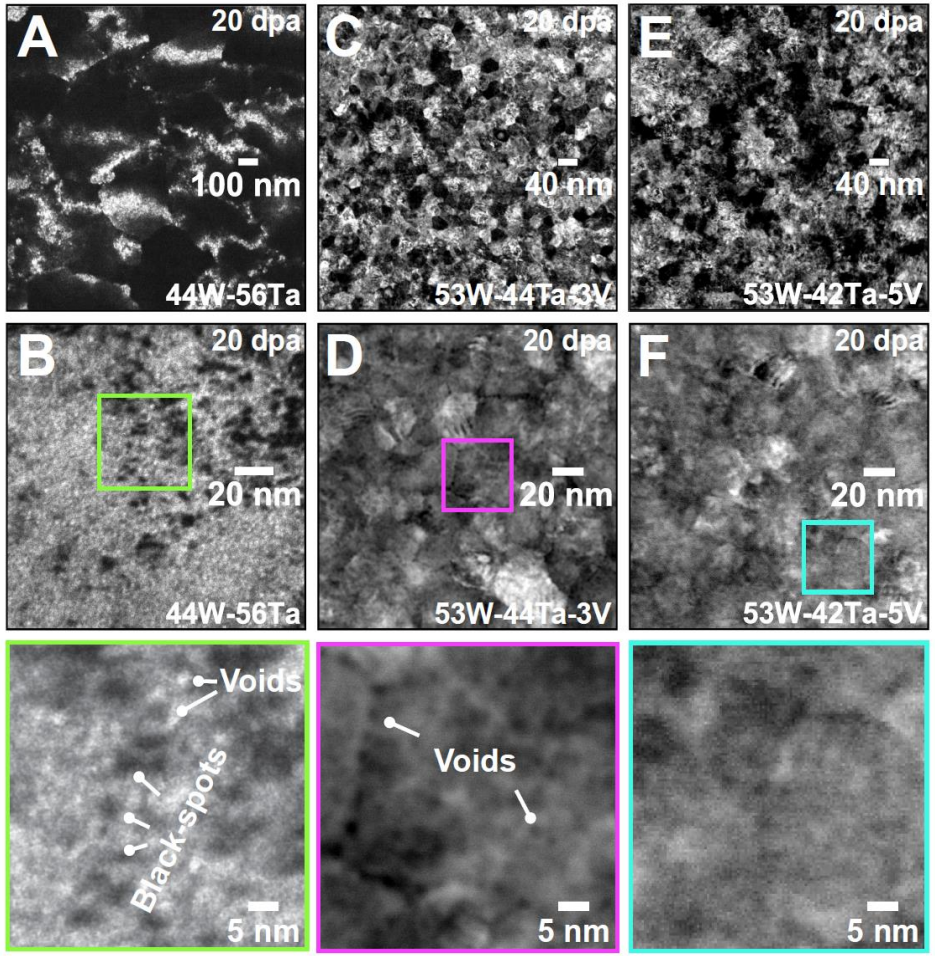

Table 2: Average void size (diameter) and areal densities for all samples after irradiation.

Irradiated Alloy (20 dpa at 1073 K)	Average Void Size [nm]	Average Areal Density [#·nm^{-2}]
$W_{44}Ta_{56}$	1.9±0.1	$8.9\pm0.2\times10^{-3}$
$W_{53}Ta_{44}V_3$	1.7±0.1	$7.0\pm1.1\times10^{-3}$
$W_{53}Ta_{42}V_5$	Not observed/detected	Not observed/detected

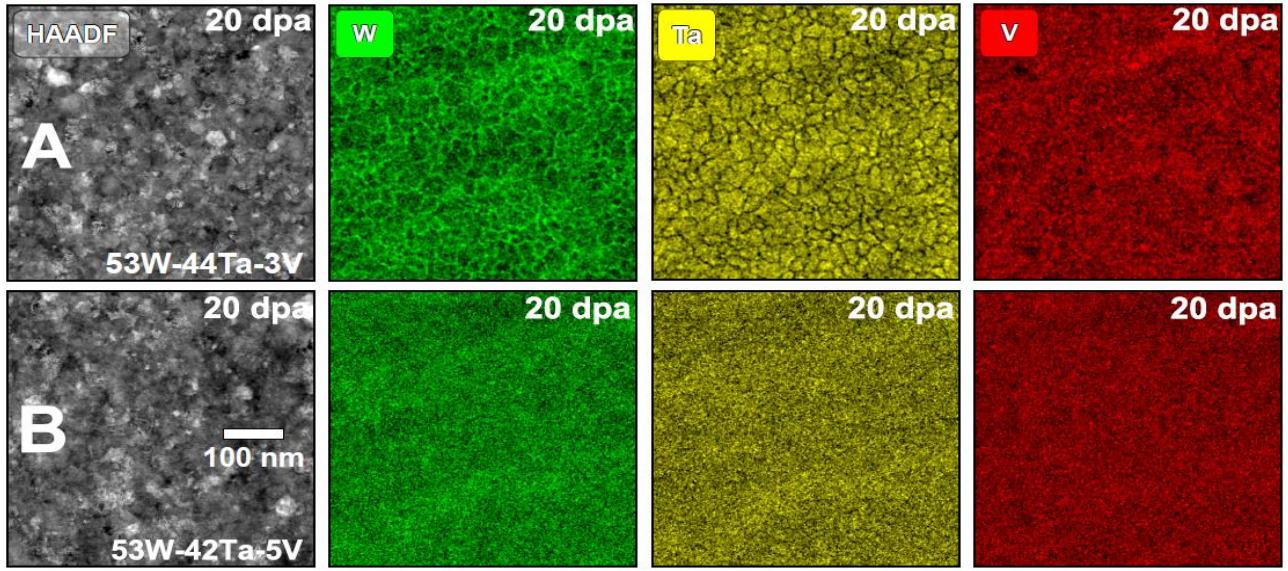

Figure 3: **Nanoscale chemistry of the WTaV HCRAs after irradiation at 20 dpa** | High-magnification STEM-EDX mapping collected from both $W_{53}Ta_{42}V_5$ (top row) and the $W_{53}Ta_{44}V_3$ (bottom row) HCRAs reveal W segregation and Ta depletion at the nanocrystalline grain boundaries upon decreasing the V content in the W–Ta–V system. The $W_{53}Ta_{42}V_5$ HCRA neither exhibit radiation-induced segregation nor radiation-induced precipitation or phase instabilities/transformations, indicating a high-radiation tolerance at 20 dpa.

M.A. Tunes et al., (2025), Science Advances

Chemical SRO between V-Ta and V-W in a ternary W-Ta-V systems are different to binaries

UK Atomic Energy Authority

W-Ta binary with voids

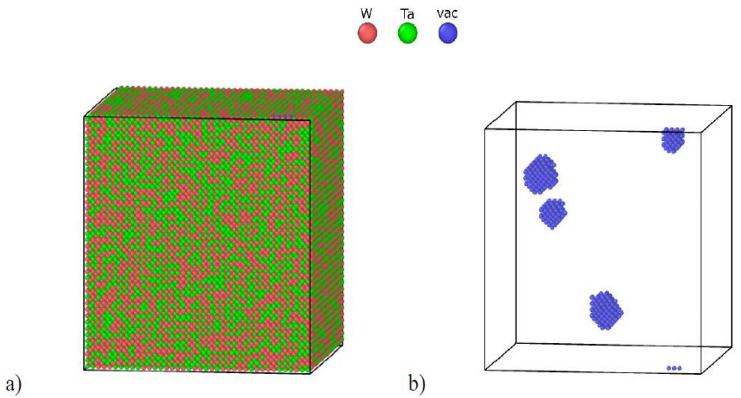

Figure S1: (a) The structure of $W_{44}Ta_{56}$ alloy obtained using DFT-based Monte Carlo simulations at 1100 K; (b) The same structure without showing the atoms of W and Ta.

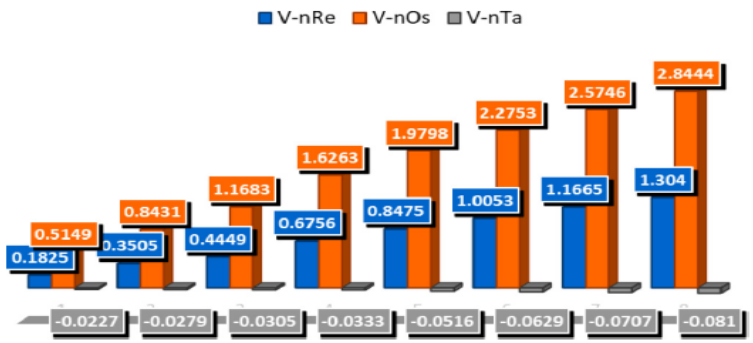

FIG. 3. Binding energies of a single vacancy interacting with the first-nearest-neighbor atoms from 1 to 8 for separated solute Re, Os, and Ta elements in bcc-W.

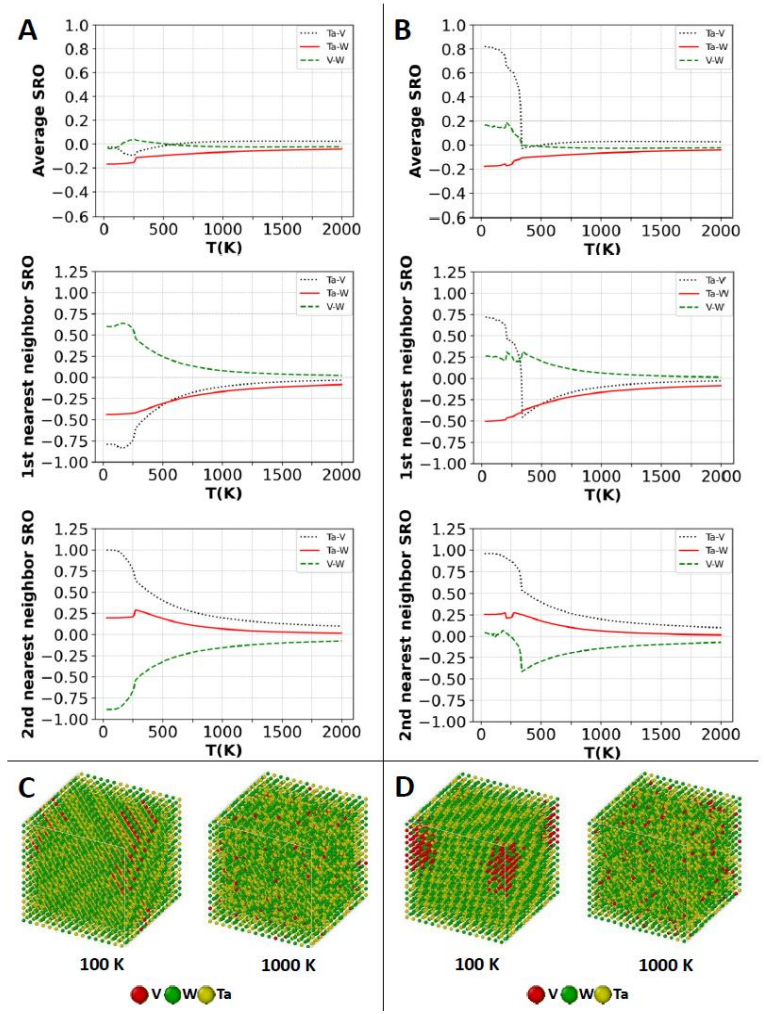

- 1NN CSRO between V-Ta changes from W53Ta44V3 to W53Ta42V5 at low temperature.
- **Free energy shows that W53Ta42V5 is thermodynamically more stable than those of W53Ta44V3**

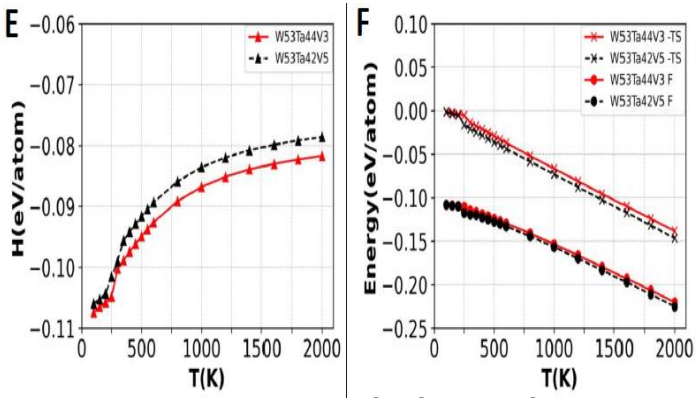

M. Tunes et al. (2024)

Prediction of void reduction in W-Ta-V as a function of V composition from MD simulations using MLPs

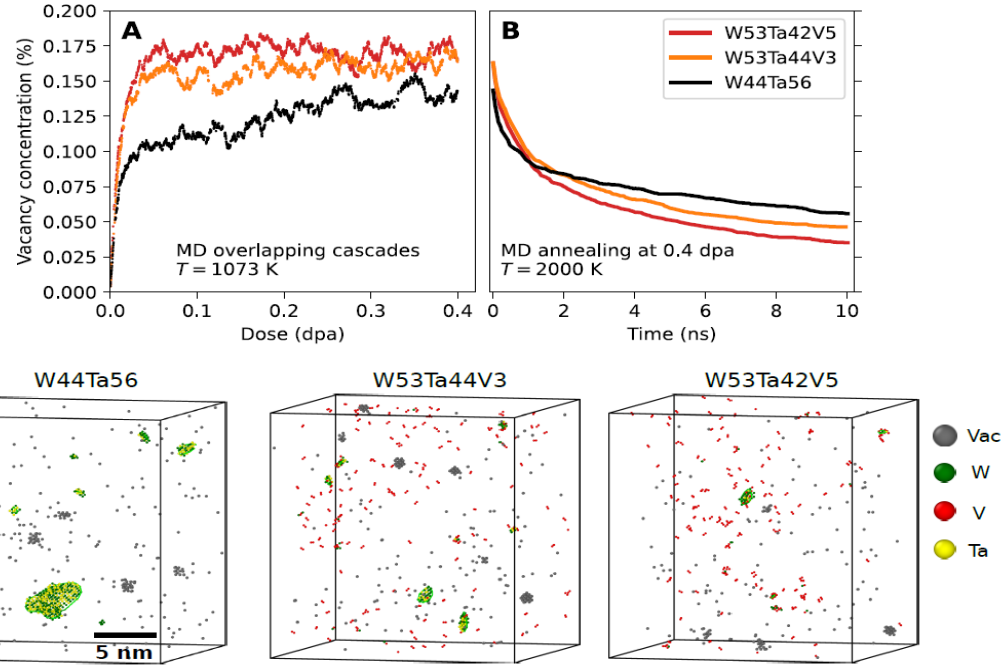

Figure 6: **MD simulations of damage accumulation and defect recombination during annealing** | Irradiation-induced vacancy concentrations as functions of dose in the three HCRAs in A. Vacancy concentrations as functions of time during MD annealing at 2000 K in B, showing the recombination efficiency of the HCRAs. Snapshots of the defect structure after annealing, showing vacancies (grey atoms), self-interstitial atoms (coloured by element) and dislocation loops (green lines) in C.

Overlapping cascade and annealing MD simulations

- 498 960 atoms
- 1073 K
- Potential: W-Ta-Cr-V tabGAP (unpublished)
- 10 keV recoils, short *NPT* relaxation after each cascade
- Expt. compositions: W44Ta56, W53Ta44V3, W53Ta42V5
- Annealing: 2000 K for 10 ns, *NPT*.

M. Tunes et al. Science Advs. Accepted (2025)

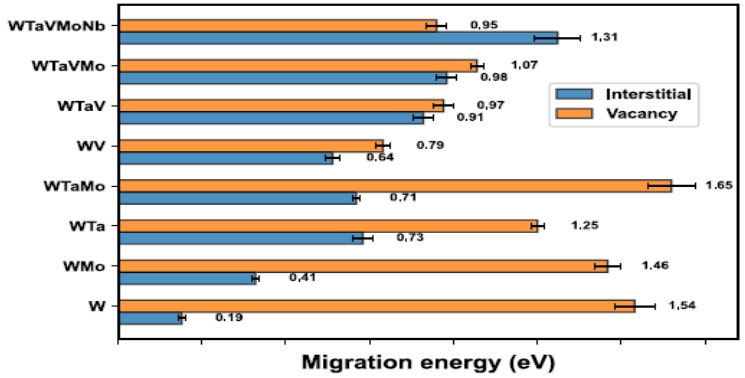

Fig. 6. Single interstitial and vacancy migration energies obtained from Arrhenius fits to mean-squared-displacement simulation data in all considered materials.

Critical role of V in radiation damage of multi-component W based alloys, G. Wei et al., Acta Mat., 274 (2024) 119991

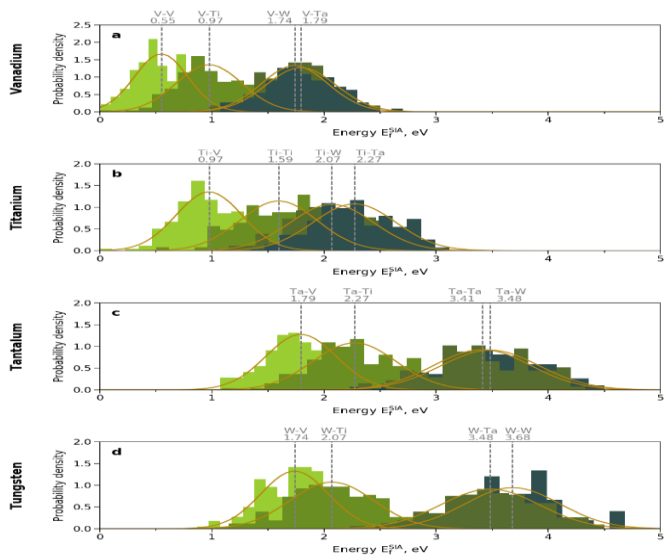

V presence in W-Ta-Ti alloys significantly reduces the SIA formation energies
J. Wrobel et al. Npj Comp. Mater. submitted (2024)

He damage resistance in W-Ta-Cr-V alloys

- Experimentally it is overserved an enhanced He bubble resistance.
- He bubbles grown at slow rate marked with no preferential formation at the grain boundaries
- **DFT calculations demonstrate low diffusivity and accumulation of He in HEAs compared with pure W**.
- Lower solution and formation of He in W-Ta-Cr-V
- Confirmation of enhanced vacancy-self interstitial defect recombination.

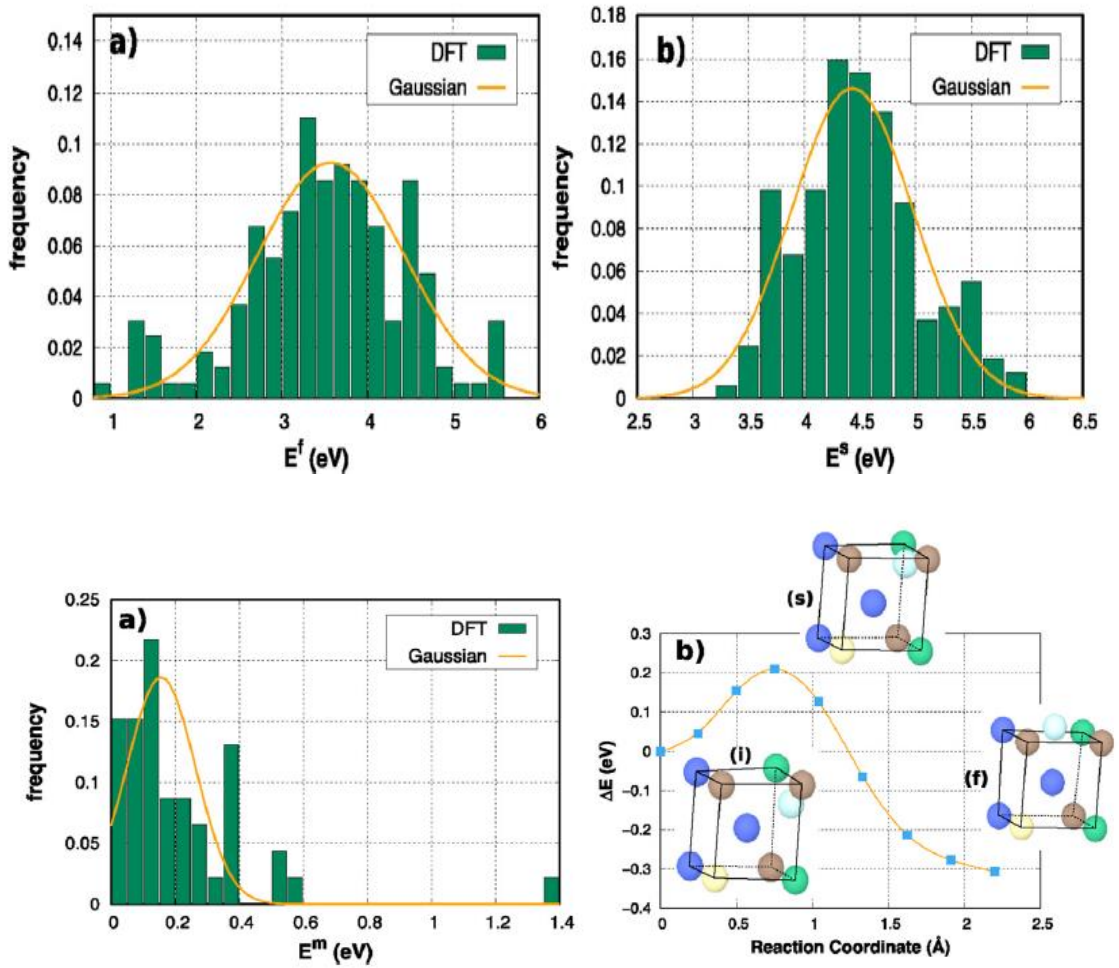

O. El-Atwani et al., Materials Today Energy, 19 (2021) 100559

Surface modification after He irradiation: A thinner fuzz layer, See more from C. Yin, NF, 64 (2024) 086035

Summary

- First-principles constrained thermodynamic formalism has been developed to predict composition dependence multi-component alloy system irradiation in which point defects are being considered as the additional elements in the system
- It has been employed to understand void decorated by transmutation elements in neutron irradiated W as well as anomalous Cr-rich precipitation in Fe-Cr model alloys and RAFM steels due to interaction with impurities (C, N) under irradiation and the important role of spinodal decomposition dependence on Y and Zr alloying into W-Cr system in stabilising microstructure in SMART alloys for oxidation resistance as well as under neutron irradiation.
- The outstanding radiation resistance in W-based (W-Ta-Cr-V) is predicted from SRO dependence as function of HEAs composition and temperature demonstrating the important role of rich Cr-V precipitation in microstructural evolution of materials with irradiation dose.
- It can be understood from MD simulations with newly developed machine-learning potentials (MLPs) based on DFT training database that the recombination mechanism in these materials are fundamentally different comparing with those in pure materials
- It is found that radiation-induced refinement and stability of microstructural grains under heavy irradiation can be designed and integrated with experimental studies to develop new compositionally complex structural materials for nuclear fusion/fission applications

Detritiation of plasma facing materials within JET decommissioning activities

As one of the most promising materials for plasma-facing components, there are extensive experimental studies of detritiation in Tungsten (W) for designing future fusion devices such as ITER, STEP and DEMO as well as for JET decommission and repurposing (JDR)

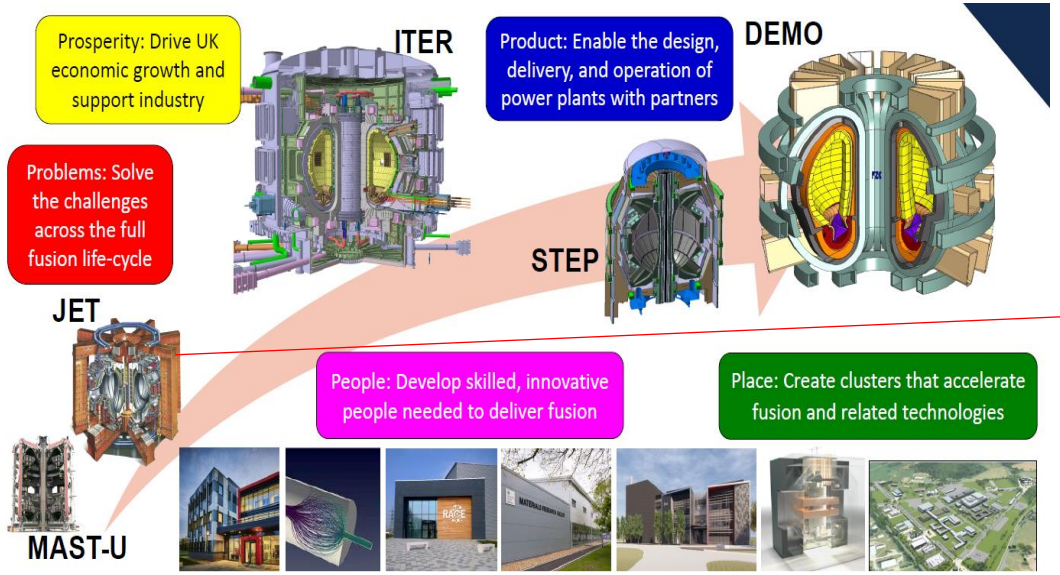

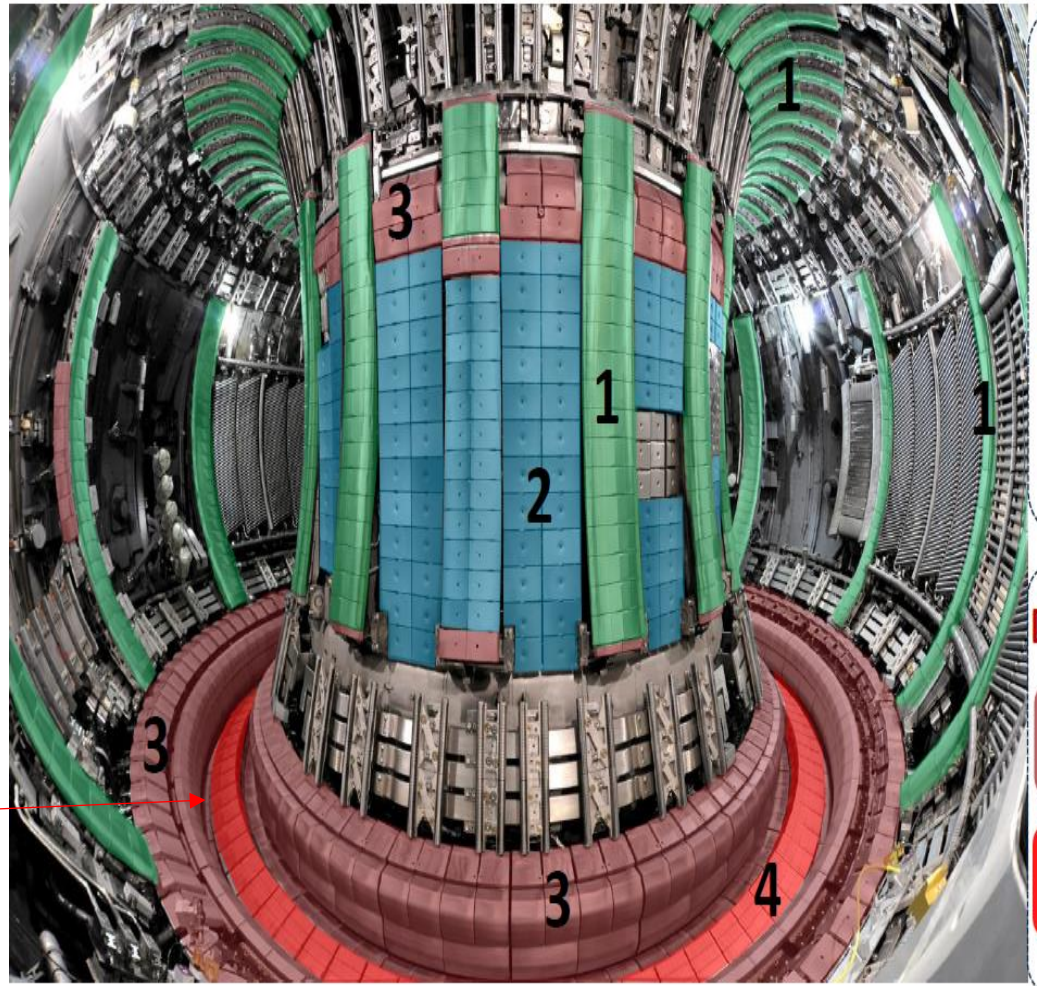

Main chamber

1 Bulk Be

2 Be coated inconel

3 W – coated CFC

DIVERTOR

3 W – coated CFC

4 Bulk W

See more from A. Widdowson talk

Tritium retention in plasma-facing materials: Oxidation and detritiation of tungsten

UK Atomic Energy Authority

JET ITER-like wall divertor

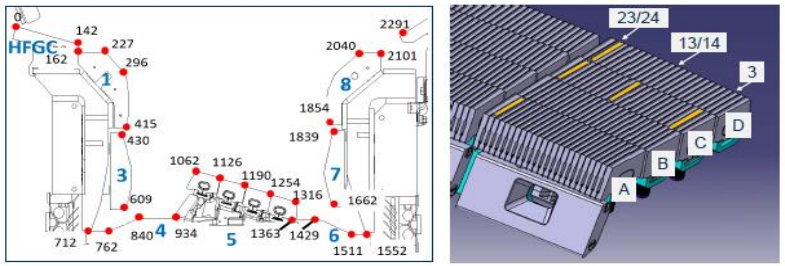

$(D + D \rightarrow 1.01\ MeV\ T + 3.03\ MeV\ p)$

Where D is deuterium, T is tritium and p is a proton.

JET Decommissioning Repurposing (JDR)
Materials Detritiation Facility (MDF)
Tritium Analysis Laboratory (TAL)

Post 650°C	Post 750°C (1)	Post 750°C (2)
21SID182	21SID187	21SID191
2.081	2.112	2.14
	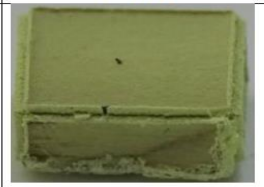	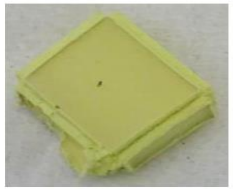

$F = 1 - C_f / C_0$

$DF = 1/(1 - F)$

Extraction Factor (F)	0.88 ± 0.1
Detritiation Factor (DF)	8.063 ± 1.11

The oxidation behaviour of fusion materials under maintenance, waste handling environment or in accident scenarios and impact on tritium recovery and storage

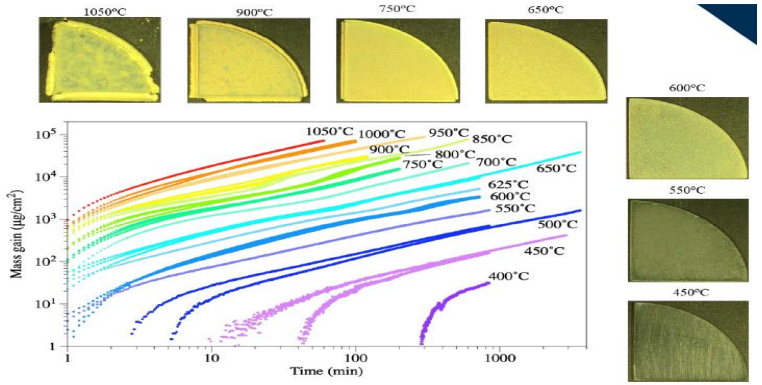

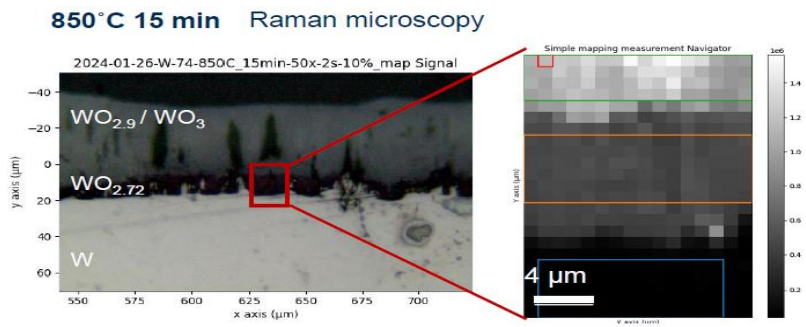

E. Prestat, STEP Report, 2024

Influence of thin surface oxide films on HI release from self-ion irradiated tungsten

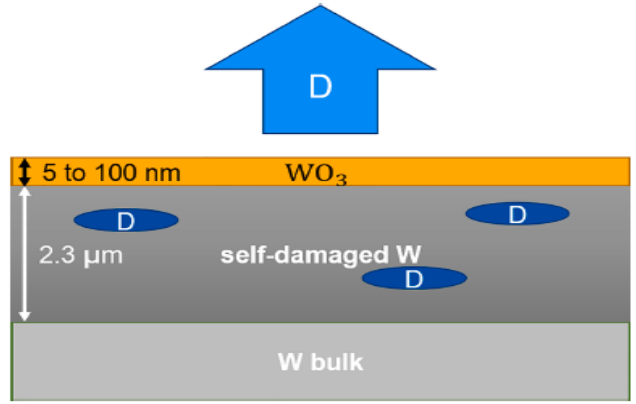

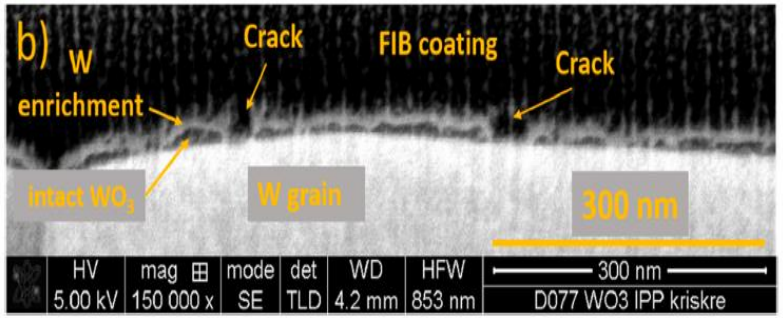

K. Kremer et al. (2021, 2022, 2023)

Tritium Inventory Modelling activities at UKAEA

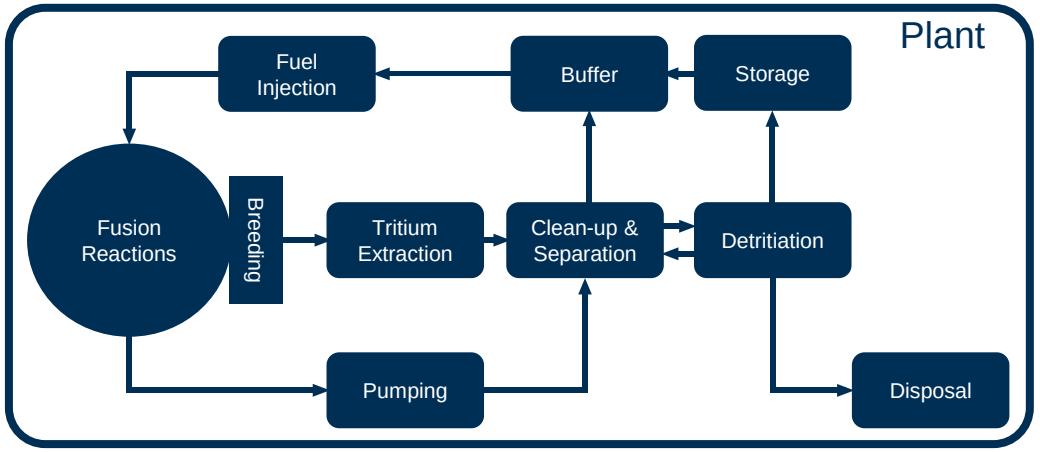

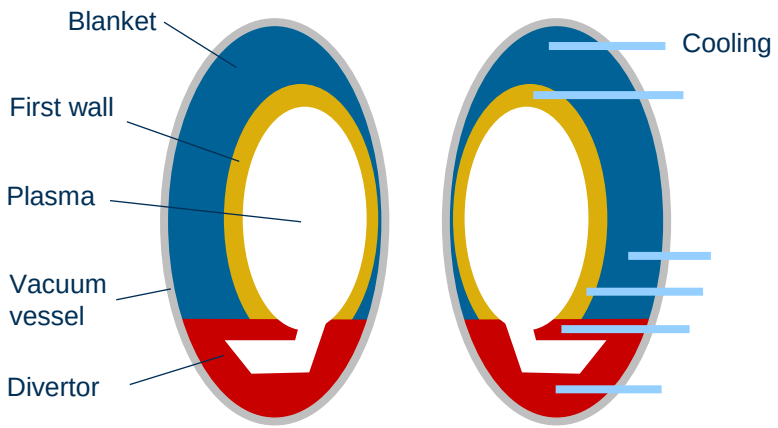

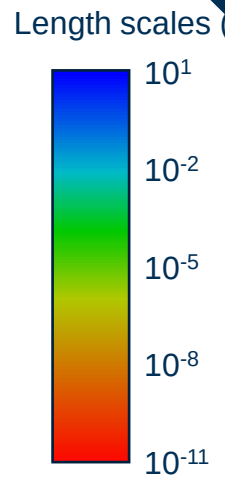

WP0: Process Architecture Modelling Modular approach, optioneering and analysis of full tritium cycle

Fuel Cycle BC
Plasma modelling, regulation

WP1: Process Technologies Modelling
Dynamic subsystem response

Pilot Plants AGHS, H3AT

WP2: Multi-physics Modelling
Component level, gradients in operating conditions

Lab-scale Experiments (other projects)
Permeability, desorption

See also from D. Mason talk

WP3: Diffusion and Trapping Mechanisms
Irradiation damage, microstructure, temperature and stress

WP4: Ab-Initio Models
Fundamentals of retention, isotopic effects

WP5: Model Interfacing, UQ and Analysis
Linking different models, improving model understanding, efficiency

WP6: Computational Frameworks and tools
Code maintainability, scalability, computational resourcing

Multi-scale and multi-physics modelling of hydrogen retention and diffusion

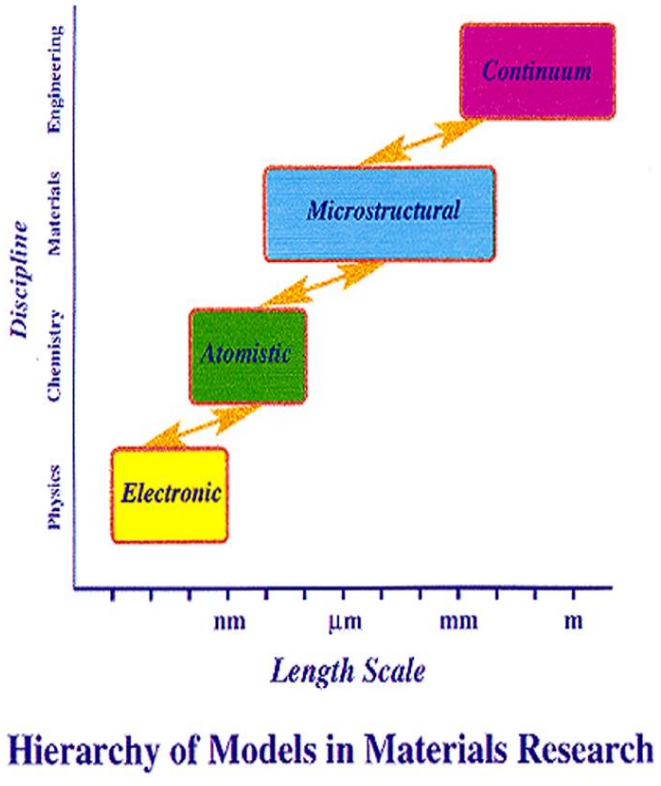

Hierarchy of Models in Materials Research

DNM et al., Phil. Trans. Royal Soc. London, 315, 529 (1995)

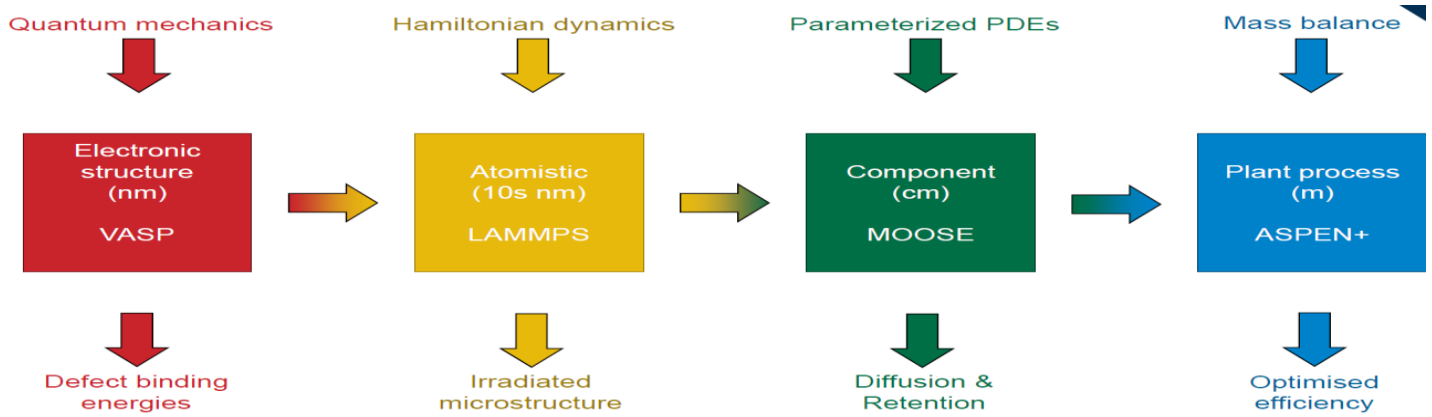

PALIOXIS code: D. Mason et al., UKAEA Materials Science Seminar, 2nd July (2024)

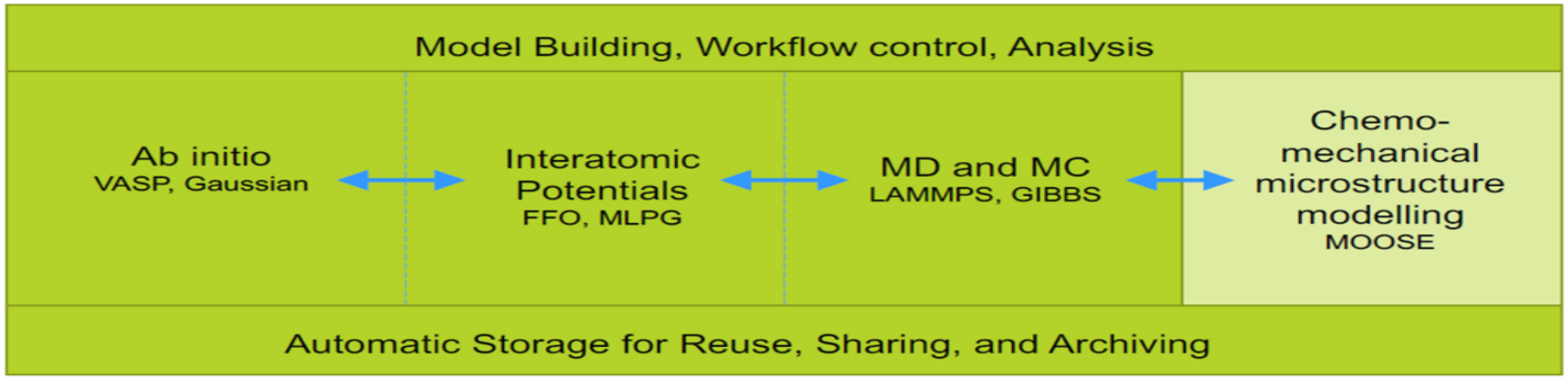

Multi-physics model suitable to scale-up to engineering component scale

UK Atomic Energy Authority

➢**PALIOXIS code developed within TIM program at UKAEA for finite-element hydrogen-isring otope modelling of diffusion and retention in metallic materials from first-principles ab-initio calculations for use with MOOSE**

❑**multi-trap** from extensible as DFT/MLEP database extends

❑**multi-gas** allows for He-HI interaction with chemical potentials

❑**multi-occupancy** correct thermodynamics for trapping energies

❑**multi-dynamics** long-lived transients & steady state together

➢**PALIOXIS is a new multi-scale materials modelling code and not TMAP/FESTIM clone**

➢**The code used will be made public after the acceptance of 2024 paper written in collaboration with Advanced Computing**

➢**Movie:** 3D mono-block multi-isotopes and multi-occupancy test simulations with 0.1 at. % of mono-vacancy for W/Cu-Cr-Zr/Cu layers with equal flux of D and T at surface (10^{19} ions/m2/s), head load of 8MW/m2, inside pipe convective cooling to water at 320Ke

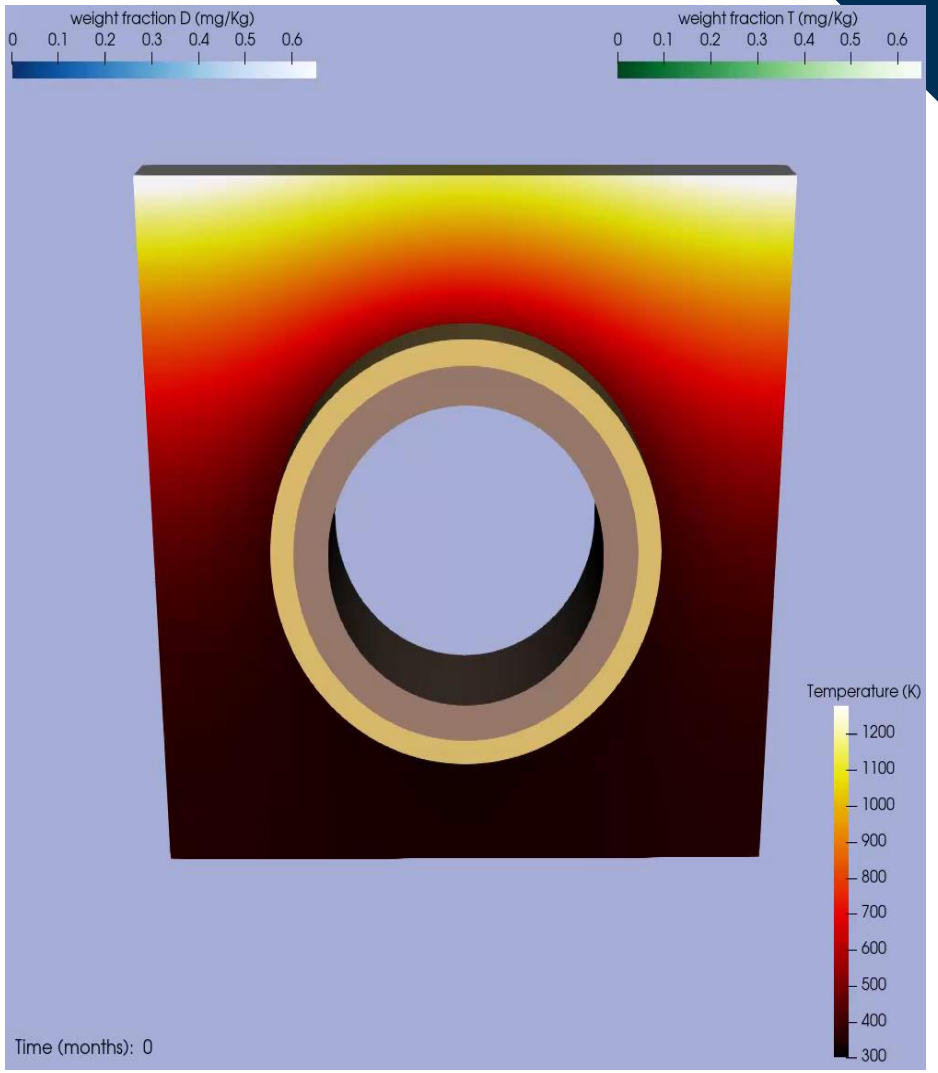

Stability of tungsten oxide phases

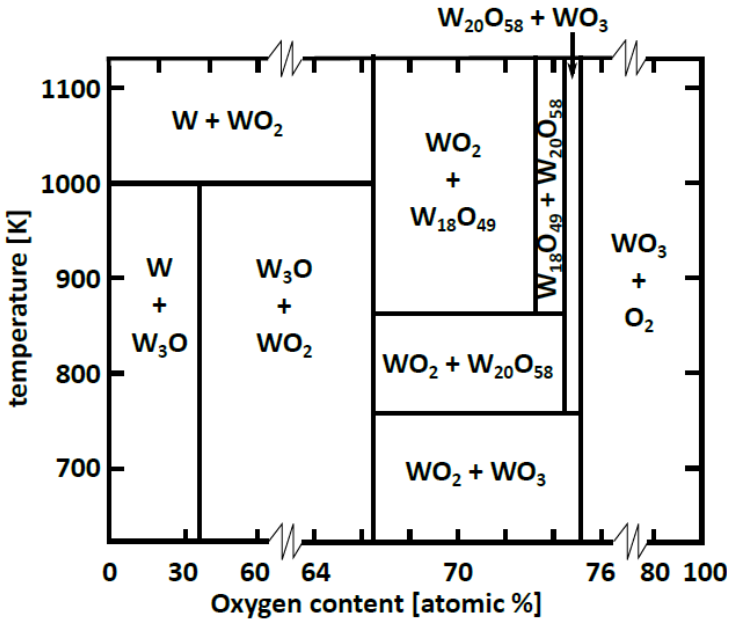

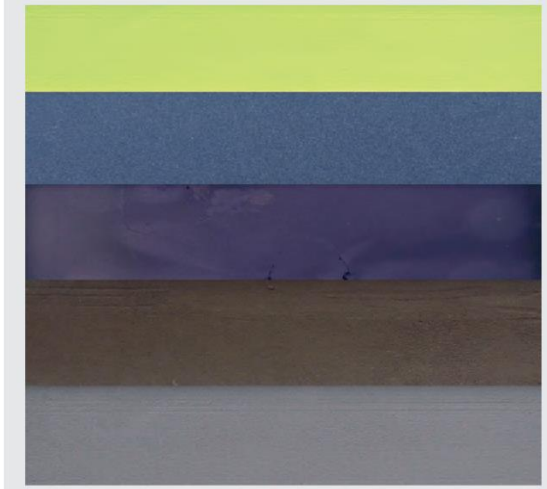

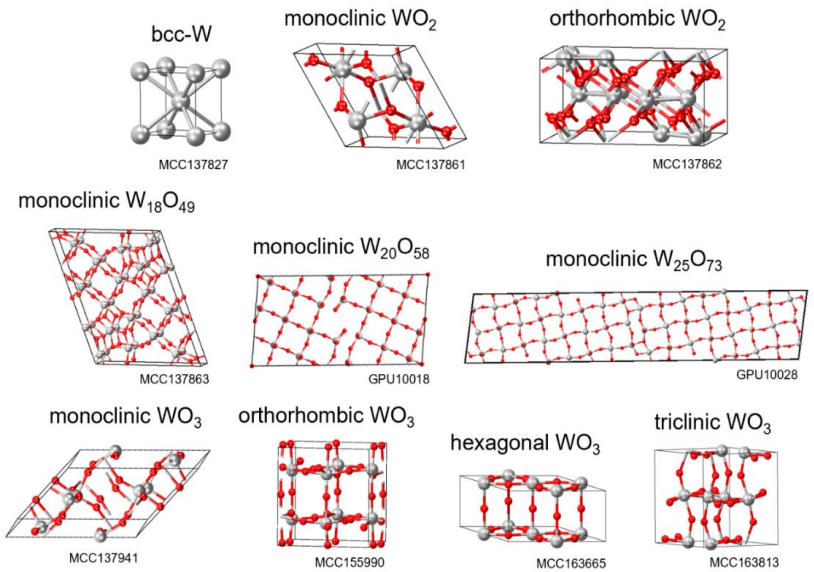

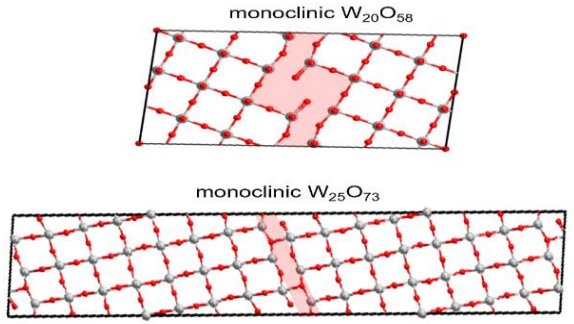

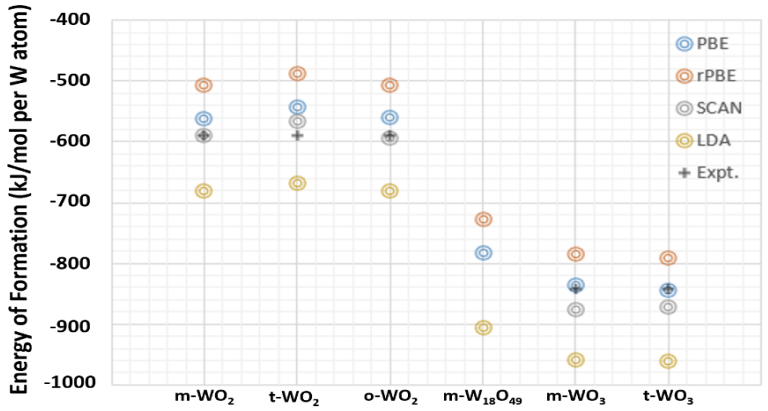

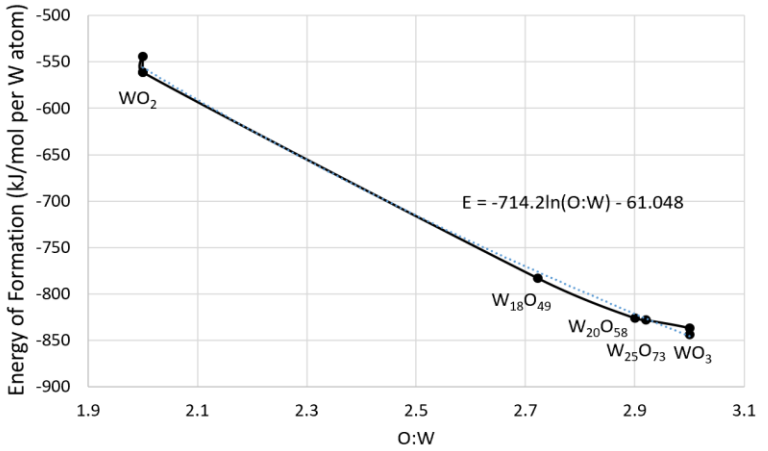

Predicted vs. experimental data for enthalpy of formation as a function of O concentration

Free energy of solution for T(H, D) in W-O phases

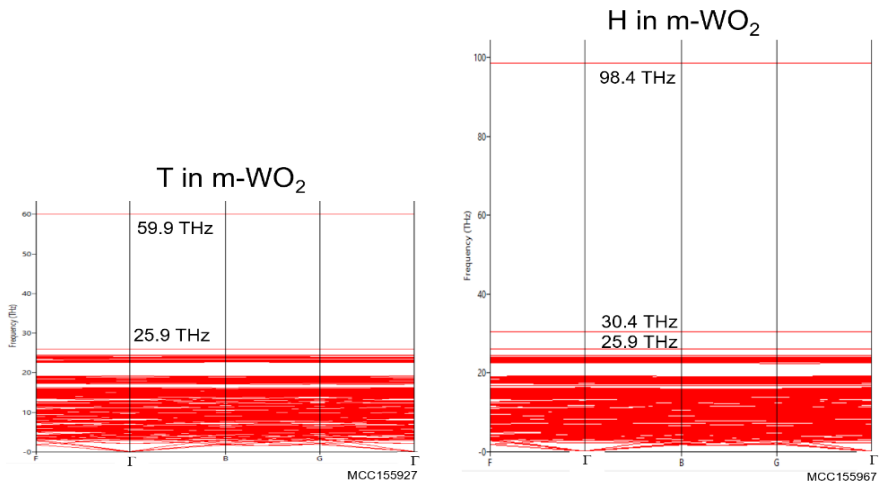

	O-H (THz)	O-D (THz)	O-T (THz)
bcc-W	35.2, 45.8	24.9 32.4	20.5, 26.5
WO_2 (monoclinic)	22.8, 30.4, 98.4	17.3, 21.8, 71.4	11.1, 15.6, 19.2, 59.9
WO_2 (orthorhombic)	34.5, 40.6, 42.6	24.8, 29.5, 32.1	20.9, 24.6, 28.6
$W_{18}O_{49}$ (monoclinic)	16.3, 29.6, 99.5	14.0, 19.7, 72.3	10.5, 17.1, 60.5
WO_3 (monoclinic)	20.9, 37.1, 88.9	16.1, 27.1, 64.2	14.3, 22.0, 54.5
WO_3 (orthorhombic)	23.0, 38.9, 84.2	16.3, 27.5, 59.6	14.4, 23.7, 51.8
WO_3 (hexagonal)	6.4, 29.6, 110.8	4.5, 20.9, 78.4	3.7, 17.2, 64.3
WO_3 (triclinic)	12.7, 31.5, 107.8	9.0, 22.3, 76.3	7.4, 18.3, 62.5

Active Raman modes of H, D, T in W-O phases

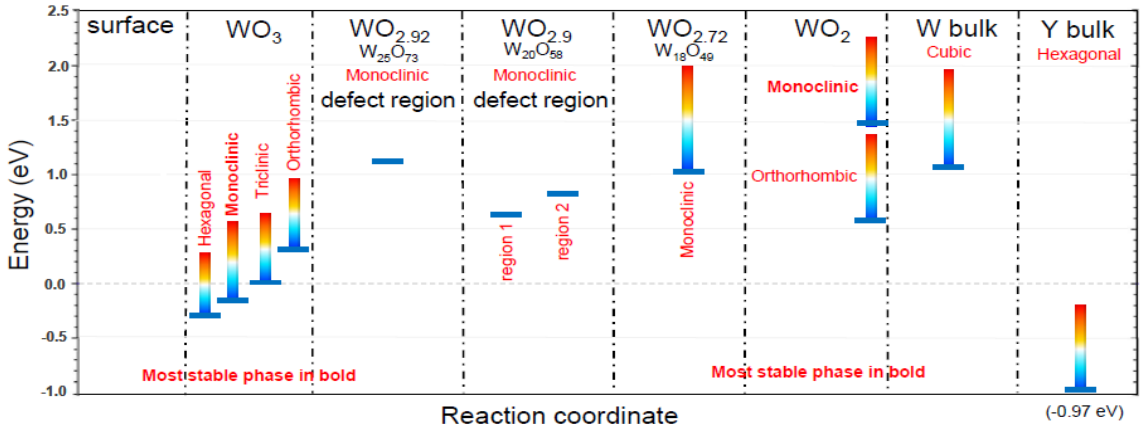

Exothermic reaction of T(H) in monoclinic WO3 at T=0K. Free energy of insertion of H and T in m-WO3 becomes positive as function of temperature in an excellent agreement with experimental data at T=0K

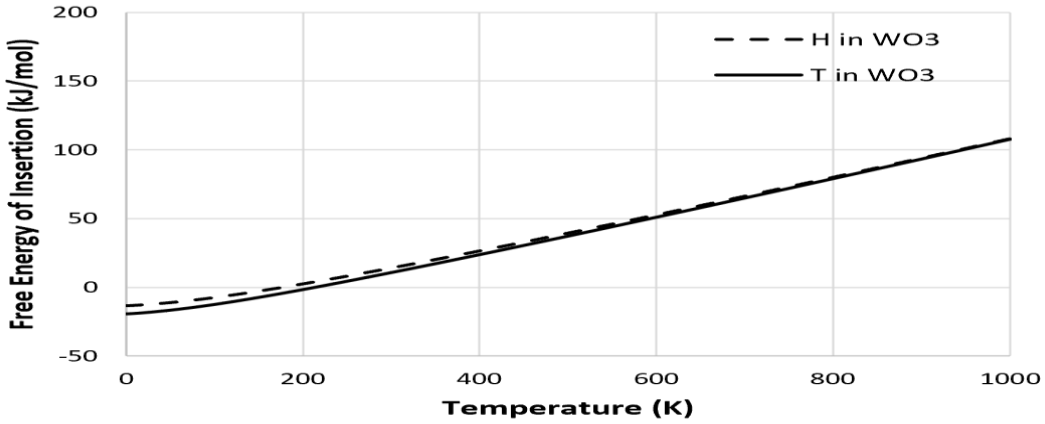

Tritium diffusion in W & W-O systems

The temperature-dependent diffusion coefficients of interstitial T(H) in bcc-W and W-O phases are computed using Kinetic Monte Carlo and transition state theory. The jump rate is given by

$$\Gamma = \frac{kT}{h} \frac{\prod_{i=1}^{3N-7}\left[2\sinh\left(\frac{h\nu_i^{TS}}{2kT}\right)\right]^{-1}}{\prod_{i=1}^{3N-6}\left[2\sinh\left(\frac{h\nu_i^{0}}{2kT}\right)\right]^{-1}} e^{-\frac{\Delta E_{el}}{kT}}$$

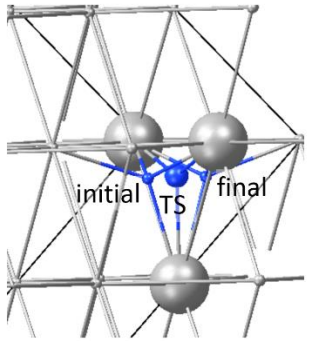

MLFF trajectory

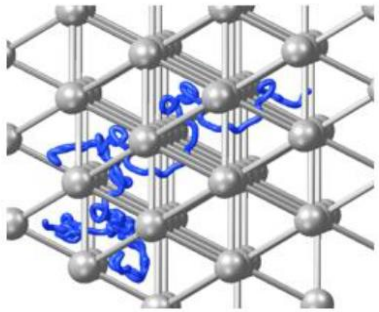

Connecting tetrahedral sites

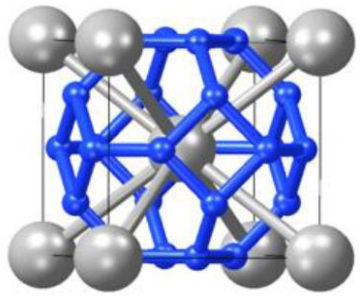

Truncated octahedron shape

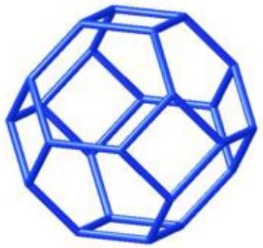

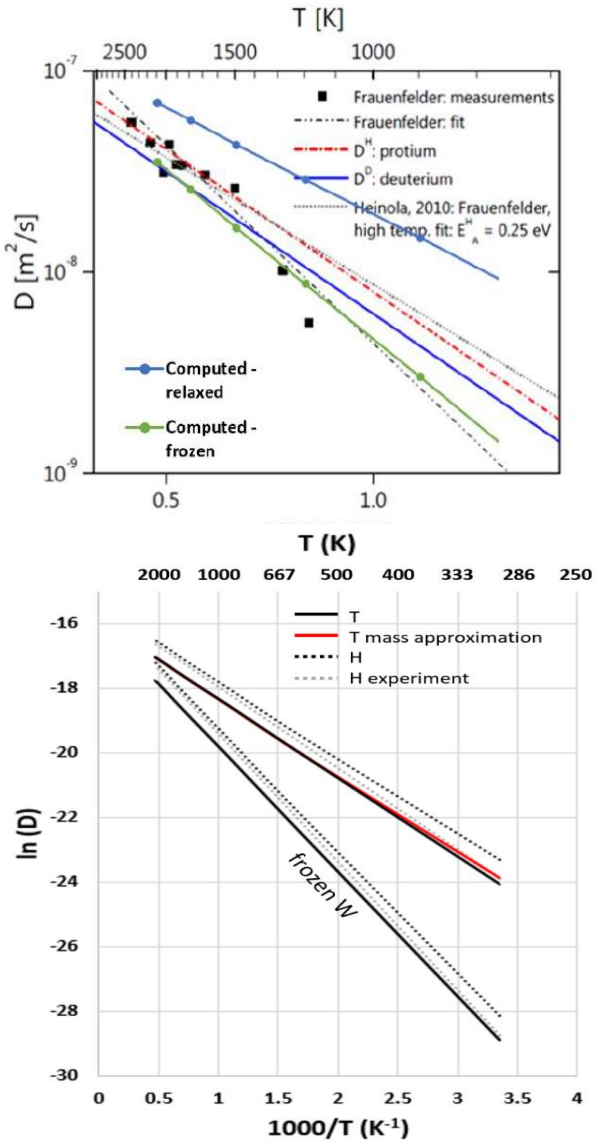

- The Arrhenius plot gives a pre-factor of D_0 = **2.06×10^{-7} m²/s** and **effective barriers E_A of 0.20 eV** and 0.33 eV (frozen lattice), respectively
- The ab-initio computed plots are in excellent agreement with experimental data recently compiled by Holzner et al. (2000) for H in W

HI diffusion paths in WO2 and WO3

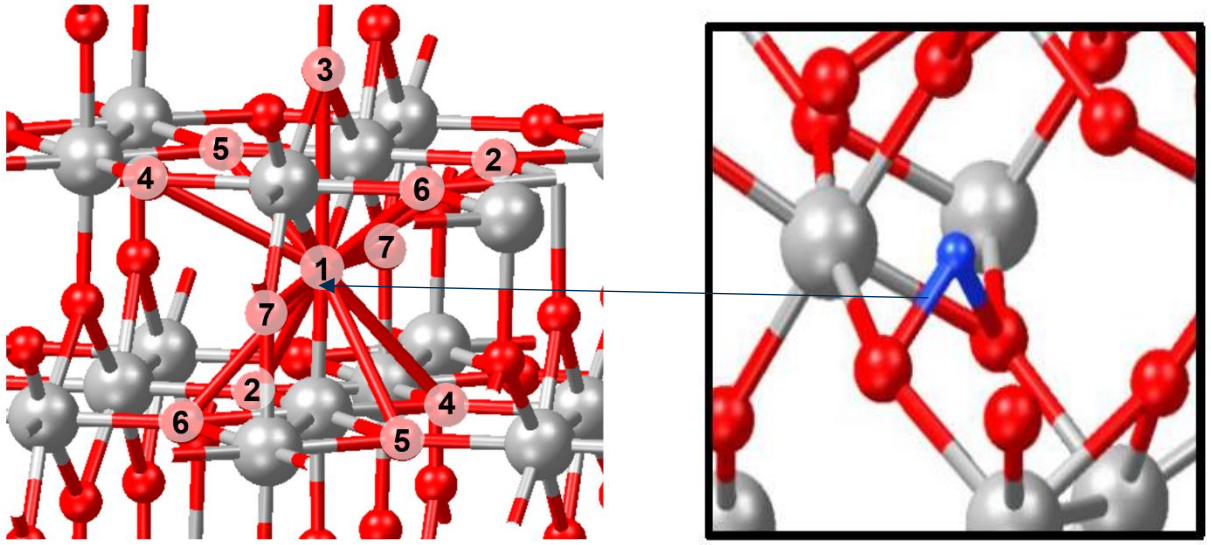

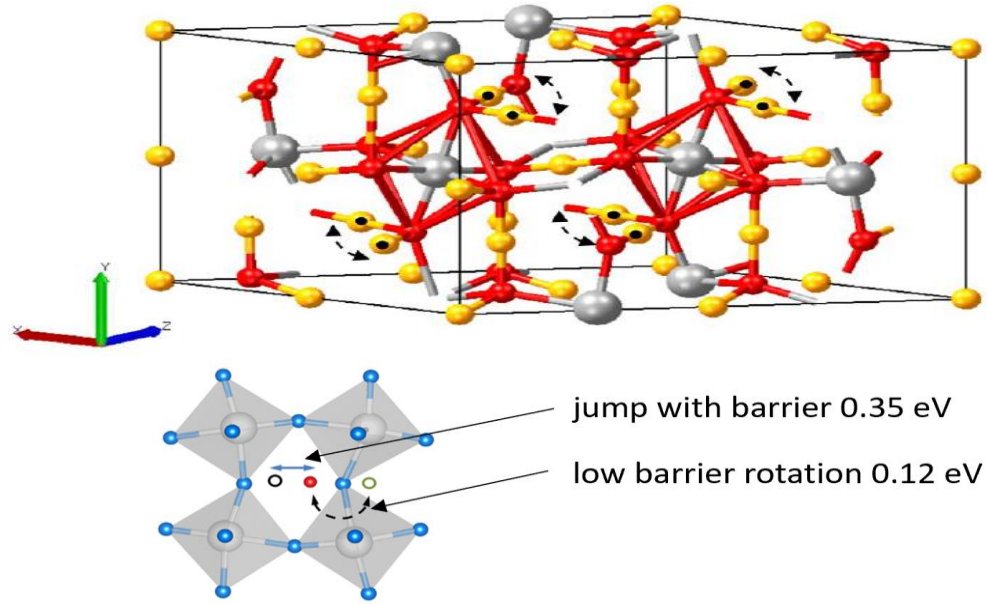

Table 5-3. Computed diffusion barriers for T(H) in m-WO_2. The jumps refer to the site labels in Figure 5-33. The values include zero-point energies.

Jump	*Barrier for H (eV)*	*Barrier for T (eV)*
1→2,4,5,6	0.77	0.81
1→3	1.01	1.06
1→7	0.96	1.03

Table 5-4. Diffusion barriers for tritium in m-WO_3. The values include zero-point energy. Entries indicated by "small" are just a few hundredths of eV.

Jump	1	2	3	4	5	6	7	8	
Barrier (eV)	small	0.81	0.71	0.86	0.40	0.51	small	0.77	
Jump	9	10	11	12	13	14	15	16	
Barrier (eV)	0.62	0.62	0.88	0.59	0.66	small	0.69	0.80	
Jump	17	18	19	20	21	22	23	24	25
Barrier (eV)	0.73	0.72	small	0.74	0.64	small	small	0.78	0.73

Diffusion of H(T) in tungsten oxides

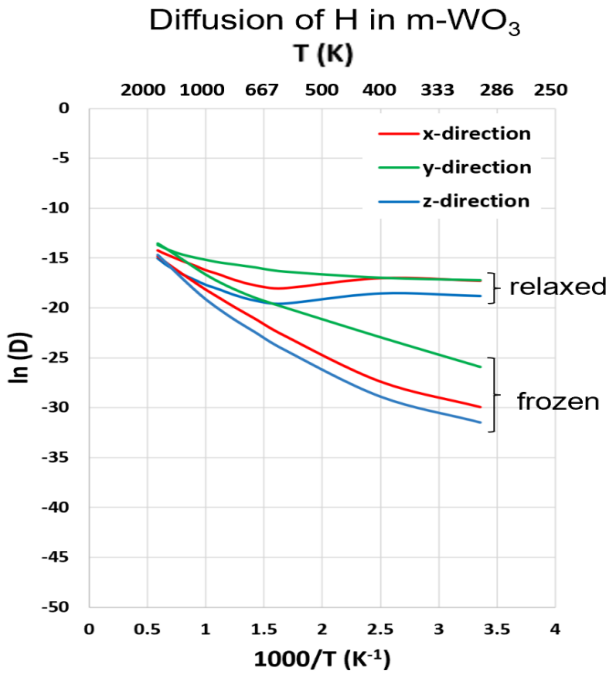

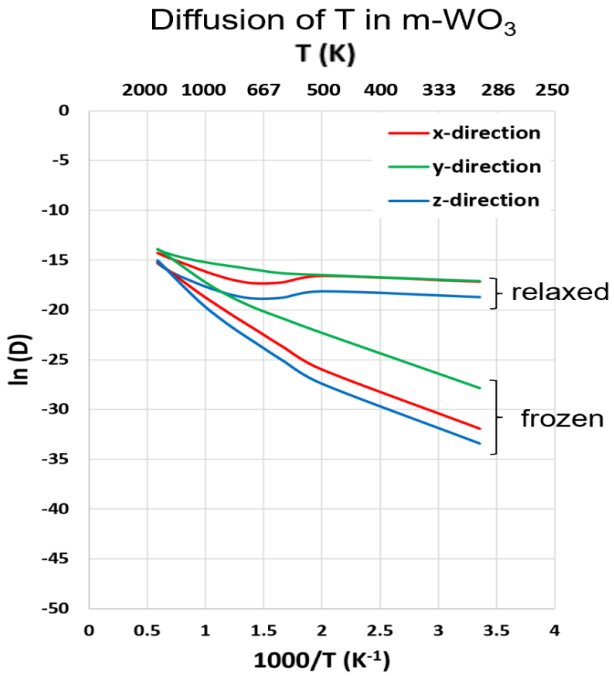

$D_0 = 4.56\times10^{-8}$ m^2/s T ≤ 600 K

$E_A = 0.02$ eV

$D_0 = 2.65\times10^{-6}$ m^2/s T > 600 K

$E_A = 0.24$ eV

$D_0 = 7.84\times10^{-8}$ m^2/s T ≤ 700 K

$E_A = 0.03$ eV

$D_0 = 2.44\times10^{-6}$ m^2/s T > 700 K

$E_A = 0.25$ eV

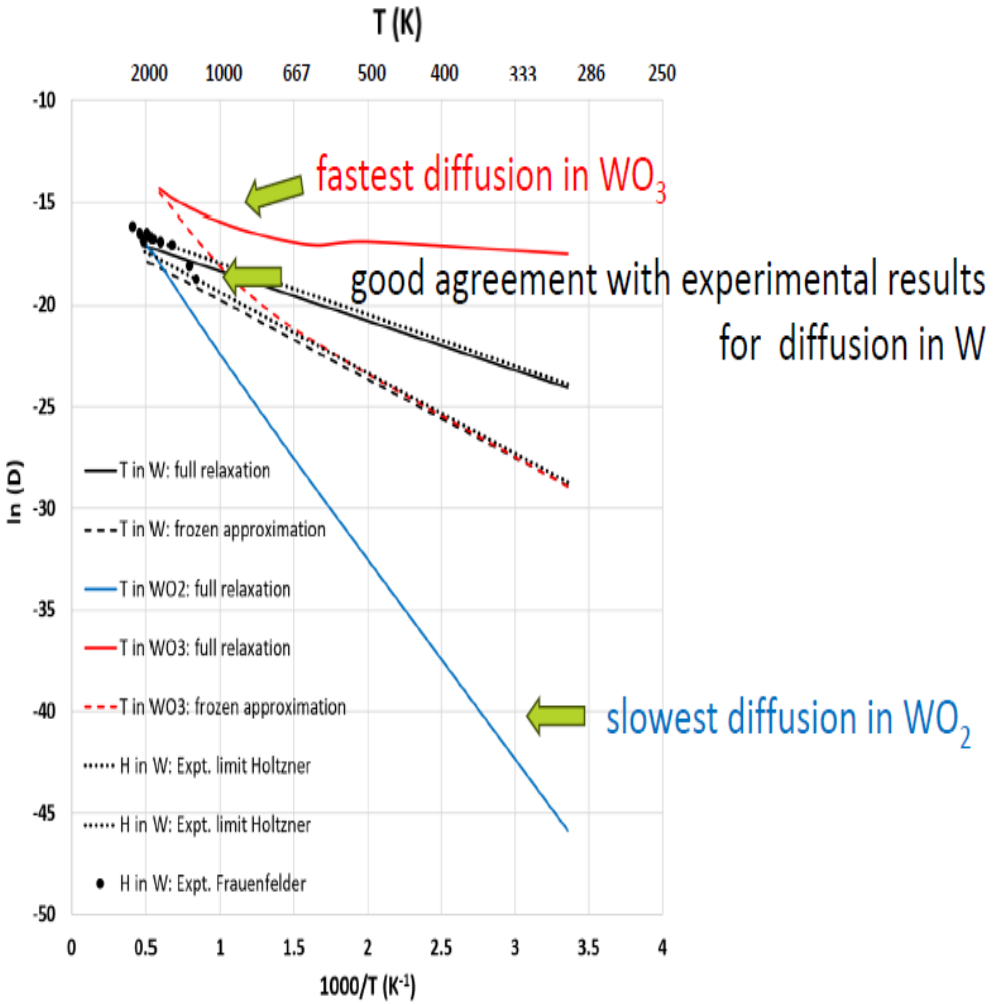

The diffusion coefficients for H and T within the diffusion models (frozen vs.relaxed) in tungsten trioxide (m)

T trapping by defects (vacancy, SIA) in W

Trapping free energy of tritium in bcc-W at different temperature

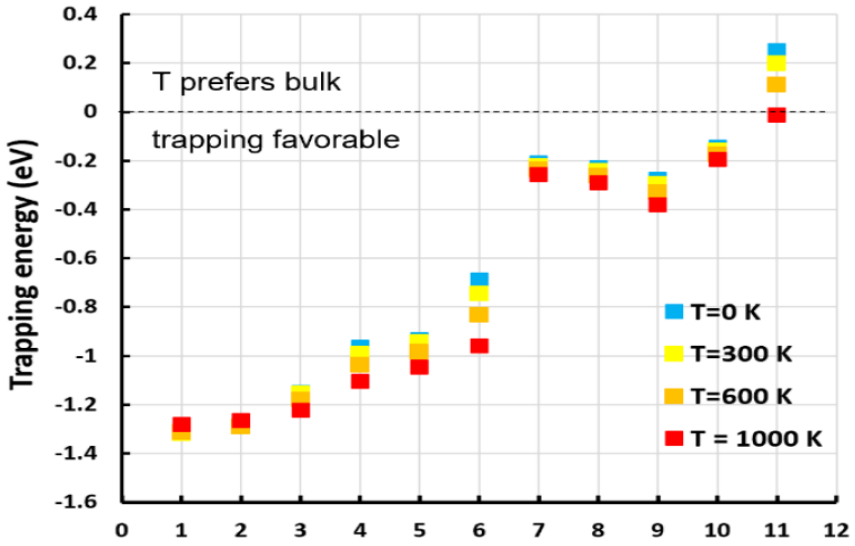

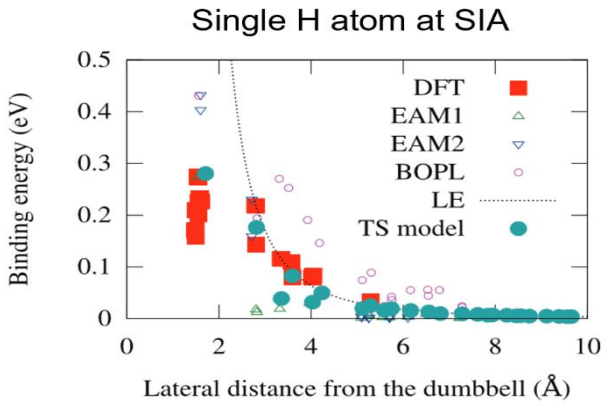

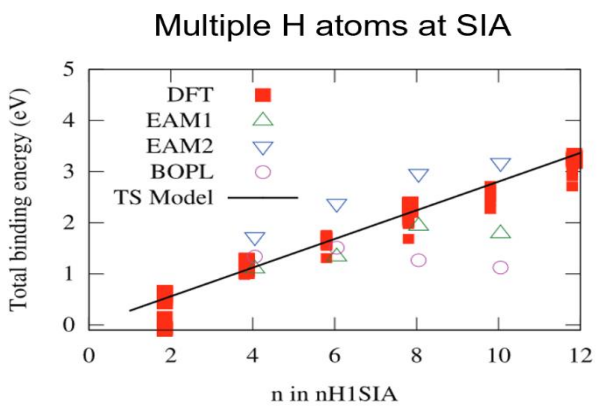

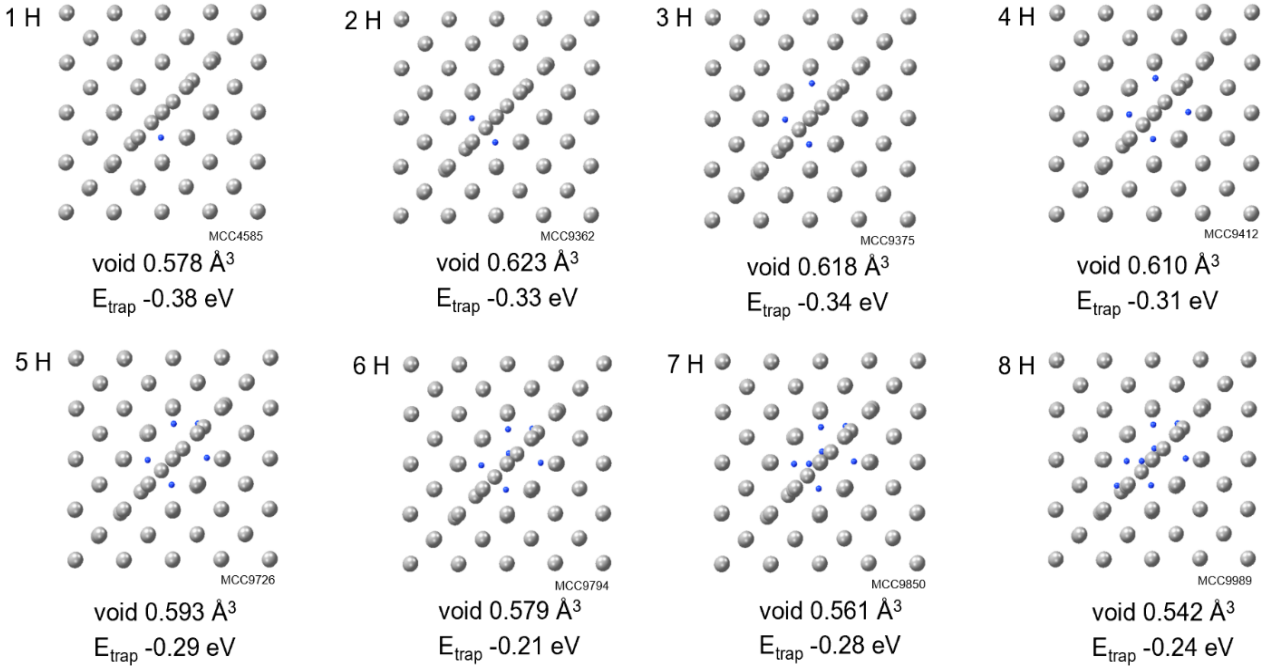

Trapping of H at an SIA in W. The H atoms are successively inserted into the largest voids at the SIA (the void volumes are given for each configuration).

Binding energies of H atoms at an SIA in W, [A. De Backer et al., Nucl. Fusion 58, 016006 (2018)]

Trapping of multiple H atoms in a W/O vacancy in m-WO_2

UK Atomic Energy Authority

Trapping of multiple H atoms (1-6) in an W vacancy in m-WO_2.

. The O vacancy can accommodate 3 H atoms, and additionally 2 H atoms that are weakly bound.

2 H atoms (pos 1 and 2)

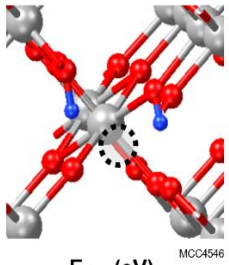

E_{trap} (eV)

2^{nd} H atom: -1.50

2 H atoms (pos 1 and 3)

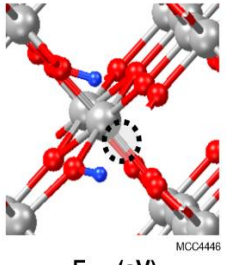

E_{trap} (eV)

2^{nd} H atom: -1.53

3 H atoms (pos 1, 2 and 3)

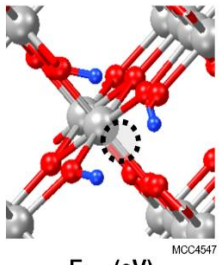

E_{trap} (eV)

3^{rd} H atom: -1.26

3 H atoms (pos 1, 2 and 4)

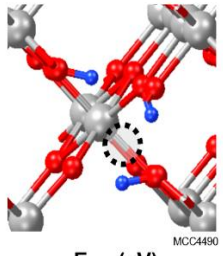

E_{trap} (eV)

3^{rd} H atom: -1.17

4 H atoms (pos 1, 2, 3, 4)

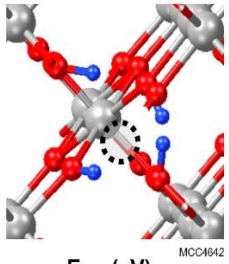

E_{trap} (eV)

4^{th} H atom: -0.31

4 H atoms (pos 1, 2, 3, 5)

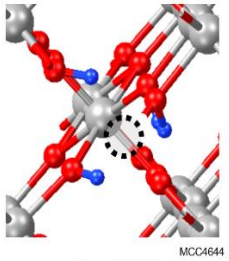

E_{trap} (eV)

4^{th} H atom: -0.36

5 H atoms (pos 1, 2, 3, 4, 5)

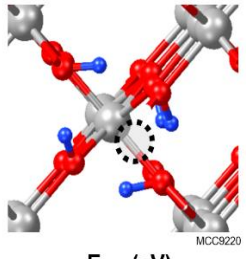

E_{trap} (eV)

5^{th} H atom: -0.74

6 H atoms (pos 1, 2, 3, 4, 5, 6)

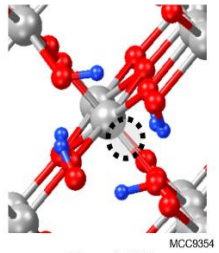

E_{trap} (eV)

6^{th} H atom: -0.38

1 H

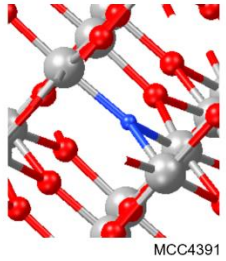

E_{trap} (eV)

-2.14

2 H

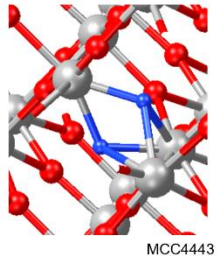

E_{trap} (eV)

2^{nd} H atom: -0.71

3 H

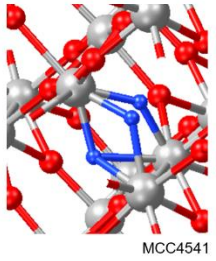

E_{trap} (eV)

3^{rd} H atom: -0.31

4 H

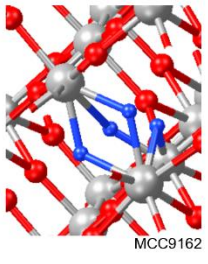

E_{trap} (eV)

4^{th} H atom: -0.05

5 H

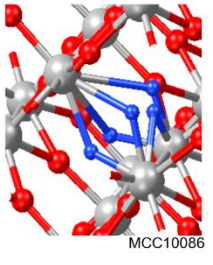

E_{trap} (eV)

5^{th} H atom: -0.12

Trapping of H at an O interstitial in m-WO_2. The interstitial binds one H atom strongly

1 H

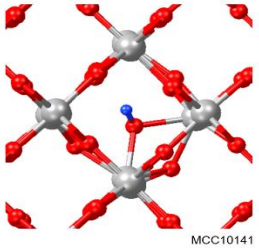

E_{trap} (eV)

-1.47

2 H

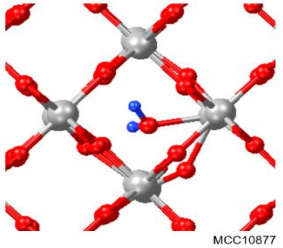

E_{trap} (eV)

-0.17

3 H

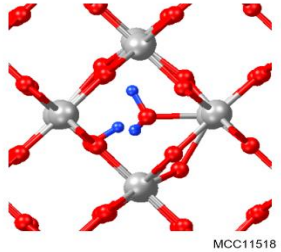

E_{trap} (eV)

+0.15

O vacancy/interstitial as the HI trapping defects in m-WO3

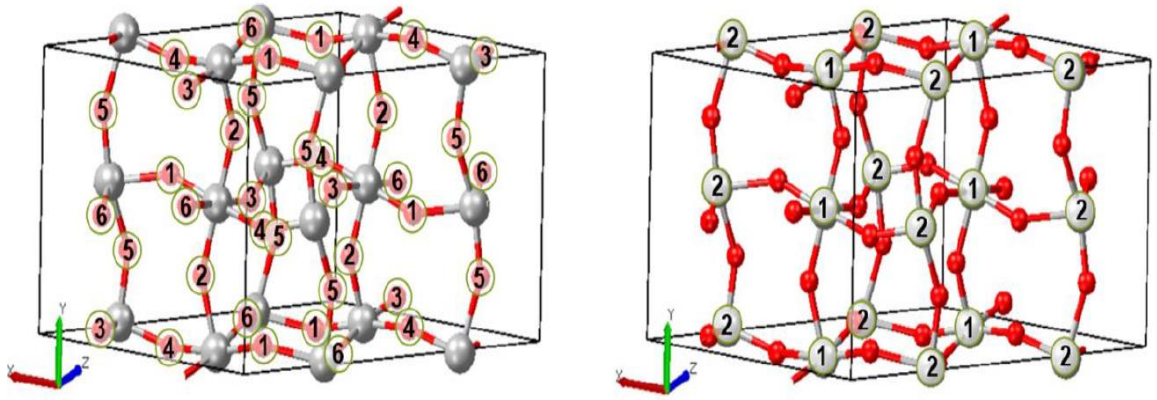

Figure 5-67. (Left) There are six symmetry independent O atoms in m-WO_3. (Right) There are two symmetry independent W atoms in m-WO_3.

Vacancy configuration	E^f_{vac} (eV)	$E_{vac\text{-}vac}$ (eV per vac)	V^f_{vac} ($Å^3$ per vac)
1	3.30		+3.1
1-2	3.32	+0.02	+4.8
1-2-3	3.40	+0.09	+7.3
1-2-3-4	3.49	+0.19	+7.6

Free energies of trapping of T(H) by O vacancy in m-WO3 phase

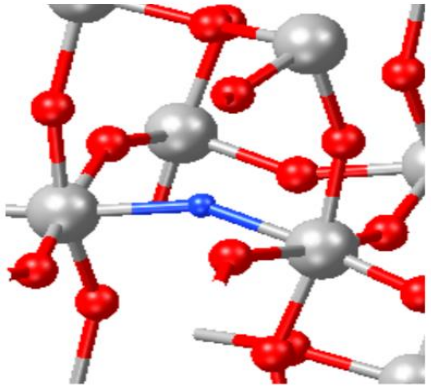

Temperature (K)	E_{trap} for T (eV)	E_{trap} for H (eV)
0	-0.88	-0.92
300	-0.94	-0.98
600	-1.07	-1.10
1000	-1.28	-1.30

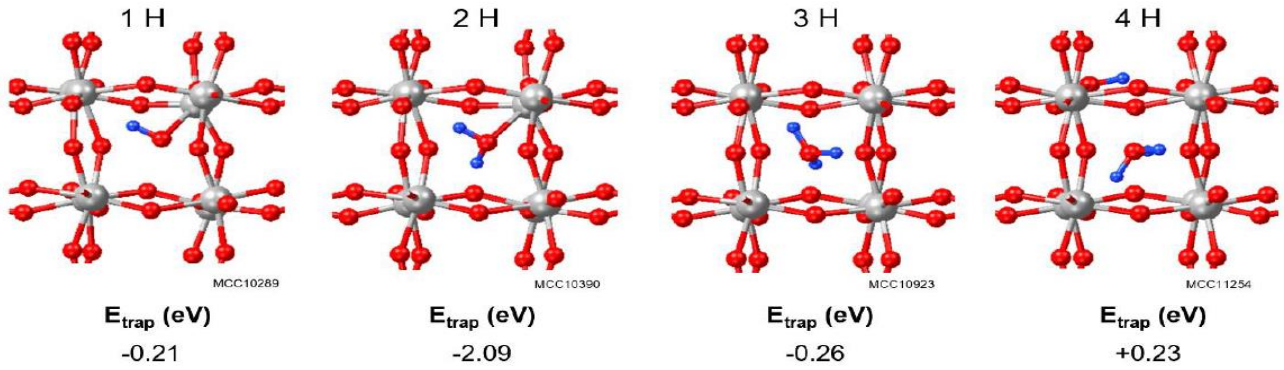

Trapping of H at O interstitial in m-WO3.
Water (H2O) molecule is formed with 2H atoms

Ab-initio results vs. empirical model

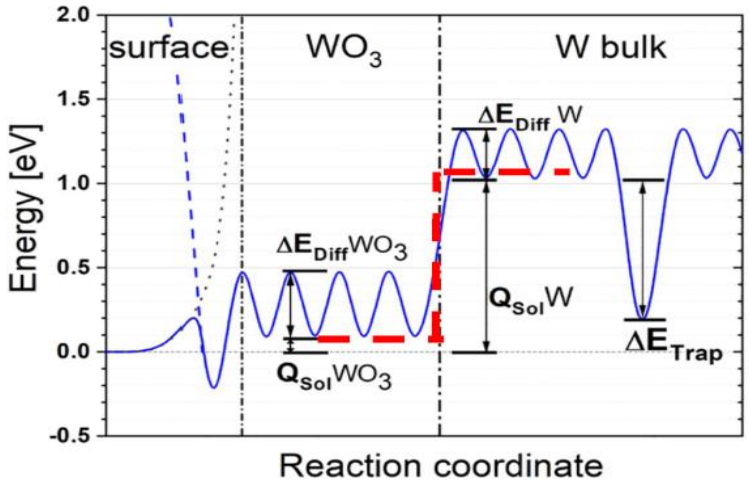

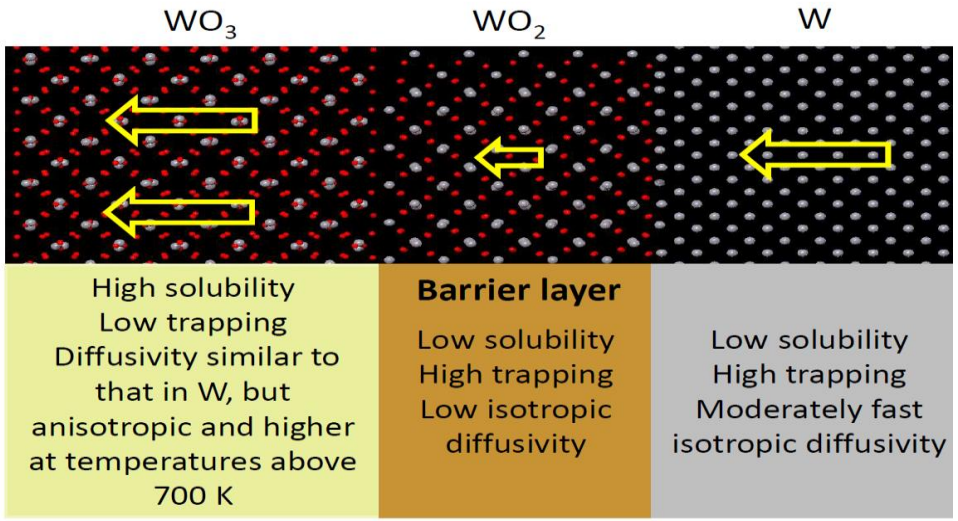

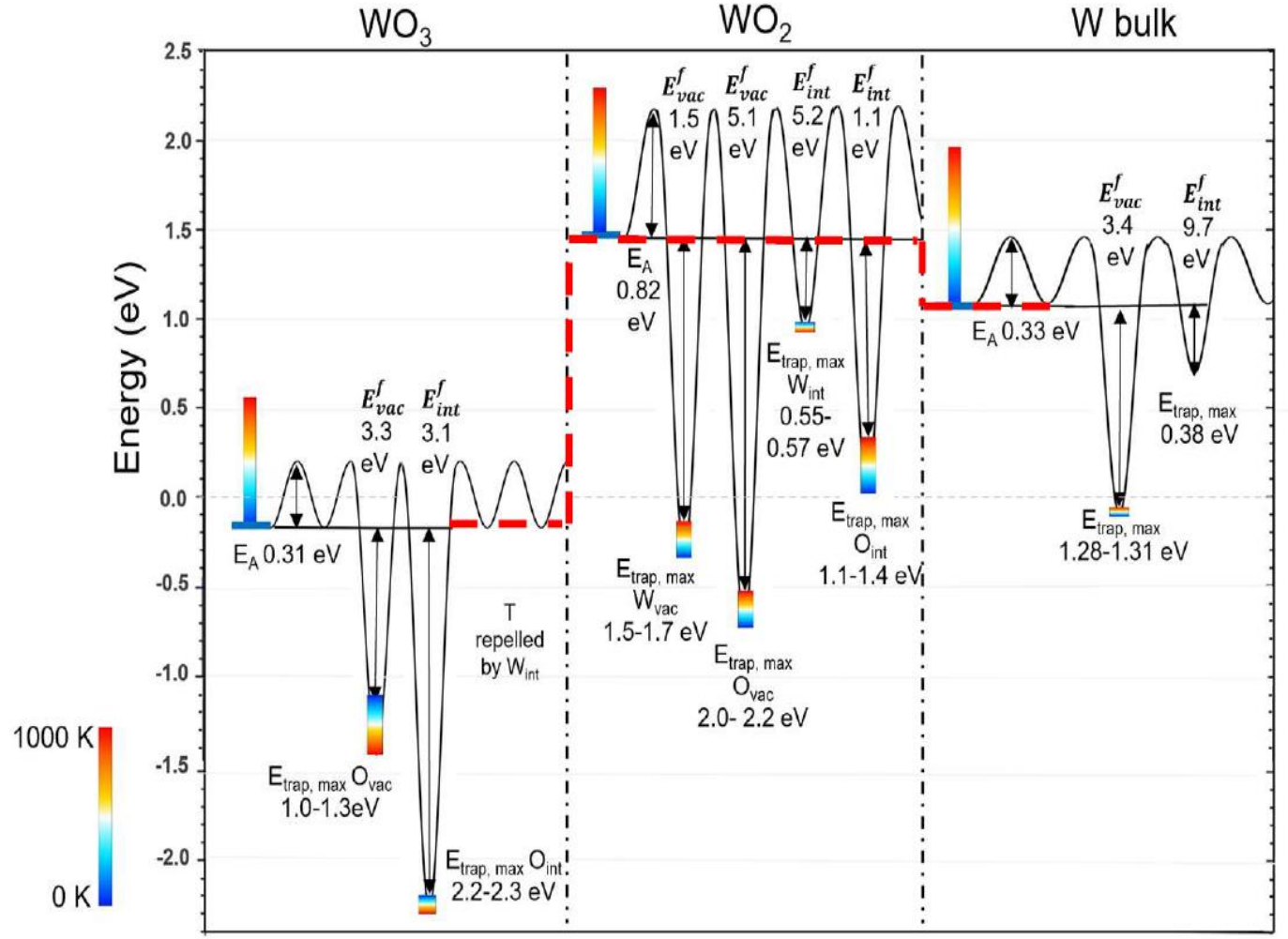

M. Christensen et al., Nucl. Mater. Energy, 38 (2024) 101611

HI adsorption and surface segregation (free) energies in W and WO2

$$E_{ads} = E_{surf,\ H} - E_{surf} - \tfrac{1}{2}\ E_{H2}.$$

$$E_{segr} = E_{surf,H} + E_{bulk} - E_{surf} - E_{bulk,H}$$

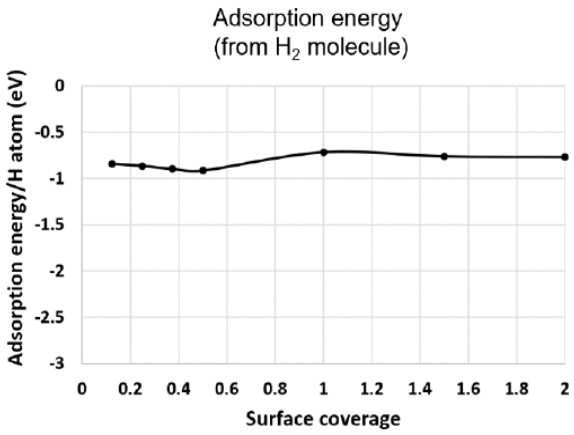

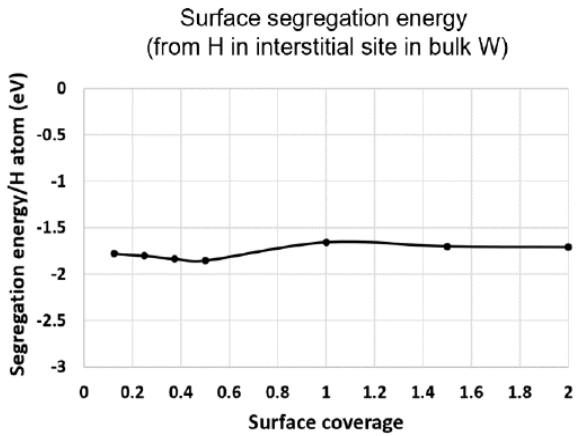

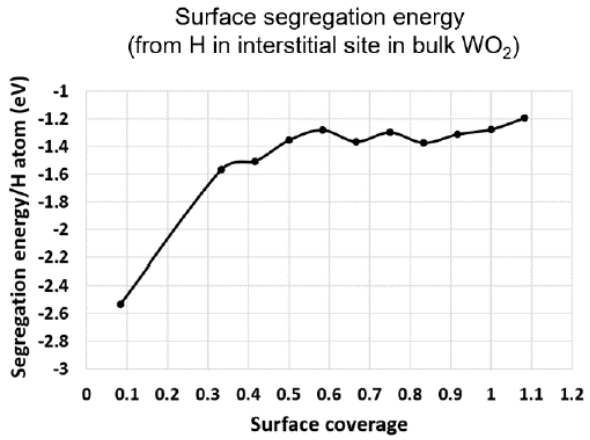

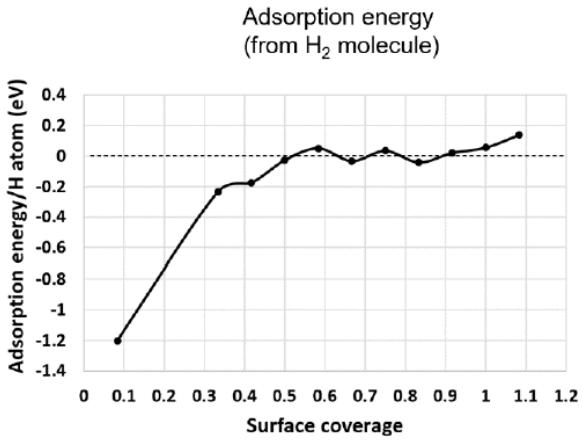

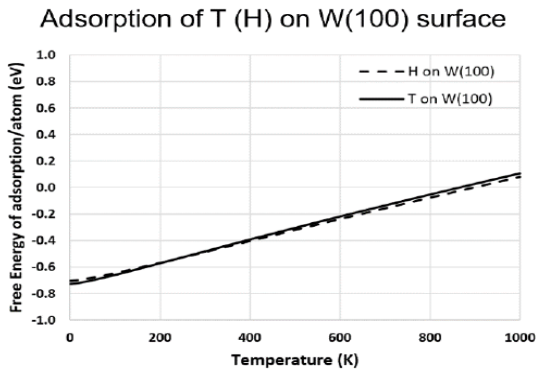

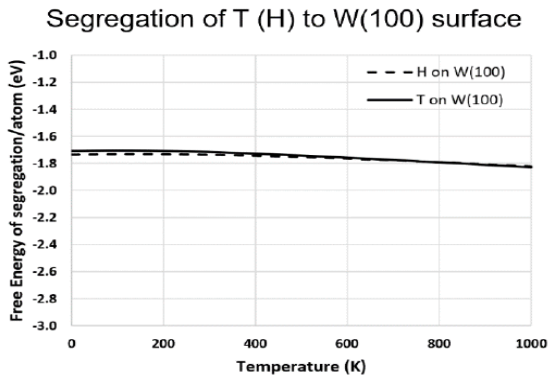

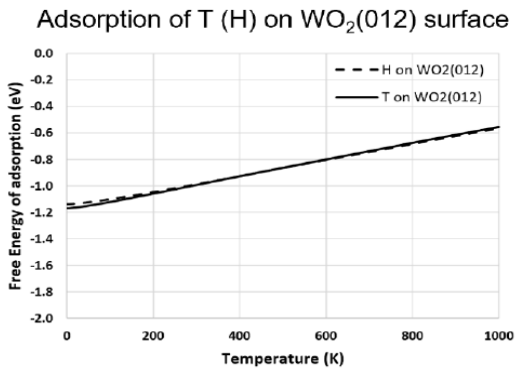

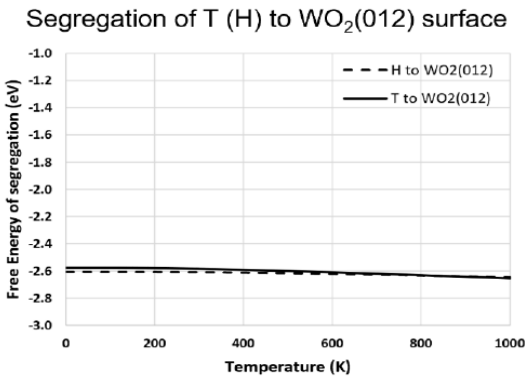

HI adsorption and segregation free energies in WO3

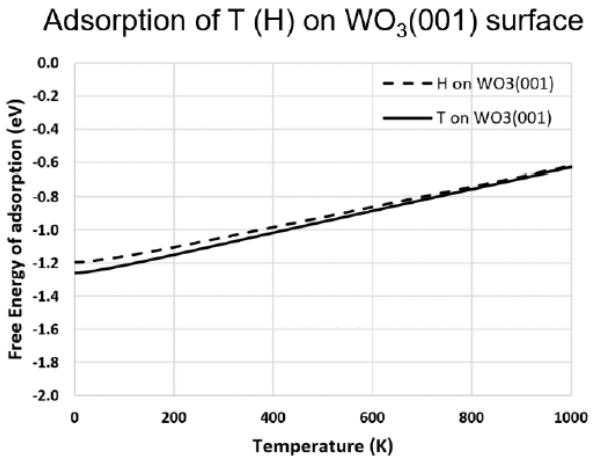

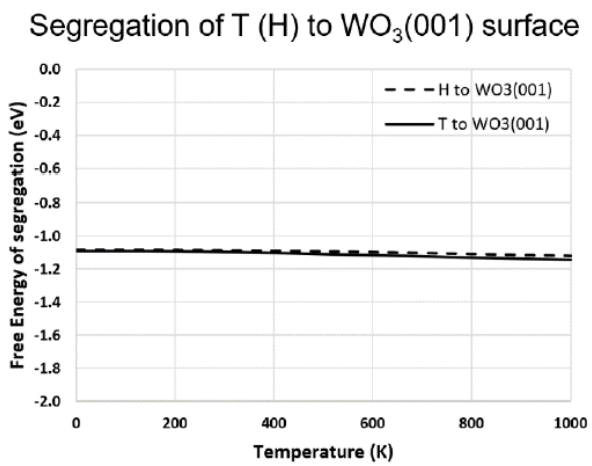

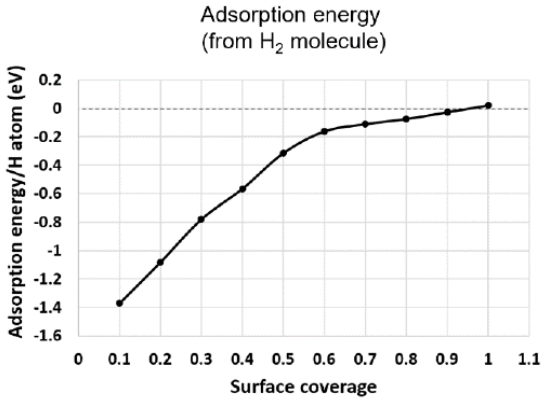

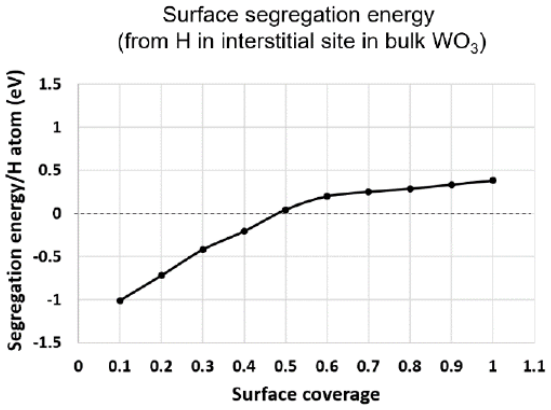

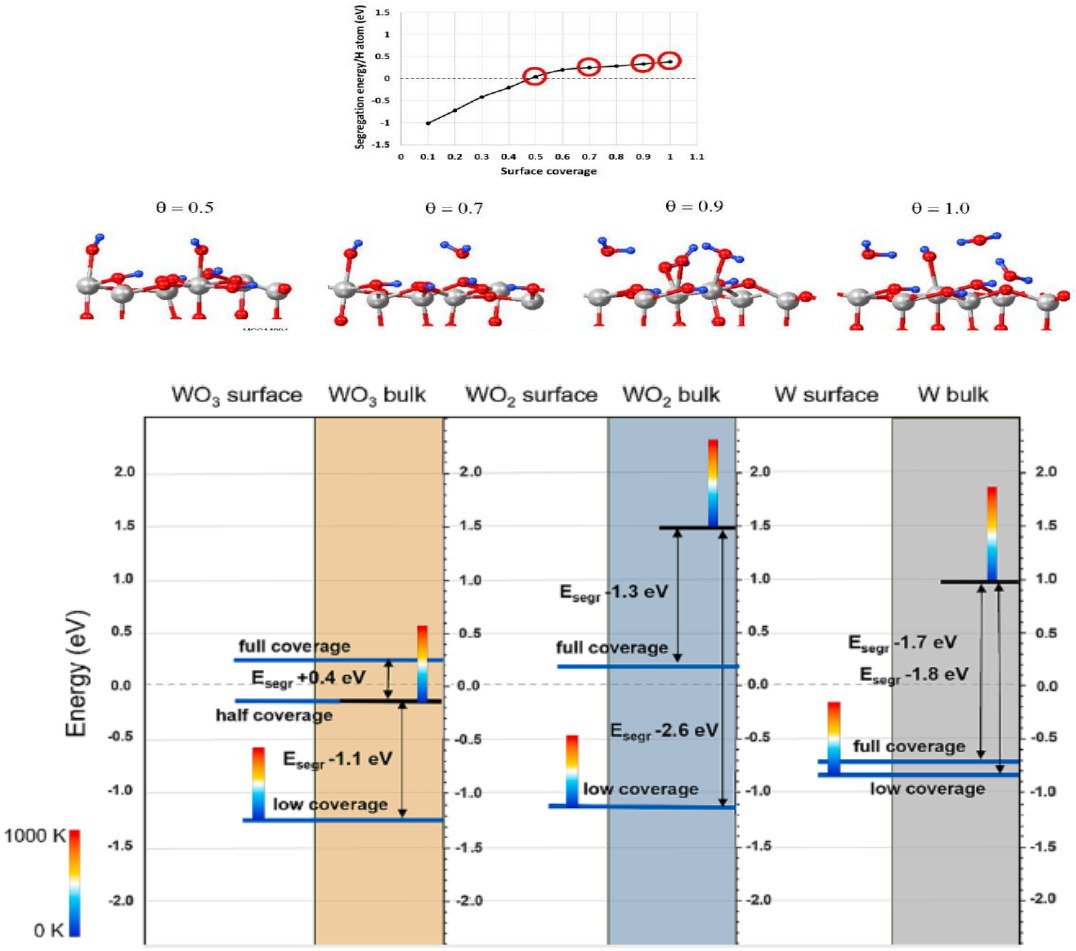

Colour of W oxides from optical spectra calculations

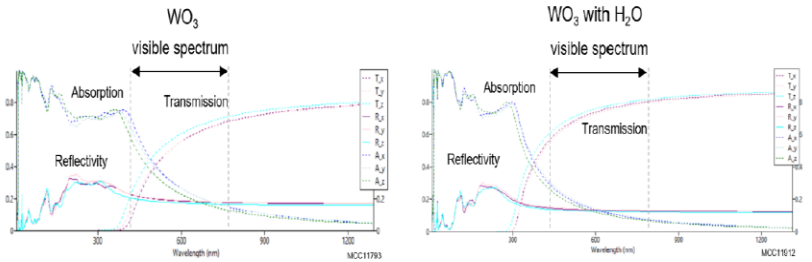

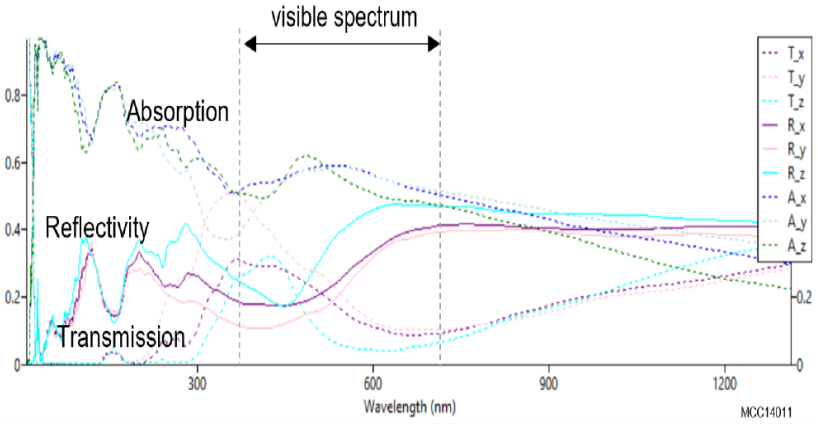

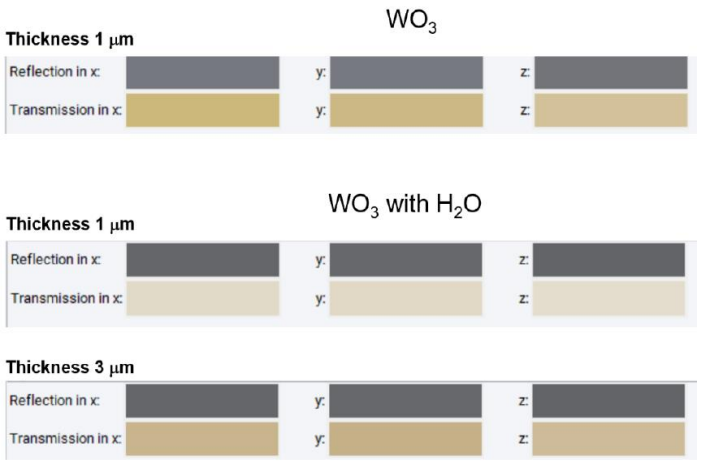

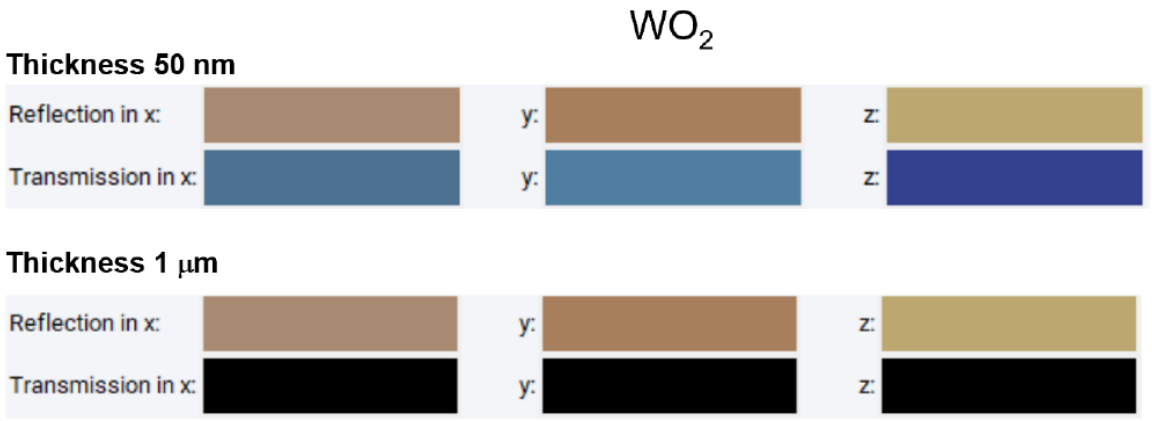

Development MLPs for microstructure modelling of detrititation in W and its oxides based on ~17,000 DFT data of configurations

UK Atomic Energy Authority

R. Jinnouchi, F. Karsai, and G. Kresse, *On-the-Fly Machine Learning Force Field Generation: Application to Melting Points*, Phys. Rev. B **100**, 014105 (2019).

MLPs based on GAPs (VASP 6.4)

System	Number of structures
H_2	102
W-H	3747
WO_2-H	5109
WO_3-H	3455
W-WO_2-H (interfaces)	3359
W-WO_3-H (interfaces)	882
WO_2-WO_3 (interfaces)	428

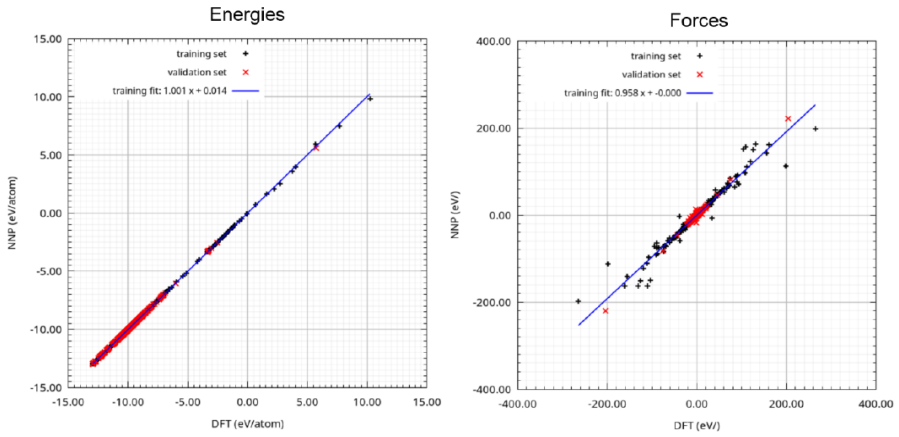

The construction of polycrystalline models is based on a Seed & Growth algorithm and Voronoi decomposition.

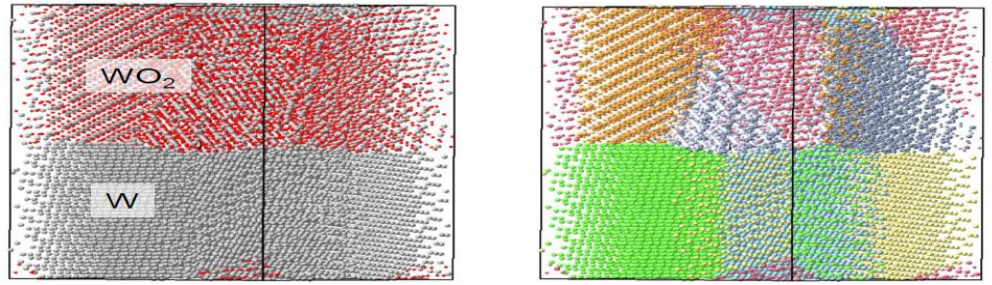

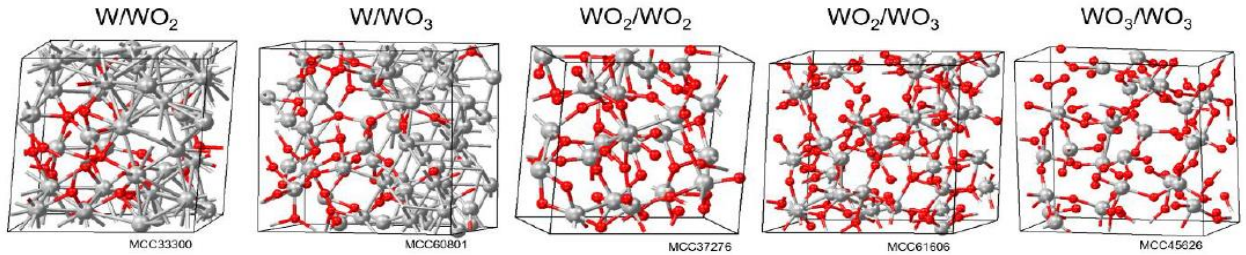

W/WO2 interface

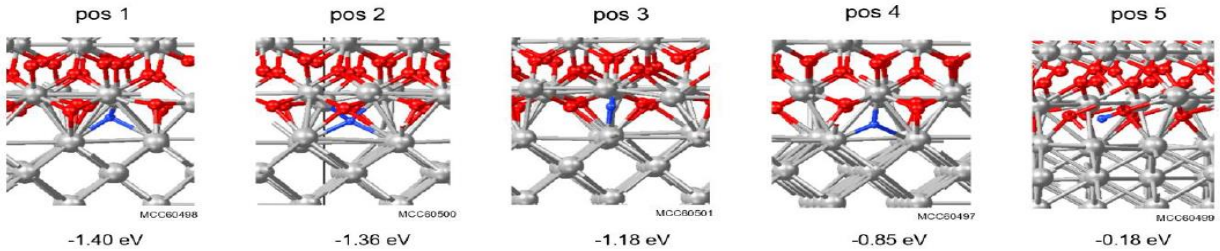

MD simulations using MLPs of tritium diffusion in W & oxides

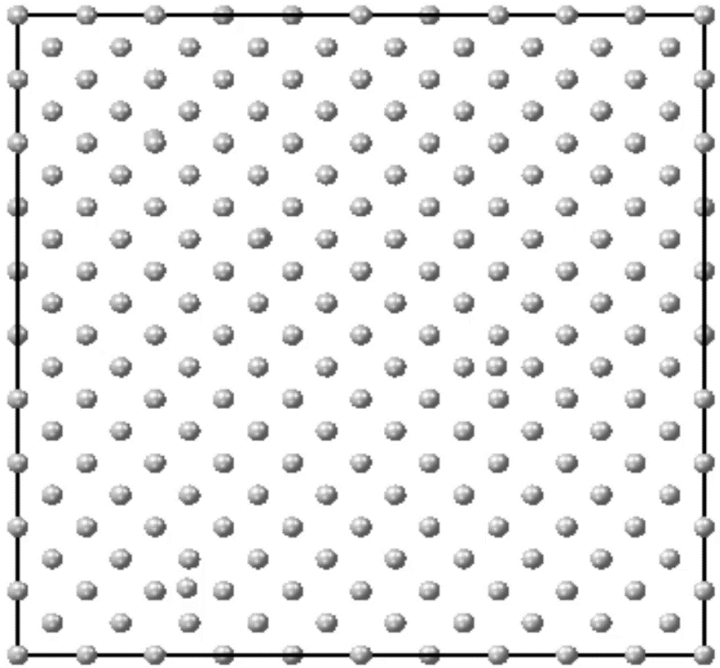

300 ps MD simulation at 700 K of 40 SIAs in a 16000 atom model. Many of the SIAs have formed clusters. A few SIAs are still isolated crowdions. The SIA interaction energy E_{SIA_SIA} = -3.4 eV.

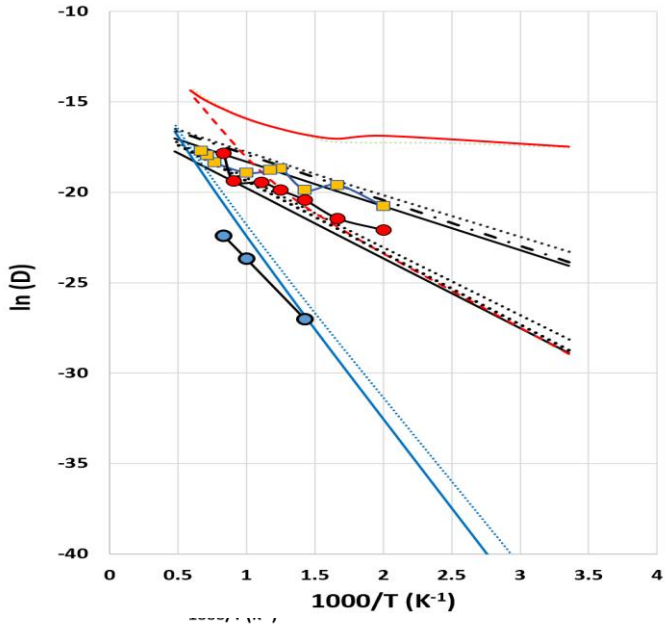

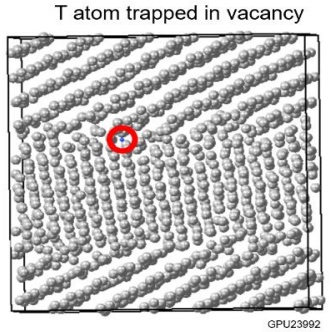

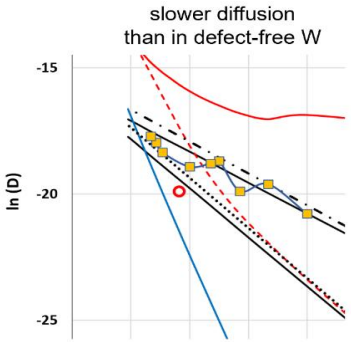

Diffusion simulation at T = 1100 K of tritium at coherent grain boundary

T diffusion at W(100)/W(110) grain boundary model in W

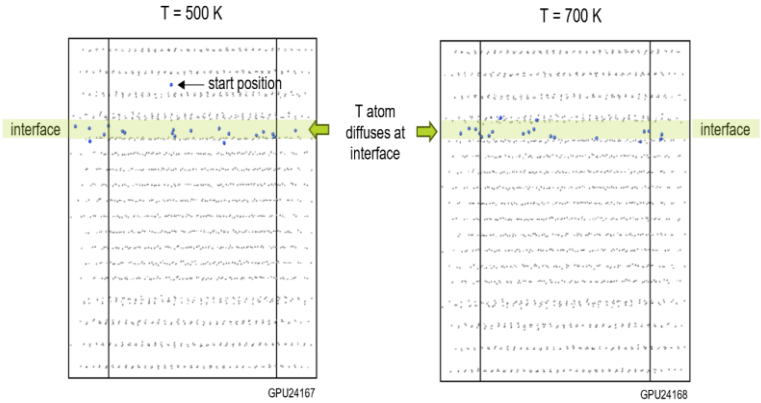

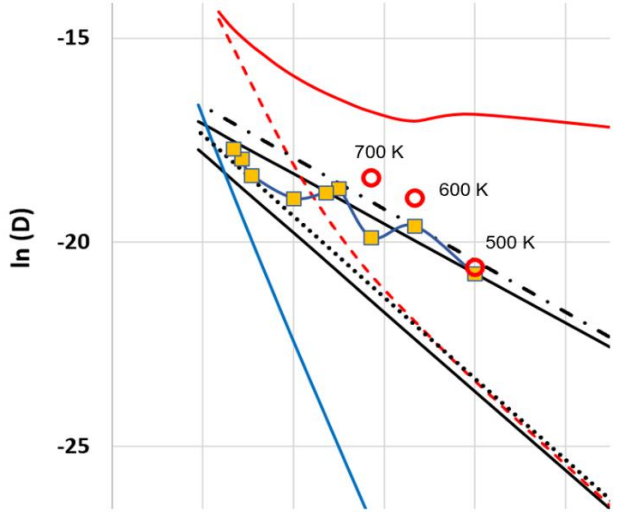

T diffusion at interfaces W/WO2

W-terminated interface

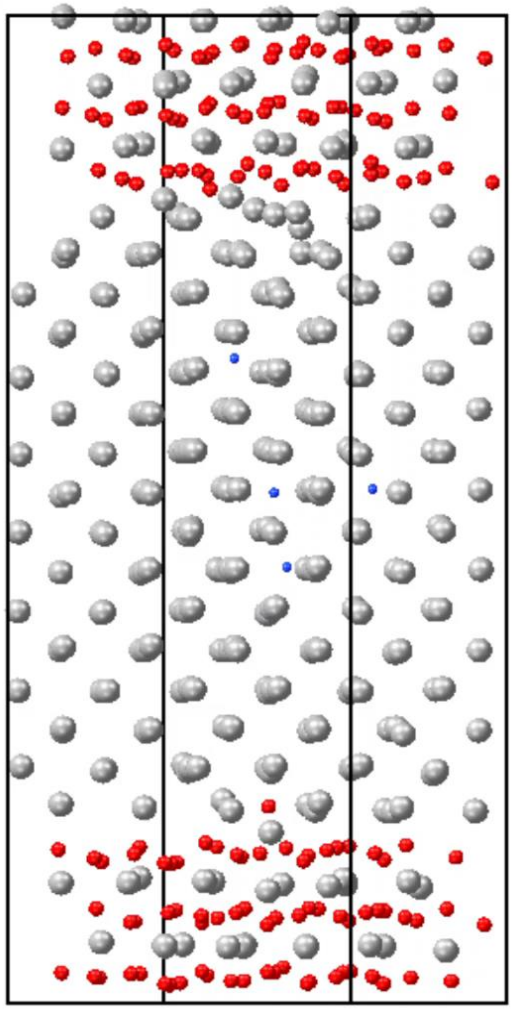

MD simulations at T=700K

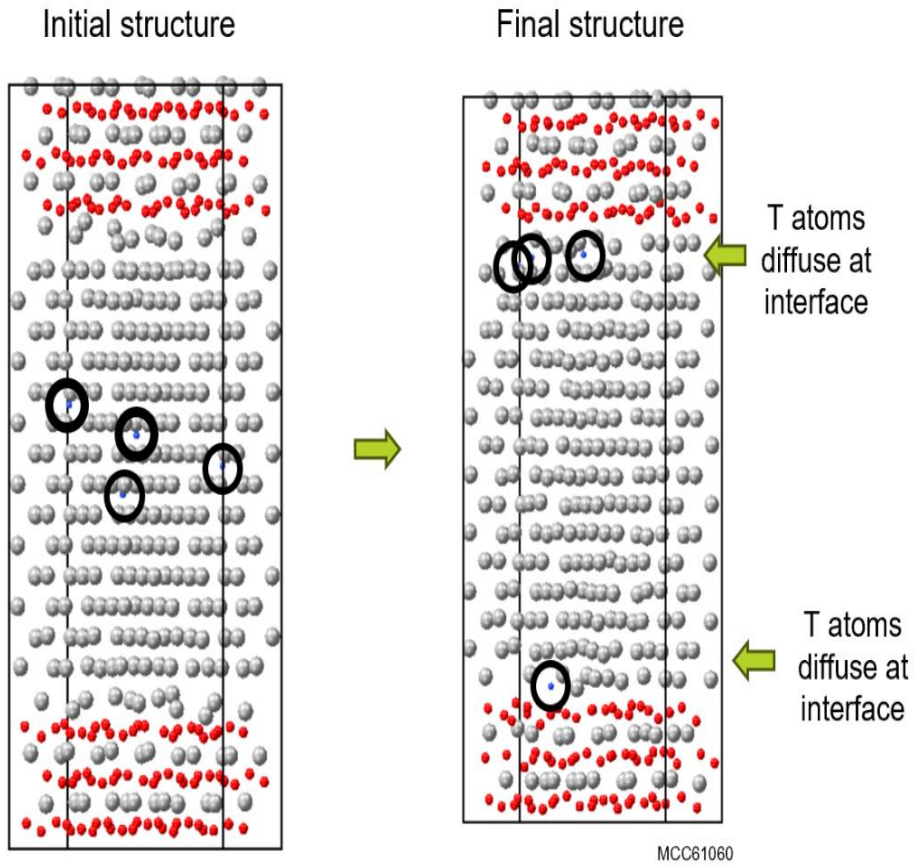

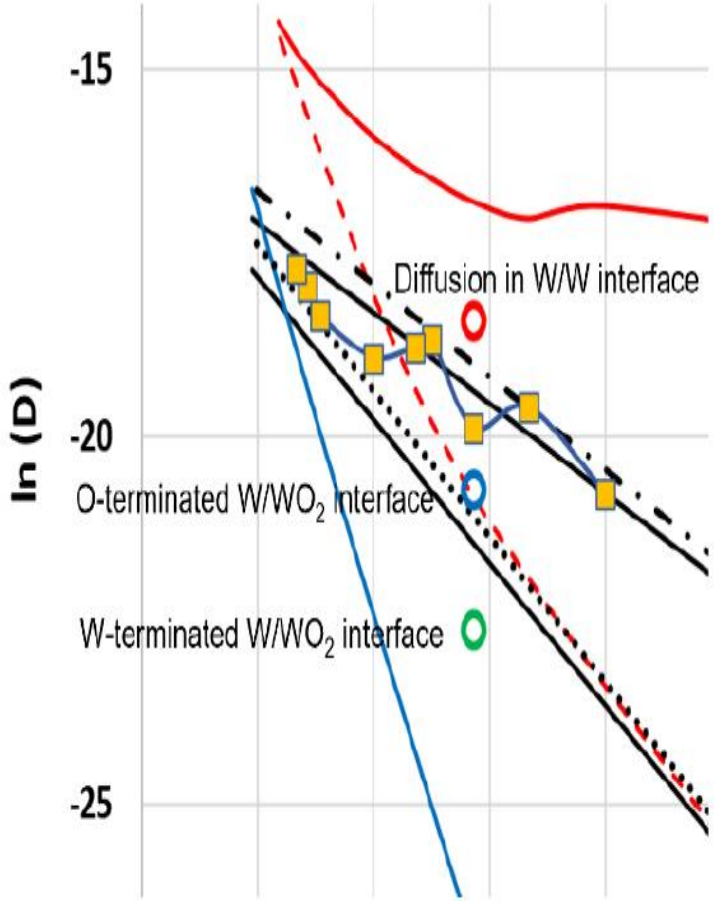

Tritium diffusion and trapping at W/WO3 interface

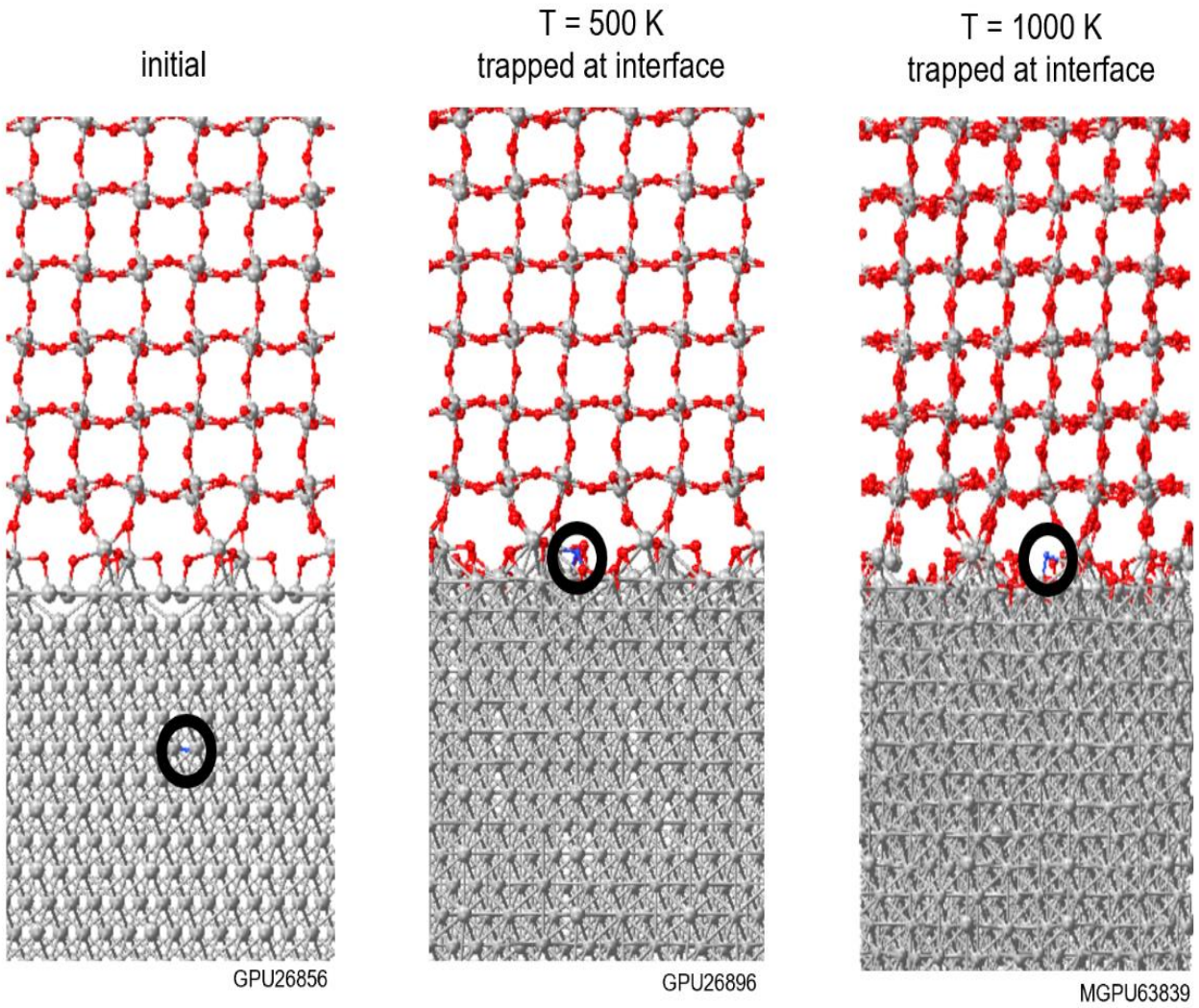

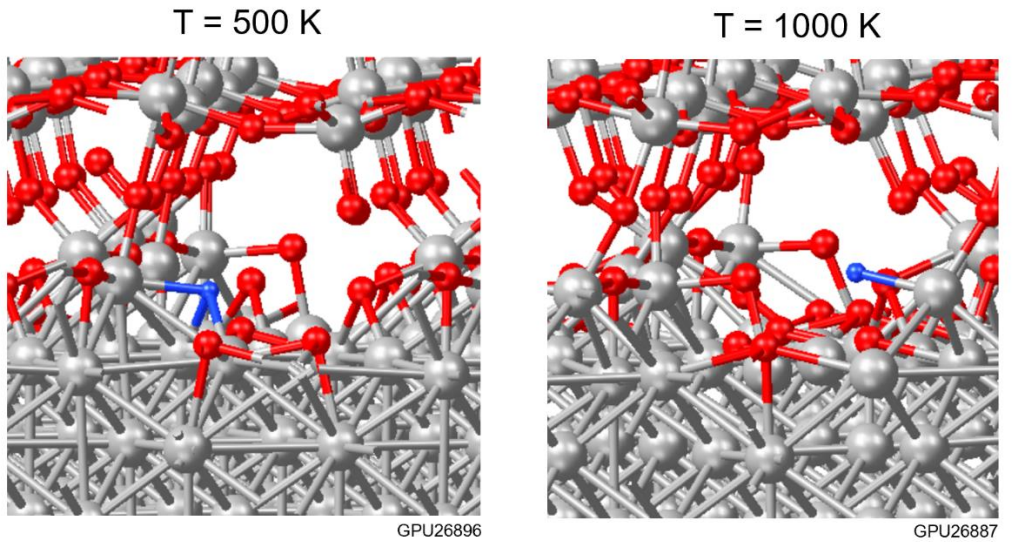

Diffusion simulation of T at a W/WO_3 interface. The T atom diffuses from the bulk of the W phase to the W/WO_3 interface where it gets trapped. Ther trapping sites are similar for the T = 500 K and T = 1000 K simulations.

Multi-scale approach to model T retention and permeation and extraction in fusion reactor materials

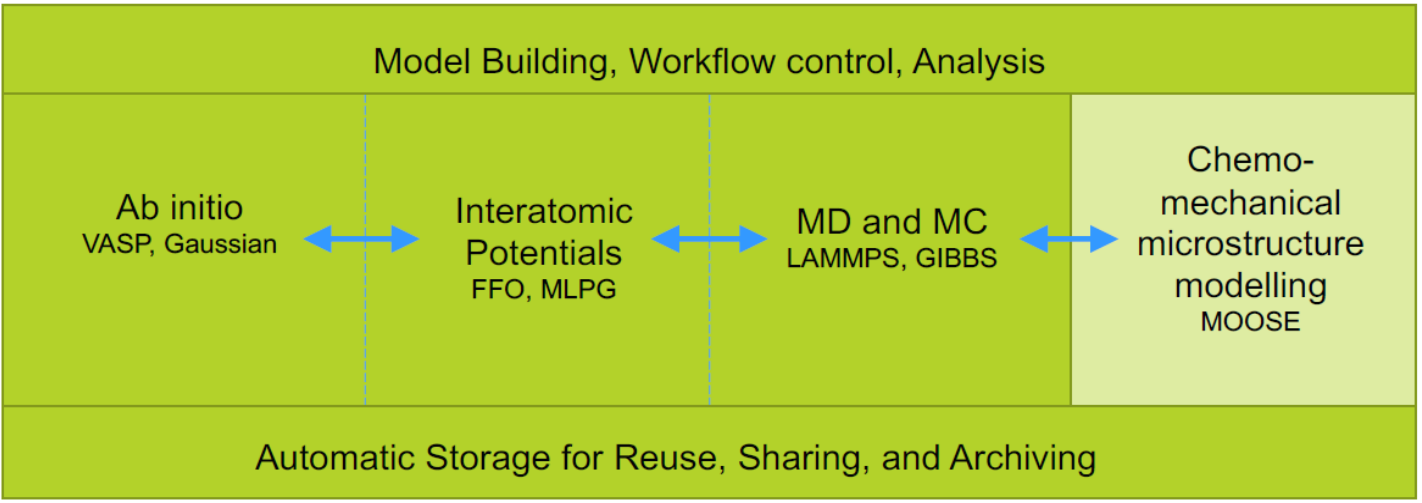

	B (GPa)	G (GPa)	E (GP
W			
Expt. (0 K) (Fetherston)	314	163	418
Expt. (300 K) (Fetherston)	311	160	410
this work	308	152	393
Qian et al.	303	148	383
Wu et al.	318	154	397
WO_2			
this work	301	133	347
$W_{18}O_{49}$			
this work	203	103	263
WO_3			
Expt. (Besozzi)	-	50	127
Expt. (Polcar)	-	-	110
this work	59	49	114

Driving forces

$$F = \int dV \left[f_{chemical} + f_{interface} + f_{elastic} + f_{nucleation}\right]$$

$$\frac{\partial c}{\partial t} = \nabla M(c, \eta, \boldsymbol{\sigma}, d) \nabla \frac{\delta F}{\delta c}$$

$$\frac{\partial \eta}{\partial t} = -L \nabla \frac{\delta F}{\delta \eta}$$

$$\nabla \cdot \boldsymbol{\sigma} = \mathbf{0}$$

Update

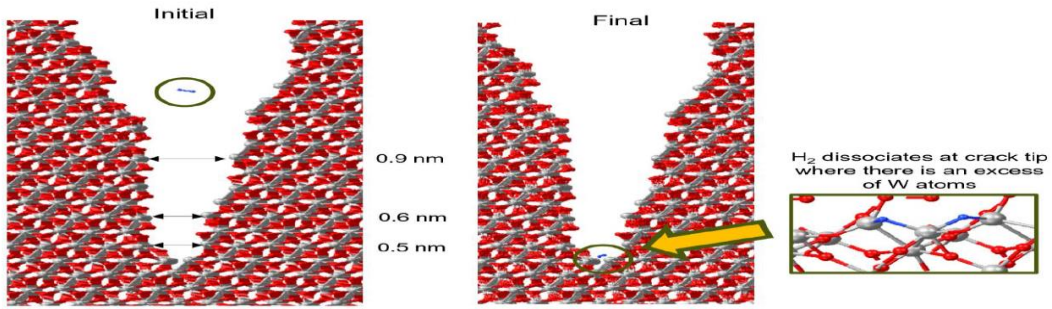

Phase field from first-principles modelling

UK Atomic Energy Authority

Diffusion

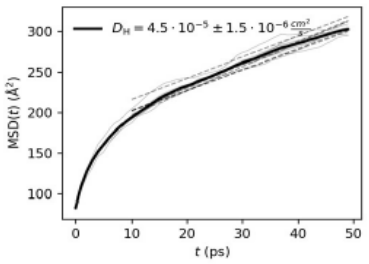

Free energy

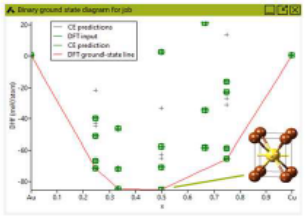

$$E = N \sum_F d_F \Pi_F(\mathbf{s})$$

Interfaces

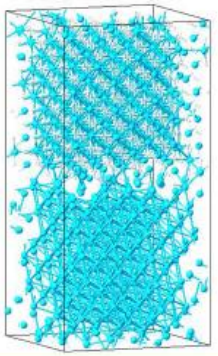

Elastic energy

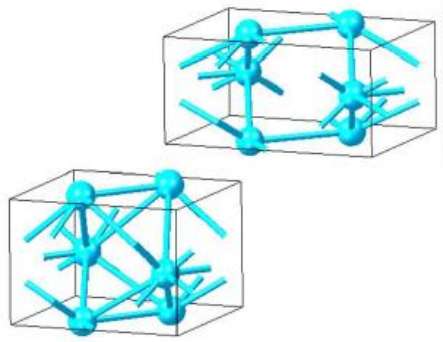

The energy becomes a functional of the order parameters, concentration variables, and other fields

Driving forces

$$F = \int dV \left[f_{chemical} + f_{interface} + f_{elastic} + f_{nucleation} \right]$$

$$\frac{\partial c}{\partial t} = \nabla M(c, \eta, \boldsymbol{\sigma}, d) \nabla \frac{\delta F}{\delta c}$$

$$\frac{\partial \eta}{\partial t} = -L \nabla \frac{\delta F}{\delta \eta}$$

$$\nabla \cdot \boldsymbol{\sigma} = \mathbf{0}$$

Update

Different PDEs are numerically solved, and fields are propagated in time to minimize the functional (e.g., Fick's diffusion equation, Allen-Cahn equation, etc):

Multi-physics and multi-scale modelling

UK Atomic Energy Authority

To move further up length and timescales, we must coarse-grain away information about atom positions and move towards a continuum approach where phases are represented as fields

$$\eta_A = \begin{cases} 1 & \text{Phase A} \\ 0 & \text{other phases} \end{cases}$$

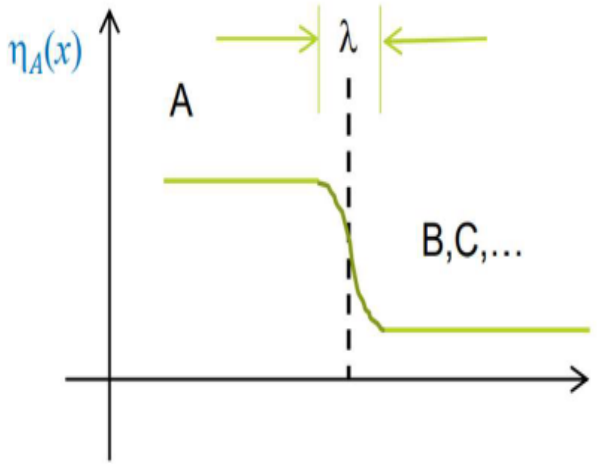

Order parameters (η_A) are used to delineate different **phases**/grains
→ Phase field

Phase field

Flux

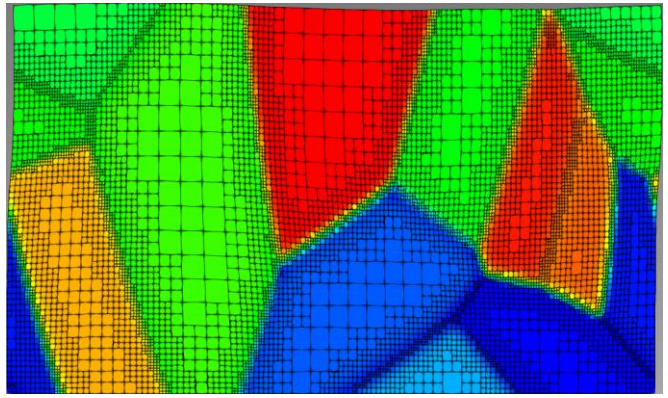

From phase field equations to adaptive mesh using finite element method (FEM)

MLPs from first-principles data base

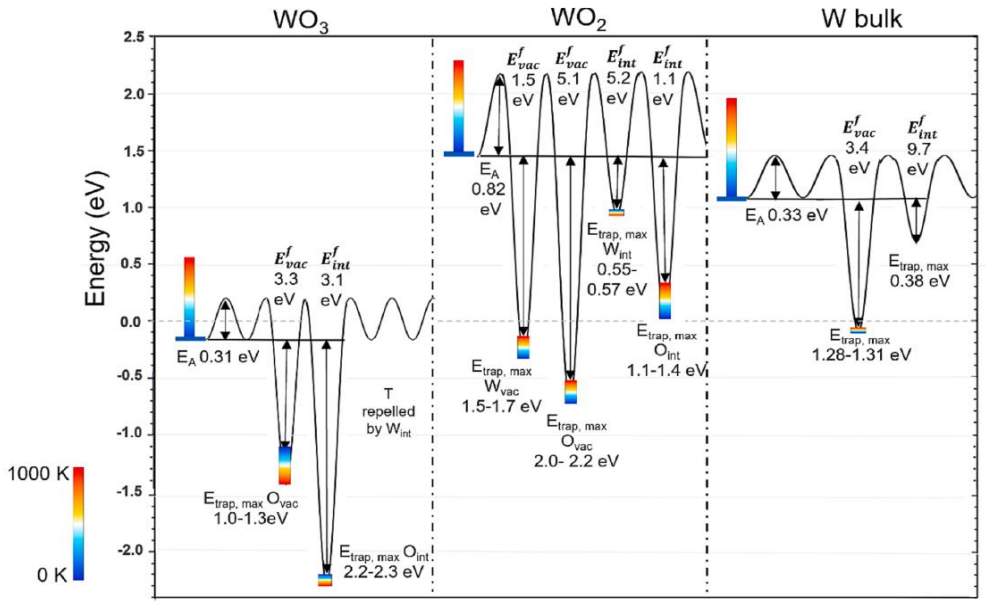

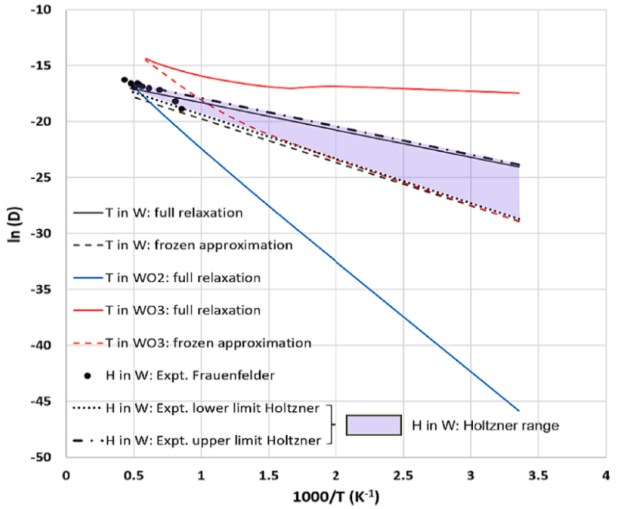

https://doi.org/10.1016/j.nme.2024.101611

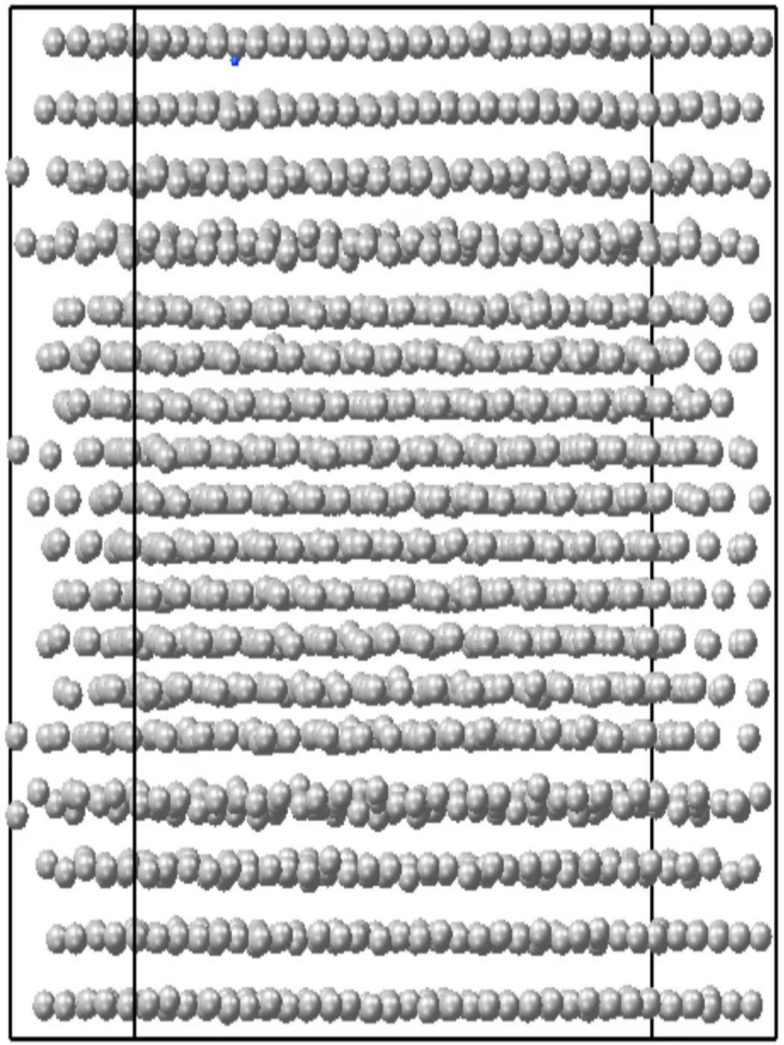

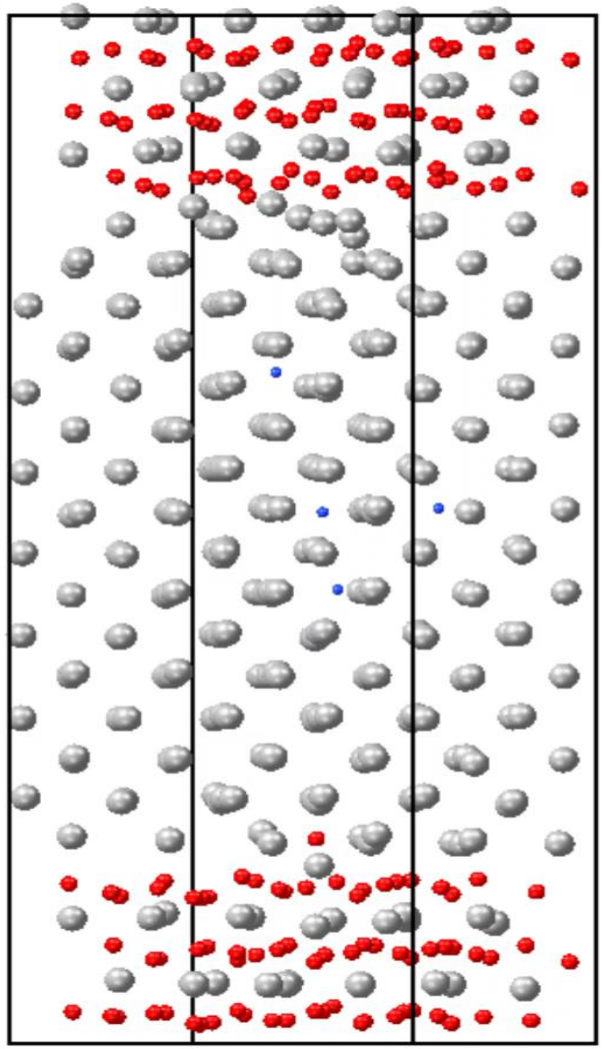

WO_3 & W: 1D oxidation modeling at 600K: simulation and initial kinetics curve

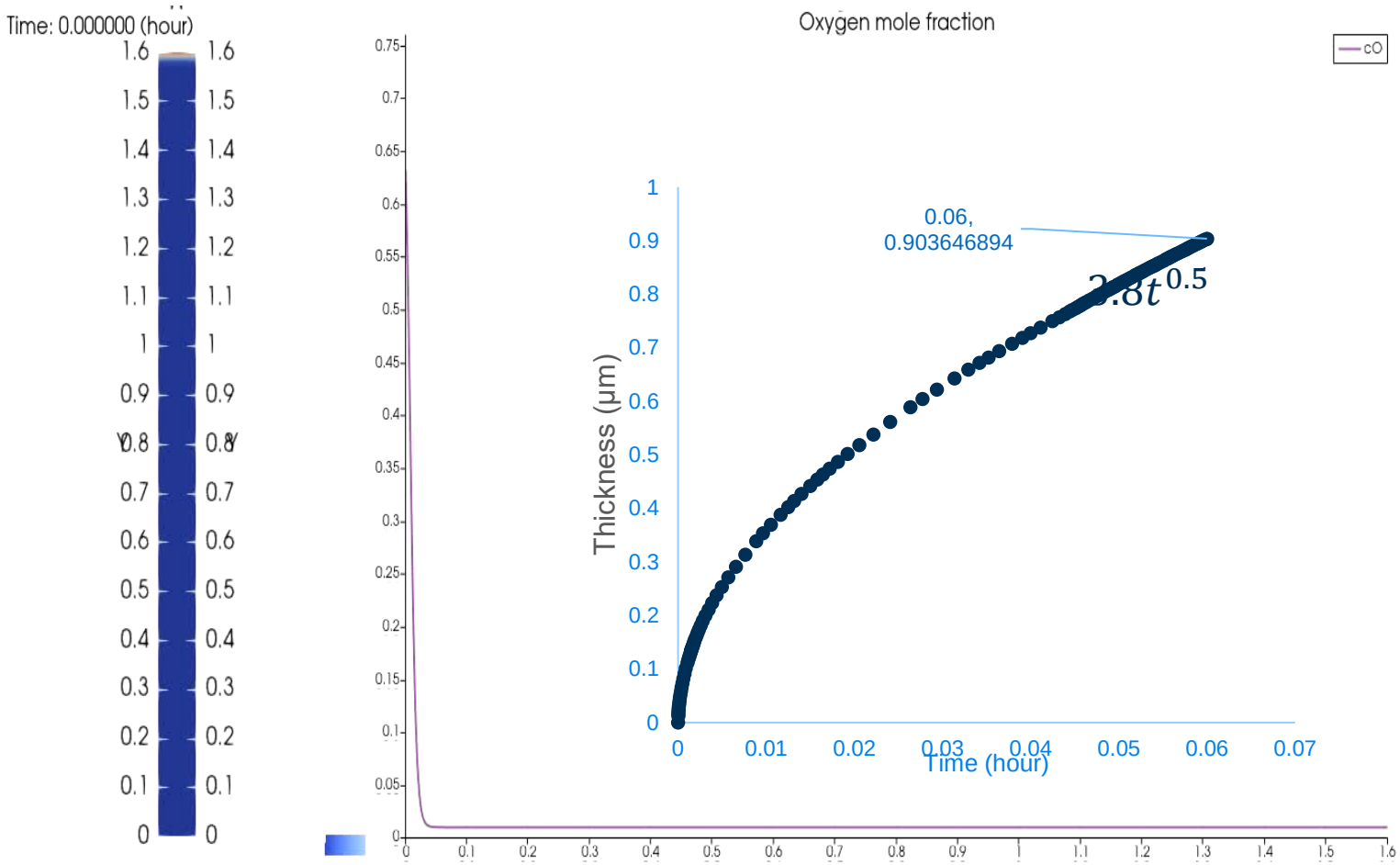

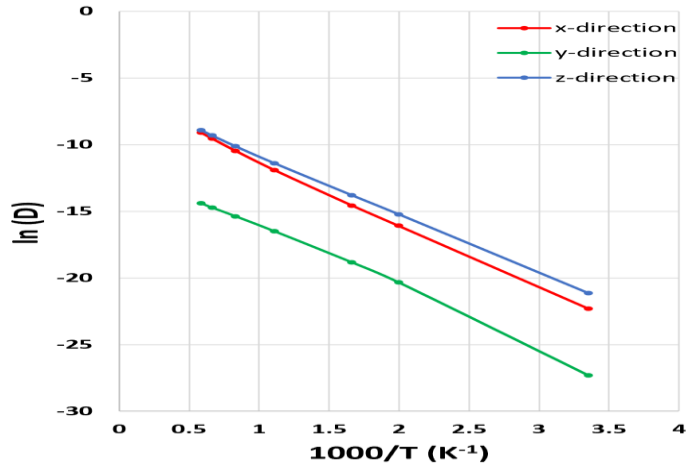

Diffusion coefficients

x-direction: $D_0 = 1.51\times10^{-3}$ m^2/s

$E_A = 0.41$ eV

y-direction: $D_0 = 1.04\times10^{-5}$ m^2/s

$E_A = 0.40$ eV

z-direction: $D_0 = 1.60\times10^{-3}$ m^2/s

$E_A = 0.38$ eV

Simulation of 3 phase system (W, WO_3 & $W_{18}O_{49}$) with interface nucleation & chemical driving forces

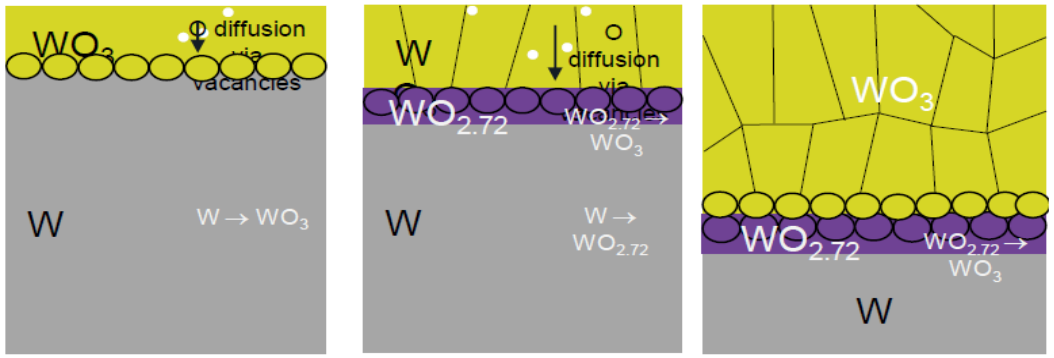

- Heterogeneous nucleation of WO_3 at the W/WO_3 interface is responsible for WO_3 grains
- Followed by nucleation of $W_{18}O_{49}$ at the W/WO_3 interface
- There is a potential to nucleate $W_{18}O_{49}$ grains at the W/ $W_{18}O_{49}$ interface
- WO_3 grains continue to nucleate at $W_{18}O_{49}$ /WO_3 interface as oxide grows

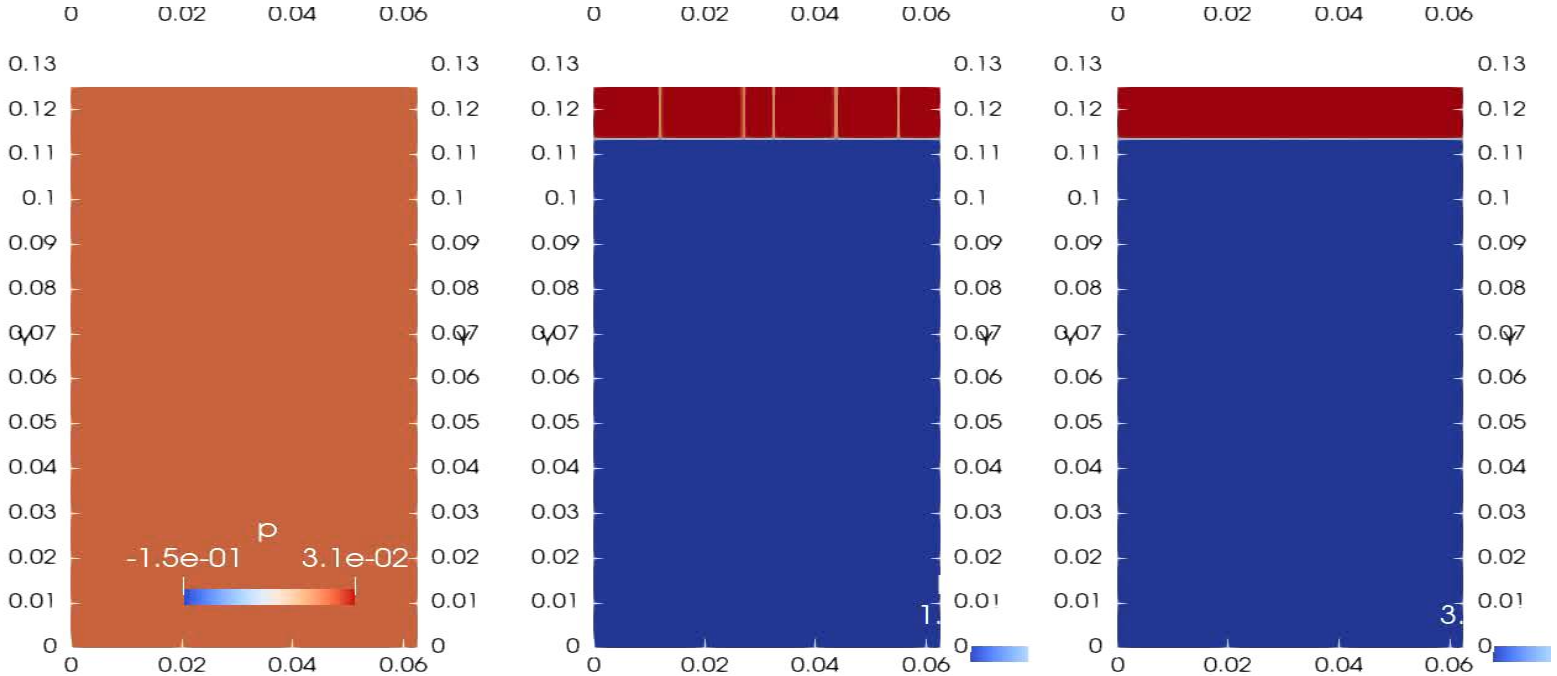

1) Pressure
2) Grain/Void distribution
3) Phase distribution

Crack modelling at W/W oxide interfaces with different Pilling-Bedworth ratios

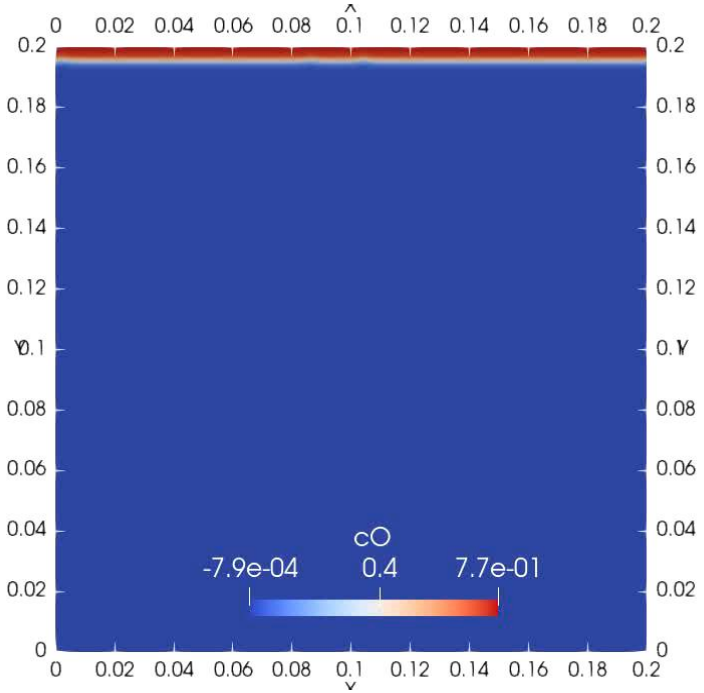

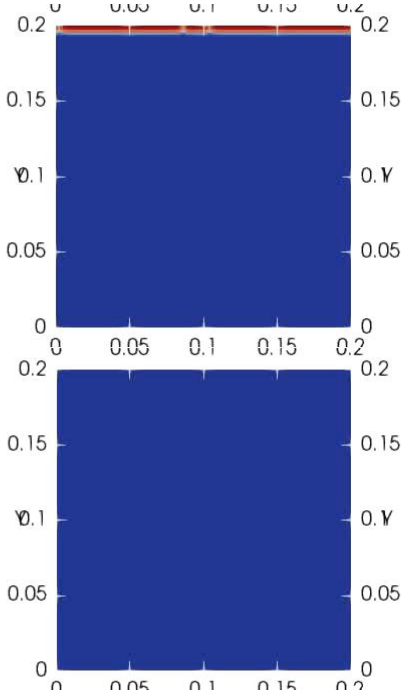

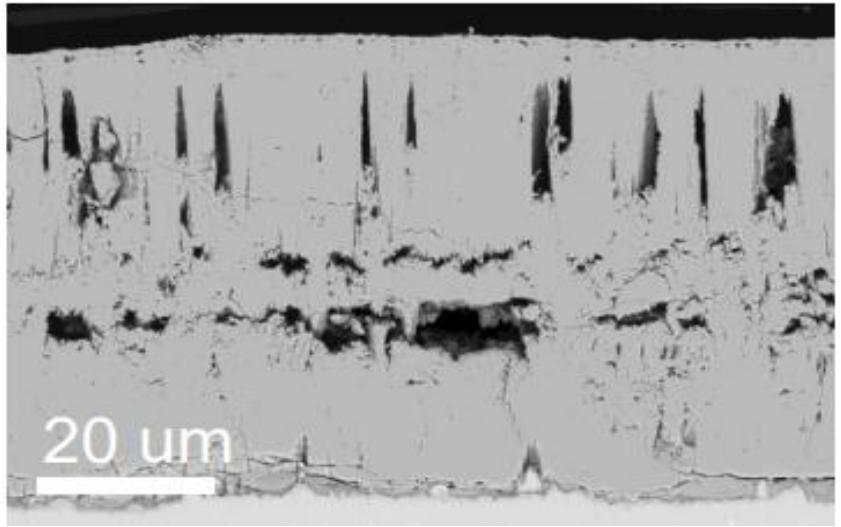

From the STEP samples, it seems like one of the most probable nucleation sights for voids is at the WO_3 / WO_x interface

Regions near cracks show high concentrations of oxygen

$$\text{PBR} = \frac{V_{oxide}}{V_{metal}}$$

Role of crack on oxidation grows from parabolic to linear transition regime

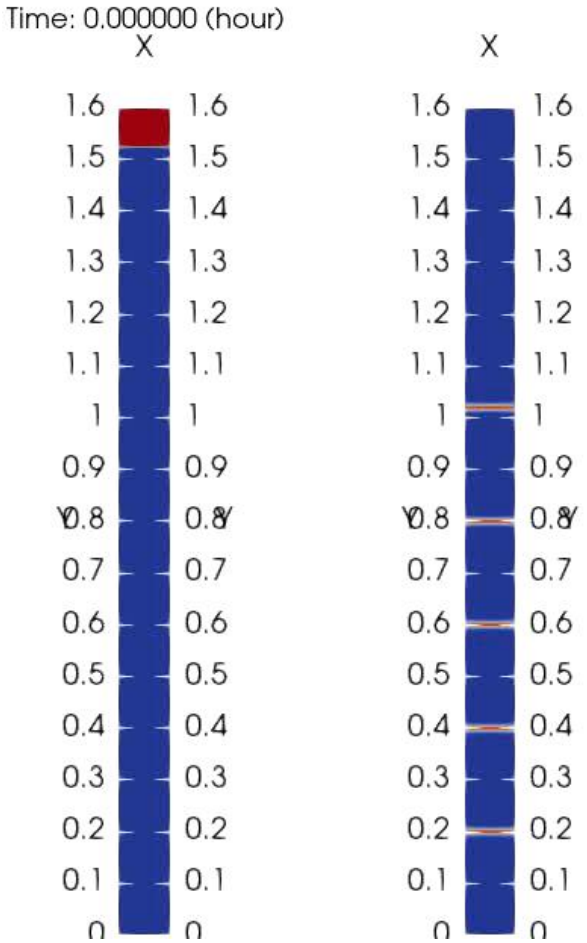

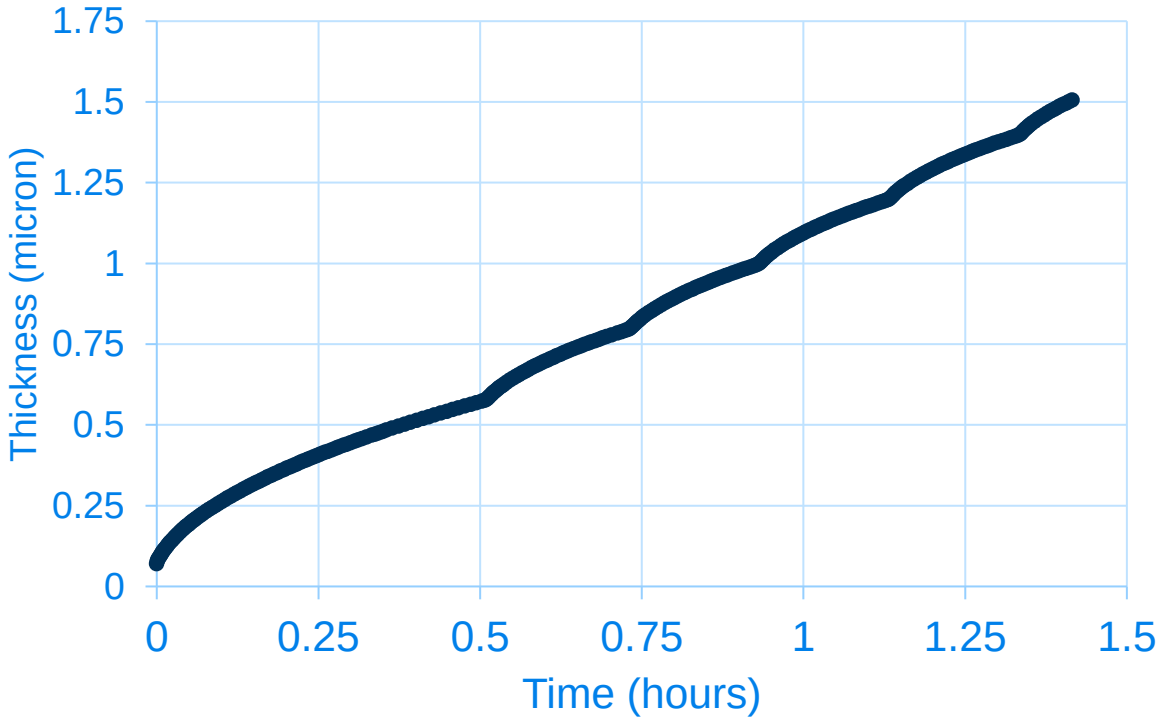

To decrease computation time, we artificially introduced cracks spaced 0.2 microns apart. The cracks only act as sources once the oxide grows over them.

H segregation to WO_3 (010)/(001) grain boundary

UK Atomic Energy Authority

Grain boundary 1 (WO-O terminated)

site 1

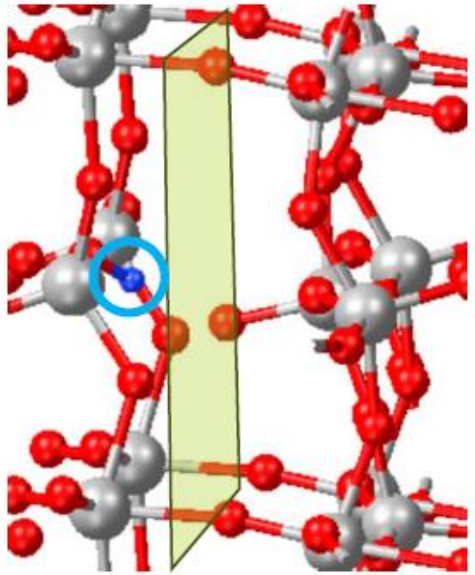

$E_{segr.}$ = -1.09 eV

site 2

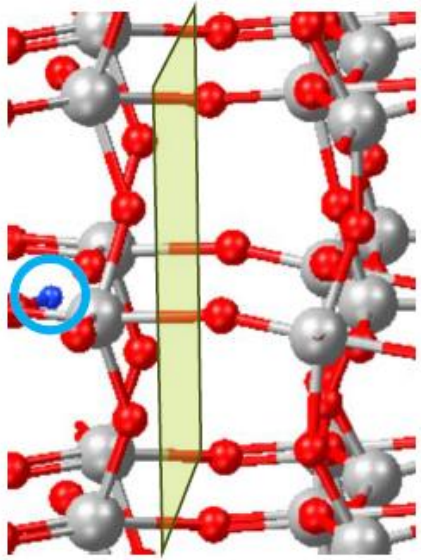

$E_{segr.}$ = -2.12 eV

H rotates in towards

Grain boundary 2 (WO-WO terminated)

site 1

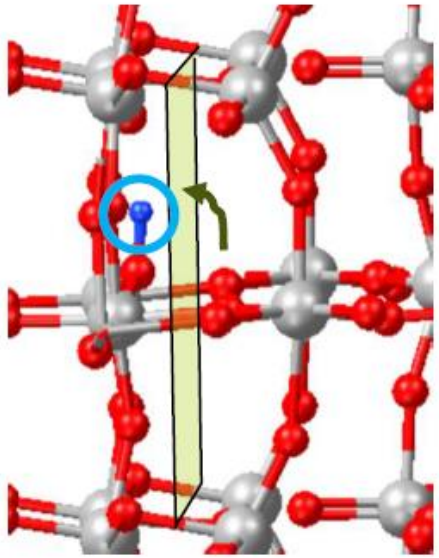

$E_{segr.}$ = 0.10 eV

H rotates in from GB

site 2

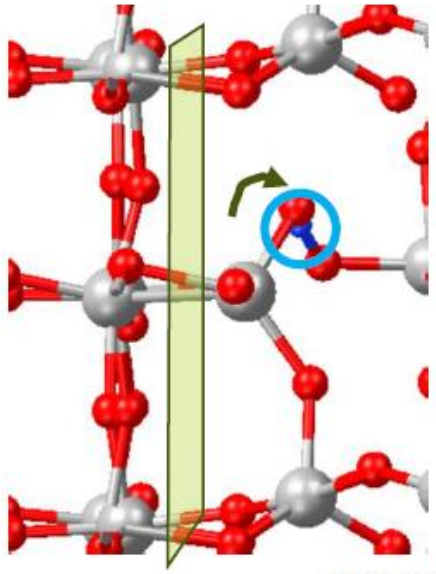

$E_{segr.}$ = 0.24 eV

H rotates in from GB

Tritium transport modelling at W/WO3 interface

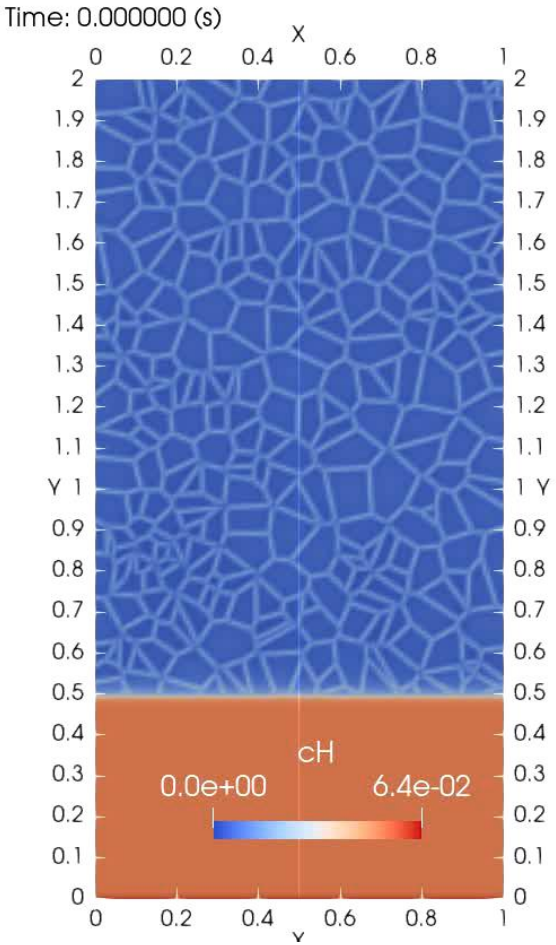

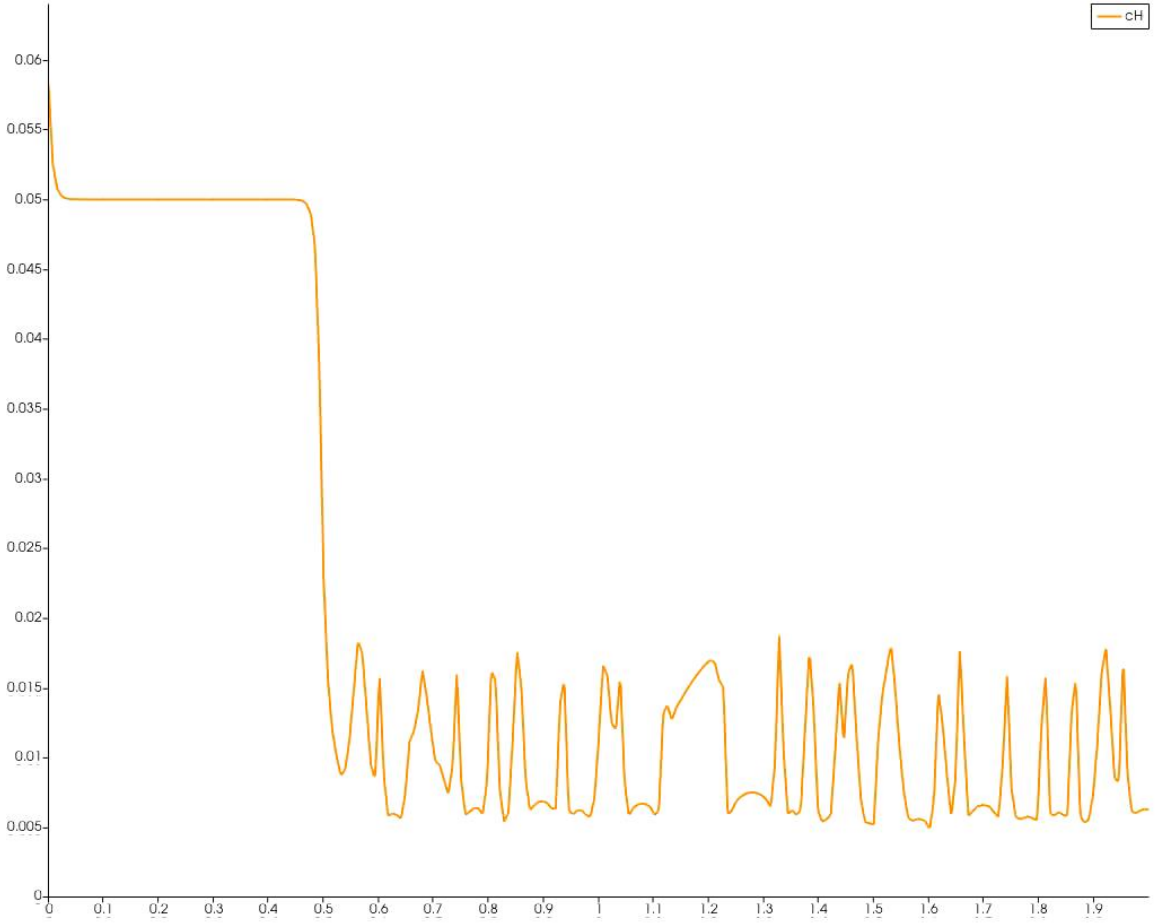

- The oxide grains act as a significant trap for tritium.
- The amount of tritium that is stored scales with the surface area density of the trioxide grains
- Trapping at tungsten vacancies may also be a source of significant trapping in the tungsten & oxide grains, but this effect has not yet been included in the model.

Summary

- Assuming there are no trapping, the presence of a dense, adherent WO_2 oxide layer on substrate surfaces could act to retain T within the substrate and could impede T extraction. On the other hand, a purely WO_3 surface oxide with no underlying WO_2 stratum likely would present fewer difficulties. These facts suggest **that a strategy to create an oxidising environment favouring WO_3 formation over WO_2 may facilitate efficient T extraction**.
- Conversely, if a dense (without transverse cracks or large voids) and adherent **WO_2 surface oxide were in place prior to T exposure, it could serve to limit T uptake by W components**. Subsequently, components could be heated in an oxidising atmosphere to convert the pre-existing WO_2 layer into WO_3, in order to facilitate T extraction.
- If W surface oxides formed during preceding service cycles are not removed from W system components between service cycles, **high-energy neutron fluxes likely will produce high W and O vacancy and interstitial concentrations within them. Such point defects in WO_x are capacious T traps with predicted strong free binding energies**
- Current development of **MLPs allow not only to investigate deeper microstructure evolution of HI diffusion at grain boundaries and interface between W and different oxides layers** but also **influence of oxidation cracking and formation of voids on HI retention** via chemo-mechanical 3D simulations at macroscopic scale